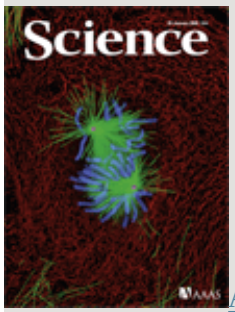

About the Cover

20 January 2006
Vol 311, Issue 5759, Pages 299-399

- Author Index
- Subject Index
- Set E-Mail Alerts
- Order an Issue/Article
- RSS Feeds

Search the Journal
Enter Keyword

Select Issue

Issue Highlights

- The Soil Antibiotic Resistome
- Glacier Formation on Mars
- Keeping Chromosomes Aligned
- Impacts of Structural Genomics

Contents

For all checked items

News of the Week

Random Samples
Science 20 January 2006: 313.
|Full Text »

Newsmakers
Science 20 January 2006: 333.
|Full Text »

News Focus

DRUG DEVELOPMENT: Drugs Inspired by a Drug
Jean Marx
Science 20 January 2006: 322-325.
Summary »| Full Text »| PDF »|

ARCHAEOLOGY: Rising Water Poses Threat to Egypt's Antiquities
Andrew Lawler
Science 20 January 2006: 326-327.
Summary »| Full Text »| PDF »|

ARCHAEOLOGY: Archaeological Pharaoh Sets Determined Course for Egypt
Andrew Lawler
Science 20 January 2006: 326-327.
Summary »| Full Text »| PDF »|

BIOMEDICAL TRAINING PROGRAMS: NIH Told to Get Serious About Giving Minorities a Hand
Jeffrey Mervis
Science 20 January 2006: 328-329.
Summary »| Full Text »| PDF »|

BIOMEDICAL TRAINING PROGRAMS: Will This Bridge Take Me to the Lab?
Jeffrey Mervis
Science 20 January 2006: 329.
Summary »| Full Text »| PDF »|

SOCIETY FOR INTEGRATIVE AND COMPARATIVE BIOLOGY MEETING: Sea Slug Inks Its Way to Safety
Elizabeth Pennisi
Science 20 January 2006: 330-331.
Summary »| Full Text »| PDF »|

SOCIETY FOR INTEGRATIVE AND COMPARATIVE BIOLOGY MEETING: Was Lucy's a Fighting Family? Look at Her Legs
Elizabeth Pennisi
Science 20 January 2006: 330.
Summary »| Full Text »| PDF »|

SOCIETY FOR INTEGRATIVE AND COMPARATIVE BIOLOGY MEETING: Water Launches Spores Like a Rocket
Elizabeth Pennisi
Science 20 January 2006: 331.
Summary »| Full Text »| PDF »|

SOCIETY FOR INTEGRATIVE AND COMPARATIVE BIOLOGY MEETING: Crab, Raccoon Play Tag Team Against Turtle
Elizabeth Pennisi
Science 20 January 2006: 331.
Summary »| Full Text »| PDF »|

Letters

This Week's Letters
Science 20 January 2006: 335.
Summary »| PDF »|

Editorial Retraction
Donald Kennedy
Science 20 January 2006: 335.
Published online 12 January 2006 [DOI: 10.1126/science.1124926] (in *Science* Express Letters)
Full Text »| PDF »|

Madison and Climate Change Policy
Jonathan B. Wiener, Richard B. Stewart, James K. Hammitt, Jean-Charles Hourcade;, David G. Victor, Joshua C. House, and Sarah Joy
Science 20 January 2006: 335-336.
Full Text »| PDF »|

Advising on Publication
Stewart Simonson
Science 20 January 2006: 336-337.
Full Text »| PDF »|

HIV Prevention in Adolescents
Rose E. Frisch
Science 20 January 2006: 337.
Full Text »| PDF »|

Corrections and Clarifications
Science 20 January 2006: 337.
Full Text »| PDF »|

Books *et al.*

CHEMISTRY: Light Scattered by Air
Gerald R. Van Hecke
Science 20 January 2006: 338-339.
Summary »| Full Text »| PDF »|

NEUROSCIENCE: Linking Neurons and Ethics
Xavier Bosch
Science 20 January 2006: 339.
Summary »| Full Text »| PDF »|

Books Received
Science 20 January 2006: 339.
Summary »|

Policy Forum

PLANETARY SCIENCE: Risks in Space from Orbiting Debris
J.-C. Liou and N. L. Johnson
Science 20 January 2006: 340-341.
Summary »| Full Text »| PDF »|

Perspectives

MICROBIOLOGY: Weapons of Microbial Drug Resistance Abound in Soil Flora
Alexander Tomasz

Review

Brevia

Reports

Science 20 January 2006: 359-361.
Lorentz microscopy shows that helical spin order groups of electronic spins oriented in a helix in different crystallographic layers is greatly influenced by defects in a crystal.
Abstract »| Full Text »| PDF »| Supporting Online Material »|

Solvent-Free Oxidation of Primary Alcohols to Aldehydes Using Au-Pd/TiO_2 Catalysts

Dan I. Enache, Jennifer K. Edwards, Philip Landon, Benjamin Solsona-Espriu, Albert F. Carley, Andrew A. Herzing, Masashi Watanabe, Christopher J. Kiely, David W. Knight, and Graham J. Hutchings
Science 20 January 2006: 362-365.
Gold-palladium nanocrystals on titanium dioxide efficiently catalyze aldehyde synthesis from primary alcohols, an important class of industrial reactions.
Abstract »| Full Text »| PDF »| Supporting Online Material »|

Internal Rotation and Spin Conversion of CH_3OH in Solid para-Hydrogen

Yuan-Pern Lee, Yu-Jong Wu, R. M. Lees, Li-Hong Xu, and Jon T. Hougen
Science 20 January 2006: 365-368.
Methanol in a para-hydrogen matrix can still undergo internal torsion, revealing spin conversions that are obscured in more complex gas-phase spectra.
Abstract »| Full Text »| PDF »|

Formation of Glaciers on Mars by Atmospheric Precipitation at High Obliquity
F. Forget, R. M. Haberle, F. Montmessin, B. Levrard, and J. W. Head
Science 20 January 2006: 368-371.
Climate simulations show that when Mars' axis was tilted by 45° in the recent past, water ice glaciers could have formed on the flanks of Mars' large volcanoes where glacial deposits are now seen.
Abstract »| Full Text »| PDF »| Supporting Online Material »|

South-Seeking Magnetotactic Bacteria in the Northern Hemisphere
Sheri L. Simmons, Dennis A. Bazylinski, and Katrina J. Edwards
Science 20 January 2006: 371-374.
It has been assumed that marine bacteria in the northern hemisphere all swim toward magnetic north, but blooms of south-seeking ones are actually mixed in.
Abstract »| Full Text »| PDF »| Supporting Online Material »|

Sampling the Antibiotic Resistome
Vanessa M. D'Costa, Katherine M. McGrann, Donald W. Hughes, and Gerard D. Wright
Science 20 January 2006: 374-377.
Of 480 bacterial strains isolated from diverse soil samples, each was resistant to at least seven antibiotics and some to as many as 20.
Abstract »| Full Text »| PDF »| Supporting Online Material »|

Vaccinia Virus-Induced Cell Motility Requires F11L-Mediated Inhibition of RhoA Signaling
Ferran Valderrama, João V. Cordeiro, Sibylle Schleich, Friedrich Frischknecht, and Michael Way
Science 20 January 2006: 377-381.
Vaccinia virus causes infected cells to migrate and alters their adhesion properties by rearranging the actin cytoskeleton.
Abstract »| Full Text »| PDF »| Supporting Online Material »|

Core Knowledge of Geometry in an Amazonian Indigene Group
Stanislas Dehaene, Véronique Izard, Pierre Pica, and Elizabeth Spelke
Science 20 January 2006: 381-384.
Children and adults of an indigenous group from Amazonia use geometrical concepts despite the lack of specific words to describe them.
Abstract »| Full Text »| PDF »| Supporting Online Material »|

A Molecular Framework for Plant Regeneration
Jian Xu, Hugo Hofhuis, Renze Heidstra, Michael Sauer, Jirí Friml, and Ben Scheres

Science 20 January 2006: 385-388.
After a plant is wounded, flow of a growth factor in plant roots is disrupted, causing differentiation of cells that then redirect the growth factor to trigger regeneration.
Abstract »| Full Text »| PDF »| Supporting Online Material »|

Chromosomes Can Congress to the Metaphase Plate Before Biorientation
Tarun M. Kapoor, Michael A. Lampson, Polla Hergert, Lisa Cameron, Daniela Cimini, E. D. Salmon, Bruce F. McEwen, and Alexey Khodjakov
Science 20 January 2006: 388-391.
During mitosis, duplicated chromosomes pulled by a fiber toward one pole of the cell move back to the middle by hitching a ride on a fiber of an already-positioned chromosome set.
Abstract »| Full Text »| PDF »| Supporting Online Material »|

Metagenomics to Paleogenomics: Large-Scale Sequencing of Mammoth DNA
Hendrik N. Poinar, Carsten Schwarz, Ji Qi, Beth Shapiro, Ross D. E. MacPhee, Bernard Buigues, Alexei Tikhonov, Daniel H. Huson, Lynn P. Tomsho, Alexander Auch, Markus Rampp, Webb Miller, and Stephan C. Schuster
Science 20 January 2006: 392-394.
Published online 20 December 2005 [DOI: 10.1126/science.1123360] (in *Science* Express Reports)
Recovery and sequencing of large amounts to mitochondrial and nuclear DNA from an 18,000-year-old mammoth support the evolution of mammoths from elephants about 6 million years ago.
Abstract »| Full Text »| PDF »| Supporting Online Material »|

Methylation of $tRNA^{Asp}$ by the DNA Methyltransferase Homolog Dnmt2
Mary Grace Goll, Finn Kirpekar, Keith A. Maggert, Jeffrey A. Yoder, Chih-Lin Hsieh, Xiaoyu Zhang, Kent G. Golic, Steven E. Jacobsen, and Timothy H. Bestor
Science 20 January 2006: 395-398.
A methyltransferase widely thought to add methyl groups to DNA actually covalently methylates transfer RNA.
Abstract »| Full Text »| PDF »| Supporting Online Material »|

For all checked items

Magnetism with a Twist >>

In helical spin order, the spins in a crystallographic plane of a material tend to align, and this direction rotates by a constant angle between adjacent planes. Knowledge of, and the ability to control, the relative orientation of the magnetic moment between the planes could have important consequences for the flow of spin-controlled current through such a structure. Reciprocal-space imaging probes such as neutron scattering only provide an average view of the overall spin structure. **Uchida *et al.*** (p. 359; see the Perspective by **Nori and Tonomura**), using Lorentz microscopy, found that the real-space structure of helical spin ordering is much richer than that expected from the averaged techniques. They also visualized the real-time dynamics of magnetic defects in response to changes in temperature and magnetic field, which may yield important information for spintronic devices that would rely on this effect.

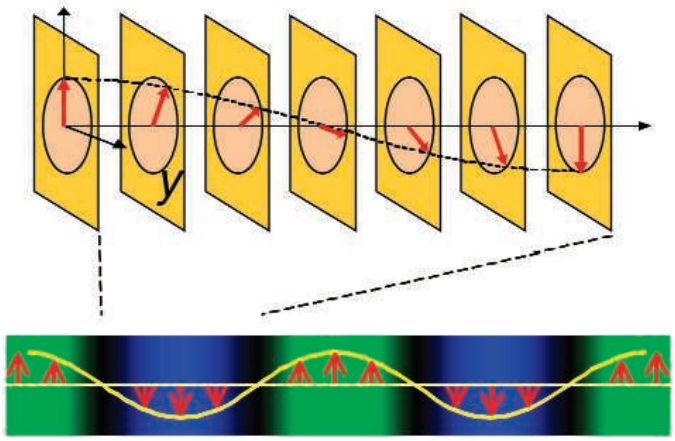

Spotlight on Structural Genomics Centers

Projects in structural genomics aim to expand our structural knowledge of biological macromolecules, while lowering the average costs of structure determination. **Chandonia and Brenner** (p. 347) quantitatively review the novelty, cost, and impact of structures solved by structural genomics centers, and contrast these results with traditional structural biology.

Spinning Membranes from Phospholipids

Electrospinning is a simple but powerful method for making very thin polymer fibers that can then be collected to create porous films. **McKee *et al.*** (p. 353) expand the range of this technique by making fibers from small molecules, namely phospholipids. The phospholipids form wormlike micelles in specific concentration ranges of mixed solvent systems, and under these conditions they behave like polymers for electrospinning. The membranes formed from phospholipids should exhibit high biocompatibility.

Bridging Nanotube Contacts

In molecular electronics, the contacts between metal electrode and molecule are often the weakest link, and it can be difficult at times to exclude changes in this electrode contact as the cause of switching behavior. **Guo *et al.*** (p. 356) show how small gaps (less than 10 nanometers) in single-walled carbon nanotubes (SWNTs) can be bridged covalently with short oligomeric molecules whose conjugation makes them conductive. After metal contacts were made on a SWNT, patterning allowed a gap to be cut between two contacts. This oxidative cutting left terminal carboxylic acid groups that were bridged by making amide linkages to molecules bearing amine groups at each end. The devices formed are robust, and molecules that bear basic nitrogen atoms in the chain changed conductance with pH.

Restricted Motion

The assignment of gas-phase spectra to specific atomic motions for molecules with even as few as five or six atoms can prove challenging. Such assignments are of particular interest in piecing together the interactions of molecules in deep space, for which spectroscopic signatures are the sole source of data. **Lee *et al.*** (p. 365) take advantage of the unusual properties of solid para-hydrogen (p-H_2) to simplify, and thus interpret, the vibrational spectrum of methanol. By embedding methanol in a matrix of the quantum solid, they prevent overall rotational motion but still observe internal torsion of the methyl group about the C–O bond.

Mist-Made Martian Glaciers

Water ice glaciers flank mountains and volcanoes in the tropics and midlatitudes of Mars. Current conditions on Mars are cold and dry and restrict water ice to regions near the poles, so the origin of these young glaciers at lower latitudes is a puzzle. **Forget *et al.*** (p. 368) used climate simulations of the planet at high obliquity to explain the locations of the glaciers. A few million years ago, the rotation axis of Mars was tilted by up to 45°, which caused more water vapor to evaporate from the poles into the atmosphere. Circulating across the planet, this watery mist then precipitated to build up glaciers on the leeward side of volcanoes and in mountainous regions.

Rho, Rho, Rho Your Vaccinia

Viruses subvert a variety of host cell mechanisms during infection, replication, and dissemination. **Valderrama *et al.*** (p. 377) now describe how vaccinia virus promotes cellular motility by interfering with the activity of RhoA, a small guanosine triphosphase–binding protein involved in intracellular signaling, which particularly affects the actin cytoskeleton. A conserved vaccinia protein, F11L, directly interacts with RhoA, mimicking one of its endogenous substrates, ROCK, and inducing cellular motility. The induced motility is likely to facilitate the spread of the virus within tissues.

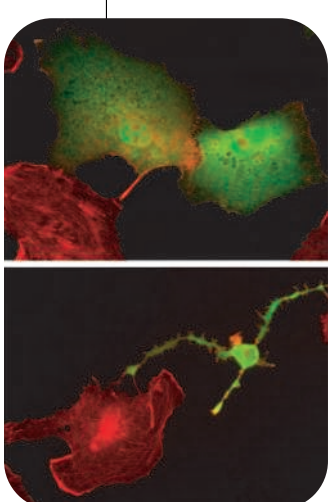

Continued on page 301

CREDITS (TOP TO BOTTOM): UCHIDA *ET AL.*; VALDERRAMA *ET AL.*

Published by AAAS

Continued from page 299

Squares in the Sand

Language is so intimately linked with our thoughts that it is hard to imagine thinking without it, but how language influences thought remains a lively topic of discussion. **Dehaene *et al.*** (p. 381; see the news story by **Holden**) bring new evidence to light from their studies with an Amazonian group, the Mundurukú. Both Mundurukú children and adults proved competent at grasping and using geometric concepts, such as parallel lines and right-angled triangles, even though they lack the words for such terms and concepts. Furthermore, the Mundurukú used relations diagrammed on paper to locate hidden objects, and again performed as well as American children, but not as well as adults. Thus, the Mundurukú possess a basic sense of geometry, in addition to their previously discovered sense of arithmetic.

Ubiquitous Antibiotic Resistance

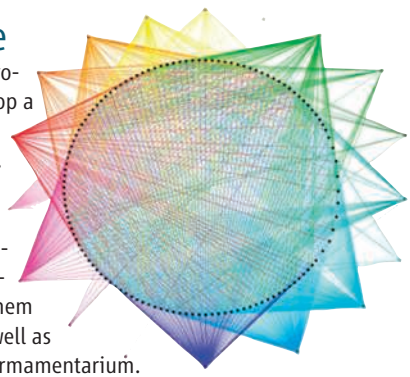

A major source of antibiotic resistance genes is soil microorganisms that produce antimicrobial agents and develop a variety of resistance mechanisms as a way of self-defense against their own toxic products. **D'Costa *et al.*** (p. 374; see the Perspective by **Tomasz**) show that soil microbiota also represent an enormous reservoir of antibiotic-resistant organisms, most of which do not produce antimicrobial agents themselves. The authors characterized strains of spore-forming bacteria and tested them against 21 antimicrobial agents—some in long use as well as compounds recently introduced into the antimicrobial armamentarium. Every strain was multidrug resistant and exhibited resistance to at least 7 to 8 antibiotics, and sometimes to as many as 20.

Turning Cuttings Back into Whole Plants

Plants regenerate much better than do animals—an entire plant can regenerate from a small snip of tissue, whereas the best that animals can do is the occasional amphibian regeneration of a limb or tail. **Xu *et al.*** (p. 385) now analyze subcellular dynamics in the root tip of *Arabidopsis* to understand how regeneration is directed in response to localized cell ablation. Surprisingly, as new tissues are built, establishment of unidirectional flow of the hormone auxin follows, rather than precedes, cell fate specification. A suite of transcription factors that respond early to changes in auxin distribution directs cell fate respecification.

Got to Hitch a Ride

During cell division, chromosomes must establish connections to the opposing spindle poles and become positioned at the spindle equator. Uncorrected errors in this biorientation inevitably lead to aneuploidy and are associated with cell transformation and cancers. How chromosomes attach properly to the mitotic apparatus is not understood. **Kapoor *et al.*** (p. 388; see the cover and the Perspective by **Heald**) used live-cell two-color fluorescence, correlative light and electron microscopy, as well as chemical biology, to demonstrate surprisingly that chromosomes can congress to the spindle equator before they become bioriented. During congression, the leading kinetochore glides alongside kinetochore fibers of other already bioriented chromosomes toward microtubule plus ends. The gliding is mediated by the kinetochore-associated motor protein. Thus, cells possess a mechanism for repositioning monooriented chromosomes from the periphery to central areas of the spindle where they can establish connections to the other spindle pole.

Mammoth DNA Sequences

The sequencing of ancient DNA is hoped to lend insight into evolutionary studies of a variety of species, including mammals. **Poinar *et al.*** (p. 392, published online 12 December 2005) used a roughly 28,000-year-old bone from a woolly mammoth that had been preserved in the Siberian permafrost to directly sequence ancient DNA without prior repair or amplification bias. A total of 137,000 reads (13 megabases) of mammoth DNA were generated, with only traces of human DNA contamination. Genomic comparisons were used to establish the rate of sequence divergence between extinct species and modern elephants. Examination of microbial and plant sequences isolated from the same source may also give clues about the mammoth's environment.

CREDIT: D'COSTA *ET AL.*

Donald Kennedy is Editor-in-Chief of *Science*.

Acts of God?

THE VARIOUS INTERRELATIONSHIPS AMONG NATURE, GOD, AND THE LAW, IT SEEMS TO ME, ARE BECOMING more complex and confusing in the modern world. These three concepts, all important elements in the human narrative, carry historical understandings that are being rearranged by the needs of contemporary society and by our ability to affect the world around us. It is worth exploring how science has influenced the restructuring of these interrelationships and how it might contribute to a better understanding of them.

Charles Darwin's predecessor, the geologist Sir Charles Lyell, launched a stunning revision of the world's view of how nature came to be what it is. Landforms such as mountains were thought of not as the result of some endogenous process but as punishments dealt to Earth by a Creator disappointed at the misbehavior of its inhabitants. This "catastrophist" view affected public attitudes in ways that seem remarkable today. In her notable book *Mountain Gloom and Mountain Glory*, the historian Marjorie Hope Nicholson traces the literary transition from mountains seen as excrescences to mountains praised as glorious nature. It is said that in the 18th and early 19th centuries, well-born ladies making the Grand Tour in Europe would pull down their window shades to avoid viewing the Alps.

For the catastrophist idea, Lyell, Darwin, and their successors substituted the notion that the world is at work changing itself. Mountain building, subsidence, erosion by wind and water, floods, and earthquakes—these were the forces that have been making our landscape over millennia. The geological doctrine emphasizing such gradual changes—uniformitarianism—is accepted today even by schoolchildren, save perhaps those being taught that Earth is only 6000 years old.

Nevertheless, the law still sometimes speaks of unexpected events affecting Earth's systems as "acts of God." Of course judges and lawyers know this is nonsense; they might better be called "acts of nature" or "natural disasters." Both descriptions are useful because they distance such events from human hands, leaving no place to put human liability for the resulting damage. Earthquakes, tidal waves, landslides, floods, and wind damage occur unexpectedly and apparently randomly; nobody causes them. Thus, in insurance policies, exceptions are sometimes made for "acts of God" so that harms of this kind will be uncompensated.

But now serious difficulties confront the idea that some of these events, especially recent disasters, can fit comfortably into these domains of human exemption. Problems are already cropping up with the traditional insurance exemptions. For example, in the aftermath of Hurricane Katrina, some residents had their homes destroyed by floodwater, whereas hurricane winds damaged others. Victims in the second category received insurance payments, but most policies did not cover flood damage, so homeowners in the first group didn't, causing major distress for them and leaving open the prospect of endless litigation.

Contemporary science is making it difficult to sustain such distinctions, and perhaps it can do something to clarify matters. As Katrina and two other hurricanes crossed the warm Gulf of Mexico, we watched them gain dramatically in strength. Papers by Kerry Emanuel in *Nature* and by Peter Webster in this journal during the past year have shown that the average intensity of hurricanes has increased during the past 30 years as the oceans have gained heat from global warming. Emanuel's Web site at the Massachusetts Institute of Technology (http://wind.mit.edu/~emanuel/holem/holem.html) explains the thermodynamic aspects of the relationship. The winds around the low-pressure center (the eye of the hurricane) travel across the warm surface water in a circular pattern, picking up energy. As water molecules evaporate from the surface, they contribute their energy to the storm column as they condense to form droplets, becoming sensible heat. About a third of that energy powers the hurricane's wind engine.

We know with confidence what has made the Gulf and other oceans warmer than they had been before: the emission of carbon dioxide and other greenhouse gases from human industrial activity, to which the United States has been a major contributor. That's a worldwide event, affecting all oceans. When Katrina hit the shore at an upgraded intensity, it encountered a wetland whose abuse had reduced its capacity to buffer the storm, and some defective levees gave way. Not only is the New Orleans damage not an act of God; it shouldn't even be called a "natural" disaster. These terms are excuses we use to let ourselves off the hook.

– Donald Kennedy

10.1126/science.1124889

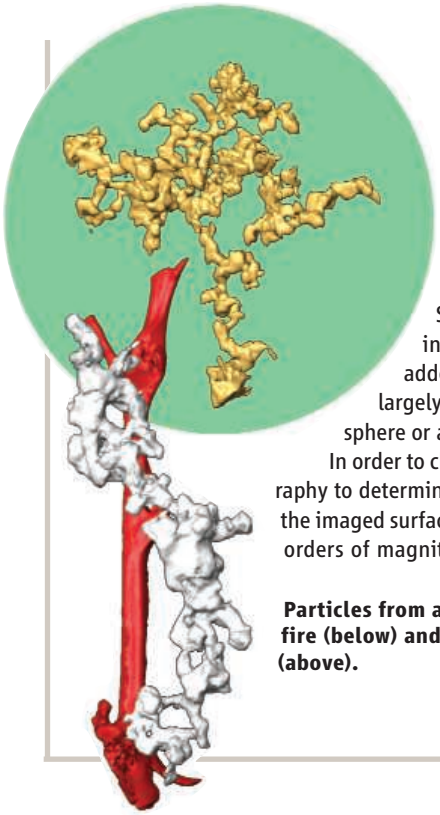

CLIMATE SCIENCE

The Shape They're In

Soot, the product of the incomplete combustion of fossil fuels and biomass, is emitted in large quantities globally and is one of the more important climate-forcing agents added to the atmosphere. The radiative and chemical properties of soot particles depend largely on their shape, which generally is not well defined and hence is usually modeled as a sphere or an elongated cylinder.

In order to characterize the actual morphology of soot, van Poppel *et al.* have used electron tomography to determine shapes, volumes, and surface areas of clusters of soot nanoparticles. They find that the imaged surface areas and volumes can differ from the geometrically modeled values by one and two orders of magnitude, respectively. This result has important implications for the chemical aging of soot—the process of changing hydrophobic soot particles into a hydrophilic and more readily scavenged aerosol—which affects its atmospheric lifetime and its radiative forcing potency. – HJS

Geophys. Res. Lett. **32**, 10.1029/2005GL024461 (2005).

Particles from an agricultural fire (below) and diesel exhaust (above).

BIOMATERIALS

A Degrading Approach

Biocompatible scaffolds are used to enhance cell survival and to improve the integration of tissues grown ex vivo and for in vivo implantation. As cells respond to external cues and require nutrients for growth, an ideal environment should be able to adjust dynamically in accordance with their needs.

Mahoney and Anseth have designed a series of polyethylene glycol (PEG) hydrogels in which the cross-links hydrolyze slowly; thus the mesh size increases over several weeks. Neural precursor cells were encapsulated in the hydrogels and followed with confocal microscopy. Cells cultured within this three-dimensional environment grew to form microtissues and were able to proliferate and differentiate into neurons and glial cells. When exposed to the neurotransmitter γ-aminobutyric acid, calcium transients were observed in cells in the interior and exterior of the microtissues and in cell processes. The mechanical strength of the gels is such that they are suitable for injection into tissue, and by changing the degradation rate of the linker, the authors could alter the time scale for neural cell extension from 1 to 3 weeks. – MSL

Biomaterials **27**, 2265 (2006).

PSYCHOLOGY

Asian/American Views

There is ample evidence that people in different cultures can exhibit dissimilar ways of thinking. For instance, Asians pay more attention to context and to the relationships between focal (foreground) objects and background in their descriptions of visual scenes, whereas Americans mention the focal items with greater frequency. Why this occurs is unclear, as is the cognitive source of the differences in behavior.

Miyamoto *et al.* present a set of studies that begin to identify the underlying processes and how the physical environment may serve to reinforce cultural distinctions. They presented Japanese and American study participants with photographs taken of hotels, schools, and post offices located in large, medium, and small cities in Japan and the United States. People of both nationalities rated the scenes of Japan as being more complicated (more objects, more chaotic, more obscured parts); although the U.S. scenes increased in complexity with city size, the Japanese scenes did not and were all more complex than those from the large U.S. city (New York). A similar ranking was obtained by analyzing the photos with the NIH Image program. In order to assess the influence of complexity on behavior, both nationalities were tested for their ability to detect changes in focal objects and background information in neutral vignettes after having been primed with the photos of Japan or the United States. Having first viewed a more complex scene improved the abilities of both the American and Japanese participants in reporting contextual, as opposed to focal, changes. – GJC

Scenes of Japan.

Psychol. Sci. **17**, 113 (2006).

GENETICS

The Grandmother Effect

Women's postreproductive years, the immaturity of newborns, and strong kinship networks combine to make it reasonable that the grandmother effect could be important in the evolution of human life-span structure. For guppies, on the other hand, with live-born young that require no further care and with a lack of familial structures, the female postreproductive life phase is not likely to be a target of evolutionary forces. In fact, because guppies produce eggs throughout adulthood, a nonreproductive late-adult phase seems unlikely.

Nonetheless, guppies do have a postreproductive life phase, and, as Reznick *et al.* show, this phase seems to be an accident of extended reproductive life span rather than a point of evolutionary leverage. Guppies that face high rates of predation mature earlier and

Continued on page 307

CREDITS (TOP TO BOTTOM): VAN POPPEL *ET AL.*, *GEOPHYS. RES. LETT.* **32**, 10.1029/2005GL024461 (2005); MIYAMOTO *ET AL.*, *PSYCHOL. SCI.* **17**, 113 (2006)

Continued from page 305

reproduce more often than guppies in more benign bends of the river. When reared in the lab, safe from predators, these two populations continued to show different life histories, and the predator-intense family of guppies lived longer. Many of these individuals had a post-reproductive life phase, suggesting that reproductive senescence precedes somatic senescence. The length of the postreproductive life phase seemed to be an accidental outcome of the generally longer reproductive life span that the high-predation environment had brought about. – PJH

PLoS Biol. **4**, e7 (2006).

CHEMISTRY

Coping Well with Crowding

Perylene bisimides, which are highly efficient and tunable fluorophores, are linear molecules with two imide groups (-CONRCO-) straddling the naphthalenic ends. Ilhan *et al.* report the synthesis of "Z-shaped" analogs in which the imide groups attach symmetrically but to only one aromatic ring each on opposite sides of the molecule, through the Diels-Alder trapping of a diketone-substituted anthracene with *N*-octylmaleimide, which produces *o*-xylyenols. Subsequent dehydration and aromatization steps yielded the Z-shaped bisimides; the more crowded substitution pattern as compared to the linear isomers causes twisting of the perylene core. Despite this twisting, the absorption and emission spectra show only a slight blue shift. This route should allow the synthesis of other perylene bisimides substituted at the imide and phenyl positions. – PDS

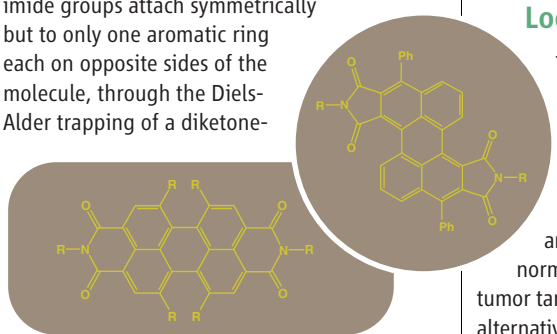

Linear and Z-shaped adducts.

CREDIT: ILHAN *ET AL., J. AM. CHEM. SOC.* 10.1021/JA056912O (2005)

J. Am. Chem. Soc. 10.1021/ja056912o (2005).

APPLIED PHYSICS

Spin Injection Withstands the Heat

The efficient injection of polarized spins into semiconductors is the keystone capability for spintronics applications. Recent work has shown that epitaxially grown MgO on a ferromagnetic layer results in a dramatic enhancement of the spin-polarized injection efficiency, which has been demonstrated in several practical structures such as ferromagnet/oxide/ferromagnet spin filters and ferromagnet/oxide/semiconductor systems. However, polarized photoluminescence from a semiconductor quantum well, a technique routinely used to determine the extent of the spin polarization and spin injection efficiency, usually exhibits somewhat complex behavior in terms of temperature dependence.

Salis *et al.* report that the spin injection efficiency from CoFe/MgO electrodes is around 70% and is actually independent of temperature from 10 K all the way up to room temperature. The temperature dependence of the photoluminescence arises from the temperature dependence of the carrier recombination rate in the quantum well itself, a result that bodes well for the application of such spin-injecting electrodes in other spintronic devices. – ISO

Appl. Phys. Lett. **87**, 262503 (2005).

BIOMEDICINE

Localized Therapy

The past two decades have brought remarkable progress in the development of more effective chemotherapeutic drugs for breast cancer. Unfortunately, many of these drugs produce undesirable side effects, largely because they are delivered systemically—to vulnerable normal tissue as well as to the intended tumor target. The mammary gland provides an alternative route for tumor access: the mammary ductal networks that terminate at the nipple. Indeed, the vast majority of human breast cancers arise in the epithelial lining of these ducts.

Studying two rodent models, Murata *et al.* investigated whether mammary tumors could be prevented and treated by injection of chemotherapeutic drugs directly into the mammary ducts, a strategy that in principle would maximize drug concentrations around the premalignant and malignant cells, while sparing normal tissue. Intraductal delivery of derivatives of tamoxifen or doxorubicin—two of the most commonly used drugs for human breast cancer—was found to be equal or superior to intravenous delivery in suppressing tumor growth, and there was no evidence of systemic toxicity. Because the mammary ducts of rodents and humans are anatomically distinct, it is unclear whether a similar drug delivery protocol would be effective clinically, but these promising results should stimulate further work in this direction. – PAK

Cancer Res. **66**, in press (2006).

Editors' Choice is edited by Gilbert Chin

RESOURCES

EVOLUTIONARY BIOLOGY'S NEW STAR

The starlet sea anemone *Nematostella vectensis* (above) has no head, no brain, and uses the same body opening for eating and excreting. But the genes of this seemingly simple mud dweller may hold clues to vexing puzzles in animal evolution, such as the emergence of bilateral symmetry and the origin of mesoderm, the versatile embryonic layer that gives rise to muscles and some organs. Researchers can learn more about the creature and analyze its genome at this pair of sites from evolutionary biologist John Finnerty of Boston University and colleagues.

Nematostella has oozed into the spotlight partly because it's the only species near the base of the animal evolutionary tree whose genome has been sequenced. At the new StellaBase,* users can compare the anemone's genome to those of other model organisms or hunt down a particular gene or gene family. To help lab mavens, the site lists nearly 700 primers for copying *Nematostella* DNA sequences and points to sources of specimens from North America and the U.K. You can find out more about *Nematostella*'s anatomy, distribution, and habitat at this companion site.† >>

* www.stellabase.org † www.nematostella.org

DATABASE

The Dope on Drugs

The online pharmacopoeia DrugBank profiles about 4100 approved or experimental medicines, offering data for drug designers, molecular biologists, and other researchers. Compiled by David Wishart of the University of Alberta in Edmonton, Canada, the site furnishes a DrugCard for each compound that is crammed with information in more than 80 categories. Users can corral chemical details such as solubility and molecular weight, browse nuclear magnetic resonance and mass spectra, and analyze three-dimensional structure models. For scientists investigating a drug's action, the cards include the gene and amino acid sequences of its target and identify the enzymes that break it down. Above, the antibiotic dactinomycin. >>

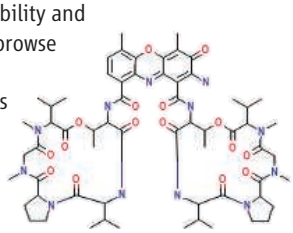

redpoll.pharmacy.ualberta.ca/drugbank

RESOURCE

Quantifying The Mouse

Female mice from the C57BL/6J strain are daredevils—by rodent standards, at least. The average mouse dithers for nearly a minute before entering an open space, but C57BL/6J females scurry in after a mere 6 seconds. From brain weight to daily water intake to heat sensitivity, the Mouse Phenome project from the Jackson Laboratory in Bar Harbor, Maine, houses vital statistics on more than 100 inbred mouse strains. Mouse aficionados from around the world are stocking the site with their measurements of more than 600 anatomical, physiological, and behavioral traits. The data provide researchers with standards of comparison as they attempt to decipher the effects of different genes. Tools let users compare values among strains, tease out sex differences, and perform other analyses. >>

www.jax.org/phenome

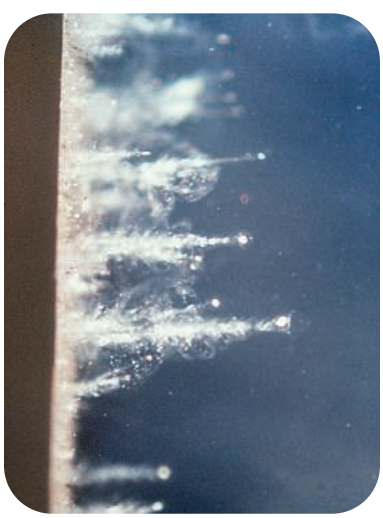

WEB PROJECT

<< Spot Some Space Dust

Astronomy buffs who've hankered to name a bit of the cosmos after themselves may soon get their chance. To coincide with the return of NASA's Stardust spacecraft to Earth on 15 January, researchers are inviting home computer users to help search through digital images for interstellar dust grains in a project dubbed Stardust@home.

Interstellar dust, which emanates from supernovas and aged stars, remains an enigma. "No one has ever had a contemporary interstellar dust particle in the lab, ever," says Stardust@home lead investigator Andrew Westphal of the University of California, Berkeley. "My prediction is there's going to be some huge surprises."

Volunteers who pass an online training session will download a virtual microscope and use it to peer at images of the spacecraft's foamy aerogel traps, probing for tracks burrowed by particles (above). Researchers expect to find only about 50 micrometer-sized grains in the 1.6 million images. To ward off frustration and encourage competition, many pictures will be spiked with artificial particle tracks. Lucky discoverers will get to name their particles and be listed as co-authors on scientific papers. >>

stardustathome.ssl.berkeley.edu

Send site suggestions to >> netwatch@aaas.org. Archive: www.sciencemag.org/netwatch

CREDITS (TOP TO BOTTOM): JOHN FINNERTY; DRUGBANK; NASA


Scottish harbor where U-boat sank the *HMS Royal Oak*.

THE MOON AND THE NAZI SUB

One of the most famous naval attacks during World War II occurred in 1939 when a German U-boat sneaked into a Scottish harbor and sank a British battleship. Günther Prien, captain of submarine U-47, became a celebrity in Germany after his daring nighttime invasion. But few are aware that Prien's knowledge of astronomy played a critical role in the attack.

Astronomer Bradley Schaefer of Louisiana State University in Baton Rouge recently examined charts and logbooks from the attack, held in British archives in London. Speaking last week at a meeting of the American Astronomical Society in Washington, D.C., he related that Prien used astronomical calculations to convince his superiors that his sub could sneak past shallow blockades to torpedo the British fleet at Scapa Flow, a sheltered harbor in the Orkney Islands. His brilliant plan, says Schaefer, relied on "the highest of the highest of high tides," which were created at midnight on 13–14 October by the moon's closest approach to Earth in its orbit and its alignment with the sun. U-47 was able to scrape into the inlet and sink the battleship *HMS Royal Oak*, killing 833 sailors. An unexpected and very bright aurora borealis foiled further attacks, forcing the sub to withdraw. Says Schaefer: "The skies affect historical events on Earth, more than most people realize."

Bog Men as Sacrifices

After 18 months of investigation, archaeologists have revealed that the two Iron Age men whose bodies were found in 2003 in Irish bogs were probably ritually sacrificed. Both were tortured before being killed about 2300 years ago. One was stabbed and had his nipples cut off prior to being beheaded and dismembered.

Much can be learned from bog bodies, which are preserved in the peat. Analysis of hair from one of the recent finds indicates a largely vegetable diet, suggesting he died in the summer, according to scientists at the National Museum of Ireland, where the bodies are being held. The hair also was coated in a gel made from resins that probably came from southern Europe. The other man was a striking 2 meters tall and apparently a man of leisure. "His nails were well-manicured, showing that he never did any manual work," says the museum's Isabella Mulhall. The two bodies, the subject of a 20 January BBC documentary, will go on exhibit at the museum in May.



Bog torso. (Inset: Manicured hand.)

Many of the more than 100 bog bodies discovered in northwest Europe show marks of violent deaths. Museum archaeologist Ned Kelly says 40 of those found in Ireland, as well as the two latest finds, were discovered on the borders of ancient tribal lands, which leads him to suspect they were killed as offerings to the gods of fertility.

VIDEOS AND BRAIN-NUMBING

A new entry in the perennial debate about video violence uses brain waves to argue that violent video games "desensitize" players, making them more aggression-prone.

Researchers led by psychologist Bruce D. Bartholow of the University of Missouri, Columbia, asked 34 male college students about their exposure to violent video games. The researchers then wired up the men to see how their brains reacted to different types of pictures. They found that the violent game afficionados showed a diminished P300 brain wave—a wave that responds to stimuli the brain registers as significant—in response to violent pictures compared with the other game players. And the smaller P300 correlated with higher levels of aggression in a test allowing subjects to punish an unseen "opponent" with a blast of noise. "To our knowledge, this is the first study to link violent video game exposure to a brain process associated with desensitization to violence and to link that brain response to aggressive behavior," says Bartholow.

The study, in press at the *Journal of Experimental Social Psychology*, still fails to show that video games cause violent behavior, says psychologist Jonathan Freedman of the University of Toronto in Canada. Although games can "habituate" the brain to violent images, Freedman says "there is no good evidence that exposure to lots of [video] violence desensitizes you to real violence."


Scary picture has little effect on violent video fans.

Betting on Bird Flu

When public health officials talk about the chances that H5N1 will reach the United States this flu season, most don't back up their chatter with cold cash. But a gaming house has, offering a 20-to-1 payoff should people start coming down with the much-watched virus before 6 April.

General manager Peter Ross of YouWager.com says his house based its odds on the speed and direction the virus has been moving in Asia and Europe. Ross says 4 days into wagering, the public appears pessimistic—so if bird flu arrives, the company stands to lose big. Neuroscientist Adil Khan of the Buck Institute for Age Research in Novato, California, a seasoned wagerer, points out that chance may not play the only role: "The last thing you want to get is a big bettor who goes out and brings back the bird flu themselves."

CREDITS (TOP TO BOTTOM): DOUG HOUGHTON; BBC; BRADLEY LANG AND B. N. CUTHBERT, *INTERNATIONAL AFFECTIVE PICTURE SYSTEM (IAPS): INSTRUCTION MANUAL AND AFFECTIVE RATINGS* (UNIVERSITY OF FLORIDA, 2001)

India: Trouble with the nuclear deal?
318

Journals clean house
321

AVIAN INFLUENZA

Amid Mayhem in Turkey, Experts See New Chances for Research

ANKARA—It's Turkey's turn to wage war against H5N1. More than 2 months after it first emerged in this country, the feared avian influenza strain has suddenly exploded in the past 3 weeks: Twenty people are assumed to have been infected, and four have died—including three children from one family. Across the country, massive and at times chaotic culling operations are in full swing in an attempt to prevent the virus from becoming endemic.

But amid the devastation, scientists also see a unique opportunity to study questions about H5N1 whose answers may benefit not just Turkey but also the entire world. Members of an international team of experts, flown in 2 weeks ago to assist the government in investigating and controlling the outbreaks, say Turkey has been exceptionally open and has welcomed studies that may help prepare for a possible pandemic. Although he's cautious not to criticize other countries, epidemiologist Guénaël Rodier of the World Health Organization's (WHO's) European office in Copenhagen, who heads the team, says, "we do have better access here."

In an interview last week, Rodier rattled off a series of proposed studies to which the Turkish government has reacted favorably. They include a detailed epidemiological investigation to establish the virus's potential for human-to-human transmission; a so-called serosurvey—a study looking for antibodies—among patients' family members, poultry cullers, health care workers, and the rest of the community in affected areas; and a study to find out risk factors for severe disease among those infected. Completing them all would take months, Rodier says.

Some have suggested that Turkey is opening up in order to further its candidacy for E.U. membership; others say the country realizes it needs all the help it can get. Juan Lubroth of the U.N. Food and Agriculture Organization, who was in Turkey last week, credits the government with "mature, good governance" and notes that FAO has had good relations with Turkey in the past.

Turkey's struggle. Quashing the large avian influenza outbreak in Turkey will require international assistance, scientists say.

The international team, which includes epidemiologists, microbiologists, lab experts, and veterinarians, swarmed out last week to visit hospitals, stricken villages, labs, and health authorities to help collect information and control the outbreak. Roughly half of the experts have set up camp in Van, a city in the eastern part of the country that has been hit the hardest; the other half is based closer to the Turkish government, in a heavily fortified U.N. office building in a hilly suburb of the capital.

Several factors, in addition to the hospitality, make Turkey a valuable site for research, experts say. For instance, Turkish doctors appear to record more elaborate histories of their patients than do those in East Asia, which can be invaluable for understanding viral exposure, says pediatrician Angus Nichol, former head of the U.K.'s Communicable Disease Surveillance Centre. (Nichol is currently seconded to the European Centre for Disease Prevention and Control in Stockholm.)

The large number of human cases in a short period is another factor that makes the outbreak particularly interesting. The first recorded poultry cases in Turkey occurred on a turkey farm in the western province of Balikesir in early October; for 2 months after that, no new outbreaks were reported. But in late December, the number of poultry outbreaks started to skyrocket, and human cases followed quickly. As of Tuesday, the agriculture ministry had confirmed outbreaks in 12 of the country's 81 provinces, situated in the western, northern, and eastern parts of the country, and was investigating reports in 19 others. Human cases have occurred in nine provinces.

Researchers are not certain why the country is seeing so many cases, whereas East Asia has had fewer than 150 over the past 2 years. So far, they have not seen any signs of human-to-human virus transmission, the feared overture to a pandemic. Sequencing of the virus from one Turkish patient at the National Institute for Medical Research (NIMR) in London—one of four WHO collaborating centers for flu—has shown a genetic mutation, previously seen in patients in China and Vietnam, that makes the virus bind more easily to human cells. But whether that makes any difference for epidemiology is unclear, says NIMR Director Alan Hay, who was in Ankara last week.

The human cases may have occurred in the cold, mountainous eastern part of the country simply because many villagers brought their animals indoors when the winter began in earnest, Rodier says. Rural dwellings there are often simple, one-room structures where people and animals live together, which might create conditions conducive to transmission. But this needs to be investigated further, Rodier says.

Researchers are asking another question: Why does the disease appear to be milder here than in eastern Asia? The death rate of about 25% is half that of previously known outbreaks, and there have been five mild or completely asymptomatic cases. One theory holds that milder cases have been occurring ▶

CREDIT: MURAD SEZER/AP PHOTO

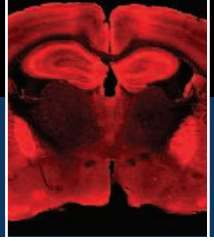

Enthused about endocannabinoids 322

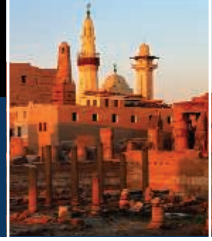

Nile threatens Egypt's temples 326

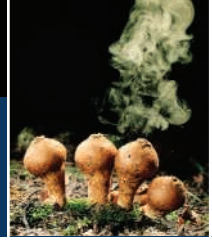

Rocketing spores 331

elsewhere but aren't being recorded. Indeed, a study among 45,000 Vietnamese by Anna Thorson and colleagues at the Karolinska Institute in Stockholm, published recently in the *Archives of Internal Medicine*, showed that those who lived in households where poultry became sick or died had an increased risk of influenza-like symptoms, especially after close contact with the birds.

Such studies can suffer from so-called recall bias, however; people who had sick chickens may just remember their symptoms better. A broad serosurvey—among patients' contacts, those exposed on the job, and the community in general—would be a better gauge of the true extent of H5N1's spread. Several such studies have been carried out in affected Asian countries, but the results have not been published, to the frustration of many flu experts. "Serological studies are often very hard to get out of countries—they're politically sensitive, even in Western countries," says Nichol. But from what he has heard about completed H5N1 serosurveys, they do not point to widespread infection beyond the recorded H5N1 cases, he says.

Yet another possible explanation for the milder cases may be that worried Turkish parents, exposed to wall-to-wall media coverage, take their children to a hospital earlier. Once there, they are immediately given oseltamivir, an antiviral drug known to work best when given early in infection. Indeed, oseltamivir efficacy against H5N1 is another important topic to be studied, says Rodier.

Early this week, experts weren't ruling out that some of the milder cases might actually be false positives. Flu testing in Turkey is done by the National Influenza Centre, based at the Refik Saydam Hygiene Institute in central Ankara. Although the first four positive tests there were confirmed by NIMR and have been added to WHO's official tally, the others, which included the milder cases, were not. Kurban Bayrami, a major 4-day religious festival, brought the country to a standstill last week, making sample shipments impossible.

Although patients with flu are well cared for, even in remote areas, and a vigorous education campaign is now under way to prevent more infections, reining in the poultry outbreak remains a daunting task. A top priority now is to establish exactly where the virus is and isn't present in birds, says Stefano Marangon, director of science at the Istituto Zooprofilattico Sperimentale delle Venezie in Padua, Italy, who also visited Turkey last week. Massive culling in affected areas may prevent the disease from becoming endemic.

But to succeed, Turkey needs help from the international community, Marangon adds; for instance, several of the nation's eight regional animal health labs don't have equipment for rapid testing and need to be upgraded. Turkey was set to offer a battle plan and make a request for international support at a large donor meeting for avian influenza scheduled for this week in Beijing.

–MARTIN ENSERINK

AVIAN INFLUENZA

WHO Proposes Plan to Stop Pandemic in Its Tracks

Ever since the H5N1 avian influenza strain began racing through Asia 2 years ago, the World Health Organization (WHO) has been urging the world to prepare for a possible pandemic. Now it is going a step further, planning a rapid response that just might quash a pandemic before it starts. To work, any country and WHO would have to recognize that the virus had acquired the ability to be transmitted easily among humans while its spread was still limited. Then, with international support, that country would have to impose quarantines and launch massive campaigns to administer antiviral drugs to contain the virus.

"Clearly, there is no guarantee that we would stop a pandemic," admits WHO virologist Keiji Fukuda. "But if successful, this could prevent enormous [amounts] of illness and death." At the moment, however, few of the developing countries hardest hit by H5N1 have the necessary capabilities, and it is unclear whether developed countries will offer sufficient technical and financial support.

CREDIT: REUTERS/ANATOLIAN NEWS AGENCY

Rapid response. The outbreak in Turkey has underscored the need for bold interventions. Above, Minister of Health Recep Akdag visits a child being treated for a possible H5N1 infection.

WHO proposed the plan at a Japan-WHO Joint Meeting on Early Response to Potential Influenza Pandemic in Tokyo on 12 and 13 January, announcing that it will form a new Global Task Force for Influenza. The 20 or so outside experts in virology and public health will be on standby to help the agency assess the signals that may presage a pandemic.

Two modeling studies published late last summer gave weight to the idea that early intervention was at least theoretically possible, says Fukuda. One, from a team led by Ira Longini of Emory University in Atlanta, Georgia, appeared in *Science* (12 August 2005, p. 1083). The second team, led by Neil Ferguson of Imperial College London, published its results in the 8 September issue of *Nature*. Both concluded that, under the right circumstances, early intervention could stop a pandemic in its tracks (*Science*, 5 August 2005, p. 870).

But the gap between the ideal and current reality was apparent at the Tokyo meeting. The first step in this rapid-response scenario would be spotting a virus soon after it has acquired human-to-human transmissibility. This would be extremely difficult in the remote mountainous areas of Laos where technical capabilities are weak, said Baunlay Phommasack, a Department of Health official from that country. His views were borne out by an ▶

analysis of some 70 human cases in Asia in the past 2 years. As Hitoshi Oshitani, a public health specialist at Tohoku University in Sendai and consultant to WHO, described, on average, it took 2 weeks after the onset of symptoms for cases to be identified and notification sent to WHO. Lab confirmation of suspect H5N1 samples can add several days to 2 more weeks. "This is too late to contain the virus," he said. He also noted that imposing an effective quarantine would be logistically difficult and could well run into opposition on human-rights grounds. Wide-scale administration of the antiviral Tamiflu, generically known as oseltamivir, also hinges on having sufficient stockpiles readily available. And even if supplies are on hand, recent studies have raised questions about proper dosing for H5N1, several meeting participants pointed out.

All these unknowns mean that an early response "is not a panacea," says Shigeru Omi, director of WHO's Regional Office for the Western Pacific. But Omi and other WHO officials emphasize that even if it fails to thwart a pandemic, early intervention might slow the spread of disease, providing precious days or weeks for other countries to put pandemic plans into action and for drug companies to start developing a vaccine.

At the meeting Oshitani pointed out that few countries, if any, currently include early response as part of national pandemic-preparedness plans. Fukuda adds that the next step for WHO will be to launch "intensive discussions to develop plans reflecting each country's needs." Most developing countries, he said, will need to upgrade both local surveillance and lab capabilities to deal with agricultural and human health threats. But that won't come cheap, cautioned World Bank official Jacques Baudouy, who reported bank estimates that globally between $1.2 billion and $1.5 billion will be needed over the next 3 years. Issues of international support for building such capacities in developing countries were due to be taken up at an International Donor Conference in Beijing on 17 and 18 January.

–DENNIS NORMILE

COSMOLOGY

Astronomers Push and Pull Over Dark Energy's Role in Cosmos

WASHINGTON, D.C.—The claim was a headline writer's dream: Dark energy, a hidden force that is blowing the universe apart, had varied dramatically over time and at one point even reversed direction. But while science reporters at the astronomy meeting* rushed to file their stories, most researchers were saying, "Not so fast."

The debate revolves around whether gamma ray bursts (GRBs), enormous explosions deep in space, can help astronomers measure distances in the universe. In the late 1990s, two research teams used the less-violent explosions of supernovae as "standard candles" of known brightness to illuminate how quickly the cosmos grew in the past. The results pointed to an accelerating universe, powered by a repulsion that seems to arise from space itself. But supernovae are too faint to shed light on cosmic expansion just a few billion years after the big bang. "Gamma ray bursts can fill in the gap," says astronomer Bradley Schaefer of Louisiana State University in Baton Rouge.

Schaefer studied a database of 52 GRBs detected by various satellites. Although GRBs differ wildly in their energy outputs, Schaefer claims that a careful accounting of up to five burst properties—such as their peak wavelengths of energy and their patterns of brightening and fading—enabled him to calibrate GRBs as rough standard candles and thus ascertain their distances. He found that nearly all of them—including the 12 farthest—were brighter than expected if dark energy had been constant throughout cosmic history.

To explain the discrepancy, Schaefer maintains that the expansion of space after the big bang slowed down much more markedly than predicted, because dark energy exerted an *attractive* pull at that time. The force first dwindled and then, in the past 10 billion years or so, became increasingly repulsive. But Schaefer notes there's a 3% chance his conclusion is a statistical fluke. "This is not high enough confidence to make any claims that I have formally rejected the cosmological constant," he says. "I don't want to push the results too much."

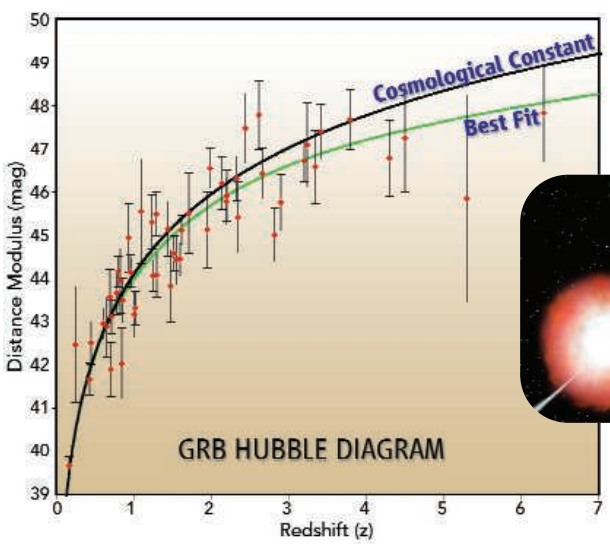

Tug of more. Dozens of distant gamma ray bursts (artist's view, *inset*) suggest that the repulsive force of dark energy is not the "constant" that many believe.

Reaction to the presentation was decidedly mixed. "It's absolutely worth pursuing," said astronomer George Ricker of the Massachusetts Institute of Technology in Cambridge. "It's the germ of a very productive idea." And a key figure in the dark energy quest, cosmologist Michael Turner of the National Science Foundation in Arlington, Virginia, offered his guarded blessing. "The history of standard candles is extraordinarily checkered," Turner said. "But it's a very intriguing result."

Others objected that Schaefer was overreaching. GRBs, they point out, arise from giant stars across a vast range of masses, spins, and compositions. When such stars create black holes at their cores and erupt with gamma rays and x-rays, the blasts are so different from one another that many observers doubt Schaefer's calibrations can succeed. What's more, several astronomers said, that variability makes GRBs ill suited to detect changes in dark energy when the universe was small, because its force at that time was nearly negligible. "It's a blunt tool to do a problem that's kind of delicate," says supernova expert Robert Kirshner of Harvard University.

Cosmologist Adam Riess of the Space Telescope Science Institute in Baltimore, Maryland, has even deeper qualms. Nearly all GRBs are billions of light-years away. Without nearby points of known luminosity to anchor it, Riess says, Schaefer's distance curve is mathematically unreliable and creates the illusion of a shifting constant. "I believe it is a calculation error, and he will recognize that," Riess says.

Schaefer intends to press onward. "Supernovae have been tremendously improved in their accuracy of standard candle–ship" in the past decade, he notes. "I expect the same will happen with GRBs." At the very least, tracking dark energy will be the field's one constant for years to come.

–ROBERT IRION

CREDITS: B. SCHAEFER/LSU; (INSET) D. AGUILAR/HARVARD-SMITHSONIAN CENTER FOR ASTROPHYSICS

* 207th meeting of the American Astronomical Society, 8–12 January.

PSYCHOLOGY

Hunter-Gatherers Grasp Geometry

Are triangles and other geometric shapes embedded in the brain? The question of whether scientific concepts are innate is a tantalizing one for cognitive scientists. Now scientists studying villagers in a remote area of the Amazon report on page 381 that core geometric concepts are part of basic human cognitive equipment.

Several research teams have probed the inherent mathematical sense of hunter-gatherer groups, documenting, for example, that in the absence of words for numbers, number sense grows hazy after 3 or 4 (*Science*, 20 August 2004, p. 1093, and 15 October 2004, p. 499). A team led by cognitive scientist Stanislas Dehaene of the Collège de France in Paris has now delved into the less-studied area of geometric knowledge. The researchers tested children and adults in an Amazonian group called the Mundurukú to see if Euclidean geometry dwells in the minds of a people who have little or no schooling, and no artifacts, such as rulers or maps, that employ geometric or metric concepts.

Anthropologist Pierre Pica of Paris VIII University tested 14 Mundurukú children aged 6 and up and 30 adults, getting them to point to shapes displayed on his solar-powered laptop. They were shown sets of six figures and asked to point to the one in each set that diverged from a geometric figure such as a triangle or a basic concept such as parallelism or symmetry. The subjects overall got about two-thirds of the answers correct.

For a more interactive test, the researchers concocted a map-reading task. Three containers, one holding a hidden object, were set out in a right-angled triangle in a room-sized area. After looking at a map representing the three containers, with one marked to indicate the object, the subjects were asked to find it. This required several abilities: translating two-dimensional information into three dimensions; perceiving the same pattern in a 10-fold change in scale, and locating the object based on the relationship of the three points. The success rate averaged 71%.

On both tests, the Mundurukú children and adults performed at about the same level as a control group of 26 U.S. children tested by Harvard cognitive scientist Elizabeth Spelke. (A group of 28 U.S. adults did better.) The tests presented the same profile of difficulty in both cultures, says Dehaene, showing that "even without education, and living in isolation without artifacts such as maps, you can have a developed geometrical intuition." As for why the Mundurukú adults, despite their experience, did no better than the children, Dehaene speculates that "they have no language for these concepts, so they stay where they are in the state of core knowledge."

Harvard University cognitive scientist Steven Pinker calls the paper "a nice addition to the literature on cognitive universals." The map study, he says, "may show that everyone applies a sophisticated analysis of visual shape and configuration" even if it's not part of conscious reasoning.

Euclid in the Amazon. Anthropologist Pierre Pica tests Mundurukú children on geometric concepts (*top*). Other villagers read a map to identify a hidden object (*bottom*).

CREDITS (TOP TO BOTTOM): PIERRE PICA/CNRS PHOTOTHÈQUE; S. DEHAENE *ET AL.*, *SCIENCE*

Linguist Daniel Everett of the University of Manchester, U.K., who studies another Amazon tribe, the Pirahã, calls the work "very significant" and says he plans to test related abilities in the Pirahã. But he cautions that interpretation of such results is difficult "unless one has done a grammar of the language and a fairly thick ethnography."

Rosalind Arden, who has tested cognitive abilities in a South American tribe, the Aché in Paraguay, has stronger reservations about the research. Arden, a doctoral student in behavioral genetics at King's College London, contends that the tests used in the study have less to do with a "shared core of geometric knowledge" than with "general reasoning ability." In other words, she says, the Mundurukú were simply taking a "garden-variety, nonverbal intelligence test."

–CONSTANCE HOLDEN

A Dash for Hare Eggs

Researchers in the United Kingdom have ruffled some feathers by saying they will apply for a license to use rabbit egg cells in nuclear transfer experiments designed to produce human embryonic stem (ES) cells. Chris Shaw of King's College London says his team had been considering attempting the technique. But recent retractions by Korean scientists have provided "an impetus" for using animal eggs instead of hard-to-obtain human eggs.

The scientists plan to remove the DNA from a rabbit egg and then fuse the cytoplasm with a human cell, hoping to reprogram the human DNA to express embryonic genes. In 2003, a group led by Hui Zhen Sheng of Shanghai Second Medical University published a paper in the Chinese journal *Cell Research* claiming to have coaxed such hybrids into becoming embryos, from which ES cells were harvested, but many scientists remain unconvinced. Shaw's trial balloon has prompted several groups to question the ethics of creating such chimeric embryos. A spokesperson for the U.K.'s Human Fertilisation and Embryology Authority has said that "the resulting embryo would be almost indistinguishable from a human embryo," so Shaw and his colleagues would need a new license to start their rabbit research.

–MICHAEL SCHIRBER

Like Physics? Pony Up

Research patrons bailed out a particle collider at the Brookhaven National Laboratory (BNL) after Congress slashed its budget. A group led by mathematician and hedge-fund billionaire James Simons is donating $13 million to the Department of Energy laboratory in Upton, New York, to run the Relativistic Heavy Ion Collider a full 20 weeks in 2006 instead of, at most, 6 weeks (*Science*, 18 November 2005, p. 1105). BNL director Praveen Chaudhari says he was "stunned" when Simons made the offer last month.

As long as donors work with funding agencies, such philanthropy is welcome, says presidential science adviser and former Brookhaven director John Marburger. "It will help us get more out of our facilities," he says. But American Physical Society public affairs director Michael Lubell fears that the donation could set a troubling precedent if the federal government uses it as an excuse to further shrink public funding of basic research.

–ADRIAN CHO

NONPROLIFERATION

India Struggles to Put Its Nuclear House in Order

Last year, the United States set out to bring India into the fold with a landmark agreement that would end the country's pariah status as a nonsigner of the Nuclear Nonproliferation Treaty (NPT). But that deal is now at risk as U.S. and Indian officials in New Delhi wrangle over a plan to split up India's vast nuclear establishment into distinct civilian and military programs. The thorniest issue, *Science* has learned, is that India's draft separation plan designates several key facilities—including all R&D centers—as military installations, placing them off-limits to nonproliferation safeguards.

India's stance could scuttle the deal, nonproliferation experts warn. The two countries are racing to find a compromise before U.S. President George W. Bush visits India for a summit with Indian Prime Minister Manmohan Singh in early March.

Sweeping aside decades of animosity over India's nuclear ambitions, Bush and Singh last July signed an agreement that would end an embargo that forbids NPT signers from trading with India in nuclear materials and technology. In exchange, India would allow the International Atomic Energy Agency (IAEA) to inspect civilian facilities. India pledged to erect a firewall between these installations, which would acquire nuclear know-how from abroad, and military ones beyond the IAEA's reach. This separation is "arguably the most important of [India's] commitments," the U.S. State Department's lead negotiator, R. Nicholas Burns, under secretary for political affairs, testified in Congress last November.

It's also deeply challenging to India's government—and a political lightning rod. In India, "the hard-liners do not want this agreement, because they feel it will impinge on the military effort," says Kenneth Luongo, executive director of RANSAC, a nonproliferation think tank in Washington, D.C. As part of the agreement, India would forswear further nuclear weapons tests, thus freezing development of its arsenal.

Also disconcerting to hawks within India is that the separation plan would unravel the deliberate ambiguity around India's nuclear program. "For historical reasons, no facilities are clearly demarcated as civilian or military," says T. S. Gopi Rethinaraj, an arms-control expert at the National University of Singapore. Hundreds of nuclear specialists divide their time between civilian and weapons R&D. Like an operation to separate conjoined twins who share vital organs, splitting the nuclear establishment will be complex. "In identifying civilian nuclear facilities, we have to determine that they are of no national-security significance," Anil Kakodkar, chief of India's Atomic Energy Commission, told reporters at a recent press conference. "We will do this in a phased manner."

Other concerns divide U.S. policymakers, the nuclear industry, and the nonproliferation community. The United States stands to gain lucrative contracts to supply fuel and technology to India's fast-growing nuclear energy sector, and India has pledged not to export enrichment or reprocessing technologies to states without such a capacity. But some have doubts: What if India were not a reliable partner? What if it diverted new technology to weapons R&D, either on the sly or by reneging on the deal? "India may well become another source for illicit nuclear trade," asserts nonproliferation expert David Albright, president of the Institute for Science and International Security, a think tank in Washington, D.C.

As Burns explained to Congress, "We concluded we had a better chance to have India meet international nonproliferation standards if we engaged rather than isolated it." He added that he has urged India "to craft a credible and transparent plan."

Its outlines are now emerging. In December, a delegation to Washington, D.C., led by Indian Foreign Secretary Shyam Saran shared with U.S. officials the first draft of a separation plan. It fell short of U.S. expectations, with several supposedly civilian facilities on the military list, says a U.S. State Department official. The tug of war includes CIRUS, a reactor in Mumbai presumed to have produced plutonium for weapons; a centrifuge hall in Mysore that enriches uranium for naval reactors, analysts claim; and fast-breeder reactors and a fuel reprocessing plant in Kalpakkam (see map).

CIRUS is burdened with Cold War baggage. When India purchased the heavy-water research reactor from Canada in 1956, it pledged to use it only for peaceful purposes. But analysts assert that CIRUS cranked out plutonium for India's first fission devices, tested in 1974. Despite claims that the devices were for peaceful uses, like oversized sticks of dynamite, the United States assumed the worst and spearheaded a 30-year drive to choke off the flow of nuclear technologies to India. India declared itself a nuclear power after a second round of tests in 1998.

CIRUS was the sole source of plutonium for India's stockpile until Dhruva, a larger heavy-water reactor, came on line to augment production in 1985. India's December opening bid places CIRUS on the military list, excluding it from inspection. But U.S. officials argue that declaring it civilian would dissipate lingering bitterness over India's failure to keep its "peaceful uses" pledge in the past. If India were to acquiesce and declare CIRUS civilian, it might build an upscale version of Dhruva or convert a power reactor into a weapons facility, says Rethinaraj. Construction of new military facilities is not prohibited under the U.S.-India deal. Further complicating matters, CIRUS is located in the heart of the Bhabha Atomic Research Centre (BARC), much of which, including Dhruva, is on the military list.

Kalpakkam represents a different kind of headache. The fast-breeder reactors there are testing a blend of uranium and plutonium fuel for civilian power reactors. But the reprocessing facilities that extract plutonium from spent fuel could just as well produce nuclear material for bombs. India's breeders are meant to be a bridge from its current power plants, which draw on India's dwindling uranium reserves, to future reactors that tap the country's vast supplies of thorium (*Science*, 19 August 2005, p. 1174). (India has placed its thorium facilities on the ▶

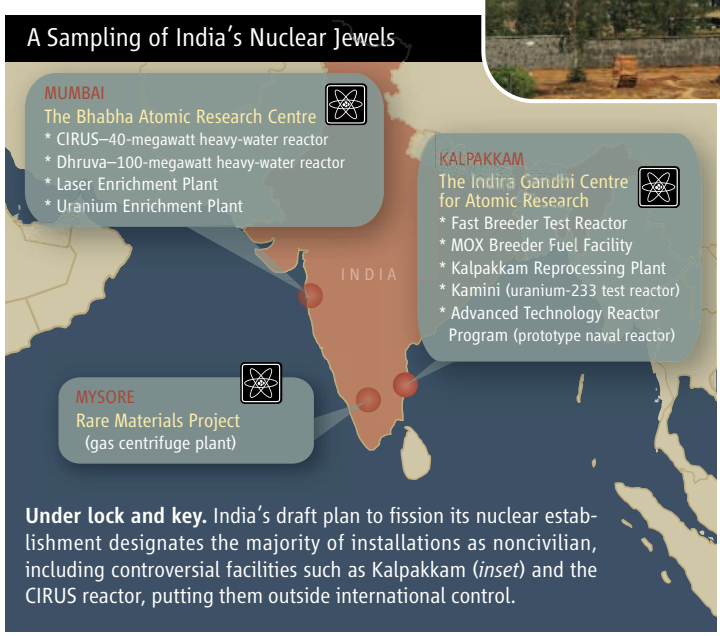

Under lock and key. India's draft plan to fission its nuclear establishment designates the majority of installations as noncivilian, including controversial facilities such as Kalpakkam (*inset*) and the CIRUS reactor, putting them outside international control.

SOURCE: INSTITUTE FOR SCIENCE AND INTERNATIONAL SECURITY; (PHOTO INSET) P. BAGLA

military list as well, it says, to protect the intellectual property of its designs.)

Some observers hold that the nuclear pact undercuts Kalpakkam's economic rationale because India could import uranium, postponing the use of thorium reactors. Kakodkar insisted that India will stick with the development of fast breeders, not only for electricity generation but also because thorium reactors would benefit from the design experience. The bottom line, he said, is that India will not submit any of its R&D centers to safeguards, including the Indira Gandhi Centre for Atomic Research in Kalpakkam.

A third flash point is the Rare Materials Project (RMP) in Mysore. At this facility, uranium hexafluoride gas is fed into a centrifuge cascade that boosts the concentration of the fissile isotope uranium-235. Analysts link this enrichment facility to India's classified program to develop naval reactors; they point out that it could just as easily churn out bomb-grade uranium for weapons. Last month, A. N. Prasad, a former BARC director, insisted in *The Hindu* newspaper that the RMP "cannot even be discussed, let alone safeguarded."

Whatever happens to the facilities, some experts argue that by pledging to uphold a moratorium on testing, India has in effect sworn not to refine its nuclear arsenal. "That's the greatest achievement of the deal," asserts Rethinaraj. It's unclear whether the U.S. Congress will buy that if it has qualms over the separation plan. Burns and his team were in New Delhi earlier this week for further negotiations. Engagement with India—or continued isolation—is still on the table.

–RICHARD STONE

With reporting by Eli Kintisch in Washington, D.C., and Pallava Bagla in New Delhi.

CNRS SHAKEUP

France's Basic Science Agency Hopes New Lineup Will Resolve Crisis

PARIS—France's leading basic research agency, CNRS, is struggling to get back on course after the abrupt loss of two top managers. CNRS President Bernard Meunier resigned on 5 January; 4 days later, the number two, Director Bernard Larrouturou, was fired. This ended a damaging standoff at CNRS over the selection of department directors, according to Research Minister François Goulard, who told *Science* that Prime Minister Dominique de Villepin approved his decision to replace Larrouturou. It had been an open secret for months that the two Bernards were at loggerheads (*Science*, 27 May 2005, p. 1243).

Larrouturou, meanwhile, vigorously defended his tenure at a press conference on Tuesday and in a letter to the CNRS staff. (A handout for reporters listed 12 frequent criticisms of the agency and declared each of them "FALSE!") In the letter, Larrouturou said that the decision to fire him was "reactionary" and that the disagreement between Meunier and him was "deliberate and organized" to thwart the reform plans (www.cnrs.fr/Lettre_aux_personnels_01051.pdf).

Most of the CNRS management team backed Larrouturou in a public statement last week. The research unions and the protest movement Sauvons La Recherche (SLR) also objected to his ouster, even though they had opposed his plans for CNRS and continue to oppose the government's science reform bill that will become law this month. SLR decried the government's "hostile decision" to remove Larrouturou, saying that it was illogical to approve the reform and then fire its architect. But Goulard rejects that argument: "One can agree with a director's reform but not necessarily agree with all his policies."

Moving swiftly, the government last week installed a new president: Catherine Bréchignac, a physicist and CNRS director from 1997 to 2000. Arnold Migus, a physicist and director of the French Institute of Optics in Orsay, was set to take Larrouturou's place, but Goulard intends to merge the two top CNRS positions by decree.

CREDIT: E. LEGOUHY/CNRS PHOTOTHÈQUE

Return engagement. Catherine Bréchignac gets a second tour at the CNRS.

Bréchignac will be the first to hold the new post, he says. Migus will remain second in command.

Jacques Fossey, general secretary of SNCS, the leading research union, says that despite previous disagreements with Bréchignac, "we were able to work with her." Whether Bréchignac will heed calls to scrap Larrouturou's reform plan and start over remains to be seen. "It is up to the management to decide on the agency's internal organization," says Goulard. It's not likely to be thrown out, he adds, although he doesn't rule out some improvements. **–BARBARA CASASSUS**

With reporting by Martin Enserink.

Bush Aide Fan of Research

Reading the tea leaves, science advocates are hoping that White House Chief of Staff Andrew Card's endorsement of a high-profile National Academies report on U.S. science presages a surprise funding bonus in the 31 January State of the Union address or subsequent 2007 budget. Recommendations from the October report, entitled *Rising Above the Gathering Storm*, include an annual extra $10 billion to fund physical sciences and expansive new science education and training efforts (*Science*, 21 October 2005, p. 423).

Speaking to the U.S. Chamber of Commerce last week, Card called the report "compelling." He said the report had many "appropriate suggestions, but we have to put them in the context of [White House Budget Director] Josh Bolten's budget." **–ELI KINTISCH**

Pact Seeks Climate Volunteerism

Nations representing half the world's greenhouse emissions cemented a voluntary technology-sharing pact last week in Sydney, Australia. The Asia-Pacific Partnership on Clean Development and Climate, which includes the United States, China, India, Korea, Japan, and Australia, agreed to examine technologies to allow cleaner cement production and coal burning. U.S. President George W. Bush plans to ask Congress for $52 million to promote and deploy technologies "off the shelf" through voluntary exchanges among companies, says Energy Department official Karen Harbert. Critics say mandatory emissions caps better stimulate technologies. **–ELI KINTISCH**

Toxics List Scrutinized

The Environmental Protection Agency (EPA) is planning to loosen reporting rules for chemicals on its Toxic Release Inventory (TRI) list. An advocacy group thinks that's a bad idea.

Under EPA regulations, companies must tell the agency every year how much of 666 chemicals on the TRI they release to the environment. Under a revised rule, EPA will increase the reporting thresholds and only require reports every 2 years. Those changes will make it harder for the public to track dangerous chemicals, argues the Environmental Working Group in Washington, D.C., including five chemicals EWG says, by EPA's own rules, should be subject to even stricter reporting thresholds. "They're chemicals that we ought to track, because they're so hazardous," says Richard Wiles of EWG. EPA expects to finalize the rule by the end of the year.

–ERIK STOKSTAD

SOUTH KOREAN SCIENCE

Armed With Cash, Institute Chief Launches an Education 'Blitzkrieg'

DAEJEON, SOUTH KOREA—For months, Robert Laughlin has talked up plans for transforming one of South Korea's top science universities into an academic powerhouse able to compete with the likes of the Massachusetts Institute of Technology. Now the Nobel laureate physicist has a war chest to make it happen. South Korea's legislature has approved the first installment of a $97 million "globalization package" for the Korea Advanced Institute of Science and Technology (KAIST) in Daejeon, a science city 150 kilometers south of Seoul. "It's time for a blitzkrieg," Laughlin says.

Bold moves. Robert Laughlin says he aims to "internationalize" the Korea Advanced Institute of Science and Technology.

In December 2004, a few months after being appointed KAIST president, Laughlin roiled the campus with a proposal to triple KAIST's enrollment and shift the balance toward undergraduates, quadruple tuition charges, and transform in-house research from an industry subsidy into a money spinner. Critics denounced the plan as disruptive (*Science*, 25 February 2005, p. 1181). "It was such a shock," says nuclear engineer Chang Soon Heung, a KAIST vice-president. "We were afraid he would mess up our efforts to raise funds and attract students." Science ministry officials repeatedly ruled out tuition hikes. "They said, 'No, no, no,' " Laughlin says, but promised support. "I said, 'Show me the money.' "

Now they have. The ministry has set up a special fund of 20 billion won ($19.4 million) per year over the next 5 years to make KAIST more competitive; on 30 December 2005, the National Assembly approved the 2006 allotment. Although the increase is less than 10% of KAIST's $200 million budget, it will allow the university to raise the fraction of foreign faculty to 15% and aim to teach all graduate courses in English by 2010, among other changes. (Currently, about one in three are in English.) "We're trying a bold experiment to internationalize students," Laughlin says. "It's what the parents want."

Top science students tend to enroll at Seoul National University, Laughlin says, unless they flunk SNU's tough English entrance exam. That means that the best KAIST students often have poor English skills. Many KAIST faculty members, however, are SNU grads proficient in English. Last year, Laughlin canvassed faculty members to see who would lecture in English rather than Korean. "They didn't want to do this at first," he says, "but I got big smiles when I mentioned they'd be paid a bonus." The fund will also strengthen KAIST's R&D, allowing Laughlin to award seed money for innovative projects and lure talent with handsome start-up packages.

Although Laughlin now has more spending power, the blunt-talking reformer also has fences to mend. He has made enemies in prodding professors to compete for grants and for failing to aggressively court corporate R&D sponsors, such as the semiconductor giant Samsung Electronics. "He just pushes his way without listening to us and thus lowers our morale," claims one senior professor.

Even Laughlin's fiercest critics, though, admire the accomplished scientist as a role model for Korean students and credit him for attracting more top-notch students to KAIST. "This is a conflict between two different visions," says Kim Sang-Soo, KAIST's vice president of operations. Laughlin agrees—and vows to press ahead with implementing his vision. The "real reforming," he says, "hasn't happened yet." **–RICHARD STONE**

With reporting by Ahn Mi-Young, a freelance writer in Seoul.

SCIENTIFIC PUBLISHING

Hwang Aftereffects Reverberate at Journals

As *Science* announced its retraction last week of two fraudulent papers by teams led by Woo Suk Hwang of Seoul National University, other journals that had published papers by the disgraced Korean scientist or his colleagues at MizMedi Hospital in Seoul were investigating whether phony or misleading data had appeared in their pages, too.

Hwang and his co-authors published a flurry of papers in at least nine journals within the past 2 years. *Molecules and Cells*, a Korean journal that published several papers last year on human embryonic stem (ES) cells and cloning by the MizMedi co-authors, told *Science* it would formally retract three papers on 28 February. Associate Editor Ahn Kwangseog said photographs used in those papers also appeared in papers submitted to *Science*, *Stem Cells*, *Reproduction*, and *Biology of Reproduction*.

Biology of Reproduction has already retracted one paper—on an animal-free culture system for human ES cells—because of apparent duplication of images that also appeared in the 2004 *Science* paper. Judith Jansen, managing editor of the journal, says she does not know whether additional papers have problems; the journal has published at least four co-authored by either Hwang or the MizMedi group. "We're looking at everything that we have," Jansen says.

The journal *Stem Cells* has expressed "concern" about a technical paper from MizMedi researchers on the cultivation of human ES cells, citing apparent duplications of images within the paper as well as use of an image that also appeared in the 2004 *Science* paper. Editor-in-Chief Curt Civin of Johns Hopkins University in Baltimore, Maryland, says the authors have acknowledged "mistakes." The journal is awaiting results of investigations under way in Korea to determine whether the paper is still valid.

At *Molecular Reproduction and Development*, editors are sifting through at least six Hwang-authored papers, all of them involving research with animals, while they await results of investigations under way in Korea and at the University of Pittsburgh, according to Susan Spilka of the publisher, John Wiley & Sons.

Several other journals published papers detailing animal studies by Hwang or the MizMedi group. Anthony Trioli of Elsevier, publisher of *Theriogenology*, says it is looking into an unspecified number of papers; the results aren't expected for several weeks.

No end in sight. More papers by the Hwang team are under investigation.

A spokesperson for the publisher of the *Korean Journal of Veterinary Science*, said the journal is not investigating a Hwang paper from last year. **–JENNIFER COUZIN, CONSTANCE HOLDEN, AND SEI CHONG**

CREDITS (TOP TO BOTTOM): COURTESY OF KAIST; LEE JAE-WON/REUTERS

Endocannabinoids, substances in the brain and body mimicked by marijuana's active ingredient, are inviting therapeutic targets for conditions from obesity and pain to addiction and osteoporosis

Drugs Inspired By a Drug

WHATEVER ONE'S VIEW OF ITS LEGALITY, there's no denying that marijuana is a potent drug that has a strong impact on the brain and the rest of the body. In addition to producing an intoxicating "high," marijuana can ease anxiety and pain, stimulate hunger, and impair memory. The drug also has a long history in folk medicine. Over the centuries, it's been used for ills such as menstrual pain and the muscle spasms that afflict multiple sclerosis sufferers and others.

Now, medicine may be on the doorstep of a new era of drug development, one centered not on marijuana itself but instead inspired by the discovery more than a decade ago that its primary active ingredient, a chemical called tetrahydrocannabinol (THC), mimics natural chemicals acting in the brain and elsewhere in the body. Like many other drugs, THC exerts its effects by binding to receptors, proteins located on the surface of neurons and other cells that are the targets of naturally occurring regulatory molecules—in this case, ones dubbed endocannabinoids, after the marijuana-producing plant *Cannabis sativa*.

In the past few years, a torrent of research has pointed to the endocannabinoids and their receptors as major targets for drug development. "Endocannabinoids apparently act in just about every system people have looked at," says THC discoverer Raphael Mechoulam of Hebrew University Medical Faculty in Jerusalem, Israel. The systems include those controlling learning and memory, appetite and metabolism, blood pressure, emotions such as fear and anxiety, inflammation, bone growth, and even the growth of certain cancers. Consequently, depending on the condition they aim to treat, drug developers are rushing to identify compounds that either turn up endocannabinoid function or dampen it.

The drug closest to the clinic is rimonabant, an endocannabinoid blocker under development by the French pharmaceutical company Sanofi-Aventis. Clinical trials reported last year showed that the drug can aid in controlling obesity, as well as metabolic syndrome, a constellation of conditions including high blood pressure and elevated blood lipids that often accompanies obesity and predisposes individuals to cardiovascular disease. Researchers from Sanofi-Aventis and elsewhere are now exploring whether rimonabant can be used to help smokers and alcoholics kick their habits.

Although efforts to develop agents that enhance endocannabinoid activity are less advanced, such compounds are undergoing preclinical testing for the treatment of several conditions, including epilepsy, pain, anxiety, and diarrhea. "There are several possible therapeutic strategies we can use to exploit our knowledge of how endocannabinoids are regulated," says Vincenzo Di Marzo of the University of Naples, Italy.

Target identified

Endocannabinoid research got off to a slow start. The modern era began in 1964 when Mechoulam and his colleagues isolated THC and determined its structure, which proved to be lipidlike. That may have been one reason why interest in THC lagged early on. Lipids are "greasy, messy little molecules that are hard to do anything with," says Bradley Alger, an endocannabinoid researcher at the University of Maryland School of Medicine in Baltimore.

Most known signaling molecules, such as neurotransmitters and hormones, are amino acids and peptides: substances that need to interact with specific receptors to exert their effects. But lipids can pass directly into cell membranes, and some researchers thought that THC might exert its effects by simply dissolving in, and disrupting the function of, nerve cell membranes. Such a nonspecific mechanism of action would make it very difficult to design drugs that mimic THC's desirable effects without causing the psychoactive ones as well.

In the mid-1980s, however, the tide turned in favor of a distinct THC receptor when Allyn Howlett's team, then at St. Louis University Medical School in Missouri, linked THC activity to adenylate cyclase, an enzyme well known to help transmit signals from receptors to the cell interior. In 1990, Lisa Matsuda, Tom Bonner, and colleagues at the National Institute of Mental Health finally cloned a THC

CREDIT: CORDELIA MOLLOY/PHOTO RESEARCHERS INC.

Triple threat. Can drugs that block endocannabinoids help people lose weight and stop smoking and drinking?

receptor, from a rat brain, although it's since been found in many peripheral tissues as well.

The discovery of this receptor, now called CB_1, meant that the brain must have its own THC-like molecules, as the body doesn't maintain receptors just for the components of psychoactive weeds. Mechoulam's group identified the first of these endogenous cannabinoids, called anandamide, in 1992, and a few years later followed up with a second, 2-arachidonylglycerol (2-AG). These compounds have more than one target: In 1993, Muna Abu-Shaar and colleagues at the Medical Research Council Laboratory of Molecular Biology in Cambridge, U.K., cloned a second cannabinoid receptor, CB_2, which occurs mainly on cells in the body periphery.

Stopping the munchies

The endocannabinoid field began to take off in the years that followed. "We have made a lot of progress, mainly due to the fact that we've discovered the receptors and their endogenous ligands," says Daniele Piomelli of the University of California (UC), Irvine. Researchers began to pursue several strategies for exploring the functions of the endocannabinoids. For example, they designed chemicals that either mimic endocannabinoid action at their receptors or block it.

Rimonabant, which was identified in 1994 by a team of Sanofi-Aventis scientists, was one of the first inhibitors to come out of these efforts. The researchers found that it preferentially binds to CB_1, thereby blocking endocannabinoid action at that receptor but not at CB_2. They also found that rimonabant promotes weight loss.

Marijuana users have known for years that smoking a joint causes the "munchies," stimulating their appetite for food. Indeed, people suffering from debilitating diseases such as AIDS sometimes use marijuana as an appetite aid. It therefore hasn't been a huge surprise that several teams have shown that THC and endocannabinoids stimulate food intake by mice. In contrast, mice administered rimonabant eat less.

Endocannabinoids may be part of the system by which the hormone leptin controls food intake and metabolism. One hint of this came in a 2001 study on mutant mice that don't make leptin and therefore overeat and become extremely obese. George Kunos, Di Marzo, who was then on sabbatical in the Kunos lab, and their colleagues at the Medical College of Virginia in Richmond found that in such mice, endocannabinoid levels are much higher than normal in the hypothalamus, a brain region involved in appetite control. Treating the rodents with leptin brought the levels down.

In the 22 December 2005 issue of *Neuron*, Lorna Role and her colleagues at Columbia University College of Physicians and Surgeons in New York City provided a possible mechanism to account for how leptin suppresses endocannabinoids: Endocannabinoid production is stimulated by the influx of calcium ions that occurs when nerve cells respond to appropriate neurotransmitters, and leptin inhibits this influx.

> **"There's an overwhelming flood of literature** on endocannabinoids."
>
> —Beat Lutz, Max Planck Institute of Psychiatry

Even as the evidence linking endocannabinoids to appetite control was building, Sanofi-Aventis embarked on a series of clinical trials designed to test rimonabant's effectiveness as an antiobesity drug. The promising results from two of these, one including 1507 subjects, most of whom live in Europe, and the other, including 1306 North American subjects, were published last year. (The European study appeared in the 16 April 2005 issue of *The Lancet*, and the North American study was in the 17 November 2005 issue of the *New England Journal of Medicine*.)

In both studies, which produced similar findings, all the patients were on a reduced-calorie diet. But whereas controls lost only 2 to 3 kilograms of weight over the year's course of treatment, individuals who also took 20 milligrams of rimonabant a day lost 8 to 9 kilograms. Perhaps even more important, says Jean-Pierre Després of the Laval Hospital Research Center in Montreal, Canada, who directed the North American study, those taking the drug showed greater reduction in abdominal fat deposits, which are a known risk factor for diabetes and heart disease. "To me," he adds, "rimonabant is more of a cardiovascular drug than a weight-loss drug."

Indeed, rimonabant appears to have benefits beyond simple weight loss. In order to be eligible for the trials, the subjects also had to have additional risk factors for heart disease, such as high blood pressure or elevated levels of blood lipids including cholesterol. Those risk factors also showed greater improvement in the treated subjects than in controls, apparently even more than could be expected from the weight loss alone. "Only about 50% of the metabolic effects were due to weight loss," says Di Marzo. "There seems to be some direct effect on fat cells."

There is support for that idea from animal work. For example, Beat Lutz's team at the Max Planck Institute of Psychiatry in Munich, Germany, working with that of Uberto Pagotto at Sant Orsola-Malpighi Hospital in Bologna, Italy, found that mice lacking the CB_1 receptor stay very lean throughout life. This can't be totally due to reduced feeding: Although the animals do eat less while young, they eventually eat more food—but still maintain their sleek physiques.

Researchers, including the Sanofi-Aventis team and that of Kunos, now at the National Institute on Alcohol Abuse and Alcoholism (NIAAA) in Bethesda, Maryland, have found that endocannabinoids can act directly on both fat and liver cells in ways that lead to increased synthesis of fatty acids. "Blocking this promotes fat-burning," Kunos says. This may be another way rimonabant keeps weight down.

Diet drugs, which typically have to be taken long term, have had a checkered history, so

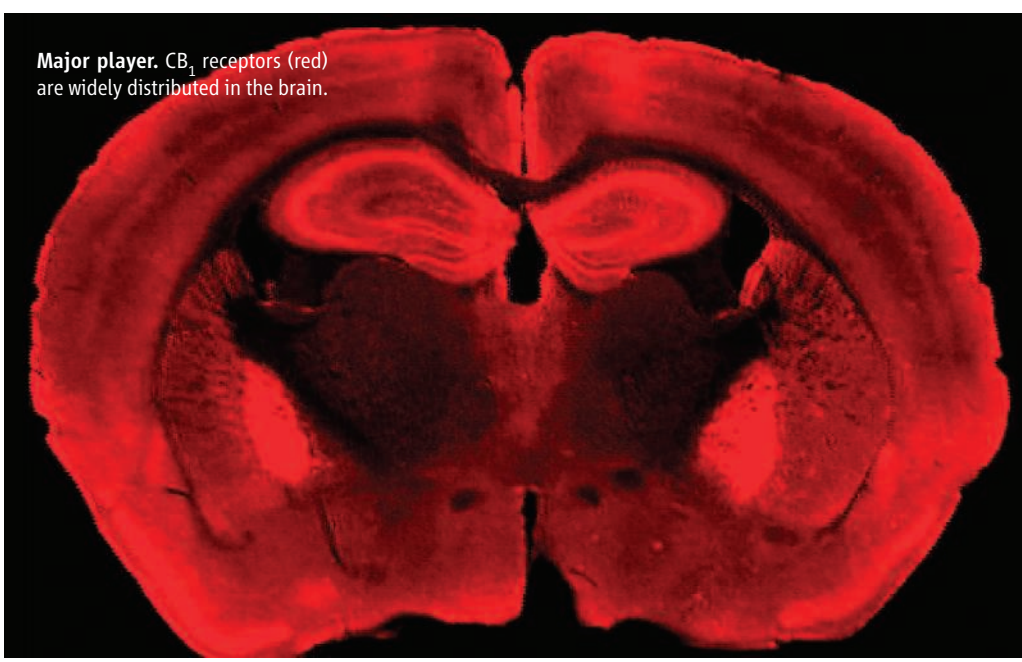

Major player. CB_1 receptors (red) are widely distributed in the brain.

CREDIT: K. MACKIE/UNIVERSITY OF WASHINGTON

researchers will be closely watching the safety of rimonabant. So far, it appears to be well tolerated. Robert Anthenelli of the University of Cincinnati College of Medicine in Ohio, who has conducted clinical trials with the drug, describes its side effects, including nausea, diarrhea, and depression, as generally "mild and transient."

Smoke signals

Anthenelli directs an effort aimed at finding out whether rimonabant can help with another major cardiovascular risk factor: smoking. About 3 years ago, Caroline Cohen, Philippe Soubrie, and their colleagues at Sanofi-Aventis showed that the drug reduces self-administration of nicotine by rats. Nicotine, like other addictive drugs, hooks its users by triggering release of the neurotransmitter dopamine in the brain's pleasure centers, and the researchers found that rimonabant reduces that release. These results suggested that the drug might aid smoking cessation and, given its other effects, help prevent something that is often a bane for smokers trying to quit: weight gain.

None of the results from the smoking trials have yet made it into print, but about 2 years ago, Anthenelli described early findings from STRATUS-US (Studies with Rimonabant and Tobacco Use in the United States) at the annual meeting of the American College of Cardiology. The 787 participants were divided into a control group whose members received a placebo and two treatment groups, one of which got 5 milligrams of rimonabant a day whereas the other got 20 milligrams. The quit rates of people in those two groups were about double those of the controls, Anthenelli says, "and they had less weight gain, at least in the short term."

NIAAA is also currently sponsoring a phase II trial to see whether rimonabant curbs alcohol consumption in heavy drinkers. And although the work is not yet nearly as advanced as that on obesity and smoking, rimonabant and other CB_1 inhibitors are being tested as possible therapies for a number of additional conditions in which endocannabinoids are implicated. Last year, for example, Di Marzo, working with Jonathan Brotchie at Toronto Western Research Institute in Canada, reported results indicating that endocannabinoid activity contributes to Parkinson's disease symptoms.

The researchers created a nonhuman primate model of the disease by treating marmosets with the chemical MMTP, which destroys the same brain area that degenerates in Parkinson's disease. They found that treating these animals with rimonabant improved their ability to perform voluntary movements, which are impaired in Parkinson's disease. In addition, when administered together with levodopa, the standard Parkinson's drug, rimonabant ameliorated the abnormal involuntary movements that are a distressing side effect of levodopa treatment.

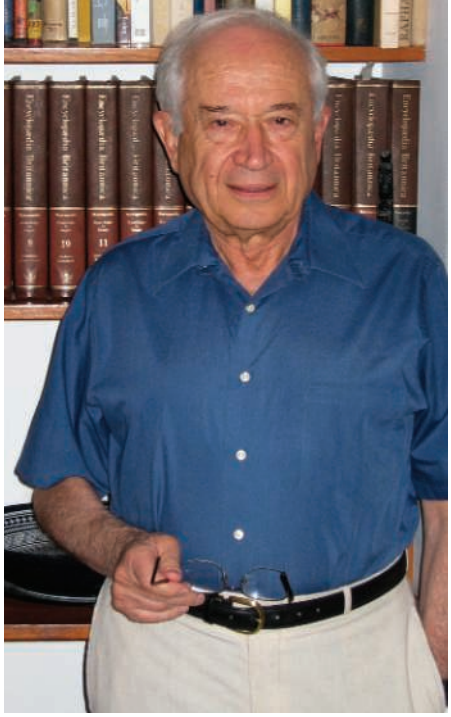

"Endocannabinoids apparently **act in just about every system** people have looked at."

—Raphael Mechoulam, Hebrew University

The actions of endocannabinoids outside the brain are also stirring clinical interest. In the late 1990s, Kunos and his colleagues showed that the chemicals underlie the low blood pressure of hemorrhagic shock. As a result of hemorrhagic bleeding, Kunos says, "the macrophages of the immune system are activated. They produce anandamide, which attaches to the linings of the blood vessels and heart. This causes vasodilation and thus decreased blood pressure."

Since then, the Kunos team has shown that endocannabinoids also contribute to low blood pressure associated with cirrhosis of the liver and with septic shock, which is induced by the toxins produced by certain pathogenic bacteria. In those instances as well, activated macrophages are apparently releasing anandamide. In all these cases, rimonabant blocked the drop in blood pressure, suggesting that the CB_1 inhibitor might be useful for treating the conditions.

Strong bones, no high

In many other conditions, the goal is not blocking endocannabinoids but the somewhat more difficult task of enhancing their activity. One way to do this is with compounds that mimic endocannabinoid actions on their receptors, as long as this can be done without also causing the high that marijuana is famous for.

This may be easier to accomplish with the CB_2 receptor, which is found mostly on peripheral cells. In 1999, for example, Mechoulam and his colleagues came up with a compound dubbed HU-308 that specifically triggers CB_2 receptors. HU-308 produces no behavioral effects, at least in mice. In this week's issue of the *Proceedings of the National Academy of Sciences*, Itai Bab (also at the Hebrew University of Jerusalem), Mechoulam, and colleagues describe results indicating that a CB_2 activator might help combat osteoporosis, the common bone-thinning disease. They found that if CB_2, but not CB_1, is knocked out in mice, the animals show bone loss much like that in osteoporosis patients. HU-308 can counteract that by stimulating the activity of bone-forming cells while at the same time turning down the activity of cells that degrade bone. The drug also prevented most of the bone loss that ordinarily occurs in female mice whose ovaries have been removed to mimic the osteoporosis that occurs in women after menopause.

Stimulating CB_1 receptors could be more problematic. They are so widely distributed throughout both the brain and body periphery that activating them indiscriminately could cause a host of unwanted side effects. So instead of turning up the receptors, researchers are taking a different tack: blocking the enzymes that inactivate endocannabinoids after they've done their job. Drug developers have an advantage here in that the compounds are not made all the time, but only when and where needed, and then are quickly destroyed. "These lipid signaling molecules are probably made and broken down 'on demand,' " says Benjamin Cravatt of the Scripps Research Institute in La Jolla, California.

So even though an inhibitor of a degradative enzyme would be present throughout the body, it should only buttress an endocannabinoid's action at the sites where it is actually being produced. The Cravatt team has discovered an enzyme called fatty acid amidohydrolase (FAAH), which breaks down anandamide. Cravatt, Piomelli, and others have identified inhibitors of FAAH and also of monoacylglycerol lipase, the enzyme that degrades 2-AG. These inhibitors may have several therapeutic applications given that endocannabinoids seem to protect against a variety of ills.

One such ill is high blood pressure. Two years ago, the Kunos team found elevated levels of both anandamide and CB_1 receptors in the blood vessels and hearts of rats that spontaneously develop hypertension. Given that anandamide is known to lower blood pressure, Kunos speculates that the changes are an effort by the body to counteract the blood pressure rise, even though it does not return the animals' blood pressures to normal. Consistent

CREDIT: COURTESY OF RAPHAEL MECHOULAM

with this idea, Kunos and his colleagues found that an FAAH inhibitor lowers the blood pressure of the hypertensive rats.

Recent research suggests that tissue-damaging inflammation might also be treated with agents that bolster endocannabinoid activity. In 2004, for example, Lutz's group showed that mice lacking CB_1 receptors developed much more severe inflammation of the intestines when treated with a chemical irritant than did normal animals. In contrast, animals unable to make FAAH were protected from the irritant's effects—an indication that drugs that inhibit the anandamide-degrading enzyme might treat inflammatory bowel conditions such as Crohn's disease.

Endocannabinoid protection against inflammation extends into the brain. In the January issue of *Neuron*, Oliver Ullrich of Otto von Guericke University in Magdeburg, Germany, and his colleagues report elevated anandamide concentrations in the brains of multiple sclerosis patients. Further work with mouse brain tissue in lab cultures suggests that the anandamide increase is an effort by the brain to ward off the damaging effects of immune cells called microglia.

By causing inflammation, microglia ordinarily worsen the damage caused to brain neurons by the excitatory neurotransmitter glutamate. But the researchers found that anandamide suppressed that inflammation whereas CB_1 and CB_2 inhibitors increased it. Such data may help explain why the drug Sativex, a standardized extract of marijuana plants produced by GW Pharma in the United Kingdom, seems effective against MS spasticity.

Endocannabinoids may also protect brain neurons directly against excitotoxic damage. About 2 years ago, Lutz, now at the University of Mainz in Germany, and his colleagues genetically engineered mice so that they lacked CB_1 receptors in the main neurons of the forebrain, but not in the mossy neurons that feed them inhibitory signals. The researchers then injected the excitotoxin kainic acid into the brains of both those animals and of normal mice. They found that anandamide levels went up in the hippocampus of all the mice, but those lacking the CB_1 receptors in their forebrain neurons suffered much more severe seizures and neuronal damage than did the controls.

"The endocannabinoid system is like a brake in the brain so as not to have excessive neuronal activity," says Lutz. Drugs that boost endocannabinoid action by inhibiting their breakdown might therefore be useful for treating epilepsy, which occurs when neurons fire excessively, and neurodegenerative conditions such as Alzheimer's and Parkinson's disease, where excitoxicity is thought to play a causative role.

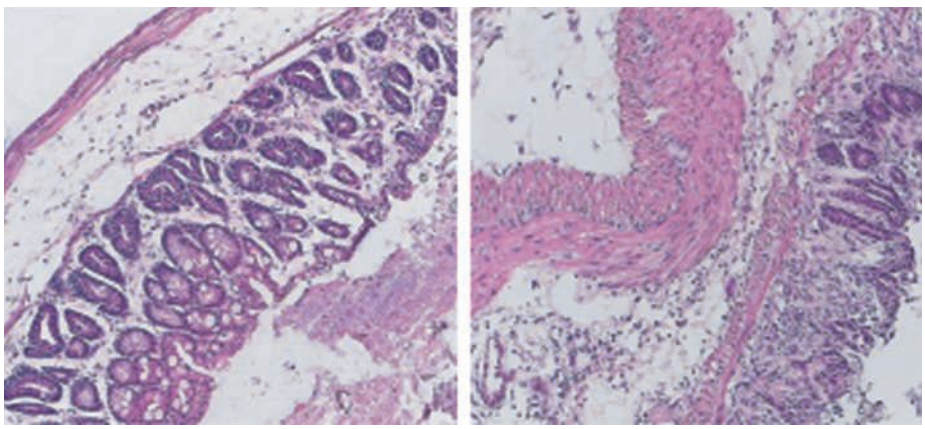

Gut protector. An irritating chemical causes much more severe inflammatory changes in the colon of a mouse lacking CB_1 receptors (*right*) than in a normal colon (*left*).

Combating pain and anxiety

If drug companies can develop safe and effective ones, endocannabinoid boosters might also tackle pain. Several years ago, UC Irvine's Piomelli and his colleagues showed that injecting anandamide into the paws of mice before injecting the noxious chemical formalin ameliorates the pain responses the animals would otherwise show. In contrast, injections of both CB_1 and CB_2 receptor inhibitors exacerbated those responses.

In that case, the endocannabinoid was acting to block the initiation of pain responses in the periphery. But about 6 months ago, the Irvine group showed that anandamide and 2-AG also contribute to something called stress-induced analgesia, in which the brain's pain-suppressing pathways are activated by an acute stress, such as an injury. They found that inhibitors of the degradative enzymes for both endocannabinoids enhance this pain suppression. Such inhibitors have also shown promising results in animal models of depression and anxiety.

Even phobias and posttraumatic stress disorder (PTSD) may be amenable to treatment with endocannabinoid boosters. When animals are repeatedly subjected to a noxious stimulus, such as a mild shock, that is paired with a innocuous stimulus, such as a tone, they will eventually learn to react with fear, by jumping, say, in response to the tone alone. Over time, that response will be lost in the absence of further shocks. About 3 years ago, Lutz and his colleagues showed this "extinction" of an aversive memory requires endocannabinoids. For example, they found that extinction did not occur in mice lacking CB_1 or given rimonabant.

About a year ago, a team led by Kerry Kessler of Emory University School of Medicine in Atlanta, Georgia, extended these results, showing a similar involvement of endocannabinoids in extinction of aversive memories in rats. The Emory team also demonstrated that they could enhance that effect by giving the animals a compound that inhibits endocannabinoid breakdown. Because there are parallels between fear conditioning in animals and PTSD, phobias, and other types of human anxieties, the researchers suggest that these conditions might be among those that would benefit from enhancing endocannabinoid activity.

And if all that hasn't been enough to draw the attention of basic scientists and drug developers, evidence from Di Marzo's group indicates that the chemicals even limit the growth of cancer cells. About 3 years ago, the researchers found that anandamide and 2-AG levels are elevated in samples of human colon cancers. This again appears to be a defensive response, as work with cultured human cancer cells, and more recently with thyroid tumors implanted in mice, shows that endocannabinoids inhibit tumor cell proliferation.

"There's an overwhelming flood of literature on endocannabinoids," Lutz says. "If you go to MEDLINE, almost every day you find a nice paper."

–JEAN MARX

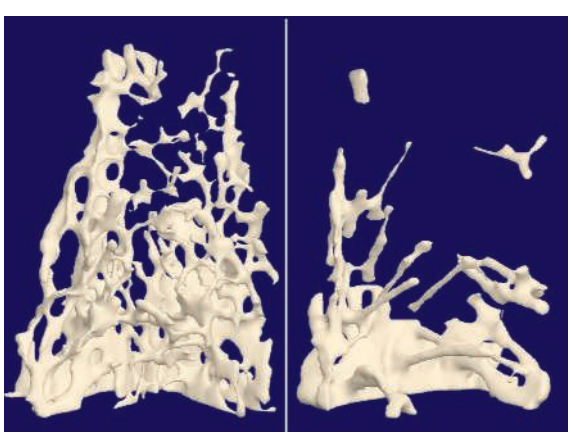

Skeleton preserver. Bone from a mouse lacking CB_2 receptors (*right*) is much less dense than bone from a normal mouse (*left*).

CREDITS (TOP TO BOTTOM): F. MASSA *ET AL.*, *JOURNAL OF CLINICAL INVESTIGATION* **113**, 1202 (2004); O. OFEK *ET AL.*, *PNAS* **103**, 696 (2006)

Crumbling splendor. A rising water table threatens Luxor Temple.

ARCHAEOLOGY

Rising Water Poses Threat to Egypt's Antiquities

Crop irrigation and inadequate sewers may sink Egypt's famed ancient temples and burial sites into a watery grave

LUXOR, EGYPT—The god Amun created the first solid ground, pushing back the waters of the primeval sea, according to Egyptian mythology. But his formidable powers may not be enough to save his own temple and other famous archaeological sites from rising waters along the Nile River. Amun's temple complex of Medinet Habu, which has survived 21 centuries in the desert, is now threatened by salty groundwater eating away at its foundations. "See this deterioration?" says University of Chicago epigraphist Brett McClain, pointing at flaking stone along the base of a temple wall. "This was not happening a few years ago."

Although officials disagree about the prime culprit, a combination of agricultural practices and inadequate sewers have combined to raise the water table several meters around Luxor, posing a silent threat to scores of temples and tombs critical to scholars such as McClain as well as to the tourism industry. "When I found out that the Temple of Luxor and the Temple of Karnak were going to completely fall apart because of the rising water table, I was shocked," says Zahi Hawass, director of Egypt's Supreme Council of Antiquities.

Hawass is overseeing efforts to reduce the damage, including digging huge channels around the threatened monuments. "Because the rising water table can damage everything, this project is my top priority," he says. But bureaucratic intransigence may stall longer-term solutions, such as convincing nearby farmers to switch crops.

In 2004, as damage reports came in from sites such as Medinet Habu, Hawass commissioned SWECO, an engineering firm based in Stockholm, to come up with a plan to protect the Luxor region. Luxor, an important religious and political center in ancient Egypt, is the source of thousands of inscriptions and images—many with their original paint still intact—that reveal the details of Egyptian life 3 millennia ago. The area also is critical for generating tourism revenue for Hawass's organization; it is second only to the Giza pyramids in popularity among visitors.

The study found that the temples' soft sandstone is absorbing rising groundwater, and with it, high levels of salt. When the water evaporates, the salt crystallizes, filling

Archaeological Pharaoh Sets Determined Course for Egypt

Zahi Hawass is arguably the most famous archaeologist in the world, as well as one of the busiest. Trained in his native Egypt and at the University of Pennsylvania in Philadelphia, the 58-year-old Hawass took over as secretary general of Egypt's Supreme Council of Antiquities in 2002. But he has been the public face of Egyptian archaeology for years, appearing in dozens of documentaries in his trademark Indiana Jones–style hat to lead viewers into dusty tombs.

Behind the scenes, he controls access to thousands of archaeological sites and also keeps his hand in several excavations; he administers $5.2 million to $7 million in tourist revenues annually. With 37 years in the field and a Western Ph.D., Hawass is reshaping Egyptian archaeology, raising standards and demanding respect from outsiders. Unlike many of his predecessors, Hawass drives a hard bargain with foreign researchers and museum officials, forcing excavators to publish promptly, pressuring museums not to buy looted antiquities, and demanding hefty fees for traveling exhibits.

While taking phone calls, signing documents, and joking with a visiting archaeologist in his Cairo office, Hawass recently spoke in his rapid-fire manner about his strategy for Egypt's archaeological future. **–A.L.**

Q: How do you reconcile tourism—and the need for revenue—with archaeology?

We put the monuments first. We stopped the proposed ring road by the pyramids. We stopped the western paved road that was going to Abydos. And we have a program to close the pyramids at Giza—a different one every year [for restoration]. We plan to limit tourists to a certain number [to limit damage to sites].

Q: Are you placing tighter controls on archaeological work?

For the first time, we are applying very strict rules. Egypt used to be a place where foreigners and Egyptians could do anything at anytime. Now for the first time, you cannot discover anything without restoring it. Number two, no one can excavate anything new in upper Egypt at all. You can only do restoration, conservation, GIS [Geographic Information Systems], and epigraphy. If you want to excavate, you go to the Delta, because the water and agriculture are damaging critical sites, and to the desert, because no one knows what is there.

Also, [archaeologists] have to publish a report 3 months after finishing [a season]. Every 5 years, if you don't have a final publication, you will be stopped. We stopped 35 expeditions run by amateurs. We stopped a French expedition at Saqqara that had been working for 10 years excavating tombs but with no publications.

CREDIT: GAVIN HELLIER/GETTY IMAGES

the porous rock. For an immediate fix, a Cairo-based firm, Egypco, is building drainage canals around both temples to drain the water west to the Nile; the project is under SWECO's supervision and uses $7 million in funding from the U.S. Agency for International Development (USAID). The work began a year ago and is due for completion this summer, says USAID official James Harmon. The projects should lower the groundwater around both temples by 2 meters or so, protecting the massive foundations that support thousands of tons of stone.

Hawass blames most of the groundwater problem on inadequate sewers, particularly on the crowded East Bank near the temples of Luxor and Karnak. A new sewage system at Karnak has led to a half-meter drop in groundwater levels, agrees Raymond Johnson, field director at the University of Chicago's center in Luxor. But Johnson and others point to the cultivation of sugar cane as the prime culprit, especially on the West Bank, home to Medinet Habu and a host of other temples and tombs. There, irrigation canals suck water from the Nile into what was once desert. Johnson notes that farmers regularly flood fields to speed the growth of sugar cane, thus keeping the ground saturated. "The canals never dry out, so the groundwater remains high," he says.

Johnson and other foreign experts argue that the best solution is to stop growing sugar cane near monuments. "Plant beans or flowers instead—something which uses less water—with the help of economic incentives," urges Johnson. But that would require cooperation among several ministries, and the Egyptian government strongly subsidizes the sugar industry, says one foreign expert who declines to be named. All the same, "given that priceless antiquities are a key part of the GDP [gross domestic product], I don't think this is a good tradeoff," the foreign official adds. But Hawass isn't optimistic about influencing farmers: "It would be pretty much impossible to change agricultural practices, so we will focus on engineering solutions."

Flawed foundation. Epigraphist Scott McClain finds water damage at Medinet Habu.

The problem on the West Bank of Luxor—where sugar cane cultivation is pervasive—is increasingly acute. Standing water can be seen in what remains of Amenhotep III's mortuary temple; Medinet Habu lies just a kilometer or two away on what once was desert. Johnson fears that the water is creeping west toward the Valley of the Queens and even the Valley of the Kings, home to Egypt's most spectacular—and vulnerable—tombs. Hawass insists those areas will remain high and dry. But plans are on the drawing board to build large drainage systems to move water on the West Bank back to the Nile, although the cost remains uncertain.

For researchers such as Johnson, who runs the University of Chicago's cataloging and restoration effort at sites such as Medinet Habu and the Luxor Temple, the rising groundwater is not the only threat. He notes an ominous increase in humidity and rainfall that threatens the fragile carvings and paintings, the bread and butter of current Egyptology. "In the last 20 years, we've watched the monuments age," he says.

Hawass and foreign archaeologists agree that the crisis requires immediate action. "If you don't start lowering the water table now, we'll start losing these monuments," says Johnson. If the effort fails, a large portion of Egypt's illustrious past may sink back into the primordial waters.

–ANDREW LAWLER

Q: Are you seeking to have artifacts that were taken illegally returned?
When I came to this position, I opened a new department called the department for the return of stolen artifacts. We actually stopped [artifact sales at] auctions in England and New York. And if you buy [stolen] artifacts, you will never be permitted to work in Egypt.

We are restoring the tomb of Amenhotep III [in Luxor]. We discovered the head of the king['s statue] is in five locations, all taken out of the country in the last century. The director of the Louvre refused to return their piece. How can we cooperate with them in the future? If you don't want to help us, we won't help you. I'm not asking for all artifacts to come back, just the unique ones which should be in their homeland.

Q: Some argue that Egypt can't keep track of the artifacts it has, such as in the basement of the Egyptian Museum in Cairo.
This was the past. We are building 13 museums now. I cannot find the artifacts to go into these museums. Sure, the basement of the Cairo Museum is full of thousands of artifacts—such as stone vases, things that cannot be displayed. And within a year, the basement of the Cairo Museum will be better than any museum in the world. We started a database 6 months ago to record every piece. Renovation of the basement is under way.

Q: What's your biggest challenge?
Training the people I need. I'm opening a school in Cairo dedicated to training [curators and archaeologists]. If you don't know what you are doing, people can deceive you.

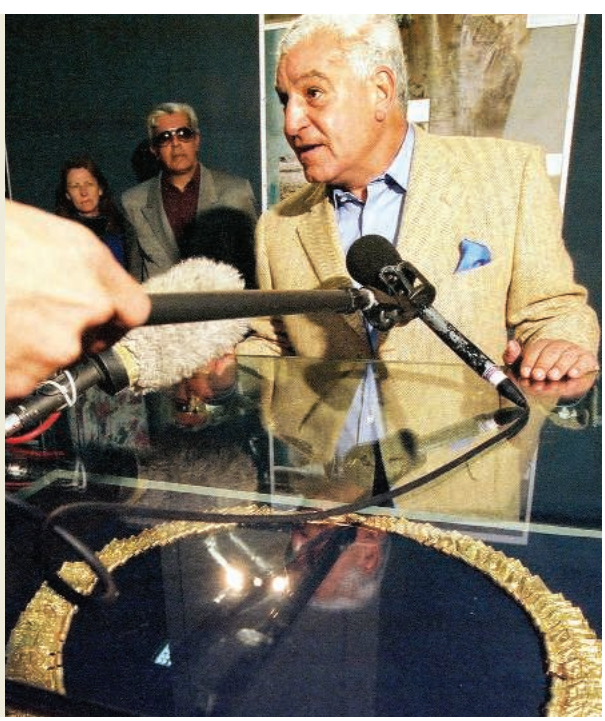

CREDITS (TOP TO BOTTOM): A. LAWLER/*SCIENCE*; K. BUCKHEIT/*SCIENCE* (MAP); MOHAMAD AL SEHETY/ASSOCIATED PRESS

BIOMEDICAL TRAINING PROGRAMS

NIH Told to Get Serious About Giving Minorities a Hand

A National Academies' report says that these controversial programs can't be assessed without better data—and better management

After more than 3 decades of trying to increase the number of minority biomedical researchers, officials at the National Institutes of Health (NIH) have a raft of anecdotal evidence that its training programs are working. One favorite success story is Erich Jarvis, a neuroscientist at Duke University in Durham, North Carolina, who, as an African-American student from Harlem, was supported by some of those programs and who in 2002 was named the nation's top young scientist. The program managers themselves exemplify NIH's goal of diversifying the nation's biomedical research workforce. Clifton Poodry, head of the division of Minority Opportunities in Research at the National Institute of General Medical Sciences (NIGMS), was born on the Tonawanda Seneca Indian Reservation in Buffalo, New York, for example, and spent 2 decades as a successful academic researcher before joining NIH.

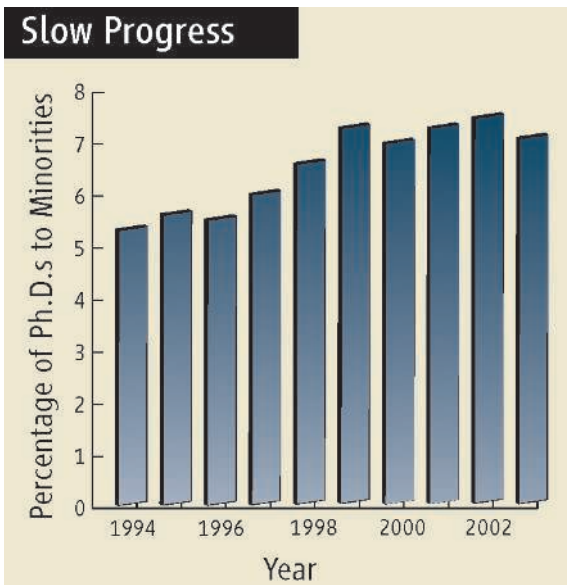

But personal success stories aren't the same as hard data. And good data, says a recent report* by a National Academies' National Research Council (NRC) panel, don't exist. Asked to assess the programs, the panel threw up its hands. It is devilishly difficult to track participants through their training and into the workforce to find out if they have indeed achieved the gold standard of becoming biomedical researchers, the panel concluded. NIH hasn't invested the time, money, or high-level interest needed for a proper evaluation, it added, nor shared what data do exist.

"There's no good way to track the success of these programs," says John Bailar, emeritus University of Chicago statistician and co-chair of the panel, part of NRC's Board on Higher Education and Workforce. "We were asked to find out what works, and we couldn't do it because of serious problems with the data." NIH can't even say how many participants are actually minorities, it noted, much less how well its programs are doing in churning out minority scientists.

The report's list of flaws is long and damning. Panel members deplored the lack of coordination among the programs, which are run by one or more of NIH's 27 institutes and centers. They questioned NIH's definition of success—the production of Ph.D. biomedical researchers good enough to win NIH funding—given the considerable opportunities open to those with less training and the importance of raising the level of public scientific literacy. They also pointed to a lack of commitment from the top. A meeting of minority-training coordinators convened by the panel, Bailar noted, was the first time all had been together in the same room. And even the report's most basic recommendation—that NIH convene such a group and have it draw up guidelines for a thorough evaluation—has yet to be implemented more than 6 months after NIH officials were briefed on the report.

"The root problem is that these programs have suffered from a lack of sustained high-level interest," Bailar asserts. Despite dedicated administrators such as NIGMS's Poodry and John Ruffin, who heads NIH's National Center on Minority Health and Health Disparities, Bailar says that "a lot of senior managers view these programs as an obligation and don't give them the attention they deserve."

Even so, the paucity of good data didn't prevent the panel from concluding that the programs are essential. Indeed, it recommended that "NIH should commit to the continued funding of minority-targeted research training programs." At a time when programs that favor members of a particular race or gender are under assault (*Science*, 25 July 2003, p. 455), supporters worry that the lack of an adequate assessment could be a serious problem.

Stinging rebuke

NIH has a long history of addressing the serious underrepresentation of African Americans, Hispanics, Native Americans, and Pacific Islanders in biomedical research. Some 79 programs serve populations from community college students (see sidebar, p. 329) to postdoctoral fellows. Despite some gains, the current output is tiny—108 blacks, 175 Hispanics, and 11 Native Americans earned biological science Ph.D.s in 2003, for example—and their 7.3% share of the total number of degrees awarded is a far cry from the group's 25% presence in the general population (see graphic, left).

The NRC panel examined 49 programs that ran between 1970 and 1999. After spending more than 4 years and $1.5 million, the panel delivered a stinging rebuke of NIH management practices.

One problem, according to the panel, is NIH's narrow definition of success. What the agency wants, in the words of veteran NIH training administrator Walter Schaffer, is "people who can do research and sit on our review panels and advisory boards." But although few participants make it through the doctorate—nobody has a clue what percentage—many still contribute to the biomedical sciences after earning a lesser degree. "Many of these programs serve quite a different population than the typical NIH training program, so a lower rate of success isn't very surprising," says Bailar. As a result, the panel concluded, NIH should consider a "broader definition of success."

Another sticking point is the inaccessibility of relevant data. Project directors submit annual progress reports, but the data generally do not include longitudinal information on a student's entire academic career. "Once a student leaves,

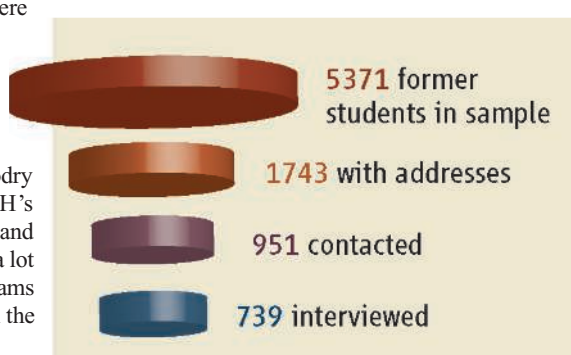

Data deficit. NIH contractors got information from only one in seven former trainees they had hoped to interview.

SOURCE: NIH

* *Assessment of NIH Minority Research and Training Programs, Phase 3*, NRC (2005).

Will This Bridge Take Me to the Lab?

The National Institutes of Health's (NIH's) "Bridges to the Baccalaureate Degree" tries to help underrepresented minority students become scientists. But measuring its impact—and, by extension, all of NIH's minority-training programs—may be a bridge too far.

The Bridges program links community colleges with research universities at dozens of sites around the country. Working with students more likely to have grown up on an Indian reservation, in an urban ghetto, or with parents speaking a language other than English than are their undergraduate peers attending research-intensive universities, the Bridges program supplements coursework with academic assistance, career counseling, paid lab jobs, lectures, and other activities.

It's an excellent way to expose them to a life in research. But it's a long way from fulfilling NIH's dream of turning them into biomedical researchers capable of winning federal grants. Even following what happens to the thousands of students who try to cross that bridge has so far proven impractical.

Why are the students so hard to track? The main reason is their educational peregrinations. Even if students earn their associate's degrees, they may not head to a 4-year school. If they do, they may not win a spot in another NIH-sponsored minority program, if one exists on campus. They may not major in science. Even if they graduate, they may not attend graduate school. And so on.

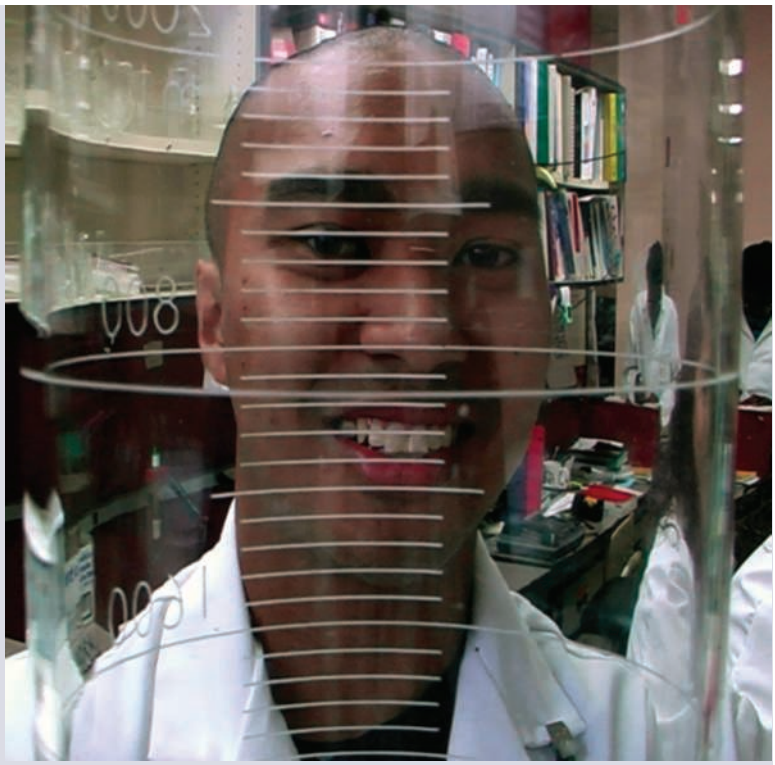

Hard to calibrate. NIH's "Bridges" program helps minority students transfer from community colleges to research universities, but there are few data on what happens to them later.

The available data are both impressive and sobering. California State University, Los Angeles (CSU-LA), has had a Bridges grant since the program's inception, giving project director Linda Tunstad an unusually long perspective on what happens to her students. From a 12-year pool of 148 students, she says, some 76% continued their education at a 4-year school, two-thirds of them at CSU-LA. At least 37%—55 and counting—have earned bachelor's degrees. Of the 75 who attended CSU-LA, 39 have earned bachelor's degrees, mostly in the biological and chemical sciences, and 22 have gone on to graduate programs.

Even if institutions take the trouble to follow their students, however, the significance of the journey may not be clear. When NIH's Adolphus Toliver told Bridges directors recently that the program has a 23% transfer rate—the share of community college students who advance to a 4-year school—the group's first question was: "Is that good or bad?" recalls biologist Thomas Landefeld of CSU Dominguez Hills, past president of the project directors' group. Toliver's answer? "We don't know."

The group would also like information on how their participants stack up against the general student population in terms of completing a bachelor's degree, entering graduate school, and earning a Ph.D. "We think that our programs are adding value," says Landefeld. "But without comparative data, it's hard to know for sure." **–J.M.**

what's the motivation for an institution to track them?" asks Ruffin. And even when grantees dig out that information and submit it to NIH in their annual reports and renewal applications, the agency hasn't found a way to compile it and use it effectively. "We had an electronic database that was also supposed to serve as a tracking mechanism," says Adolphus Toliver, who runs both the Bridges to the Baccalaureate Degree program and the Minority Access to Research Careers program for upper-level honors students. "But it didn't work, so we stopped using it."

A third problem is that students don't necessarily remain in minority-training programs throughout their education. Even programs that link different types of institutions—such as the Bridges to the Baccalaureate Degree from community colleges to 4-year institutions, and the Bridges to the Doctoral Degree from master's to doctoral programs—don't promise students a slot as they advance. That undermines the program's effectiveness, not to mention making it harder to track students.

One of the biggest complaints from the NRC panel is that NIH officials were unwilling or unable to make program data available for a rigorous analysis. NIH shared the data with a private contractor, who surveyed participants and project directors. The response rates were as low as 8%, however. "The NIH data contract achieved a very low response rate," the panel concluded. "As a result, there is a high likelihood of bias among the survey results." The restriction also prevented the NRC panel from doing its own analyses, Bailar adds.

In the long run, the failure to support claims of success could hurt these programs, which are already under threat from those who disapprove of race-based preferences. In November, for example, the U.S. Justice Department threatened to sue Southern Illinois University for running three such programs, one a "bridges" effort for underrepresented minorities pursuing science degrees, funded by the National Science Foundation (*Science*, 25 November 2005, p. 1263). Even agencies that support minority preference may balk because the evidence for these programs is weak. "When I briefed NIH on the report," says Bailar, "some of the institute directors said: 'You haven't shown any evidence that it produces a lot of Ph.D.s. So why should I bother to fund it?' "

Jarvis and Poodry harbor no doubts about the value of the training programs. "I wouldn't be where I am today without these programs," says Jarvis, who this fall won a prestigious NIH Director's Pioneer Award.

Poodry feels likewise. But he also thinks that the NRC panel is right in calling for clear and measurable outcomes. "We need a doubling [of minority Ph.D.s] every 8 years to shift the [participation] curve to where it should be," he says. "If that doesn't happen, then 20 years from now we'll probably be looking at the same results and wondering why things haven't improved."

–JEFFREY MERVIS

CREDIT: COURTESY OF BRIDGES PROGRAM

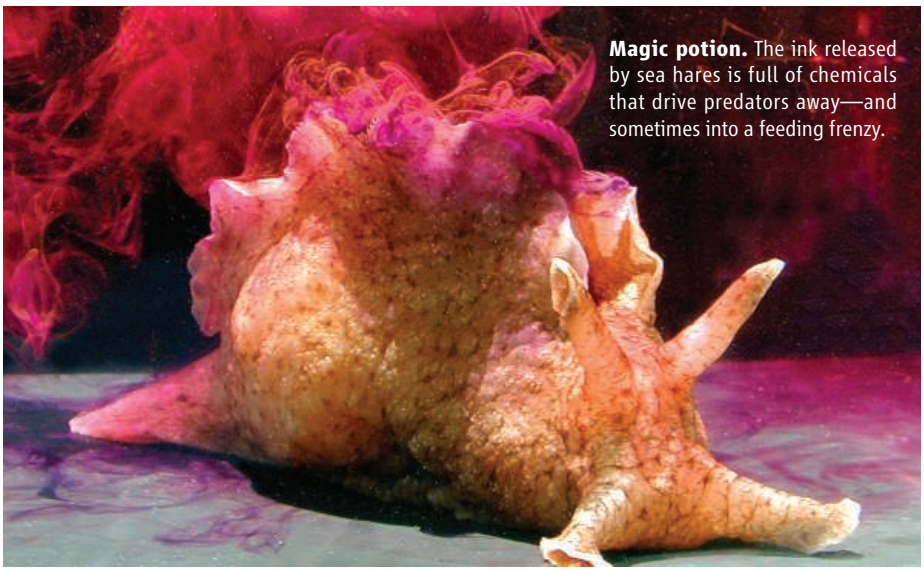

Magic potion. The ink released by sea hares is full of chemicals that drive predators away—and sometimes into a feeding frenzy.

Sea Slug Inks Its Way to Safety

Like squid and octopi, the shallow-water invertebrates known as sea hares eject ink when startled. Quick-moving squid and octopi use their inky clouds as a smokescreen, distracting potential predators while they attempt to escape. Now Charles Derby, a neuroethologist at Georgia State University in Atlanta, is discovering that the slow-moving sea hare's ink contains a host of protective compounds, some tailored to deter or confuse specific enemies.

By testing the chemical makeup of inks secreted by two sea hare species facing different predators, Derby and his colleagues have found a complex defense system of deterrents, alarm calls, and feeding stimulants within the milky purplish and pink fluid. "The ink mixture allows the sea slug to persist in the presence of multiple predators through a simultaneous array of surprising mechanisms," says Erik Sotka, a marine ecologist at the College of Charleston, South Carolina, Grice Marine Laboratory.

Although researchers have long studied chemical defenses in the sea hare's skin and digestive glands, they have not looked in depth at the ink, says Derby. Sea hare "ink" actually consists of two substances, each secreted by a different organ into the mantle cavity, where they intermingle before being ejected. The ink is colorful and thin, whereas the other substance, opaline, is viscous. Each contains its own repertoire of compounds, and Derby finds that when ink and opaline meet, innocuous enzymes and amino acids react to form noxious substances. "This animal uses 'common' biological chemicals in novel ways," notes Esther Leise, a marine biologist at the University of North Carolina, Greensboro.

At the meeting, Derby described how sea hares ward off giant sea anemones. An anemone's tentacles may snare a sea hare, but the predator immediately spits out the potential meal and vigorously retracts its tentacles once the hare ejects its inky weapon, Derby reported. His postdoc Cynthia Kicklighter has found that opaline alone has no repulsive effect: If anything, it stimulates feeding behavior by the anemone. But the ink contains all sorts of anemone-repulsing chemicals, says Derby.

In contrast, when Derby, Kicklighter, and their colleagues tested opaline and ink separately against spiny lobsters, another sea hare predator, the opposite proved true: Opaline was more protective than the ink, they reported last year. The lobster work also suggests that feeding stimulation is actually a defensive strategy. The sea hare's ink-opaline mixture contains substances, such as the amino acid taurine, that set off a feeding frenzy in a lobster—it grabs at ▶

Was Lucy's a Fighting Family? Look at Her Legs

The fossil Lucy is the most famous example of *Australopithecus afarensis*, a hominid that lived between 3.9 million and 3 million years ago. Since her discovery in 1974, anthropologists have been arguing over how she moved, because although she looks a bit like a chimpanzee, her pelvis, legs, spine, and skull suggest she walked upright. Nonetheless, her short legs, long arms, and other features indicate that she spent a lot of time in trees.

Now David Carrier, a comparative physiologist at the University of Utah in Salt Lake City, has jumped into the fray with a provocative idea about Lucy's legs. In earlier studies with dogs, he had found that short legs provide mechanical benefits during fights. Pit bulls' short limbs, for example, aid stability and are tough enough to sustain attack without breaking.

Carrier contends that Lucy and other australopithecines also had bodies built for defense against each other: Their short legs may have provided a competitive edge when males battled rival suitors.

There's no fossil evidence of ancient hominid battles, so Carrier tested his idea indirectly, by analyzing living apes. In great apes, males square off over females, and natural selection has favored large size in these males, with females being more diminutive. Fossil data indicate that males were likewise the brutes of *A. afarensis*. Other researchers have established that the more competitive the males, the larger the overall size differences between the sexes.

So Carrier used size sexual dimorphism as a proxy for aggression within a species. Using data in the literature, he was able to analyze nine primate species, including gibbons, chimps, gorillas, orangutans, African monkeys, and humans. He found that the greater the body size difference between males and females, the shorter the relative leg length. To Carrier, this confirms that apes with more male competition tend to have shorter legs. He argued at the meeting that australopithecines' short legs may have helped body stability when males fought each other for females. Thus male-versus-male competition may have outweighed the need for efficient walking or running.

But others say that so far the evidence is slim. "It's just storytelling," says comparative biologist Frank Fish of West Chester University in Pennsylvania. The work "should generate a lot of controversy," agrees Roshna Wunderlich, a physical anthropologist at James Madison University in Harrisonburg, Virginia. "He has a fairly strong correlation, but he needs to establish causality." Nonetheless, the notion that limbs are shaped by more than locomotion "is a really creative idea," says Elizabeth Brainerd, a comparative morphologist at Brown University. **–ELIZABETH PENNISI**

CREDIT: GENEVIEVE ANDERSON

the ground and ink cloud as if to ingest it, enabling the sea hare to slink away.

As an added bonus, the ink mixture spreads the word among sea hares when danger approaches. Kicklighter and her colleagues have recently presented either ink or opaline to juvenile sea hares. The animals drew in their heads and moved away from either substance. The sea hares did the same when exposed to ink from an octopus and a squid, suggesting a common warning system for all these species. The researchers have identified three of the sea hare's warning compounds, two of which also exist in the squid and octopus inks. Paul Moore, a sensory ecologist at Bowling Green State University in Ohio, calls the sea hare's arsenal "a case of deceptive chemical signaling strategy not seen before [in animals]." Such research "will open up a new avenue of thought for aquatic chemical ecology," he predicts.

Water Launches Spores Like a Rocket

It takes just a little water to send mushroom spores flying—and fast. Using a video camera that records 100,000 frames per second to capture a process never before witnessed, Nicholas Money, a mycologist at Miami University in Oxford, Ohio, has figured out the pivotal role water plays in the moments leading up to a fungal spore's rapid takeoff. The liquid can accelerate a spore more than 10,000*g*, the equivalent of almost instantaneously propelling a human 600 kilometers per hour. "The spores look like little cannonballs," says Elizabeth Brainerd, a comparative morphologist at Brown University, who has seen the video.

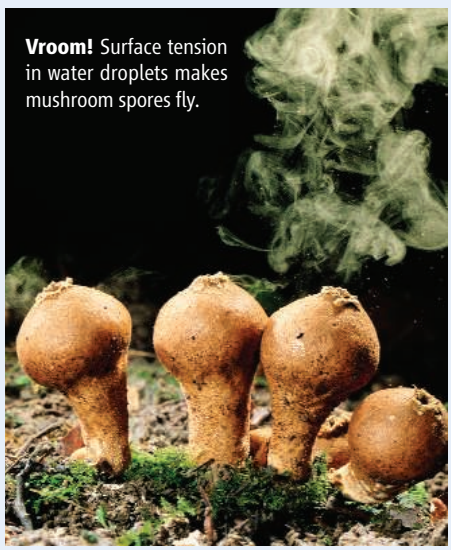

Vroom! Surface tension in water droplets makes mushroom spores fly.

Money studies how honey fungus (*Armillaria mellea*), a pathogenic mushroom that infects about 500 woody plant species, spreads. To do that, he has begun with the first step in dispersal: the launching of spores. His graduate student Jessica Stolze has found that once formed, the spores secrete sugars and sugar alcohols, which suck water out of the air. A drop then forms on a stalk at the base of the spore and expands until it makes contact with the rest of the spore surface. At that point, the water "rockets over the spore, and its motion pulls the spore off its perch," says Money.

Surface tension supplies the energy for this ballistic event, he explained. If someone disturbs the drop, say, with a micropipette, the spores stay put. Bigger drops move faster over a spore and shoot it farther, he notes.

This rapid-fire ejection is critical for spore dispersal. Taking off "is relatively difficult to do because small things have high drag," Brainerd explains. A spore's water-propelled flight may barely be a millimeter long, but on a good day, that distance gets the spore into an air current that whisks it away to a new home.

Of the 74,000 fungi, about 40% depend on water droplets to propel spores. But there are other innovative launch strategies. Money is beginning to study fungi that shoot spores out of tubes akin to pressurized cannons. The speeds attained this way can be remarkable; Steven Vogel of Duke University in Durham, North Carolina, estimates that spores can travel 34.5 meters per second, with accelerations of 870,000 times gravity. **–E.P.**

Crab, Raccoon Play Tag Team Against Turtle

Attempts by wildlife managers to help endangered Florida sea turtles may be backfiring. A field study on four beaches has shown there is a tradeoff between turtle-egg predation by raccoons and by ghost crabs that live in burrows along the beach. Management programs that remove raccoons from beaches have led to population booms in ghost crabs and even greater damage to sea turtle nests, says Brandon Barton, a graduate student in environmental studies at Yale University.

While examining the stomach contents of raccoons as part of an evaluation of the effectiveness of removal programs, Barton realized that the mammals ate more than just turtle eggs: Ghost crabs made up more than 10% of the raccoons' diets. Wondering whether fewer raccoons resulted in more turtle nest raids by ghost crabs, Barton and James Roth, a community ecologist at the University of Central Florida in Orlando, surveyed raccoon and ghost crab populations and monitored turtle-egg predation at four sites: one where wildlife managers had trapped the mammals for the past 25 years; another where cages over turtle nests thwarted raccoon raids; and two where there was no raccoon control.

Active removal reduced the raccoon population, but the crab population was about double that at the other study sites, Barton reported at the meeting. At the trapping site, the mean body size of the crabs increased as well. Moreover, nest predation was 50% higher there—with about 30% of the turtle eggs disappearing.

How much of this increased egg loss was due to ghost crabs is unclear, says Barton. Ghost crabs burrow into the sand to do their dirty work, and visits by raccoons obliterate telltale signs of crab activity. Barton also suspects that the crabs' burrows vent fumes from turtle egg and hatchling remains, helping the raccoon home in on nests.

This work "will force people to rethink programs to remove raccoons from nesting beaches," says Alessandro Catenazzi of Florida International University in Miami. Brent John Sinclair, a functional ecologist at the University of Nevada, Las Vegas, agrees: "It's another one of the classic examples of something that's not making any difference or making [a situation] worse."

–ELIZABETH PENNISI

Crime scene. Ghost crabs and raccoons can take quite a toll on sea turtle eggs and hatchlings.

CREDITS (TOP TO BOTTOM): GETTY IMAGES; BRANDON BARTON/YALE UNIVERSITY

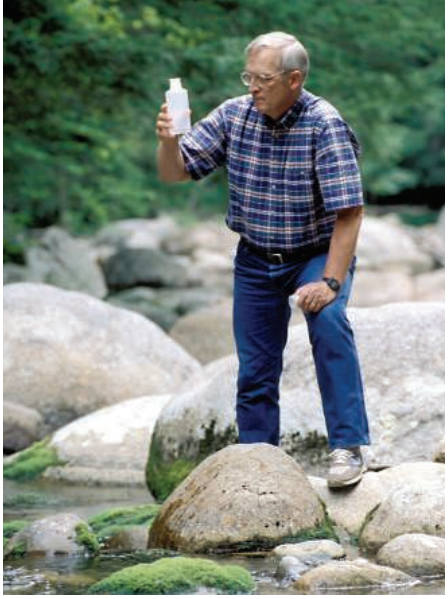

Jobs

WATERSHED. Pioneering ecologist and co-discoverer of acid rain Gene Likens announced last month that in 2007 he will step down as director of the Institute of Ecosystem Studies (IES) in Millbrook, New York. Likens, 71, plans to return to full-time research. "I'm not ready to retire," he says.

In the 1960s, Likens, F. Herbert Bormann, and other colleagues working at the Hubbard Brook Experimental Forest in New Hampshire found that the rain was abnormally acidic and suggested that air pollution was to blame. The group also devised long-term, ecosystem-scale experiments examining, for example, the impact of logging throughout an entire watershed. "The small watershed approach revolutionized the way that ecosystem science developed from the 1960s on," says Jerry Melillo of the Marine Biological Laboratory in Woods Hole, Massachusetts.

In 1983, Likens founded IES, which has since blossomed with 15 full-time ecologists, a dozen or so postdocs, and an endowment of $90 million. "IES is clearly in the crème de la crème," Melillo says, "largely because of Gene and his leadership."

NONPROFIT WORLD

UNDAUNTED. Even as the Russian government clamps down on social reformers, nuclear proliferation expert Rose Gottemoeller eagerly took the reins this week at the Moscow office of the Carnegie Endowment for International Peace. "It's a very exciting period in Russia," says Gottemoeller, 52, as the country holds the rotating G8 presidency and is a key participant in efforts to resolve nuclear crises in Iran and North Korea. But, as *Science* went to press, President Vladimir Putin was poised to sign a new law that would tighten restrictions on nongovernmental organizations. Carnegie would face "onerous reporting requirements" under the law, Gottemoeller says.

"Rose is both a policy leader and a problem solver," says veteran Russia analyst Gerson Sher. Before joining Carnegie in October 2000, Gottemoeller was deputy undersecretary for defense nuclear nonproliferation in the U.S. Department of Energy. During her 2- to 3-year tenure in Moscow, she says, expect Carnegie to hold more roundtable discussions on nuclear proliferation and on topical areas such as energy security and the health of Russia's declining population.

POLITICS

MAKING LEMONADE. The scandal in which South Korean researcher Woo Suk Hwang faked the generation of cloned human embryonic stem (ES) cells has its bright side—or so says the science community's new leading advocate for stem cell research. Sean Tipton, who took over last month as president of the 97-member Coalition for the Advancement of Medical Research, says Hwang's fraud highlights the importance of allowing federally funded research on human ES cell lines derived after 9 August 2001, which President George W. Bush has prohibited by executive order. "When you don't allow [National Institutes of Health] funding, you drive this research into the private sector and into other countries" where oversight is less stringent, Tipton says.

Tipton, whose full-time job is handling public affairs for the American Society for Reproductive Medicine, says the coalition's priority will be to win Senate approval of a bill that would overturn the presidential restrictions. The House passed the bill last year, and Senate Majority Leader Bill Frist (R–TN), after missing earlier deadlines, has promised to schedule a vote by Easter. "We think we're getting real close to a veto-proof margin" in the Senate, says Tipton about the 67 votes needed to override an expected presidential veto.

TWO CULTURES

OUT THERE. Astronauts may have the right stuff to survive in space, but can they endure the petty squabbling of "reality television"? We'll soon find out, as former astronaut Dan Barry will be on *Survivor*, the popular program in which contestants band together to scratch out a living in the wild but also vote each other off until only the winner remains. Taped earlier, the latest *Survivor* series begins 2 February on the American network CBS.

Barry, 52, holds an M.D. and a Ph.D. in electrical engineering and computer science. He flew on the space shuttle three times and in 1986–87 was associate director of the Grass Fellows program at the Marine Biological Laboratory in Woods Hole, Massachusetts. Stay tuned to Newsmakers to find out whether a scientific background helped Barry cope with the jungle on an island off the coast of Panama—and with 15 conniving competitors.

Movers >>

STEM CELL GOLD. The lure of California has proven irresistible for two U.S.-born stem cell scientists now based in Australia.

Next month, biologist Martin Pera (right) is leaving Monash University and the Australian Stem Cell Centre (ASCC) in Melbourne, where he headed embryonic stem cell research, to become director of the new Institute for Stem Cell and Regenerative Medicine at the University of Southern California in Los Angeles. A colleague, geneticist and patent law expert Dianna DeVore (below), has resigned as ASCC chief operating officer to participate in an as-yet-undisclosed commercial venture in San Diego to bring stem cell technologies, many developed in Australia, from the lab to the clinic.

Pera and DeVore say they were drawn by the rosy funding outlook for stem cell science in California, where the state plans to spend $295 million annually on the field over the next 10 years. By contrast, the Australian government has given ASCC—the nation's flagship stem cell enterprise—a total of $55 million through 2011. California also offers a flexible regulatory framework that permits somatic cell nuclear transfer, a technology currently outlawed in Australia.

Got a tip for this page? E-mail people@aaas.org

CREDITS (TOP TO BOTTOM): HO PHOTOGRAPHERS; CARNEGIE ENDOWMENT FOR INTERNATIONAL PEACE; GILLIAN PERA/USXC HEALTH SCIENCES; AUSTRALIAN STEM CELL CENTRE

LETTERS

edited by Etta Kavanagh

Editorial Retraction

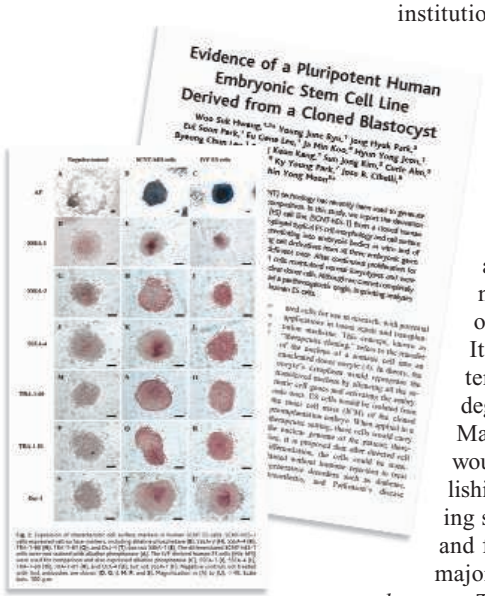

THE FINAL REPORT FROM THE INVESTIGATION COMMITTEE of Seoul National University (SNU) (*1*) has concluded that the authors of two papers published in *Science* (*2*, *3*) have engaged in research misconduct and that the papers contain fabricated data. With regard to Hwang *et al.*, 2004 (*2*), the Investigation Committee reported that the data showing that DNA from human embryonic stem cell line NT-1 is identical to that of the donor are invalid because they are the result of fabrication, as is the evidence that NT-1 is a bona fide stem cell line. Further, the committee found that the claim in Hwang *et al.*, 2005 (*3*) that 11 patient-specific embryonic stem cells line were derived from cloned blastocysts is based on fabricated data. According to the report of the Investigation Committee, the laboratory "does not possess patient-specific stem cell lines or any scientific basis for claiming to have created one." Because the final report of the SNU investigation indicated that a significant amount of the data presented in both papers is fabricated, the editors of *Science* feel that an immediate and unconditional retraction of both papers is needed. We therefore retract these two papers and advise the scientific community that the results reported in them are deemed to be invalid.

As we post this retraction, seven of the 15 authors of Hwang *et al.*, 2004 (*2*) have agreed to retract their paper. All of the authors of Hwang *et al.*, 2005 (*3*) have agreed to retract their paper.

Science regrets the time that the peer reviewers and others spent evaluating these papers as well as the time and resources that the scientific community may have spent trying to replicate these results.

DONALD KENNEDY

Editor-in-Chief

References

1. Investigation Committee Report, Seoul National University, 10 Jan. 2006. (Members: Chairman Myung-Hee Chung, SNU, Uhtaek Oh, SNU, Hong-Hee Kim, SNU, Un Jong Pak, SNU, Yong Sung Lee, Hanyang University, In Won Lee, SNU, In Kwon Chung, Yonsei University, Jin Ho Chung, SNU)
2. W. S. Hwang *et al.*, Evidence of a Pluripotent Human Embryonic Stem Cell Line Derived from a Cloned Blastocyst, *Science* **303**, 1669 (2004).
3. W. S. Hwang *et al.*, Patient-Specific Embryonic Stem Cells Derived from Human SCNT Blastocysts, *Science* **308**, 1777 (2005).

Madison and Climate Change Policy

IN THEIR POLICY FORUM "A MADISONIAN APproach to climate policy" (16 Sept. 2005, p. 1820), D. G. Victor *et al*. oppose international cap and trade agreements with binding greenhouse gas emissions limitations. They argue for bottom-up local policy experiments as the best way to promote action and eventually lead to wider cooperation to address climate change. They claim that this approach (as contrasted with top-down rules) is what Madison envisioned in *The Federalist Papers*—the laboratory of multiple states in federalism. Yet Victor *et al.* have mistaken and misappropriated Madison and advocated a policy that will not solve the global tragedy of the climate commons.

Victor *et al.* neglect that Madisonian federalism involved a strong central government with significant coercive power. Madison was advocating not pure bottom-up diversity, but a new Constitution replacing the Articles of Confederation with an overarching legal and institutional framework to govern and mobilize both the states and the private sector in the common interest.

Victor *et al.* also mischaracterize the plurilateral treaty approach advocated by Stewart and Wiener (*1*). This approach involves building agreements among plural coalitions of willing nations to create parallel systems of international emissions trading. It would not be a "top-down" system, nor would it approach the degree of centralization involved in Madison's version of federalism. It would avoid the difficulties of establishing a single universal cap and trading system under the Kyoto Protocol and focus on cooperation among the major emitting countries, as Victor *et al.* urge. The plurilateral cap and trade approach would foster a variety of trading systems to encourage precisely the diversity and experimentation in policy and practice that Victor *et al.* favor. But it would also involve binding mutual commitments by participants.

In contrast to both Madisonian federalism and plurilateral trading, Victor *et al.* argue for bottom-up local policies that they hope will somehow help move states from uncoordinated autarchy to the accretion of shared norms and informal cooperation. In certain situations under favorable conditions—generally involving small, close-knit groups—some tragedies of the commons can be successfully addressed through such informal development of shared norms (*2*). But often, especially at larger scales where reciprocity and monitoring are more elusive, the tragedies persist unless stronger institutions provide incentives for action in the common good [e.g., (*3*–*5*)]. Between bottom-up diversity and top-down rule, plurilateral cap and trade systems would provide these incentives while avoiding excessive centralization.

Effective climate policy will require emissions abatement by China, India, and other major developing countries, as well as by the United States and Europe, but purely bottom-up experiments have little chance of engaging all of these countries anytime soon. Some

kind of international transfers must occur to engage China and India. Victor *et al.* offer no way to structure that deal. International cap and trade systems do. Victor *et al.* assert that trading approaches are "doomed" because "governments that have imposed strict caps and strong institutions for trading will object to the printing of extra credits that will cause capital and effort flow into the developing countries." Yet Victor *et al.* propose just such capital and effort flows, via government aid programs, to promote natural gas technologies in China and India. Trade is better: Government aid risks political distortions, bureaucratic selection of technologies, higher costs, and a subsidy for uncapped emissions abatement that yields a potentially perverse impact on aggregate emissions. Cap and trade would avoid these problems and mobilize private-market actors via competition to deliver the "capital and effort flows" most cost-effectively and innovatively.

JONATHAN B. WIENER,[1] RICHARD B. STEWART,[2] JAMES K. HAMMITT,[3] JEAN-CHARLES HOURCADE[4]

[1]Law School and Nicholas School, Duke University, Box 90360, Durham, NC 27708, USA. [2]School of Law, New York University, 40 Washington Square South, New York, NY 10012, USA. [3]Center for Risk Analysis, Harvard University, 718 Huntington Avenue, Boston, MA 02115, USA. [4]Centre International de Recherche sur l'Environnement et le Développement, 45 bis, avenue de la Belle Gabrielle, 94736 Nogent sur Marne, France.

References

1. R. B. Stewart, J. B. Wiener, *Reconstructing Climate Policy: Beyond Kyoto* (AEI Press, Washington, DC, 2003).
2. E.g., R. Ellickson, *Order Without Law* (Harvard Univ. Press, Cambridge, MA, 1991).
3. G. Hardin, *Science* **162**, 1243 (1968).
4. E. Ostrom, *Governing the Commons: The Evolution of Institutions for Collective Action* (Cambridge Univ. Press, Cambridge, 1990).
5. T. Dietz, E. Ostrom, P. C. Stern, *Science* **302**, 1907 (2003).

Response

THERE ARE MANY OBVIOUS DIFFERENCES between the U.S. federal government and an international world of autarchic states. Nonetheless, we label our approach "Madisonian" to underscore the similarities in mechanisms for governance from the "bottom up." These mechanisms inform more effective strategies for providing global public goods and also more sober expectations about when such efforts will bear fruit.

We agree with Wiener *et al.* that effective international coordination can't rely on powerful central government. That's why international measures, much more so than national policies, must be tailored carefully to the underlying interests of constituents. For countries that are willing to spend resources to control emissions—notably the European Union (EU) and Japan, but also Canada and parts of the United States—international emission caps can work. What matters, however, is not the "international" aspect of the cap but rather the intranational (or intraregional in the case of the EU) institutions that enforce the cap and provide integrity to the system. Once those institutions are functional, there will be strong pressures to interconnect the systems for reasons that would be quite familiar to Madison—namely, the gains that arise from coordinated trading at larger scale. For

Madison, coordination through a relatively weak center was a matter of constitutional design; for the international system, it is a necessity. Stewart and Wiener have made a similar point elsewhere [(*1*), p. 132].

Where we disagree is on the best strategy for engaging developing countries. We criticized Stewart and Wiener's plurilateral approach as "top down" because it requires a heroic, central first step of allocating valuable "headroom" emission credits to countries that have no interest in limiting their emissions or creating the law-based institutions that are necessary to enforce an emission cap. Stewart and Wiener themselves indicate [(*1*), p. 72] exactly why this approach won't work—these countries will cash in the credits and then exit, which will undermine the integrity of emission caps in every trading country (*2*, *3*). Wiener and Stewart point to reputation as a reason why that won't happen [(*1*), pp. 72–74], but reputation is a very poor deterrent in the international system when governments and their policies are transient but commitments, as in the Kyoto Protocol, extend over long time periods. Only in special cases is reputation an effective glue for collective action (*4*).

We also disagree with their claim that our alternative approach to engaging developing countries requires a politically impossible transfer of resources. In fact, the resources transferred in our approach are connected to large, irreversible changes in energy infrastructures, providing assurances that make them politically more palatable to donors. Moreover, our scheme is remarkably cheap and may introduce commercial and security benefits attractive to the industrialized world.

We don't claim that the Madisonian approach is the best of all imaginable solutions to collective action (*5*). Our argument, rather, is that it offers a realistic vision for how systems where formal government is weak are, nonetheless, able to provide public goods that are the essence of governance.

DAVID G. VICTOR,*† JOSHUA C. HOUSE, SARAH JOY

Program on Energy and Sustainable Development, Stanford, CA 94305–6055, USA.

*D.G.V. is adjunct senior fellow at the Council on Foreign Relations.

†Author for correspondence. E-mail: david.victor@stanford.edu

References

1. R. B. Stewart, J. B. Wiener, *Reconstructing Climate Policy: Beyond Kyoto* (AEI Press, Washington, DC, 2003).
2. D. G. Victor, *Collapse of the Kyoto Protocol and the Struggle to Slow Global Warming* (Princeton Univ. Press, Princeton, NJ, 2001).
3. D. G. Victor, J. C. House, *Harvard Int. Rev.* **26** (no. 2), 56 (summer 2004).
4. E. Ostrom *et al.*, *Governing the Commons* (Cambridge Univ. Press, Cambridge, 1990).
5. R. G. Lipsey, K. Lancaster, *Rev. Econ. Stud.* **24**, 11 (1956–57).

Advising on Publication

DONALD KENNEDY'S EDITORIAL "BETTER NEVER than late" (14 Oct. 2005, p. 195) appears to misunderstand the role of the National Science Advisory Board on Biosecurity (NSABB), as well as Secretary Leavitt's decision to ask the NSABB to review the Tumpey manuscript ("Characterization of the reconstructed 1918 Spanish influenza pandemic virus," T. M. Tumpey *et al.*, Research Articles, 7 Oct. 2005, p. 77).

When briefed on this manuscript authored by CDC staff and others, the Secretary noted the dual-use nature of the work and wanted additional expert advice on the position the Department should take concerning publication. The NSABB was specifically created to provide advice on dual-use research and its communication. The charter states that the NSABB is to "advise on national policies governing publication, public communication, and dissemination of dual-use research methodologies and results." The Editorial asserts that the NSABB's "charter makes clear that it does not screen individual papers." As one of the drafters of that charter, I take issue with this statement. While it was never the Department's intention to screen all dual-use papers, it was understood that special cases would occur from time to time and that the Secretary would need to seek advice on individual papers. Indeed, the charter provides that the NSABB shall "address any other issues as directed by the Secretary."

Out of an abundance of caution, Secretary

Leavitt sought the NSABB's advice on publication of this manuscript and a companion manuscript planned for publication in *Nature*. The Department expedited the NSABB review process. NSABB members and staff worked long hours to ensure that any disruptions caused by this additional layer of review were minimized. In the end, the NSABB recommended that the Department support publication. Given the significance of the 1918 virus, it was both reasonable and appropriate for the Secretary to seek the advice of the NSABB. It might have caused some concern among the Editorial staffs at the two publications, but under the circumstances I say, "Better safe than sorry."

STEWART SIMONSON

Assistant Secretary for Public Health, Emergency Preparedness, U.S. Department of Health and Human Services, 200 Independence Avenue, SW, Washington, DC 20201, USA.

HIV Prevention in Adolescents

MOST HIV PREVENTION PROGRAMS AT PRESENT (for example, the World Health Organization) are aimed at 15- to 24-year-olds (*1*). This age range unfortunately disregards the well-established fact that girls mature sexually two to three years earlier than boys (*2*, *3*): Girls attain menarche (the first period) in well-nourished populations on average at 12.5 years, whereas boys reach sexual maturity on average at 14.5 years. In developing countries, with poorer nutrition levels or female physical work, girls' menarche can be 13 to 15 years, and boys' sexual maturity can be later by three years, at 16 to 18 years (*2*, *3*). Completion of growth for girls is therefore also earlier than for boys in both well-nourished and poorly nourished populations (*4*, *5*).

Because an important aim of HIV/AIDS prevention programs is to inform girls of the dangers to their health of early, unprotected sexual intercourse, education programs should start at ages 11 to 12 years, and the realistic standard for both sexes should be ages 12 to 24 years.

ROSE E. FRISCH

Associate Professor of Population Studies Emerita, Harvard School of Public Health, Harvard Center for Population and Development Studies, 9 Bow Street, Cambridge, MA 02138, USA.

References

1. World Health Organization, www.who.int/child-adolescent-health/HIV/HIV_adolescents.htm, 5/24/2005.
2. R. E. Frisch, R. Revelle, *Science* **169**, 397 (1970).
3. R. E. Frisch, R. Revelle, *Hum. Biol.* **41**, 536 (1969).
4. R. E. Frisch, R. Revelle, *Hum. Biol.* **41**, 185 (1969).
5. R. E. Frisch, *Science* **199**, 22 (1978).

Letters to the Editor

Letters (~300 words) discuss material published in *Science* in the previous 6 months or issues of general interest. They can be submitted through the Web (www.submit2science.org) or by regular mail (1200 New York Ave., NW, Washington, DC 20005, USA). Letters are not acknowledged upon receipt, nor are authors generally consulted before publication. Whether published in full or in part, letters are subject to editing for clarity and space.

CORRECTIONS AND CLARIFICATIONS

News of the Week: "Scientific drill ship to be reborn" by R. A. Kerr (23 Dec. 2005, p. 1890). The correct name of the cited program is the Integrated Ocean Drilling Program.

News of the Week: "How fast does your dinosaur grow?" (16 Dec. 2005, p. 1751). The article incorrectly stated that dinosaurs are not reptiles. Dinosaurs, along with birds, are members of the clade Reptilia. The article also incorrectly stated that "dinosaur" means "thunder lizard" rather than the correct "terrible lizard."

Perspectives: "The changing picture of volatiles and climate on Mars" by B. M. Jakosky *et al.* (2 Dec. 2005, p. 1439). In reference 6, the third author's name was incorrect. It should be M. K. Rifkin.

CHEMISTRY

Light Scattered by Air

Gerald R. Van Hecke

Urban legend at my institution has it that once upon a time a physical chemistry instructor asked on a final examination one question: "The sky is blue, calculate Avogadro's number." While the legend might make a good story, its factual basis has been denied by all past and current physical chemistry instructors. So what does the question have to do with Peter Pesic's book *Sky in a Bottle*? I teach a course on lasers in chemistry, in which one assignment involves calculating Avogadro's number from a selected set of data on atmospheric light scattering. As a result of personally understanding that exercise, I thought that I had a good grasp on why the sky is blue. However, reading Pesic's remarkable and delightful book has made me realize I was naïve. Perhaps my use of such descriptors tips my hand as to the nature of this review. Nevertheless, let me continue and try to convince you that this short volume—a text of some 177 pages, with additional notes and experiments—is indeed a very worthy read.

Sky in a Bottle

by Peter Pesic

MIT Press, Cambridge, MA, 2005. 270 pp. $24.95, £16.95. ISBN 0-262-16234-2.

Blue is a theme throughout the book—and not just sky blue. Each of the ten chapters has blue in its title, from the opening "Out of the Blue" to the concluding "The Perfect Blue." Pesic (a physicist and musician who teaches at St. John's College, Santa Fe, New Mexico) not only traces the scientific legacy of concepts and discoveries that have led to our current understanding of the sky's usual color, he also weaves into his tale cultural uses of the color blue. Through examples including Athena's blue eyes, the blue gates of the temple entrance to the underworld in ancient China, and the almanac *The Blue Rider* artists Wassily Kandinsky and Franz Marc founded in 1911, Pesic parallels the science of blue with its "poetry." Whereas the cultural aspects of blue covered by Pesic were eye-opening to me, the litany of intellectual giants who make appearances in his account reads like a Who's Who. Aristotle, da Vinci, Descartes, Newton, Euler, Goethe, Maxwell, Kelvin, and Einstein were all to a greater or lesser extent involved with the puzzle of why the sky is blue. Of course, much of the real progress in solving the puzzle of the blue sky came through the work of initially less well known investigators such as the 10th-century Arabic scholar Ibn al Haytham, the 19th-century astronomers Gilberto Govi and John Herschel, and the physicists John Tyndall and the third Lord Rayleigh.

It is not possible to mention all of the individuals who appear in Pesic's account nor their contributions. But the complete story follows so much of the pattern of scientific discovery: some steps forward, then some backward, until eventually a satisfactory understanding is reached. What is fascinating to realize is how many of what are viewed today as major scientific concepts had to be developed before the currently accepted explanation for the color of the sky could be produced. We needed to understand that white light is made up of many colors and that each color has its own wavelength. Further, the wave nature of light had to be accepted. The phenomenon of particulate scattering that depends on the size of the particles and the wavelength of the light scattered needed to be recognized as something different from refraction and reflection. Indeed, it was necessary to accept the existence of molecules whose dimensions were small with respect to the wavelength of visible light. Moreover, that scattered light is polarized had to be understood. The recognition of this polarization played a crucial role in abandoning the idea that reflection and refraction from water droplets could be responsible for blue sky.

Of course, any of us with some knowledge of Rayleigh's work would recognize that he enunciated the principle that light is scattered according to the inverse fourth power of its wavelength. This principle provides a quantification of why blue light is scattered more than red light as well as a fundamental piece of the explanation of why our sky is blue. However, probably many of us, including me, would not have realized that Rayleigh was led to his fourth-power law by "dimensional analysis." Pesic devotes one of his endnotes to working through Rayleigh's analysis. In addition to the extensive and informative endnotes—and even more to the author's credit—Pesic provides a selection of experiments readers can perform to further illustrate the textual material and satisfy their curiosity.

Observations of clear, moonless skies after the sun has set led to the recognition that the midnight sky is blue—hence our term and color midnight blue—and understanding why required another whole set of discoveries. As Pesic's discussion indicates, findings such as the expanding universe, the finite lifetime of stars, and the existence of galaxies other than ours are all necessary ingredients for explaining the appearance of our sky in the dark of night.

But Pesic's story does not end with midnight blue. In his last chapter, he considers some of the effects of human visual perception, the density of Earth's atmosphere, and the presence of atmospheric particles larger than molecules. For example, the changing sky—with variations in the depth of coloration from blue at the zenith to some other color on the horizon, the often rather whitish appearance on

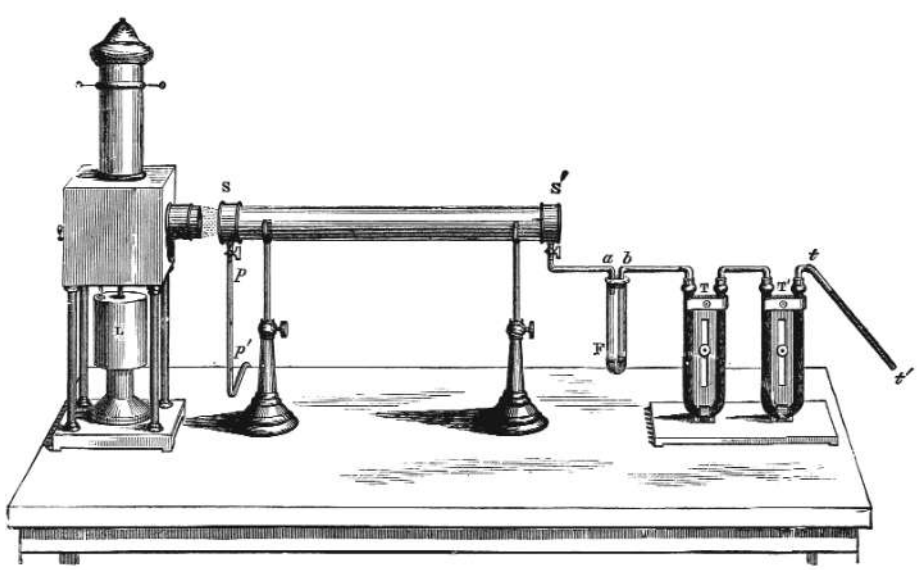

Bottle for blue. To recreate the sky in a bottle, Tyndall used a glass cylinder filled with a mixture of dilute gases and illuminated with a narrow beam from an electric lamp.

CREDIT: FROM J. TYNDALL, *FRAGMENTS OF SCIENCE FOR UNSCIENTIFIC PEOPLE* (APPLETON, NEW YORK, 1987)/COURTESY PETER PESIC

The reviewer is in the Department of Chemistry, Harvey Mudd College, 301 Platt Boulevard, Claremont, CA 91711, USA. E-mail: Gerald_VanHecke@hmc.edu

humid days, white clouds, and colored sunsets—calls into play the role of multiple light scattering and the existence of ozone in the upper atmosphere.

Sky in a Bottle is, as I said at the onset, a delightful and informative read. It seems appropriate to finish this review with Pesic's own concluding paragraph:

> The quest to understand the sky and its color leads inward, for the sky cannot be blue if atoms are not real. Gazing at the sky, we confront the most beautiful proof of atomic theory. The quest also leads outward, to the furthest galaxies, whose distribution determines the brightness of the night. Contemplating its light, we receive silent evidence of the universe's vastness in space and time. Between day and night is twilight. There, the zenith color tells of the fragile condition of the earth itself, poised between macrocosm and microcosm.

10.1126/science.1121021

NEUROSCIENCE

Linking Neurons and Ethics

Xavier Bosch

Current advances in neuroimaging are leading to unprecedented feats. It is now possible to control cursors on a computer screen by detecting electrical signals from the brain. A recently devised computer game allows people to play table tennis on a screen using nothing more than the power of their minds. All they need is a functional magnetic resonance imaging (fMRI) machine, which picks up magnetic signals from oxygen bound to the iron in hemoglobin in the bloodstream.

Furthermore, our understanding of the interplay between higher cognitive abilities and the brain's biological and structural properties is skyrocketing. In "neuromarketing," brain imaging is used to measure the limbic system's response to a product, which may indicate consumers' unconscious desire for it. Functional neuroimaging offers a rough measure of personality, and that raises the possibility that employers and judges will in the near future treat brain images as a sort of indisputable truth. And as new techniques and insights into human brain function provide a strikingly revised concept of what may be possible, we are also witnessing the emergence of the subject of neuroethics. This young discipline addresses the myriad ways in which developments in neuroscience intersect with ethical and social issues. As cognitive scientist Martha Farah has pointed out, most topics in neuroethics fall into one of two general categories: "what we can do" and "what we know" (1, 2). The first includes ethical problems posed by advances in neuroscience techniques such as fMRI or the pharmacological enhancement of cognition. In contrast, concerns raised by our increasing understanding of the neural bases of behavior, personality, consciousness, and states of spiritual transcendence fit into the second category, with responsibility being a core issue.

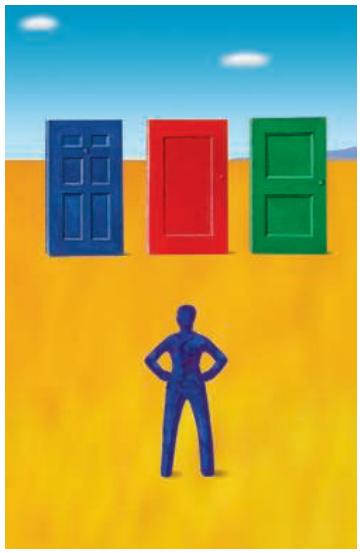

The Ethical Brain

by Michael S. Gazzaniga

Dana Press, Washington, DC, 2005. 221 pp. $25, £17.50. ISBN 1-932594-01-9.

In *The Ethical Brain*, renowned cognitive neuroscientist Michael Gazzaniga addresses these issues and offers his own thoughts on several of the most provocative questions. In the opening section, the author, an outspoken member of the U.S. President's Council on Bioethics, explains how the field of neuroethics contributes to debates about the boundaries of human life. After providing a short summary of the neurobiology of fetal brain development, he makes his case in favor of embryonic stem cell research, arguing that "a fertilized egg, a clump of cells with no brain, is hardly deserving of the same moral status we confer on the newborn child or the functioning adult." Notably, Gazzaniga defines consciousness as a landmark for both the beginning and end of meaningful life and points out that in some diseases, such as Alzheimer's, a state exists in which consciousness is lost.

Further along, he tackles the sensitive issue of brain enhancement and wonders whether parents should be allowed to genetically engineer or pharmaceutically dose their children to become more intelligent. After introducing the philosophical notion of hyperagency ("a Promethean aspiration to remake nature, including human nature, to serve our purposes and satisfy our desires"), he advocates self-regulation of the use of drugs for brain enhancement: "In my view, the fear of hyperagency is misplaced; society as a whole seems always to return to the reasonable use of new knowledge." More explicitly, he argues that "just as most people don't drink all the liquor in their liquor cabinet…our society will absorb new memory drugs according to each individual's underlying philosophy and sense of self."

In the first of three chapters on neuroethics and law, Gazzaniga discusses the interface between brain function and personal responsibility. Recent investigations appear to indicate that our brains have already made their decisions before we become consciously aware of their doing so. Although a murderer may argue that his brain was wired for the assassination, Gazzaniga dismisses the validity of such a defense in the courtroom. He clearly aims to reconcile the materialist idea that brain activity is determined with the notion of moral responsibility, which normally depends upon the idea that humans possess free will. He contends that "[b]rains are automatic, rule-governed, determined devices, while people are personally responsible agents." I cannot agree: even though responsibility is assessed in a social context, the ability to learn social norms and to act consequently relies upon individual brain functions. Elsewhere in this section, Gazzaniga explores possible impacts of neuroscience findings and techniques on the right to privacy and considers forensic implications of the unreliability of memory.

In a final section on moral belief and universal ethics, the author tackles the neurological basis for beliefs, with an emphasis on religion. From the fact that people with temporal lobe epilepsy display hyperreligious behavior during seizures and in the periods between seizures, he suggests that religiosity "could have an organic basis within the normally functioning brain."

The Ethical Brain offers a short and comprehensible account whose main strengths are conferred by the range of neuroscience research the author incorporates into his thinking and by his expertise in cognitive neuroscience. The enjoyable, thought-provoking book will introduce readers to the complex interplay between neuroscience and ethics. Nonetheless, carefully and properly interpreting the relationship between understanding brain function and our own concept of self is undoubtedly very difficult. As Gazzaniga rightly cautions, modern neuroimaging techniques read brains, not minds.

References

1. M. J. Farah, *Cerebrum* **6**, 29 (2004).
2. M. J. Farah, *Trends Cogn. Sci.* **9**, 34 (2005).

10.1126/science.1121898

The reviewer is at the Department of Internal Medicine, Villarroel 170, University of Barcelona, 08036-Barcelona, Spain. E-mail: xavbosch@ub.edu

PLANETARY SCIENCE

Risks in Space from Orbiting Debris

Space junk represents a growing threat to commercialization and other activities in space.

J.-C. Liou[1] and N. L. Johnson[2]

Since the launch of Sputnik I, space activities have created an orbital debris environment that poses increasing impact risks to existing space systems, including human space flight and robotic missions (*1*, *2*). Currently, more than 9000 Earth-orbiting man-made objects (including many breakup fragments), with a combined mass exceeding 5 million kg, are tracked by the U.S. Space Surveillance Network and maintained in the U.S. satellite catalog (*3*–*5*). Three accidental collisions between catalogued objects during the period from late 1991 to early 2005 have already been documented (*6*), although, fortunately, none resulted in the creation of large, trackable debris clouds. The most recent (January 2005) was between a 31-year-old U.S. rocket body and a fragment from the third stage of a Chinese CZ-4 launch vehicle that had exploded in March 2000.

Several studies conducted during 1991–2001 demonstrated, with assumed future launch rates, the potential increase in the Earth satellite population, resulting from random, accidental collisions among resident space objects (*7*–*13*). In some low Earth orbit (LEO) altitude regimes, where the number density of objects is above a critical spatial density, the production rate of new debris due to collisions exceeds the loss of objects due to orbital decay.

LEGEND (LEO-to-GEO Environment Debris model), is a high-fidelity three-dimensional physical model developed by the U.S. National Aeronautics and Space Administration (NASA) that is capable of simulating the historical environment, as well as the evolution of future debris populations (*14*, *15*).

The LEGEND future projection adopts a Monte Carlo approach to simulate future on-orbit explosions and collisions (*16*). A total of 50 (*17*), 200-year future projection Monte Carlo simulations were executed and evaluated, under the assumptions that no rocket bodies and spacecraft were launched after December 2004 and that no future disposal maneuvers were allowed for existing spacecraft (few of which currently have such a capability) (*18*).

The simulated 10-cm and larger debris populations in LEO (defined as the region between altitudes of 200 and 2000 km) between 1957 and the end of a 200-year future projection period indicate that collision fragments replace other decaying debris (due to atmospheric drag and solar radiation pressure) through 2055, keeping the total LEO population approximately constant (see chart, above). Beyond 2055, however, the creation of new collision fragments exceeds the number of decaying debris, forcing the total satellite population to increase. An average of 18.2 collisions (10.8 catastrophic, 7.4 noncatastrophic) would be expected in the next 200 years (*19*, *20*).

A detailed analysis indicates that the predicted catastrophic collisions and the resulting population increase are nonuniform throughout LEO (see chart on page 341, top left). About 60% of all catastrophic collisions occur between 900- and 1000-km altitudes. The number of objects 10 cm and larger triples in 200 years, leading to a factor of 10 increase in collisional probabilities among objects in this region (see chart on page 341, top right). This population growth is due to higher spatial densities, larger and more massive rocket bodies and spacecraft with near-polar inclinations, and longer orbit decay times in this region as compared with other parts of LEO.

The current debris population in the LEO region has reached the point where the environment is unstable and collisions will become the most dominant debris-generating mechanism in the future. Even without new launches, collisions will continue to occur in the LEO environment over the next 200 years, primarily driven by the high collision activities in the region between 900- and 1000-km altitudes, and will force the debris population to increase. In reality, the situation will undoubtedly be worse because spacecraft and their orbital stages will continue to be launched.

Postmission disposal of vehicles (for example, by limiting postmission orbital lifetimes to less than 25 years) is now advocated by the major space-faring nations and organizations of the world, including NASA (*21*), the Department of Defense, the Department of Transportation, and the Federal Communications Commission in the United States; the Inter-Agency Space Debris Coordination Committee (*22*); the European Space Agency (*23*); and the Japan Aerospace Exploration Agency (*24*). Postmission disposal will slow down the growth of future debris populations (*25*). However, this mitigation measure will be insufficient to constrain the Earth satellite population. Only remediation of the near-Earth environment—the removal of existing large objects from orbit—can prevent future problems for research in and commercialization of space.

For the near term, no single remediation technique appears to be both technically feasible and economically viable. Electrodynamic tethers or drag enhancement structures could rapidly accelerate the orbital decay of decommissioned spacecraft and rocket bodies, but attaching such devices to the satellites with conventional robotic means would incur excessive costs for

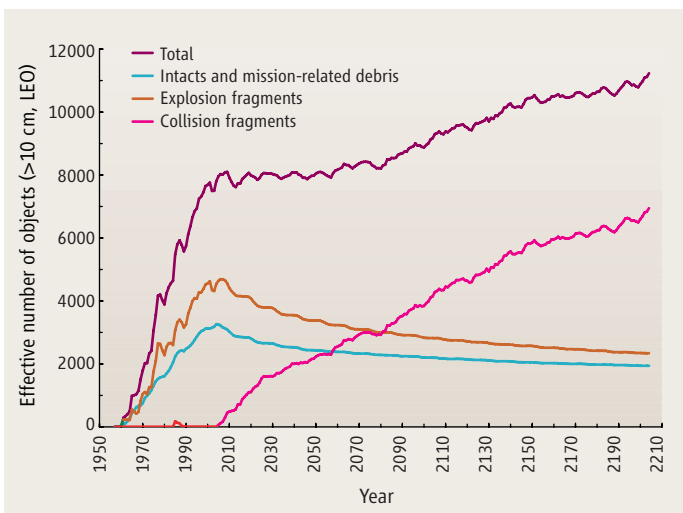

Growth of future debris populations. Effective number of LEO objects, 10 cm and larger, from the LEGEND simulation. The effective number is defined as the fractional time, per orbital period, an object spends between 200- and 2000-km altitudes. Intacts are rocket bodies and spacecraft that have not experienced breakups.

[1]J.-C. Liou is in the Engineering Science Contract Group (ESCG)/ERC at NASA Johnson Space Center, Mail Code JE104, 2224 Bay Area Boulevard, Box 7, Houston, TX 77058, USA. [2]N. L. Johnson is in the Orbital Debris Program Office, NASA Johnson Space Center, Houston, TX 77058, USA.

*Author for correspondence. E-mail: jer-chyi.liou1@jsc.nasa.gov

CREDIT: (TOP) NASA

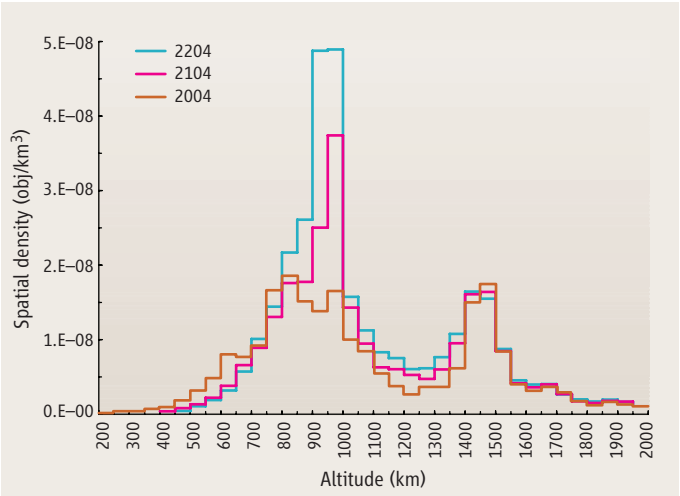

Projected environment. Spatial density distributions, for objects 10 cm and larger, for three different years.

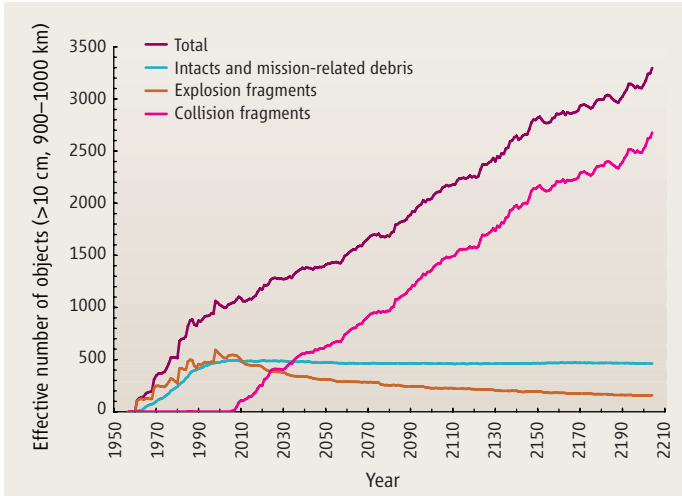

The red zone. Effective number of objects, 10 cm and larger, between 900- and 1000-km altitudes from the LEGEND simulation.

the benefit gained. Even if a single remediating vehicle carried several deorbiting packages within the same altitude and inclination, the energy requirements to visit multiple target spacecraft would normally be high due to differences in target orbital planes (*26*, *27*).

The placement of ion engines on the satellites in order to direct them back to Earth would have the same problems as the previously mentioned strategies and, in addition, would require significant, long-term power and attitude control subsystems. Current manned spacecraft cannot reach the key orbital regimes above 600 km and are even more expensive than robotic missions. The use of ground-based lasers to perturb the orbits of the satellites is not now practical because of the considerable mass of the satellites and the consequent need to deposit extremely high amounts of energy on the vehicles to effect the necessary orbital changes.

Hence, the success of any environmental remediation policies will probably be dependent on the development of cost-effective, innovative ways to remove existing derelict vehicles. The development of this new technology may require both governments and the private sector working together. Without environment remediation and the wide implementation of existing orbital debris mitigation policies and guidelines, the risks to space system operations in near-Earth orbits will continue to climb.

References and Notes

1. *Interagency Report on Orbital Debris* (Office of Science and Technology Policy, U.S. National Science and Technology Council, Washington, DC, 1995).
2. "Technical Report on Space Debris: Text of the Report adopted by the Scientific and Technical Subcommittee of the United Nations Committee on the Peaceful Uses of Outer Space" (United Nations, New York, 1999).
3. *Orbital Debris Q. News* **9** (1), 10 (2005), (www.orbitaldebris.jsc.nasa.gov/newsletter/newsletter.html).
4. *Orbital Debris Q. News* **9** (3), 10 (2005).
5. N. L. Johnson, D. O. Whitlock, P. D. Anz-Meador, E. M. Cizek, S. A. Portman, *History of On-Orbit Satellite Fragmentations* (SC-62530, NASA Johnson Space Center, Houston, TX, ed. 13, 2004).
6. *Orbital Debris Q. News* **9** (2), 1 (2005).
7. D. J. Kessler, *Adv. Space Res*. **11** (12), 63 (1991).
8. S.-Y. Su, *Adv. Space Res*. **13** (8), 221 (1993).
9. A. Rossi, A. Cordelli, P. Farinella, L. Anselmo, *J. Geophys. Res. Planets* **99** (E11), 23195 (1994).
10. L. Anselmo, A. Cordelli, P. Farinella, C. Pardini, A. Rossi, "Modelling the evolution of the space debris population: Recent research work in Pisa" [European Space Agency (ESA) SP-393, 339-344, European Space Operations Centre (ESOC), Darmstadt, Germany, 1997].
11. D. J. Kessler, "Critical Density of Spacecraft in Low Earth Orbit" (NASA JSC-28949, NASA Johnson Space Center, Houston, TX, 2000).
12. D. J. Kessler, P. D. Anz-Meador, "Critical number of spacecraft in Low Earth Orbit: Using satellite fragmentation data to evaluate the stability of the orbital debris environment" (ESA SP-473, 265-272, ESOC, Darmstadt, Germany, 2001).
13. P. H. Krisko, J. N. Opiela, D. J. Kessler, "The critical density theory in LEO as analyzed by EVOLVE 4.0" (ESA SP-473, 273-278, ESOC, Darmstadt, Germany, 2001).
14. J.-C. Liou, D. T. Hall, P. H. Krisko, J. N. Opiela, *Adv. Space Res*. **34** (5), 981 (2004).
15. J.-C. Liou, *Adv. Space Res*., in press (doi:10.1016/j.asr.2005.06.021).
16. Within a given projection time step, once the explosion probability is estimated for an intact object, a random number is drawn and compared with the probability to determine if an explosion would occur. A similar procedure is applied to collisions for each pair of target and projectile involved within the same time step. Because of the nature of the Monte Carlo process, multiple projection runs must be performed and analyzed before one can draw reliable and meaningful conclusions from the outcome.
17. A statistical analysis of LEGEND predictions, based on the bootstrap method, indicates that the average from 50 Monte Carlo runs leads to a standard error of the average on the order of 5% or less, which was sufficient for the recent study.
18. On the other hand, satellite explosions, the principal source of debris larger than 10 cm now in orbit about the Earth (*5*), were permitted at their current historical rates. All objects were propagated forward in time while decayed objects were removed from the environment immediately. Perturbations included in the orbit propagator are Earth's solar-lunar gravitational perturbations, atmospheric drag, and solar radiation pressure, as well as Earth's shadow effects. The simulation program outputs the orbital elements and other physical properties of the objects at the end of each year for post processing analysis. The solar flux F10.7 values used in the projection period have two components: a short-term projection [2005–2007, obtained from U.S. National Oceanic and Atmospheric Administration (NOAA) Space Environment Center] and a long-term projection (2008–2204). The long-term F10.7 projection is a repeat of a 13-month running smoothed average cycle derived from solar cycles 18 to 23. A simple smooth function is used to interpolate the two solar flux components during the transition. Explosion probabilities of future rocket bodies and spacecraft were based on an analysis of launch history and recent explosions. Vehicle types with a history of explosion, but which have had the breakup causes fixed, were not included. Collision probabilities among objects were estimated with a fast pair-wise comparison algorithm, Cube (*15*). The size threshold of objects in collision considerations and in populations shown in the figures in this Policy Forum was selected to be 10 cm. Historically, this is the detection limit of the Space Surveillance Network sensors, and more than 95% of the debris population mass is in objects 10 cm and larger.
19. A catastrophic collision occurs when the ratio of impact energy to target mass exceeds 40 J/g. The outcome of a catastrophic collision is the total fragmentation of the target, i.e., resident space object, whereas a noncatastrophic collision only results in minor damage to the target and generates a small amount of debris that has minimal contribution to population growth.
20. N. L. Johnson, P. H. Krisko, J.-C. Liou, P. D. Anz-Meador, *Adv. Space Res*. **28** (9), 1377 (2001).
21. NASA Orbital Debris Program Office (www.orbitaldebris.jsc.nasa.gov/).
22. Inter-Agency Space Debris Coordination Committee (IADC) members include national space agencies of the United States, the Russian Federation, China, Japan, India, France, Germany, Italy, and the United Kingdom, as well as the ESA.
23. "ESOC: focal point for ESA space debris activities" (www.esa.int/SPECIALS/ESOC/SEMU2CW4QWD_0.html).
24. "Space debris and space envionment" (www.jaxa.jp/missions/projects/engineering/space/debris/index_e.html).
25. *IADC Space Debris Mitigation Guidelines* (IADC-02-01, Inter-Agency Space Debris Coordination Committee, 2002); (www.iadc-online.org).
26. The energy requirements to visit satellites at the same altitude and inclination in different orbital planes can be reduced by maneuvering the remediating vehicle to a different altitude, taking advantage of differential precession of the line of nodes due to the Earth's oblateness, and then returning to the altitude of interest. This concept was described by one of the authors (Johnson) as means for more economically removing nuclear power reactors from Earth orbit (*27*). The amount of propellant savings derived from this technique is dependent upon the time one is willing to wait between remediation operations.
27. N. L. Johnson, *Space Policy* **2** (3), 223 (1986)].

10.1126/science1121337

MICROBIOLOGY

Weapons of Microbial Drug Resistance Abound in Soil Flora

Bacteria found in soils show robust resistance to many antibiotics. These protective mechanisms may offer clues for generating a new arsenal of therapeutic drugs.

Alexander Tomasz

Following the serendipitous discovery of penicillin in 1928 and streptomycin in 1943, the pharmaceutical industry has been screening thousands of soil samples for antimicrobial agents produced by inhabitant microbes. Chloramphenicol, clavulanic acid, erythromycin, gentamicin, rifampin, teichoplanin, tetracycline, and vancomycin represent only a few products of this spectacularly successful effort, and addition of these agents to the therapeutic arsenal has played a major role in controlling bacterial disease, the primary cause of human mortality in the preantibiotic era.

The study by D'Costa *et al.* on page 374 this issue (*1*) provides a fascinating view of the flip side of this story. The authors isolated 480 morphologically diverse spore-forming microbes from the soil and tested these not as producers of antimicrobial agents but rather as microbes that are resistant to existing antibiotics. Astonishingly, they found that every isolate was resistant to at least six to eight different antimicrobial agents and some to as many as 20! The antibiotics tested included both well-established and recently developed agents, natural products, semisynthetic derivatives, and fully synthetic antimicrobial agents.

With multidrug-resistant bacterial pathogens spreading globally and the enormous efforts to trace the source and mechanism of spread of drug-resistant genes and clones (*2*), the study by D'Costa *et al*. has particular poignancy. It illuminates the dark side of the antibiotic paradigm: Microbes that synthesize the sophisticated chemicals that have been key to humankind's success in controlling bacterial disease also possess equally sophisticated mechanisms to protect themselves against their own toxic products. Lifted out of this context, these self-protecting mechanisms represent formidable weaponry that could annul the successes of antimicrobial therapy if they were to find their way into human pathogens.

The microbes isolated and characterized by D'Costa *et al*. all belong to the genus *Streptomyces*, well known for producing multiple antimicrobial agents (*3*) that suppress the growth and/or kill other susceptible bacterial species in their vicinity. The 480 independent soil isolates examined presumably include producers of antimicrobial agents that also possess matching resistance mechanisms to protect against suicide in this chemical warfare (*4*).

The author is in the Laboratory of Microbiology, Rockefeller University, 1230 York Avenue, New York, NY 10021, USA. E-mail: tomasz@rockefeller.edu

Multidrug Resistance in *S. aureus*

Antibiotic	MSSA (1930)	MRSA (1994)	Resistance mechanism
Penicillin	S	R	+ (1945)
Streptomycin	S	R	+ (1948)
Tetracycline	S	R	+ (1950)
Methicillin	S	R	+ (1961) *mecA*
Oxacillin	S	R	+
Cephalothin	S	R	+
Cefotaxime	S	R	+
Imipenem	S	R	+
Chloramphenicol	S	R	+
Ciprofloxacin	S	R	A
Clindamycin	S	R	+
Erythromycin	S	R	+
Gentamycin	S	R	+
Rifampin	S	R	A
Vancomycin	S	S	*A (1997)* VISA
Vancomycin	S	S	*+ (2002) vanA*
Teichoplanin	S	S	+
Trimeth/Sulfa	S	R	A

Emergence of multidrug resistance in *Staphylococcus aureus*. The Brazilian clone of methicillin-resistant *S. aureus* (MRSA), isolated in 1994 (*2*), was resistant (R) to nearly all the antibiotics listed. Most of the resistance mechanisms were not adaptive (A), but acquired (+) from an extraspecies source. In contrast, an invasive strain of *S. aureus* (MSSA), recovered in 1930, was susceptible (S) to all the agents.

A number of the resistance mechanisms described by D'Costa *et al*. have not been previously characterized. Almost half of the test strains could enzymatically inactivate rifampin (often used against mycobacterial tuberculosis), in contrast to clinical isolates in which resistance is based on point mutations in a bacterial gene. Several strains could detoxify the semisynthetic drug telithromycin (for respiratory tract infections) by a glucosylation reaction not seen before among clinical isolates. Most strains were resistant to daptomycin, an agent only recently introduced for skin and soft-tissue infections. Surprisingly, many of the soil organisms also showed resistance against fully synthetic antibiotics such as ciprofloxacin (frequently used in urinary tract infections) and linezolid (for infections by drug-resistant enterococci, staphylococci, and pneumococci). In the case of ciprofloxacin resistance, the authors identified mutations in the gene encoding gyrase, an enzyme involved in DNA replication. Some mutations were the same as those seen in ciprofloxacin-resistant pathogens, but others involved unfamiliar mutational changes elsewhere in the gene. It is unknown whether active residues of the enormous amounts of antimicrobial agents deployed yearly in human and veterinary medicine and agriculture find their way back into the soil where they may participate in the selection for antibiotic resistance.

The obvious concern is that some of these resistance mechanisms may be exported from the "underground" world to the genomes of human pathogens. Actually, the majority of the most effective antibiotic-resistance mechanisms in human pathogens are acquired (see the figure). The superiority of such acquired mechanisms is illustrated by the contrast between *Staphylococcus aureus* strains that have decreased susceptibility to vancomycin through mutations (so-called VISA strains) as compared to VRSA strains, *S. aureus* that acquired a complete vancomycin-resistance gene complex via the transposon Tn*1546* (*5*). The VISA strains have low-level resistance (the minimal inhibitory concentration of vancomycin is 6 to 12 μg/ml), are often associated with reduced oxacillin resistance, and show abnormal cell wall synthesis (*6*); the multiple transcriptional changes documented by DNA microarray analysis reflect the complexity of this mechanism (*7*). In contrast, in VRSA strains, the Tn*1546*-based mechanism produces high-level vancomycin resistance (with a minimal inhibitory concentration of more than 500 μg/ml) that does not interfere with oxacillin resistance, and cell wall synthesis proceeds with a depsipeptide cell wall precursor specific to these strains (*8*).

The exact nature of the bridges that connect the underground and aboveground microbial flora through which resistance genes may find their way into human pathogens is not known.

The mechanism of resistance to aminoglycoside antibiotics in human pathogens may be traced to aminoglycoside producers in the soil flora (*9*). Also, the critical genetic determinants of vancomycin resistance—*vanH*, *vanA*, and *vanX*—appear to be very similar to the self-protection mechanism in the vancomycin producer *Actinomyces* strains (*10*). Clearly, mobilization of a resistance mechanism must involve "packaging" into a plasmid, phage, or some transposable element. However, the number of stages in the movement of such a mobilized resistance mechanism before its emergence in a human pathogen driven by the selective pressure of antibiotic use is unknown. One of the first stages in the emergence of the Tn*1546*-based vancomycin-resistance gene complex from the underground world may have occurred on European farms where a derivative of vancomycin—avoparcin—had been in extensive use until recently. The fecal flora of animals from such farms contained enterococcal strains that were highly resistant to vancomycin through the acquisition of the *vanA* gene complex (*11*). The next stages through which this transposon made its way into human strains of enterococci is unclear, but by the early 1990s, epidemic spread of vancomycin-resistant enterococcal (VRE) strains in U.S. hospitals was documented. It took another decade before the vancomycin-resistance genes found their way into the more dangerous human pathogen *S. aureus*. Here, the critical step may have been physical contact between a VRE donor and an *S. aureus* recipient, both of which were recovered from the highly immunocompromised infection site of a diabetic wound where the first VRSA isolates were identified (*12*).

The remarkable variety of mechanisms described by D'Costa *et al*. in their analysis of the microbial soil "resistome" may provide the medicinal chemist with precious clues in the design of new antimicrobial agents. Hopefully, these will be less at risk in confronting an already formidable resistance mechanism.

References

1. V. M. D'Costa, K. M. McGrann, D. W. Hughes, G. D. Wright, *Science* **311**, 374 (2006).
2. M. Aires de Sousa, H. de Lencastre, *FEMS Immunol. Med. Microbiol*. **40**, 101 (2005).
3. A. Demain, A. Fang, *Adv. Biochem. Eng. Biotechnol.* **69**, 1 (2000).
4. J. Berdy, *J. Antibiot.* **58**, 1 (2005).
5. L. M. Weigel *et al*., *Science* **302**, 1569 (2003).
6. K. Sieradzki, R. B. Roberts, S. W. Haber, A. Tomasz, *N. Engl. J. Med*. **340**, 517 (1999).
7. F. McAleese *et al*., *J. Bacteriol.*, in press.
8. A. Severin *et al*., *J. Biol. Chem.* **279**, 3398 (2004).
9. J. Davies, *Science* **264**, 375 (1994).
10. H.-J. Hong, M. S. Paget, M. J. Buttner, *Mol. Microbiol.* **44**, 1199 (2002).
11. W. Witte, I. Klare, *Microb. Drug Resist.* **1**, 259 (1995).
12. CDC, *Morb. Mortal. Wkly. Rep*. **51**, 565 (2002).

10.1126/science.1123982

CELL BIOLOGY

Serving Up a Plate of Chromosomes

Rebecca Heald

Before being pulled into their respective daughter cells, duplicated chromosomes line up at the center of the cell. Video microscopy and high-resolution electron microscopy show how this precise arrangement is set up by the cell.

Chromosomal DNA encodes the blueprint required to maintain eukaryotic cell and organism viability. Chromosomes replicate during each round of the cell division cycle and remain as pairs of sister chromatids until a bipolar apparatus, called the mitotic spindle, precisely segregates them into two sets, each destined for a new daughter cell (*1*). Accuracy in this process of mitosis is imperative, as transmission of a faulty blueprint can cause cell death or contribute to cancer. On page 388 of this issue, Kapoor *et al*. (*2*) address a long-standing question in the field: How do chromosomes efficiently achieve the right kind of spindle attachments so that they can be properly distributed?

To prepare for segregation, sister chromatids connect at their kinetochores to spindle microtubule bundles, called kinetochore fibers (K-fibers), that emanate from opposite spindle poles. The sisters are thus "bi-oriented" and poised to go their separate ways. Chromosomes gradually "congress" to the central region of the spindle, called the metaphase plate. The cell monitors this process and dissolves the glue holding sisters together only when every chromosome is properly attached and aligned at this plate. At anaphase of the cell division cycle, sister chromatids move to opposite poles as their attached K-fibers depolymerize, completing segregation.

The question of how chromosomes achieve the prerequisite bi-orientation has intrigued cell biologists for decades. The common view has been that before congressing, each sister chromatid of a pair connects to a K-fiber that is associated with the opposite spindle pole (*3*). However, spindle attachment is a stochastic process that depends on the interaction of microtubules with a subset of proteins localized at the kinetochore. As soon as one sister kinetochore "captures" a microtubule emanating from one spindle pole, the chromosome (that is, the pair of sister chromatids) is transported toward that pole, becoming "mono-oriented." How then do microtubules from the other spindle pole make contact with the unattached sister? This is a puzzle, because structural analyses of the spindle indicate that microtubules from the distal pole rarely penetrate far enough to be captured by a chromosome that has already moved toward the opposite pole (*4*). Yet chromosomes still congress to the plate and become bi-oriented.

Using a combination of sophisticated microscopy techniques, Kapoor *et al*. have documented kinetochore behavior that solves this conundrum. By following congression in living cells through video microscopy and then rapidly preparing the cells for high-resolution electron microscopy, the authors observed mono-oriented chromosomes with the kinetochore of one sister chromatid attached to the ends of microtubules extending from a proximal pole. Interestingly, its sister was laterally associated with the K-fiber of another chromosome that was already bi-oriented and congressed. Visualizing fluorescent kinetochores and micro-

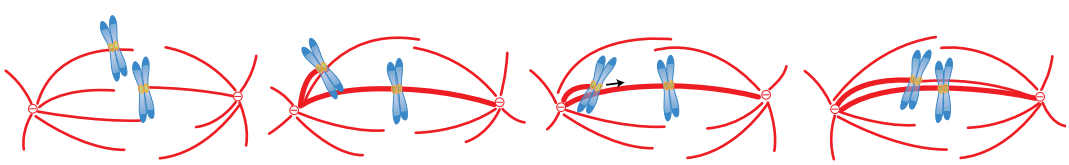

A mechanism of chromosome congression that promotes bi-orientation. Microtubules forming a mitotic spindle (red) that contains two chromosomes is shown, each with paired sister chromatids (blue) and kinetochores (yellow). Thicker red lines represent bundled kinetochore fibers. In the scenario depicted, microtubules growing from both spindle poles have been captured by sister kinetochores of one chromosome, and the chromosome is oscillating (congressed) at the metaphase plate. The other chromosome attaches initially to only one pole and becomes mono-oriented in a position where microtubules from the opposite pole are unlikely to make contact. By attaching to and sliding along the kinetochore fiber of the congressed chromosome, the unattached sister kinetochore moves toward the center of the spindle, where it makes microtubule connections to bi-orient.

The author is in the Department of Molecular and Cell Biology, University of California, Berkeley, CA 94720, USA. E-mail: bheald@calmail.berkeley.edu

tubules revealed "sliding" of mono-oriented chromosomes toward the spindle equator along other K-fibers through this lateral association, bringing the unattached sister kinetochore into range of microtubules from the distal pole (see the figure). Such excursions do not always result in capture, but they increase the probability that bipolar chromosome attachments can form.

The observed frequency of these chromosome movements suggested that sliding of unattached kinetochores along other K-fibers occurs commonly. In fact, under conditions (chemical inhibitors that perturb mitotic progression) that allowed congression and bi-orientation to be followed in a large population of chromosomes synchronously, Kapoor *et al*. observed that ~85% of kinetochores were paired such that one sister chromatid attached to a pole and the other laterally associated with a mature K-fiber from a different, bi-oriented chromosome that stretched toward the metaphase plate. This indicates the predominance of this congression mechanism to promote chromosome bi-orientation. By combining their chemical inhibitor–based assay with RNA interference, a technique capable of depleting a specific protein from cells, Kapoor *et al*. could investigate the factors behind kinetochore sliding along a lateral K-fiber. Their hunch was that the microtubule-based motor CENP-E, a member of the kinesin-7 family, was involved, because this protein localizes to the kinetochore during congression and moves with the correct polarity—toward microtubule "plus" ends that are uniformly oriented toward the metaphase plate in kinetochore fibers (*5*). Although kinetochores could still capture microtubules after CENP-E depletion, mono-oriented chromosomes that were not transported toward the metaphase plate accumulated at spindle poles. Thus, CENP-E is likely the motor responsible for gliding unattached sister kinetochores along neighboring K-fibers, helping mono-oriented chromosomes achieve congression before bi-orientation. These findings are the first to indicate bona fide kinetochore motility depending on CENP-E. Chromosome congression defects observed upon CENP-E inhibition were previously attributed to a role in microtubule capture and/or in maintaining kinetochore attachment to dynamic microtubules (*6*). CENP-E also contributes to a checkpoint signaling pathway that monitors kinetochore status (*7*), making it a central player in both the process and the fidelity of spindle function.

The spindle is a remarkable cellular machine, and the work by Kapoor *et al*. demonstrates that we are still uncovering its fundamental mechanisms. The findings explain why chromosome congression is a cooperative process, accelerating as more and more chromosomes gain bipolar attachments that can serve as tracks for mono-oriented chromosomes to congress. Once chromosomes are bi-oriented, they oscillate along the spindle axis as K-fiber microtubules coordinately polymerize and depolymerize at their plus ends. Although a large constellation of kinetochore proteins has been identified, it remains unclear which factors are operating at the dynamic kinetochore-microtubule interface, and how they are functioning. Combining state-of-the-art imaging, chemical biology, and molecular dissection is a great paradigm for elucidating the mechanistic principles of mitosis.

References

1. S. Gadde, R. Heald, *Curr. Biol.* **14**, R797 (2004).
2. T. M. Kapoor *et al*., *Science* **311**, 388 (2006).
3. A. W. Murray, T. J. Mitchison, *Curr. Biol.* **4**, 38 (1994).
4. D. N. Mastronarde, K. L. McDonald, R. Ding, J. R. McIntosh, *J. Cell Biol.* **123**, 1475 (1993).
5. K. W. Wood, R. Sakowicz, L. S. B. Goldstein, D. W. Cleveland, *Cell* **91**, 357 (1997).
6. B. T. Schaar, G. K. T. Chan, P. Maddox, E. D. Salmon, T. J. Yen, *J. Cell Biol*. **139**, 1373 (1997).
7. Y. Mao, A. Desai, D. W. Cleveland, *J. Cell Biol.* **170**, 873 (2005).

10.1126/science.1123525

APPLIED PHYSICS

Helical Spin Order on the Move

Franco Nori and Akira Tonomura

In magnetic materials, electron spins are arranged in parallel, antiparallel or other regular configurations. Electron microscopy of certain of these materials reveals the details of atomic spins that appear to be arranged in a helix.

Magnetic materials can be thought of as assemblies of billions of miniature magnets called spins. These tiny microscopic magnets can be arranged in several possible configurations, depending on how the spins line up. When all the spins are aligned with each other, they form ferromagnets, examples of which can be found on most refrigerator doors. Here, the prefix "ferro" refers to iron, which is magnetic and naturally displays this kind of parallel-spin order. Another type of magnetic order is antiferromagnetic, in which nearby spins are oriented opposite to each other. Spin arrangements more complex than these can occur, however. An example is helical spin order (see the first figure). As its name suggests, this is a helix-like arrangement of the spins distributed along chains. Like a tiny magnetic corkscrew, the spin direction rotates around the axis of the helix (*1*). These microscopic arrangements of spins can be measured by techniques such as neutron scattering. Such methods, however, yield data in reciprocal space, which requires conversion to a real-space representation.

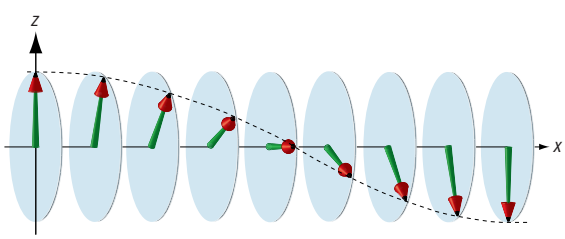

Spin order. Schematic diagram of a helical spin order.

As reported on page 359 of this issue, Uchida *et al.* (*2*) have taken the first steps to directly visualize helical spin order and especially its dynamics in real space. The spatio-temporal behavior of the magnetic spin order reported by Uchida *et al*. (*2*) is richer than expected from the averaged structure probed in the past via neutron scattering. In particular, the helical spin order exhibits a variety of magnetic defects similar to atomic dislocations in crystal lattices. By applying magnetic fields, the researchers (*2*) directly observed the deformation processes of the spin order, accompanied by nucleation, movement, and annihilation of magnetic defects.

To observe the helical ordering, Uchida *et al*. (*2*) bombarded the thin sample with electrons of sufficiently high energy to penetrate the interior of the sample. Electrons are sensitive to the magnetic fields produced by the spins. Thus, the deflection of their straight incident trajectories provides information about the spin arrangement inside the sample (see the second figure). Very fast electrons bombarding the sample are deflected by the Lorentz force: $\mathbf{F} = q\,(\mathbf{v} \times \mathbf{B})$. Here q and $\mathbf{v}$ are the electron charge and its velocity vector, and $\mathbf{B}$ is the magnetic induction vector. Only the $\mathbf{B}$ components perpendicular to the electron beam can cause deflection of the beam. The distribution of deflections, produced by magnetic structures, can be observed not in an in-focus electron micrograph but in a very defocused observation plane, since the deflection angle is extremely small. This technique, called Lorentz microscopy (*3*), has been used to directly observe magnetic domain structures in ferromagnetic materials. To be more precise, however, the incident parallel electrons have to

F. Nori is in the Department of Physics, University of Michigan, MI 48109–1040, USA, and at the Frontier Research System, Riken, Saitama 351-0198, Japan. E-mail: nori@umich.edu A. Tonomura is at the Advanced Research Laboratory, Hitachi Ltd., Hatoyama, Saitama 350-0395, Japan, and also at the Frontier Research System, Riken, Saitama 351-0198, Japan. E-mail: tonomura@harl.hitachi.co.jp

be regarded as a plane wave that interacts with the tiny magnetic fields inside the sample. In this representation, the phase of an electron wave is changed as it passes through a magnetic object, and the resulting phase changes, which cannot be directly observed, are transformed into observable intensity variations by image defocusing [see p. 151 in (*4*)].

Lorentz microscopy has been much improved through the use of a bright and collimated field-emission electron beam (allowing detection of a slight deflection of the "probe" electrons) combined with a low-temperature specimen stage. This has allowed observations of microscopic magnetic structures emerging even in low-temperature regions [see p. 147 in (*4*)], including vortices in superconductors [see, for example, (*5*)]. Magnetic domains that are likely produced by helical spin order were observed by Uchida *et al*. (*2*) using this improved technique. However, this technique only reveals the projected in-plane magnetic structures, because electrons interact with magnetic field components perpendicular to the electron trajectory. As a result, it cannot be conclusively determined with this technique whether the observed structure is really helical, or simply two-dimensional domains. Other methods will be needed to confirm the helical structure.

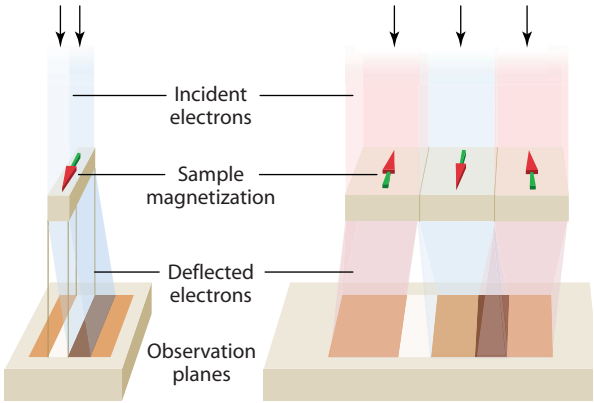

Viewing magnetic order. Schematic diagram of how Lorentz microscopy can be used to observe magnetic structures in materials for **(left)** a single domain and **(right)** three domains. The incident electrons from the top are deflected by the sample magnetization, forming dark regions (bombarded by more electrons) and lighter regions (with fewer incident electrons) in the bottom observation plane. White color in the bottom observation plane means that no electrons hit the plane. For simplicity, only deflected electrons are shown in the observation plane on the right side.

In order to capture all the information about magnetic structures, the specimen must be observed from various directions. In fact, one of us (A.T.) and collaborators have devised a method (*6*) based on electron holography (*4*), in which vector fields such as magnetic fields can be determined from the phase distributions of the transmitted electrons observed from various directions, when the sample is tilted around two perpendicular axes. The study of the rich spatio-temporal dynamics of magnetic domains by Uchida *et al.* (*2*) is remarkable, even though they observed the projected, and not three-dimensional, magnetic structures. It should be possible to obtain the latter with the use of electron holography, which could provide a fuller picture of the behavior of spins, including the formation of tiny magnetic helices. Indeed, monitoring the spatio-temporal dynamics of spin structures is like making movies of the billions of spins inhabiting the sample. This provides an unprecedented direct view inside magnets, revealing essential information about the properties of magnetic materials and the many devices using them.

References

1. A. Yoshimori, *J. Phys. Soc. Jpn*. **14**, 807 (1959).
2. M. Uchida, Y. Onose, Y. Matsui, Y. Tokura, *Science* **311**, 359 (2006).
3. J. N. Chapman, *J. Phys. D Appl. Phys*. **17**, 623 (1984).
4. A. Tonomura, *The Quantum World Unveiled by Electron Waves* (World Scientific, Singapore, 1988).
5. A. Tonomura *et al*., *Nature* **412**, 620 (2001).
6. G. Lai *et al*., *J. Appl. Phys.* **75**, 4593 (1994).

10.1126/science.1122627

ASTRONOMY

Nucleosynthesis in Binary Stars

C. Simon Jeffery, Christopher A. Tout, John C. Lattanzio

Nearly all elements in the universe heavier than helium are synthesized in stars. Binary stars, because they exert strong influences on one another, have contributed more elements than previously recognized.

The past decade has seen a revolution in the study of stellar evolution and nucleosynthesis, both in observations and theory. Despite this progress, however, the role of binary stars has been much neglected. Although their importance in iron production in some supernovae and in the production of rare isotopes of carbon, nitrogen, and oxygen in novae has been known for some time, binary stars have been treated only in isolation. Some effort to redress this situation was made in 1998 when Tout *et al.* (*1*) considered a full population of binary stars and showed how they could systematically alter the chemical evolution of carbon from one generation of stars to the next. This is because the largest stars, the asymptotic giant branch (AGB) stars, are a major source of carbon and are also the stars most likely to interact in a binary system. Recently, a more complete accounting was given at the Lorentz Workshop on Nucleosynthesis in Binary Stars, held in April 2005 (*2*). This international gathering of experts in the field and others interested in stellar evolution and nucleosynthesis featured presentations of data, models, and lengthy discussions on what problems should be tackled and how.

Enhanced online at www.sciencemag.org/cgi/content/full/311/5759/345

C. S. Jeffery is at Armagh Observatory, College Hill, Armagh BT6 9DG, Northern Ireland, UK. C. A. Tout is at the Institute of Astronomy, University of Cambridge, Cambridge CB2 1TN, UK. J. C. Lattanzio is at the Center for Stellar and Planetary Astrophysics, School of Mathematical Sciences, Monash University, Victoria 3800, Australia. E-mail: john.lattanzio@sci.monash.edu.au

Stars are the cosmic factories that manufacture nearly all atoms heavier than helium. The mechanisms that dredge these nuclei from the stellar interior and distribute them through space are crucial to seeding the next generations of stars and planets. The main events are the explosions at the end of stars' active lives, whether in supernovae (massive stars) or ejection of planetary nebulae (less massive red giants). In a cosmic recycling exercise, this material forms new stars with an enriched chemical composition. A preliminary to quantifying the effects of binary stars on these processes is, of course, a detailed understanding of the processes operating in single stars. The Lorentz Workshop began with presentations by some of the main contributors to this area from recent years, including Norbert Langer, Roberto Gallino, Lionel Siess, and John Lattanzio. Specific talks on type Ia supernovae were given by Chris Tout and Sung-Chul Yoon.

The first generation of stars must have formed essentially from hydrogen and helium, the only species produced by the Big Bang. No observations have ever found these stars. Possibly this is because they were all relatively massive and all died out long ago. But when they died they ejected newly formed elements into space. A second generation of stars formed from these ejecta, and it is likely that these stars have been identified in recent surveys of the galactic halo. Astronomers measure the compositional age of a star by using the concept of "metallicity." Traditionally, but incorrectly, astronomers refer to all species heavier than

helium as "metals" and the total mass fraction of such species is called the "metallicity" of a star. The metallicity of the Sun is about 0.015, for example. The lower this value, the older the material from which the star formed, because after the Big Bang the metallicity of the universe was essentially zero. A surrogate for the metal abundance is usually taken to be the iron-to-hydrogen ratio, Fe/H, by number, compared to the solar value. The record so far is as low as 10^{-5}, and there are several stars with less than $10^{-2.5}$. It is likely that these are indeed true second-generation stars. Possibly they formed from the ejecta of one nearby first-generation star, whether a supernova, a giant, or something else.

These putative second-generation stars show unexpected abundance patterns. Because the first stars were thought to be very massive (more than 40 solar masses), they ought to have produced far more iron than carbon. Yet about a quarter of the stars with very low metallicity show carbon and nitrogen enriched somewhat more than we expect. Carbon production is usually associated with AGB stars from 1 to 8 solar masses as well as stars of higher mass with strong winds, whereas nitrogen comes only from the AGB stars. One way around this would be to change the nature of the stars by interaction with a companion. If two stars are close enough, tides become so strong that material can flow from one to the other. This can strip off a star's envelope, exposing its processed interior, or can change its mass so much that it evolves in a different way. A recent study by Lucatello *et al*. (*3*) has found a very high occurrence of close binaries among the carbon-enriched metal-poor stars. Workshop participants thus turned to Onno Pols for a summary of what we know, and do not know, about binary evolution.

Can we actually see the effects of binary stars? In some cases, the answer is yes. Specific observations of neutron-capture elements such as Ba and Pb were discussed by Sophie van Eck, who (with collaborators) has shown that mass transfer in binaries can explain the appearance of Ba in the spectra of low-luminosity giants. Some challenges were given to the workshop participants through presentations of specific cases by Simon Jeffery and Gijs Nelemans. Many of the participants were particularly interested in some classes of stars that remain not understood, such as the R and J stars, the explanations for which may well involve binary stars. In many cases, however, observations of abundances in stars were sufficiently vague that the effects of binary companions were generally smaller than measurement accuracy.

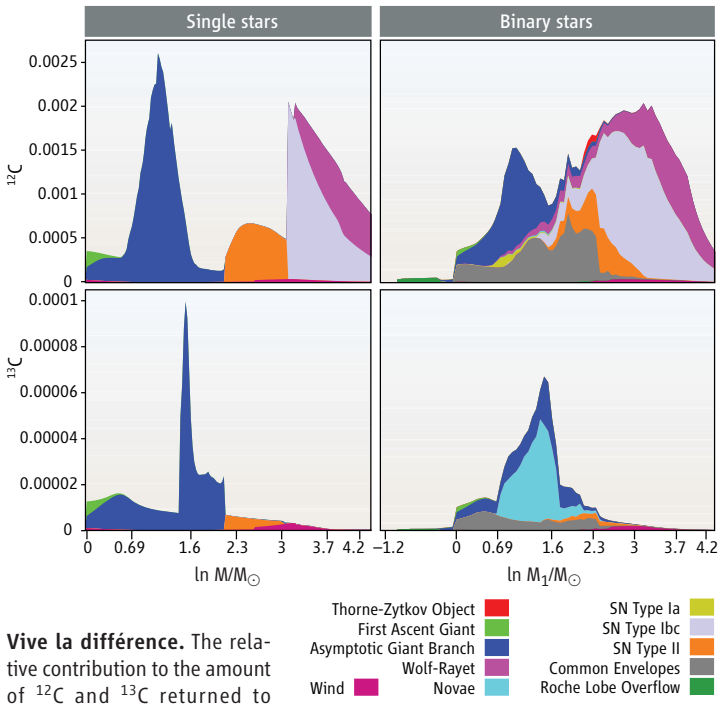

Vive la différence. The relative contribution to the amount of ^{12}C and ^{13}C returned to the interstellar medium from a population of single stars (**left**) and a population of binary stars (**right**), according to a calculation by Izzard (*6*). The relative contribution from different stages of the evolution is shown in different colors.

In the past 20 years, a revolution in what we can observe has made it all the more necessary to understand the details of nucleosynthesis. The material ejected from stars freezes out in interstellar space to form minute grains up to a few micrometers across. The composition of each grain is a signature of the star around which it formed. As the gas and dust of our Galaxy is mixed over billions of years, some grains are incorporated into planetesimals in the solar system. Some of these fall to Earth as meteorites; others have been retrieved with space missions such as NASA's Stardust. The analysis of these grains, showing compositions that predate the solar system, was reviewed by Andy Davis at the Lorentz meeting.

High-precision mass spectrometers make it possible to distinguish between isotopes embedded in the grains. The ratios of different isotopes of the same element tell us about the conditions under which they were synthesized and so act as a probe deep into the interiors of stars [see (*4*) for example]. Some grains are consistent with supernova ejecta, others are compatible with giant winds, and a few are certainly from novae in binary stars. The evolution and nucleosynthesis in novae was discussed by Jordi Jose and Chris Tout.

The fact that binary stars are more likely to interact when they become red giants makes these puzzles particularly interesting. This is precisely when a star develops a deep convective envelope that dredges products of nucleosynthesis up to the surface. At the same time, convection mixes protons (ionized hydrogen from the unprocessed surface) down to hot layers rich in heavy elements. This combination drives a complex network of nuclear reactions that produce virtually everything from lithium to bismuth.

The principal problems for theory are that (i) a binary star introduces at least two extra degrees of freedom to the model, hence it takes much longer to explore all of parameter space [there is thus much room for studies involving population synthesis, and these topics were reviewed by Jarrod Hurley and Robert Izzard (see the figure)]; (ii) it destroys the last vestiges of the assumption of spherical symmetry, which is necessary to make stellar structure calculations tractable; and (iii) many processes involved in binary star interactions occur on short time scales. Full three-dimensional (3D) hydrodynamical calculations are therefore necessary to resolve key questions. Recent technological advances are beginning to make such calculations possible. Massively parallel supercomputers are able to compute 3D stellar evolution. Djehuty, the 3D code currently running at Lawrence Livermore National Laboratory, has been used to study the flash when core helium burning ignites (*5*). This flash evidently does not disturb the overall structure of the star, nor does it provoke large-scale convective mixing. Progress and future work using this promising code were discussed at the meeting by Peter Eggleton.

There is much to learn about the evolution of stars. The role of duplicity in star systems is virtually unexplored. The consequences for understanding the chemical evolution of our Galaxy, the formation of the solar system, the origin of elements essential to life, and the structure of the universe as a whole are immense. It looks as though we are poised to start learning a lot more.

References

1. C. A. Tout, A. I. Karakas, J. C. Lattanzio, J. R. Hurley, O. R. Pols, in *Asymptotic Giant Branch Stars*, T. Le Bertre, A. Lebre, C. Waelkens, Eds. (Astronomical Society of the Pacific, San Francisco, 1999), pp. 447–452.
2. Lorentz Workshop on Nucleosynthesis in Binary Stars, Lorentz Center, Leiden, Netherlands, 4 to 15 April 2005.
3. S. Lucatello *et al*., *Astrophys J.* **625**, 825 (2005).
4. M. A. Lugaro *et al*., *Astrophys. J.* **593**, 486 (2003).
5. D. S. Dearborn, J. C. Lattanzio, P. Eggleton, *Astrophys J*., in press.
6. R. Izzard, thesis, Cambridge University, 2004 (see also www.astro.uu.nl/~izzard/ciqua/index.html and an online binary nucleosynthesis calculator at www.ciqua.org/binaryyields/index.php).

10.1126/science.1115848

The Impact of Structural Genomics: Expectations and Outcomes

John-Marc Chandonia and Steven E. Brenner*

Structural genomics (SG) projects aim to expand our structural knowledge of biological macromolecules while lowering the average costs of structure determination. We quantitatively analyzed the novelty, cost, and impact of structures solved by SG centers, and we contrast these results with traditional structural biology. The first structure identified in a protein family enables inference of the fold and of ancient relationships to other proteins; in the year ending 31 January 2005, about half of such structures were solved at a SG center rather than in a traditional laboratory. Furthermore, the cost of solving a structure at the most efficient SG center in the United States has dropped to one-quarter of the estimated cost of solving a structure by traditional methods. However, the efficiency of the top structural biology laboratories—even though they work on very challenging structures—is comparable to that of SG centers; moreover, traditional structural biology papers are cited significantly more often, suggesting greater current impact.

Structural genomics (SG) is an international effort to determine the three-dimensional shapes of all important biological macromolecules, with a primary focus on proteins [(*1*) and references therein]. A major secondary goal is to decrease the average cost of structure determination through high-throughput methods for protein production and structure determination. In the United States, the National Institutes of Health initiated pilot SG projects at nine centers through the Protein Structure Initiative (PSI), beginning in 2000. As the PSI project moves from its pilot phase to full production this year, the total funding at four large-scale centers and six specialized centers is expected to be about $60 million annually. Considerable resources have also been spent internationally, with SG projects in Japan, Canada, Israel, and Europe under way since the late 1990s. With more than 5 years of data from SG projects worldwide, this is an opportune time to examine their impact and to evaluate how much progress has been made toward the major goals.

As with other large-scale, goal-based projects, it is important to establish objective, quantitative measures of success. We aim to measure the biological importance and difficulty of solving macromolecular structures, and we rely on several proxies to estimate these. Although every new experimental structure adds to our repository of structural data, most structural biologists would agree that novel structures [e.g., the first high-resolution structures of ribosomal subunits (*2*, *3*)] are especially valuable. For example, the first protein structure in a family may be used to understand function and mechanism, infer the fold of other family members, create detailed comparative models of the most similar proteins (*4*), or identify previously uncharacterized evolutionary relationships (*5*). Novelty is not necessarily limited to new families: The structure of a previously solved protein in a different conformation or with a different binding partner could provide insight into its functional mechanisms. Consideration might also be given to the size, complexity, or quality of a structure as a way to estimate its difficulty. Over time, a structure's impact might be crudely evaluated by the number of subsequently published papers that cite the original work.

In this review, we focus on quantifying the impact of SG on expanding structural coverage of protein families, as that is the primary goal of the PSI and several international projects (*6*). We examined several sequence- and structure-based definitions of a protein family so as to reduce the potential for bias introduced by use of any single standard and to directly compare current results with expectations at the outset of the project (*7*). We contrasted the number of new families solved and the costs of structure determination at SG centers with the same metrics compiled for structural biology laboratories that are not affiliated with a SG center. We also examined several of the most productive non-SG groups as measured by our standards. Finally, we performed a preliminary analysis of citations of structural publications from both SG and non-SG laboratories.

We expect that this analysis will be helpful for informing future strategy in both SG and structural biology projects, and that it will serve as a model for quantitative analysis of the impact of a large-scale project. A complete description of our methodology and additional detailed results are provided in (*8*). Although we focus on PSI centers, we analyze the output of all SG centers that report their results to TargetDB (*9*); these centers and the specific goals of each are listed in table S1.

Berkeley Structural Genomics Center, Physical Biosciences Division, Lawrence Berkeley National Laboratory, and Department of Plant and Microbial Biology, University of California, Berkeley, CA 94720, USA.

*To whom correspondence should be addressed. E-mail: brenner@compbio.berkeley.edu

Impact of Structural Genomics on Coverage of Protein Families

The Pfam database (*10*) is a manually curated database of protein families from sequenced genomes. As of 1 February 2005, 36% of Pfam families (2736 of 7677) (*10*) contain a member with known structure, which allows the folds of all other members of the family to be inferred. We mapped each Pfam family to SG targets and proteins of known structure from the Protein Data Bank [PDB (*11*)], and we used the database deposition dates to identify the earliest structural representative from each family. The rate of first structural characterization of families rose steadily throughout the 1990s but has leveled off at around 20 new families per month since 1999 (Fig. 1B), even as the total number of structures solved continues to increase (Fig. 1A). Surprisingly, in recent years, the rate of solution of first structures in a Pfam family by non-SG structural biologists has decreased while SG centers have made up the deficit. SG centers worldwide now account for about half of new structurally characterized families, even though they contribute only about 20% of the new structures. PSI centers account for about two-thirds of the worldwide SG contribution. Only 5% of non-SG structures reported since 2000 represent a new Pfam family, whereas the PSI average was 20.4%.

We analyzed the individual contributions of each of the nine U.S. pilot centers and compared them to other SG and structural biology efforts (Table 1). Results vary widely for the nine PSI centers. The MCSG was the most productive, as measured by the total number of structures solved and the total number of new families; the BSGC (with which we are affiliated) had the highest fraction of new families and the largest total number of proteins in new families. The bulk of non-PSI SG results were produced by the Japanese center RIKEN. Note that the output of non-PSI SG centers is not expected to be equivalent to PSI centers because of varying budgets and goals, and that two of the PSI centers (CESG and SGPP) started a year later than the others.

Quantifying Novel Structures by Direct Sequence Comparison

To alleviate bias introduced by Pfam, we used the local sequence comparison methods BLAST (*12*) and PSI-BLAST (*13*), at several different levels of sequence similarity, to examine the number of structures that could not be matched to any prior solved structure. Results are shown in Fig. 2A and Table 1.

The overall fraction of structures that were classified as novel according to PSI-BLAST has decreased in the past 15 years, from about

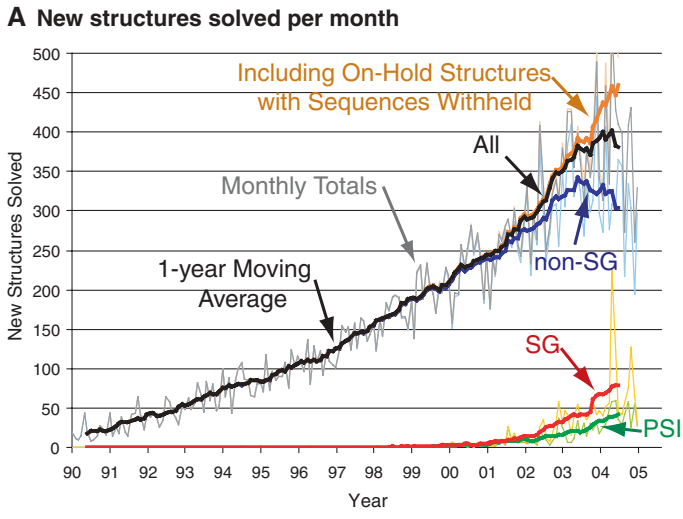

Fig. 1. Structural characterization of new families. (**A**) Black lines indicate the total number of new structures reported per month. Blue lines are contributions from non-SG structural biologists, red lines from SG centers, and green lines from the PSI centers. The orange line indicates structures that were deposited into the PDB for which the sequence is not available; these structures, which presumably come mainly from structural biologists, were not included in our analysis. (**B**) Total number of new Pfam families with a first representative solved per month, divided into the same categories as in (A). Monthly totals and a 1-year moving average are shown.

Table 1. Novel structures solved by structural genomics centers and leading structural biology groups (see also fig. S4 and table S14). Shown are the total numbers of novel structures and nonidentical polypeptide chains first structurally characterized by SG centers and several leading structural biology groups not affiliated with SG centers. Totals for non-SG structural biology groups were compiled from 1 January 2000. For non-SG centers, each PDB entry was counted as a separate target. The number of nonidentical polypeptide chains is also given for each group; this was calculated as the total number of chains with a distinct sequence from other chains within each PDB entry. The number of Pfam families for which the first structure was solved by each group is shown, along with the total number of proteins in these families. The number of novel structures shown is the number of chains with less than 30% sequence identity to any chain from a previously solved structure. Numbers of new SCOP folds and superfamilies are the numbers of domains from each group that represented the earliest reported instance of a particular fold or superfamily in the SCOP 1.67 classification.

Group or SG center	Targets and nonidentical chains	New Pfam families (total family size)	Novel structures (30% ID)	New SCOP folds	New SCOP fold or superfamily
SG centers					
Berkeley Structural Genomics Center (BSGC)	57 (57 chains)	22 (5757)	41	4	6
Center for Eukaryotic Structural Genomics (CESG)	48 (48 chains)	7 (387)	28	0	0
Joint Center for Structural Genomics (JCSG)	186 (187 chains)	32 (4875)	92	3	4
Midwest Center for Structural Genomics (MCSG)	224 (229 chains)	55 (5512)	163	18	25
Northeast Structural Genomics Consortium (NESGC)	159 (159 chains)	52 (4811)	108	15	26
New York Structural Genomics Research Consortium (NYSGRC)	166 (171 chains)	27 (3982)	90	6	9
Southeast Collaboratory for Structural Genomics (SECSG)	67 (67 chains)	6 (1079)	25	0	1
Structural Genomics of Pathogenic Protozoa Consortium (SGPP)	26 (26 chains)	1 (19)	8	2	2
TB Structural Genomics Consortium (TB)	99 (99 chains)	9 (3938)	42	0	1
PSI centers (total of 9 centers above)	1032 (1043 chains)	211 (30,360)	597	48	74
Japanese center (RIKEN)	686 (718 chains)	50 (6860)	289	10	20
Other international SG (total, excluding all centers above)	169 (183 chains)	33 (5877)	69	6	9
Non-SG groups (since 2000)					
Non-SG structural biology (total)	17,096 (23,747 chains)	928 (249,171)	2,521	269	478
Steitz group	46 (559 chains)	23 (4190)	31	7	12
Huber group	185 (273 chains)	8 (679)	38	5	10
Iwata group	14 (54 chains)	14 (7960)	20	2	3

20% in 1990 to 10% today (fig. S1). SG structures account for 44% of the total number of novel structures reported in the year ending 31 January 2005, according to the PSI-BLAST criteria. This result is slightly lower than the Pfam metric for several reasons. Although Pfam families often contain more members than can be detected in a single PSI-BLAST search, Pfam does not include many species-specific proteins. Moreover, the rate of curation of new families may be lagging behind the rate of discovery of new sequences.

A surprising result is the high proportion of solved SG targets that matched prior structures at 95% ID (sequence identity) or 30% ID thresholds of similarity. For four of the PSI centers (see Fig. 2A), more than 50% of the structures solved had 30% or more

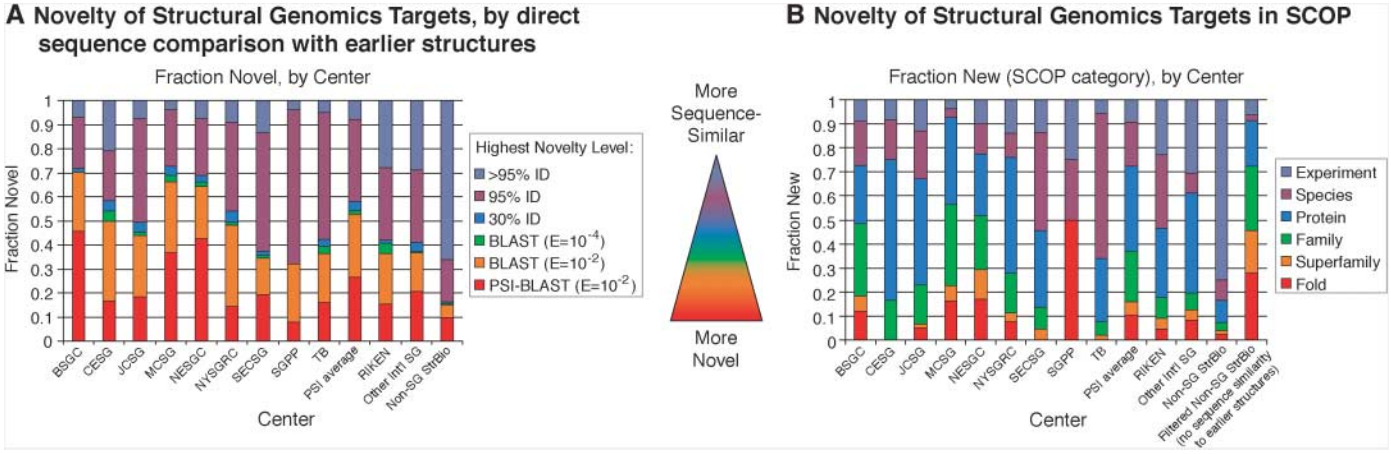

Fig. 2. Novelty rates by center. (**A**) Fractions of structures from each SG center and from non-SG structural biologists that were classified as novel according to each similarity criterion examined. Each structure was classified at the most stringent novelty threshold attained. For example, structures classified as novel at the 95% ID level were between 30% and 95% identical in sequence to a previously reported structure. (**B**) Novelty of domains from SG targets classified in SCOP, by center. Non-SG StrBio includes all domains solved by non-SG structural biologists (1972 to 2005). Filtered non-SG StrBio includes only domains from non-SG structural biologists filtered to remove all proteins with sequence similarity to previously solved structures; this represents what structural biologists might produce if they used PSI-BLAST filtering to avoid targeting structures similar to those previously solved. Note that (A) includes data on all structures reported through the end of January 2005, whereas (B) only includes those structures released by the PDB before the cutoff date for inclusion in SCOP 1.67 (15 May 2004).

sequence identity to previously solved structures. The fraction of solved targets that were 95% identical to a previously known structure ranged from 4% (SGPP and MCSG) to 21% (CESG), with an average of 8% for PSI centers and 17% for all SG efforts. Some of the variation is due to differing policies between SG centers on what is reported as a target (*8*).

Impact of Structural Genomics on Identifying New Folds, Superfamilies, and Families

To complement our sequence-based analyses, we evaluated the novelty of protein structures from all sources in the context of the Structural Classification of Proteins (SCOP) database (*14*). SCOP provides a widely used, manually curated hierarchy indicating different levels of structural and evolutionary relationship between protein domains. Domains classified together at the "family" level have a clear common evolutionary origin, and in many cases they are sufficiently similar to allow reasonably accurate comparative models to be constructed for any family member by using the structure of another as a template (*4*). Groups of families with common structural features or functions that imply a common evolutionary origin are grouped together in "superfamilies." Typically, superfamily relationships are very distant and can only be recognized with the use of structural information. The structure of a single member of a superfamily may be used to confidently predict the overall fold of the other members. Superfamilies that share similar secondary structural features and topology, but for which there is little or no evidence to suggest a common evolutionary origin, are classified together at the "fold" level.

We evaluated each PDB structure to determine how many of its domains represented the first instance of a fold, superfamily, family, protein, or species in SCOP 1.67 (table S4). For non-SG structures, more than 70% of protein domains solved in the past 10 years represent a new experiment on a protein already structurally characterized, although possibly with mutations, with bound ligands, or in a different complex. The percentage of domains that represent a new family in SCOP has fallen from 9.6% in 1995 to 4.4% in 2004 (fig. S3). This number reflects structural biologists' intentions, as they choose whether to characterize a new family as part of their research design.

Comparison of Structural Genomics Results with Expectations

In 2000, Brenner and Levitt (*7*) predicted that by using standard sequence comparison techniques such as BLAST and PSI-BLAST to avoid targeting homologs of known structures (*1*, *15*), SG centers might increase the percentage of new SCOP folds and superfamilies discovered to about 40%. Projections based on 2004 data (fig. S3) are remarkably similar.

How well have SG centers met these expectations? We analyzed all targets solved in time to be included in version 1.67 of SCOP (i.e., deposited and released by the PDB before 15 May 2004). Results are shown in Fig. 2B and Table 1. For PSI centers, the percentage of domains that represented a new SCOP fold or superfamily was 16.0%, higher than the non-SG average of 4.0% but lower than the target of 40%. Results for individual centers varied widely, with much of the difference presumably due to differences in the specific focus of each center, which resulted in differing strategies for target selection and deselection. The relatively early cutoff date for SCOP limits this analysis: For most centers, between half and three-quarters of the total output has occurred in the year ending 31 January 2005, too late for analysis by this method. For example, the analysis of SGPP data represents only 4 of 25 targets solved, although two of these four structures represent new folds. However, the centers with the highest novelty rates in sequence-based tests (BSGC, MCSG, and NESGC) also had the highest rates of discovery of new folds, superfamilies, and families.

Costs of Determining Novel Structures and Families

In cost and productivity data presented to an open session of the National Institute of General Medical Sciences Advisory Council in 2003, the average cost of solving a protein structure under an R01 grant was estimated as $250,000 to $300,000 (*16*, *17*). Because the methodology behind the estimate was not published, we extrapolated an upper and lower estimate for direct comparison to PSI results. The upper estimate is $300,000 for each PDB entry and the lower estimate is $250,000 for each PDB entry with less than 95% sequence identity to any previously solved entry. We suspect that the lower estimate is closer to the actual figure (*8*). Since the PSI project began in September 2000, the average cost per structure at the pilot centers (including direct and indirect costs) has been $211,000, or 70% to 92% of the estimated cost of solving a structure with

traditional methods. In the last year of our study (1 February 2004 to 31 January 2005), the average cost at PSI centers was $138,000 per structure, 46% to 59% of the cost of traditional methods. The most productive center, MCSG, is more than twice as efficient as the average center, having achieved an average cost of only $67,000 per structure over the last year of our study. However, structures solved by SG centers are on average smaller and contain fewer nonidentical polypeptide chains than those from traditional structural biology (table S6). When normalized to account for both of these factors, per-residue costs for SG in the year ending 31 January 2005 are 66% to 85% (rather than 46% to 59%) of those for non-SG structural biology. This normalization accounts for a presumably higher average degree of difficulty in solving larger structures.

When the costs per novel structure are compared, SG becomes even more efficient. Because the average structural biology laboratory directs most of its research effort toward structures with sequences similar to those already solved—often in order to test hypotheses concerning the function of a particular protein—novel structures are discovered relatively infrequently. Thus, the extrapolated ranges of costs per novel structure with traditional methods are relatively high: $532,000 to $1.9 million per novel structure at the 30% ID level, $1.5 to $5.5 million per new Pfam family, and $2.0 to $7.3 million per new SCOP superfamily or fold. Over the lifetime of the project, PSI centers have averaged costs of $364,000 per novel structure at the 30% ID level, $1.0 million per new Pfam family, and $2.2 million per new SCOP superfamily or fold, with costs in each category lowered by at least 20% in the most recent year of the project (table S5). The most efficient center, MCSG, was more cost-efficient than traditional labs in each category in the most recent year of the project by a factor of 5 to 17 (or, when normalized for structure size, a factor of 4 to 14).

These cost data should be interpreted with great caution because many factors are not explicitly considered. Besides the imprecision of the traditional structure cost estimate, many SG centers collaborate with non-SG biologists, a process that shifts some of the costs of protein production and structure determination to other groups not supported by the centers' budgets—and this inflates the apparent productivity of SG. Most SG centers also included targets in their lists that were solved before the official start of PSI funding, and the costs of these structures were also not included. On the other hand, most SG centers have invested substantial funds in capital equipment and technology development during the PSI pilot phase. Although some technology is already widely used throughout the field (*18*), recent investments may not have yet paid off in increased throughput. Equipment costs are presumably a major factor in structural biology laboratories as well, especially at startup. SG centers also bear additional costs of computation, data reporting, and analysis that are not required of non-SG structural biology labs. Costs of synchrotron time and nuclear magnetic resonance facilities may not be included in the total cost estimates for either SG centers or other structural biology laboratories. Finally, many structural biology projects benefit from potentially extensive prior work on the biochemical characterization of particular proteins, which is especially important for more challenging structures.

Comparison with Leading Structural Biologists

We include in Table 1 results for several individual structural biologists who have been among the leaders in determining novel structures according to our metrics since 1 January 2000. Tom Steitz's laboratory is best known for solving the structures of protein–nucleic acid complexes, including the large ribosomal subunit (*2*). Robert Huber's group has solved the structures of many macromolecular complexes, including the proteasome (*19*), DNA primase (*20*), and light-harvesting complexes (*21*, *22*). So Iwata is a leader in membrane crystallography and recently solved the structure of the photosystem II complex (*23*). The total output of each of their laboratories is comparable to that of the average SG center, and the output of novel structures surpasses the lowest performing PSI centers, although both are lower than for the best performing SG center. The area in which the three groups stood out is in solving large, challenging complexes: The Steitz group solved much larger complexes (an average of 12.2 nonidentical polypeptide chains per entry) than did SG centers, whereas the Huber and Iwata groups solved somewhat larger complexes composed of larger individual subunits. We caution that our metrics may be biased toward heteromeric complexes.

We calculated the average cost per novel structure solved by Steitz's laboratory, which operates on a total budget of about $1.5 million per year (*24*), versus about $5.7 million for the average PSI center. Since January 2000, the average cost per structure is about $166,000, but only $14,000 per nonidentical chain (less than one-quarter that of the most recent year of MCSG output). The Steitz lab is also comparable in cost efficiency to PSI centers at solving novel structures. The large ribosomal subunit structure [PDB entry 1ffk (*2*)] is especially remarkable in that it revealed six proteins with novel folds. Furthermore, our protein-based metrics underestimate the novelty of structures solved by the Steitz lab because of the large number of novel nucleic acid macromolecular structures that were solved.

Comparison of Citations

Several structural biologists have suggested that one measure of the level of interest in a scientific field is the number of published papers in the field, and the impact of a scientific report may on average be roughly estimated by the number of subsequent citations. We examined the number of citations to the primary reference in each PDB entry for the 104 SG structures deposited between 1 September 2001 and 31 August 2002 (table S12). As of November 2005, 34 of the 104 structures remain unpublished and thus have no citations. The mean number of citations for the 104 structures was 11.0 and the median number was 4. Several factors bias this analysis: The two most cited references (with 107 and 61 citations, respectively) describe the overall work of a center rather than individual structures, and each was the primary reference for two PDB entries. Also, there were several additional cases in which multiple structures shared the same primary reference, often a functional study, and these were cited more on average than other references. For comparison, we randomly selected 104 non-SG structures solved in the same time period, of which all but six had been published (table S13). Like the SG structures, several shared primary references. The 104 structures had a mean of 21.0 citations and a median of 11.5 citations. Thus, publications of SG structures have significantly fewer citations than publications of structures from non-SG laboratories [$P < 0.0001$ in a two-tailed Mann-Whitney test (*25*)]. For SG structures, novelty did not appear to correlate with the citation rate (*8*). Among non-SG structures, novel structures were cited more often than non-novel structures, as traditional structural biologists solved structures likely to have immediate impact on established biochemical research communities.

Discussion

Structural genomics has been extremely successful at increasing the scope of our structural knowledge of protein families. SG efforts worldwide account for nearly half of the protein families for which the first representative was reported solved during the most recent year of our study (February 2004 to January 2005). Despite the pace of SG, the quality of SG structures has been found to be similar to that of non-SG structures (*26*). The difference in output between the most efficient center and the average is striking.

The fraction of structures solved that are novel could be improved at all SG centers. The specific focus of a center may not be entirely compatible with the goal of producing novel structures; for example, a center focusing on medically relevant proteins may need to target multiple members of a family of therapeutic importance. Also, work on a target is not always abandoned when a detectably homologous structure is solved elsewhere, because finishing a near-complete structure may be a worthwhile use of resources. Finally, a structure may not be considered novel because the preceding struc-

ture was solved elsewhere but not reported immediately. Rapid reporting of the sequences of newly solved structures could reduce wasted effort at SG centers by at least 4 to 8% (the minimal level of redundancy observed across all SG centers), saving millions of dollars per year in the United States alone.

Relative to other structural biology laboratories, SG centers have published relatively few papers describing their structures, and these papers have a lower average number of citations. This finding suggests that publication is a bottleneck not easily adapted to high-throughput environments. Currently, our estimated costs per citation are similar between SG and non-SG structural biology laboratories, in contrast to other areas in which SG has shown greatly improved efficiency. Although SG centers are reporting results through channels other than traditional publications (*27*), such as public websites and centralized databases (*9*), it is unclear whether structures reported in this manner will individually have the same scientific impact as those reported in traditional publications. Highly cited publications often describe detailed studies of protein function, and such studies were not funded at the PSI centers in the pilot phase; however, PSI structures may be used as a starting point for such studies. Ultimately, the cumulative impact of SG, by providing comprehensive structural information covering the majority of proteins, is likely to be greater than the sum of the impact of the individual structures (as was the case for genome sequencing projects).

Finally, the cost estimates suggest a strategy for direction of future structural biology resources. New families predicted to be tractable with high-throughput methods could have basic structural characterization attempted by SG centers because of the substantial cost savings. These families should be prioritized according to significance, for example, family size or biological role (*28*, *29*). Non-SG structural biology could focus on hypothesis-driven research into the function or mechanism of individual proteins, the characterization of particularly challenging proteins and complexes, and other research that is currently impractical to conduct using high-throughput methods. Leading-edge structural biology studies often rely on integration of data from multiple length and time scales, for which most steps are not currently amenable to high-throughput experiments (*30*). During PSI phase 2, considerable resources will be spent on specialized centers aimed at developing technology for high-throughput solution of more challenging structures, such as membrane proteins, eukaryotic proteins, and small protein complexes, which we hope will lead to further gains in efficiency. We view SG and traditional structural biology as playing complementary roles. Structural genomics offers an efficient means to comprehensively survey protein families; by structurally characterizing proteins whose importance is not yet understood, it provides a foundation for the next generation of biomedical research. On the other hand, non-SG structural biology focuses on proteins whose significance is already appreciated, delving deep into particularly rewarding areas to provide immediate scientific impact.

References and Notes

1. S. E. Brenner, *Nat. Rev. Genet.* **2**, 801 (2001).
2. N. Ban, P. Nissen, J. Hansen, P. B. Moore, T. A. Steitz, *Science* **289**, 905 (2000).
3. B. T. Wimberly *et al.*, *Nature* **407**, 327 (2000).
4. D. Baker, A. Sali, *Science* **294**, 93 (2001).
5. S. E. Brenner, C. Chothia, T. J. Hubbard, A. G. Murzin, *Methods Enzymol.* **266**, 635 (1996).
6. P. Smaglik, *Nature* **403**, 691 (2000).
7. S. E. Brenner, M. Levitt, *Protein Sci.* **9**, 197 (2000).
8. See supporting material on *Science* Online.
9. L. Chen, R. Oughtred, H. M. Berman, J. Westbrook, *Bioinformatics* **20**, 2860 (2004).
10. A. Bateman *et al.*, *Nucleic Acids Res.* **32**, D138 (2004).
11. H. M. Berman *et al.*, *Nucleic Acids Res.* **28**, 235 (2000).
12. S. F. Altschul, W. Gish, W. Miller, E. W. Myers, D. J. Lipman, *J. Mol. Biol.* **215**, 403 (1990).
13. S. F. Altschul *et al.*, *Nucleic Acids Res.* **25**, 3389 (1997).
14. A. G. Murzin, S. E. Brenner, T. Hubbard, C. Chothia, *J. Mol. Biol.* **247**, 536 (1995).
15. S. E. Brenner, *Nat. Struct. Biol.* **7** (suppl.), 967 (2000).
16. R. Service, *Science* **307**, 1554 (2005).
17. E. Lattman, *Proteins* **54**, 611 (2004).
18. R. C. Stevens, *Nat. Struct. Mol. Biol.* **11**, 293 (2004).
19. J. Lowe *et al.*, *Science* **268**, 533 (1995).
20. M. A. Augustin, R. Huber, J. T. Kaiser, *Nat. Struct. Biol.* **8**, 57 (2001).
21. J. Deisenhofer, O. Epp, K. Miki, R. Huber, H. Michel, *J. Mol. Biol.* **180**, 385 (1984).
22. R. Huber, *EMBO J.* **8**, 2125 (1989).
23. K. N. Ferreira, T. M. Iverson, K. Maghlaoui, J. Barber, S. Iwata, *Science* **303**, 1831 (2004); published online 5 February 2004 (10.1126/science.1093087).
24. T. Steitz, personal communication.
25. B. L. van der Waerden, *Mathematical Statistics*, vol. 156 of *Die Grundlehren der mathematischen Wissenschaften in Einzeldarstellungen mit besonderer Berücksichtigung der Anwendungsgebiete* (Springer-Verlag, Berlin, 1969).
26. A. E. Todd, R. L. Marsden, J. M. Thornton, C. A. Orengo, *J. Mol. Biol.* **348**, 1235 (2005).
27. A. Wlodawer, *Nat. Struct. Mol. Biol.* **12**, 634 (2005).
28. J. M. Chandonia, S. E. Brenner, *Proteins* **58**, 166 (2005).
29. J. M. Chandonia, S. E. Brenner, in Proceedings of the 27th International Conference of the IEEE Engineering in Medicine and Biology Society, Shanghai, 1 to 4 September 2005.
30. S. C. Harrison, *Nat. Struct. Mol. Biol.* **11**, 12 (2004).

31. We thank J. Rine, T. Alber, T. Steitz, A. Edwards, and G. Montelione for helpful comments. Supported by NIH grants 1-P50-GM62412, 1-K22-HG00056, and 1-R01-GM073109; the Searle Scholars Program (01-L-116); a Sloan Research Fellowship; the IBM Shared University Research Program; and the U.S. Department of Energy under contract DE-AC02-05CH11231.

Supporting Online Material

www.sciencemag.org/cgi/content/full/311/5759/347/DC1
Materials and Methods
References
Figs. S1 to S4
Tables S1 to S14

10.1126/science.1121018

Post-Wildfire Logging Hinders Regeneration and Increases Fire Risk

D. C. Donato,[1]* J. B. Fontaine,[2] J. L. Campbell,[1] W. D. Robinson,[2]
J. B. Kauffman,[3] B. E. Law[1]

Recent increases in wildfire activity in the United States have intensified controversies surrounding the management of public forests after large fires (*1*). The view that postfire (salvage) logging diminishes fire risk via fuel reduction and that forests will not adequately regenerate without intervention, including logging and planting, is widely held and commonly cited (*2*). An alternate view maintains that postfire logging is detrimental to long-term forest development, wildlife habitat, and other ecosystem functions (*1*). Scientific data directly informing this debate are lacking.

Here we present data from a study of early conifer regeneration and fuel loads after the 2002 Biscuit Fire, Oregon, USA, with and without postfire logging. Because of the fire's size (~200,000 ha), historic reforestation difficulties in the region (*3*), and an ambitious postfire logging proposal, the Biscuit Fire has become a national icon of postfire management issues. We used a spatially nested design of logged and unlogged plots replicated across the fire area and sampled before (2004) and after (2005) logging (*4*).

Natural conifer regeneration on sites that experienced high-severity fire was variable but generally abundant, with a median stocking density of 767 seedlings per hectare, primarily of Douglas fir (*Pseudotsuga menziesii*) (Fig. 1A). Such density exceeds the regional standards for fully stocked sites, suggesting that active reforestation efforts may be unnecessary. Postfire logging subsequently reduced regeneration by 71% to 224 seedlings per hectare (Fig. 1A) due to soil disturbance and physical burial by woody material during logging operations. Thus, if postfire logging is conducted in part to facilitate reforestation, replanting could result in no net gain in early conifer establishment.

Postfire logging significantly increased both fine and coarse downed woody fuel loads (Fig. 1B). This wood was composed of unmerchantable material (e.g., branches), and far exceeded expectations for fuel loads generated by postfire logging (*4*, *5*). In terms of short-term fire risk, a reburn in logged stands would likely exhibit elevated rates of fire spread, fireline intensity, and soil heating impacts (*6*).

Postfire logging alone was notably incongruent with fuel reduction goals. Fuel reduction treatments (prescribed burning or mechanical removal) are frequently intended after postfire logging, including in the Biscuit plan, but resources to complete them are often limited (*7*). Our study underscores that, after logging, the mitigation of short-term fire risk is not possible without subsequent fuel reduction treatments. However, implementing these treatments is also problematic. Mechanical removal is generally precluded by its expense, leaving prescribed burning as the most feasible method. This will result in additional seedling mortality and potentially severe soil impacts caused by long-duration combustion of logging-generated fuel loads. Therefore, the lowest fire risk strategy may be to leave dead trees standing as long as possible (where they are less available to surface flames), allowing for aerial decay and slow, episodic input to surface fuel loads over decades.

Our data show that postfire logging, by removing naturally seeded conifers and increasing surface fuel loads, can be counterproductive to goals of forest regeneration and fuel reduction. In addition, forest regeneration is not necessarily in crisis across all burned forest landscapes.

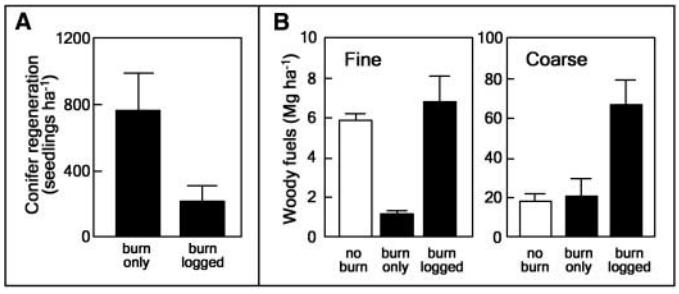

Fig. 1. (**A**) Natural conifer regeneration and (**B**) surface woody fuel loads before and after postfire logging of the Biscuit Fire, Oregon, USA. (A) shows that regeneration was abundant after the fire. Postfire logging significantly reduced seedling densities ($P < 0.01$, Wilcoxon signed rank test) from 767 seedlings per hectare to 224 seedlings per hectare. (B) shows that postfire logging significantly increased downed fine ($P < 0.01$) and coarse ($P < 0.05$) woody fuel loads (Mg ha^{-1}) relative to burn-only fuel loads by Wilcoxon signed rank test. To provide context, fuel data from unburned stands are shown as reference for prefire conditions (fuel loads in burn-logged stands were at or well above prefire levels). Graphs of seedling densities and fine (≤7.62 cm) and coarse (>7.62 cm) surface woody fuels are medians ± SE; sample size $n = 8$ stands for no burn, $n = 9$ for burn-only and burn-logged (*4*).

References and Notes

1. D. B. Lindenmayer *et al.*, *Science* **303**, 1303 (2004).
2. J. Sessions, P. Bettinger, R. Buckman, M. Newton, J. Hamann, *J. For.* **102**, 38 (2004).
3. S. D. Tesch, S. D. Hobbs, *West. J. Appl. For.* **4**, 89 (1989).
4. Materials and methods are available as supporting material on *Science* Online.
5. Timber decay associated with delays in postfire logging was anticipated to exacerbate the observed pulse of surface fuel. However, our data indicate that delay was responsible for ~10% of the woody fuel present after logging.
6. J. K. Agee, *Fire Ecology of Pacific Northwest Forests* (Island Press, Washington, DC, 1993).
7. R. W. Gorte, "Forest Fires and Forest Health" *Congressional Research Service* (Publication 95-511, 1996).
8. This work was supported by the Joint Fire Science Program and DOE grant DE-FG02-04ER63917. We thank field technicians and the Siskiyou National Forest.

Supporting Online Material

www.sciencemag.org/cgi/content/full/1122855/DC1
Materials and Methods
SOM Text
References and Notes

21 November 2005; accepted 21 December 2005
Published online 5 January 2006;
10.1126/science.1122855
Include this information when citing this paper.

[1]Department of Forest Science, [2]Department of Fisheries and Wildlife, Oregon State University, Corvallis, OR 97331, USA. [3]Institute of Pacific Islands Forestry, U.S. Department of Agriculture Forest Service, Pacific Southwest Research Station, 60 Nowelo Street, Hilo, HI 96720, USA.

*To whom correspondence should be addressed. E-mail: dan.donato@oregonstate.edu

Phospholipid Nonwoven Electrospun Membranes

Matthew G. McKee, John M. Layman, Matthew P. Cashion, Timothy E. Long*

Nonwoven fibrous membranes were formed from electrospinning lecithin solutions in a single processing step. As the concentration of lecithin increased, the micellar morphology evolved from spherical to cylindrical, and at higher concentrations the cylindrical micelles overlapped and entangled in a fashion similar to polymers in semi-dilute or concentrated solutions. At concentrations above the onset of entanglements of the wormlike micelles, electrospun fibers were fabricated with diameters on the order of 1 to 5 micrometers. The electrospun phospholipid fibers offer the potential for direct fabrication of biologically based, high-surface-area membranes without the use of multiple synthetic steps, complicated electrospinning designs, or postprocessing surface treatments.

Because of their amphiphilic chemical structure, phospholipids organize into a bilayer matrix, which serves as the building block of cell membranes (*1*). Phospholipids possess a charged head group and a hydrocarbon tail that contain various amounts of unsaturation. Significant work has focused on engineering stable biomembranes as a result of polymerizing functionalized phospholipids or postpolymerization functionalization with phospholipid reagents (*2*, *3*). For example, Nakaya *et al*. synthesized an alkyl methacrylate monomer with a phospholipid head group, which suppressed protein adsorption and platelet adhesion (*4*). Thus, phospholipid-containing polymers are attractive candidates for blood purification membranes, artificial heart valves, artificial organs, and several other prosthetic devices (*5*–*8*). An alternative method for designing biocompatible devices involves coating suitable substrates with phospholipids (*9*, *10*). The disadvantages of a coating strategy are numerous: for example, (i) multiple synthetic steps for production of a phospholipid functionalized polymer are required and (ii) grafting to or grafting from methodologies are necessary to sufficiently tailor the surface properties.

Electrostatic spinning or electrospinning is a polymer processing technique that forms fibers two to three orders of magnitude smaller than conventionally processed fibers (*11*, *12*). Electrospinning typically occurs when a charged solution or melt of a high molar mass polymer is subjected to an electric field. Because of the presence of chain entanglements in the charged fluid, the fluid does not break up into droplets but forms a stable jet when the electrostatic repulsive forces on the fluid surface overcome the surface tension. The range of fiber diameters is roughly between 100 nm and 10 μm (*13*) and is dependent on (i) process variables, including electrical field strength, fluid flow rate, and working distance between the electrodes (*14*); (ii) solution variables, including viscosity, electrical conductivity, surface tension, and solvent volatility (*15*); and (iii) environmental variables, including temperature, pressure, and humidity (*16*, *17*).

We recently correlated the electrospun fiber morphology and fiber diameter to the degree of chain entanglements and chain overlap in solution (*18*, *19*). This empirical model was applicable to a range of polymer families, molar masses, and molecular architectures. Recently Wnek *et al*. developed a semi-empirical model that predicts the fiber morphology in terms of the polymer concentration, the weight average molar mass (M_w), and the entanglement molar mass (M_e) (*20*). Because chain overlap and entanglements are necessary for electrospun fiber formation, electrospinning studies typically involve high molar mass polymers. However, our recent studies have demonstrated that high molar mass polymers are not essential for production of uniform electrospun fibers and that the presence of sufficient intermolecular interactions that effectively act as chain entanglements is the primary criterion. For example, polymers with strong quadruple hydrogen bonding capabilities displayed electrospinning behavior similar to unfunctionalized polymers of substantially higher molar mass (*21*). Given that phospholipids can form entangled, worm-

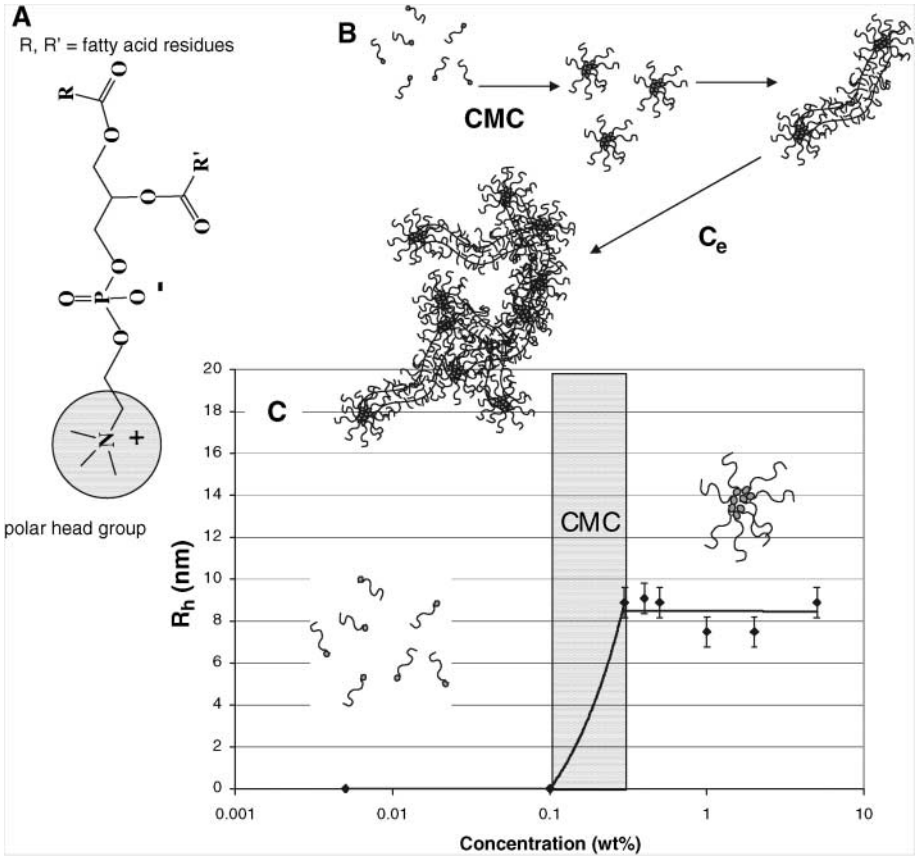

Fig. 1. (**A**) Structure of phosphatidycholine where R and R′ are fatty acid residues with different degrees of unsaturation. (**B**) Lecithin transition from amphiphilic molecules to entangled, wormlike micelles. (**C**) R_h values of lecithin micelles in 70/30 $CHCl_3$/DMF as a function of concentration. The CMC was about 0.1 wt %, and the average spherical micelle was 9 nm.

Department of Chemistry, Macromolecules and Interfaces Institute (MII), Virginia Tech, Blacksburg, VA 24061, USA.

*To whom correspondence should be addressed. E-mail: telong@vt.edu

like micelles under the appropriate solution conditions, we examined whether they can also be spun into fibers.

Lecithin, which is a natural mixture of phospholipids and neutral lipids, forms cylindrical or wormlike reverse micelles in nonaqueous solutions (Fig. 1A) (*22*). As the concentration of lecithin is raised in solution, the micellar morphology changes from spherical to cylindrical, and at higher concentrations the cylindrical micelles overlap and entangle in a similar way to that of polymer chains in semi-dilute or concentrated solutions (*23*). Water and other polar molecules serve to bridge the phosphate head groups between neighboring phospholipids through hydrogen bonds (*24*).

The morphology of lecithin micelles that formed in nonaqueous solutions was probed by using dynamic light scattering and solution rheology, and the concentration dependence of the zero shear viscosity (η_0) was compared to scaling relationships. Moreover, because of entanglements between the wormlike micelles, we evaluated the electrospinning behavior of the lecithin solutions. The fabrication of a high-surface-area, potentially biocompatible, phospholipid membrane that involves a single processing step will offer exceptional promise for diverse biomedical applications.

In dilute nonpolar solutions, phospholipids form reverse spherical micelles with their polar head groups directed toward the hydrophilic core of the micelle. These spherical micelles undergo a one-dimensional, cylindrical growth with increased surfactant concentration. Figure 1B shows the typical micellar growth and entanglement of lecithin micelles. At the critical micelle concentration (CMC), the lecithin amphiphiles rearrange to form spherical micelles. The micelles undergo cylindrical growth and entanglement couplings above the entanglement concentration (C_e). Figure 1C shows the hydrodynamic radii (R_h) of lecithin in 70/30 $CHCl_3$/*N*,*N*′-dimethylformamide (DMF) solutions as a function of concentration. The average micelle size was about 9 nm with a CMC of about 0.1 weight percent (wt %). This value is in good agreement with R_h values of lecithin micelles in cyclohexene as measured earlier by Kanamaru and Einaga (*25*). Moreover, within the concentration range investigated, the spherical micelles did not grow in size. Other researchers also observed an independence of spherical lecithin micelles size with concentration (*26*).

The lecithin solutions were characterized by using a strain-controlled solution rheometer in the semi-dilute concentration regime. The entanglement concentration (C_e) is 35 wt%, which separates the semi-dilute unentangled and the semi-dilute entangled regimes. In a similar fashion to polymer coils, the wormlike micelles form entanglement couplings above C_e. The slopes in the semi-dilute unentangled and semi-dilute entangled regimes were 2.4 and 8.4, respectively, which were substantially larger than those predicted for neutral polymers in a good solvent ($\eta_{sp} \sim C^{1.25}$ and $\eta_{sp} \sim C^{3.75}$ in unentangled and entangled regimes, respectively). Moreover, the concentration dependence of η_{sp} was also greater than predictions from the reversible chain scission model ($\eta_{sp} \sim C^{5.25}$). Solution rheological studies of micellar solutions performed by other researchers also displayed exponents larger than 5.25 (*27*). In particular, Cappelaere *et al*. observed a power-law exponent of about 12 for cetyltrimethylammonium bromide aqueous solutions (*28*). The unusually large concentration dependence suggests the presence of intermolecular associations between the wormlike micelles (*29*). Polymer chains that are modified with associating functional groups also display a very strong η_0 dependence on concentration because of the increased probability of intermolecular associations compared with intramolecular associations with increasing concentration (*30*, *31*).

We have previously described the onset of chain entanglements as a criterion for the formation of electrospun fibers. Generally uniform fibers formed at 2 to 2.5C_e due to stabilization of the electrified jet and suppression of the Raleigh instability from the entanglement couplings. It should be noted that electrospun fiber formation would not be possible if the phospholipids did not form a supramolecular entangled network, because individual phospholipids are low molar mass compounds that are incapable of forming entanglements.

All lecithin solutions were electrospun at constant conditions, 15 kV, 6-ml/hour syringe flow rate, and 10-cm working distance, from the semi-dilute unentangled and the semi-dilute entangled regimes. The solution rheological experiments and electrospinning trials were performed at the same conditions (room temperature and 70/30 wt/wt $CHCl_3$/DMF) to ensure constant hydrodynamic dimensions of the wormlike micelles in solution before experiencing the electric field. Figure 2 shows field-emission scanning electron microscope (FESEM) images of electrospun fibers that were formed from various concen-

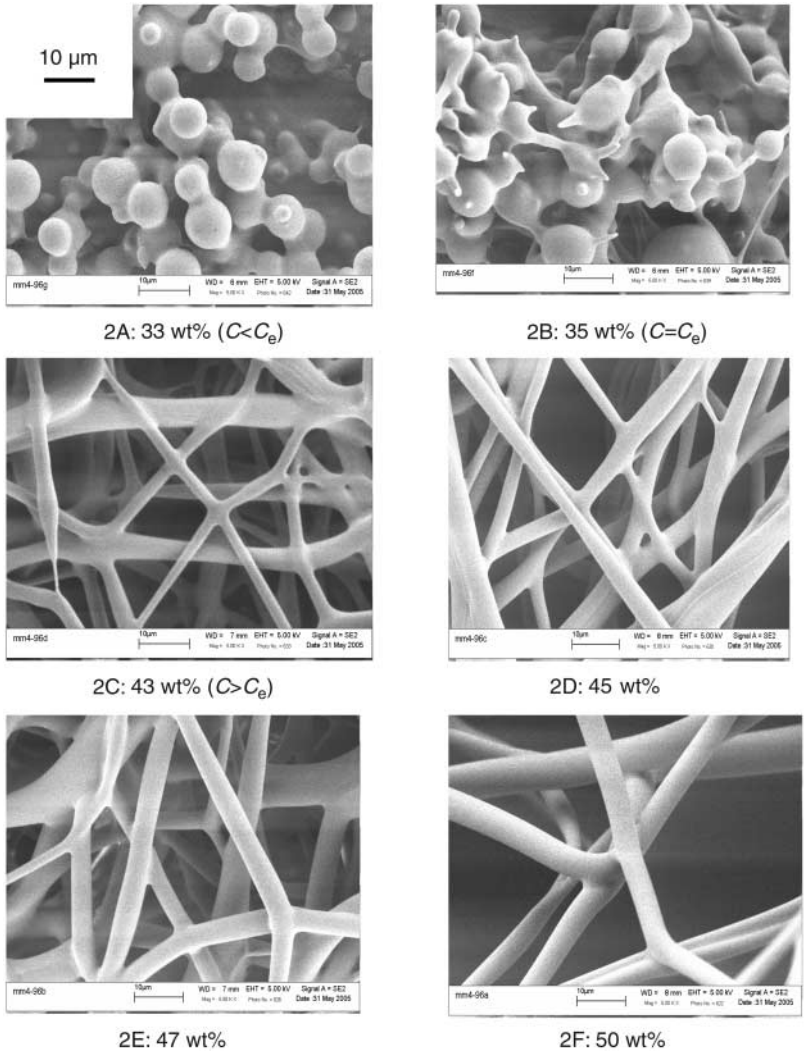

Fig. 2. (**A** to **F**) FESEM images of electrospun phospholipids (C_e = 35 wt %). All images were collected at the same magnification.

trations of lecithin in 70/30 wt/wt $CHCl_3$/DMF. At 33 wt% ($C < C_e$), droplets were formed because of the absence of chain entanglements in the supramolecular structure, which resulted in destabilization of the electrified jet (Fig. 2A). As the concentration was raised to 35 wt% (C_e), droplets still dominated the morphology, although there is evidence of a low concentration of fibers between the droplets (Fig. 2B). Figure 2C shows that electrospun fibers with an average diameter of 2.8 μm were formed at 43 wt% ($C > C_e$). Fibers were formed for $C > C_e$ because the entanglements between the wormlike micelles stabilized the electrospinning jet and prevented breakup of the jet. The transition from beaded fibers to fibers with elongated beads can be seen by comparing Fig. 2, B and C; this phenomenon was also observed for several different polymer families (*32*, *33*). Uniform, electrospun fibers with an average fiber diameter of 3.3 μm were formed when lecithin was electrospun at 45 wt% (Fig. 2D). Lastly, the average fiber diameter increased from 4.2 to 5.9 μm as the lecithin concentration was raised further from 47 to 50 wt%, respectively (Fig. 2, E and F). Energy dispersive spectroscopy (EDS) indicated that the lecithin amphiphiles were randomly oriented within the electrospun fibers without preferential layering. Moreover, ^{1}H nuclear magnetic resonance (NMR) spectroscopy confirmed that the chemical composition of the electrospun fibers and lecithin precursor were identical, which suggested that the electrospinning process did not substantially alter the chemical structure of the phospholipid.

On the basis of the normalized polymer concentration (C/C_e), we accurately predicted the average electrospun fiber diameter (D) for various polymer families, molar mass, and chain topology according to the equation $D[\mu m] = 0.18(C/C_e)^{2.7}$. The empirical correlation underpredicted the fiber diameter for poly(alkyl methacrylates) with quadruple hydrogen bonding capabilities because of the strong concentration dependence of the solution viscosity. Figure 3A compares the dependence of the phospholipid fiber diameter on normalized concentration with the electrospinning behavior of neutral, nonassociating polymers (black line). In addition, the fiber diameter dependence for poly(alkyl methacrylates) with pendant quadruple hydrogen bonding groups is included. Because of the associations that are formed between hydrogen bonding groups, the fiber diameter was substantially larger than predicted. On inspection of Fig. 3A, it appears that the lecithin electrospinning behavior was similar to associating polymers, which is consistent with the presence of intermolecular associations between the lecithin micelles. Figure 3B shows the dependence of the average fiber diameter on η_0 for the micellar solution. The electrospinning behavior was also compared to the previous correlations developed for neutral, nonassociating polymers (black line). Figure 3B indicates excellent agreement between the phospholipid fiber diameter and the neutral polymer fiber diameter at a given value of η_0. Thus, the large deviation from the fiber diameter–C/C_e relationship was due to the strong concentration dependence of η_0 for the entangled lecithin micelles solutions. This observation was also similar to the electrospinning behavior of associating polymers as discussed earlier.

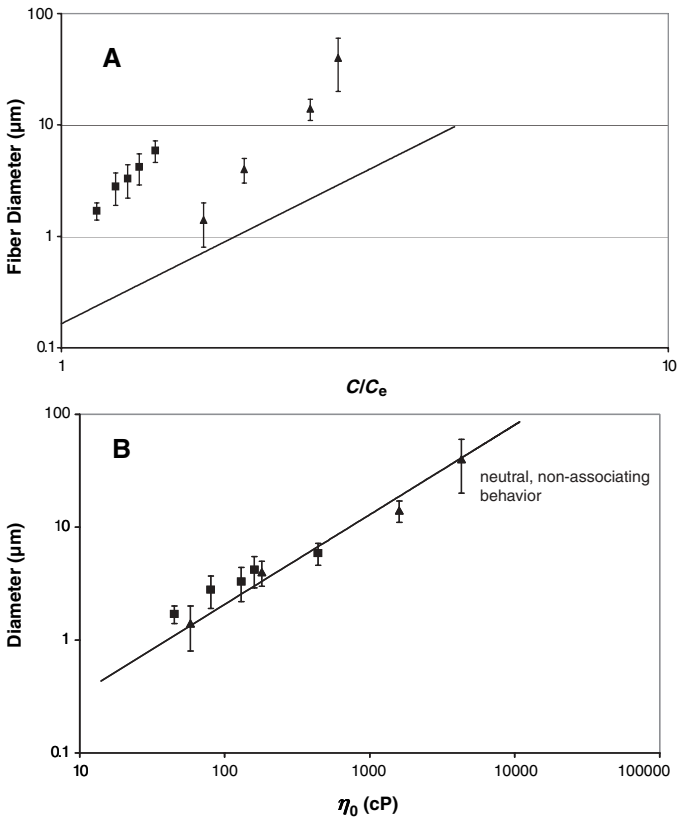

Fig. 3. Dependence of the electrospun fiber diameter on **(A)** C/C_e and **(B)** η_0. The triangles and squares correspond to fibers formed from poly(alkyl methacrylate) with quadruple hydrogen bond groups. Error bars measure the variability in the *y* axis data.

References and Notes

1. C. W. Pratt, K. Cornely, *Essential Biochemistry* (Wiley, Hoboken, NJ, 2004).
2. J. H. Fendler, *Science* **223**, 888 (1994).
3. D. Chapman, *Langmuir* **9**, 39 (1993).
4. S. Nakai, T. Nakaya, M. Imoto, *Makromol. Chem* **79**, 2349 (1978).
5. A. Korematsu, Y. Takemoto, T. Nakaya, H. Inou, *Biomaterials* **23**, 263 (2002).
6. K. Kim, K. Shin, H. Kim, C. Kim, Y. Byun, *Langmuir* **20**, 5396 (2004).
7. S. H. Ye, J. Watanabe, Y. Iwasaki, K. Ishihara, *Biomaterials* **24**, 4143 (2003).
8. N. Morimoto, Y. Iwasaki, N. Nakabayahsi, K. Ishihara, *Biomaterials* **23**, 4881 (2002).
9. H. K. Kim, K. Kim, Y. Byun, *Biomaterials* **26**, 3444 (2005).
10. P. He, M. W. Urban, *Biomacromolecules* **6**, 2455 (2005).
11. D. H. Reneker, I. Chun, *Nanotechnology* **7**, 216 (1996).
12. S. V. Fridrikh, J. H. Yu, M. P. Brenner, G. C. Rutledge, *Phys. Rev. Lett.* **90**, 144502 (2003).
13. D. Li, Y. Xia, *Adv. Mater.* **16**, 1151 (2004).
14. J. M. Deitzel, J. Kleinmeyer, D. Harris, N. C. Beck Tan, *Polymer* **42**, 261 (2001).
15. S. J. Bai, C. C. Wu, W. L. Tu, K. H. Lee, *J. Polym. Sci. B* **40**, 1760 (2002).
16. S. Megelski, J. S. Stephens, B. D. Chase, J. F. Rabolt, *Macromolecules* **35**, 8456 (2002).
17. C. L. Casper, J. S. Stephens, N. G. Tassi, B. D. Chase, J. F. Rabolt, *Macromolecules* **37**, 573 (2004).
18. M. G. McKee, G. L. Wilkes, R. H. Colby, T. E. Long, *Macromolecules* **37**, 1760 (2004).
19. P. Gupta, C. Elkins, T. E. Long, G. L. Wilkes, *Polymers* **46**, 4799 (2005).
20. S. L. Shenoy, D. W. Bates, H. L. Frisch, G. E. Wnek, *Polymers* **46**, 3372 (2005).
21. M. G. McKee, C. L. Elkins, T. E. Long, *Polymers* **45**, 8705 (2004).
22. P. Schurtenberger, R. Scartazzini, L. J. Magid, M. E. Leser, P. L. Luisi, *J. Phys. Chem.* **94**, 3695 (1990).
23. S. A. Mezzasalma, G. J. M. Koper, Y. A. Shchipunov, *Langmuir* **16**, 10564 (2000).
24. Y. A. Shchipunov, E. V. Shumilina, *Mater. Sci. Eng.* **C3**, 43 (1995).
25. M. Kanamaru, Y. Einaga, *Polymer* **43**, 3925 (2002).
26. P. A. Cirkel, G. J. M. Koper, *Langmuir* **14**, 7095 (1998).
27. L. J. Magid, *J. Phys. Chem. B* **102**, 4064 (1998).
28. E. Cappelaere, R. Cressely, J. P. Decruppe, *Colloids Surf. A* **104**, 353 (1995).
29. M. Rubinstein, A. N. Semenov, *Macromolecules* **34**, 1058 (2001).
30. E. J. Regalado, J. Selb, F. Candau, *Macromolecules* **32**, 8580 (1999).
31. M. G. McKee, C. L. Elkins, T. Park, T. E. Long, *Macromolecules* **38**, 6015 (2005).
32. H. Fong, D. H. Reneker, *Polymer* **40**, 4585 (1999).
33. K. H. Lee, H. Y. Kim, H. Y. Bang, Y. H. Jung, S. G. Lee, *Polymer* **44**, 4029 (2003).

34. This material is based on work supported by the U.S. Army Research Laboratory and the U.S. Army Research Office under contract/grant number DAAD19-02-1-0275 Macromolecular Architecture for Performance Multidisciplinary University Research Initiative (MAP MURI).

Supporting Online Material

www.sciencemag.org/cgi/content/full/311/5759/353/DC1
Materials and Methods
Fig. S1
References

6 September 2005; accepted 12 December 2005
10.1126/science.1119790

Covalently Bridging Gaps in Single-Walled Carbon Nanotubes with Conducting Molecules

Xuefeng Guo,[1,5] Joshua P. Small,[2,5] Jennifer E. Klare,[1,5] Yiliang Wang,[1,5] Meninder S. Purewal,[4,5] Iris W. Tam,[1,5] Byung Hee Hong,[2,5] Robert Caldwell,[4,5] Limin Huang,[4,5] Stephen O'Brien,[4,5] Jiaming Yan,[1,5] Ronald Breslow,[1,5] Shalom J. Wind,[4,5] James Hone,[3,5] Philip Kim,[2,5]* Colin Nuckolls[1,5]*

Molecular electronics is often limited by the poorly defined nature of the contact between the molecules and the metal surface. We describe a method to wire molecules into gaps in single-walled carbon nanotubes (SWNTs). Precise oxidative cutting of a SWNT produces carboxylic acid–terminated electrodes separated by gaps of ≤10 nanometers. These point contacts react with molecules derivatized with amines to form molecular bridges held in place by amide linkages. These chemical contacts are robust and allow a wide variety of molecules to be tested electrically. In addition to testing molecular wires, we show how to install functionality in the molecular backbone that allows the conductance of the single-molecule bridges to switch with pH.

One of the greatest challenges in molecular electronics is the ill-defined bonding between molecules and metal electrodes. For even the most well-studied system, thiolated molecules on Au contacts (*1*–*8*), there are no methods to control the type of metal-molecule bonding (*9*), although the contact itself is thought to dominate the transport properties (*10*). Even if more conductive contact chemistry is used, such as carbenes on transition metals (*11*) and on metal carbides (*12*), molecular-scale metal electrodes are extremely difficult to fabricate and lack specific chemistry for molecular attachment at their ends.

An improved strategy would create a well-defined covalent bond between the electrode and the molecule with a limited number of molecular bonding sites and would be intrinsically molecular in scale. Here we describe such a system, in which cut single-walled carbon nanotubes (SWNTs) (*13*, *14*) are covalently attached to molecules through amide linkages. All of the elements in the resulting molecular circuits are naturally at small dimensions because the SWNTs are one-dimensional (1D) conductors or semiconductors (*15*–*17*) that are intrinsically the same size as the molecules being probed. We have tested a number of different types of molecules, including species with chemical functionality that allows the molecular conductance to be switched.

The strategy for attaching molecular wires to SWNT electrodes is to cut them by local oxidation, leaving two ends that are capped with the product of this oxidation and separated by a molecular-scale gap. Given the strongly oxidizing conditions used here, we expect a prevalence of carboxylic acid groups on the cut ends of these SWNTs (*18*). A molecular bridge with amine end groups is then chemically attached to the carboxylic acid ends by a dehydration reaction to form the amide linkage (*18*–*21*). The amine-containing aromatics used here are common, easily prepared, and stable under the reaction conditions. The amine functions avoid one of the serious drawbacks of thiol chemistry, the oxidative oligomerization of dithiols. The amine-attachment chemistry is well developed in peptide synthesis, and the amide bonds that are formed are extremely stable. Moreover, much of the detrimental stochastic switching (*9*) and lateral surface mobility of metal grains (*22*) that plague thiols on gold are absent in these covalently bonded junctions.

We grew the individual SWNTs by chemical vapor deposition on degenerately doped silicon wafers with 300 nm of thermally grown SiO_2 on their surface (*23*). The SWNTs grown in this way are ~1 to 2 nm in diameter (*23*). Metallic electrodes (5 nm of Cr overlaid by 50 nm of Au) separated by 20 μm were deposited through a shadow mask onto the SWNTs. The nanotube devices were electrically tested using the metal pads as source (S) and drain (D) contacts and the silicon substrate as a back gate (G).

The method used to create molecular-scale gaps with carboxylic acid end-group functionality is illustrated in Fig. 1, A and B. First, a window that is less than 10 nm in size was opened in a spin-cast layer of polymethylmethacrylate (PMMA) by using ultrahigh-resolution electron-beam lithography (fig. S1) (*24*). The nanotubes were then locally cut through the open window via oxygen plasma ion etching (250 mTorr, 50 W RF power, 10 s exposure) (*24*). This gap is too small to be imaged in the scanning electron microscope (Fig. 1C), but it can be located and directly imaged with atomic force microscopy (AFM) (Fig. 1D). The relatively large size of the AFM tip makes it difficult to determine with precision how small these gaps are. For the AFM micrographs in Fig. 1D, we take the imaging

[1]Department of Chemistry, [2]Department of Physics, [3]Department of Mechanical Engineering, [4]Department of Applied Physics/Applied Mathematics, [5]The Columbia University Center for Electronics of Molecular Nanostructures, Columbia University, New York, NY 10027, USA.

*To whom correspondence should be addressed. E-mail: cn37@columbia.edu (C.N.), pkim@phys.columbia.edu (P.K.)

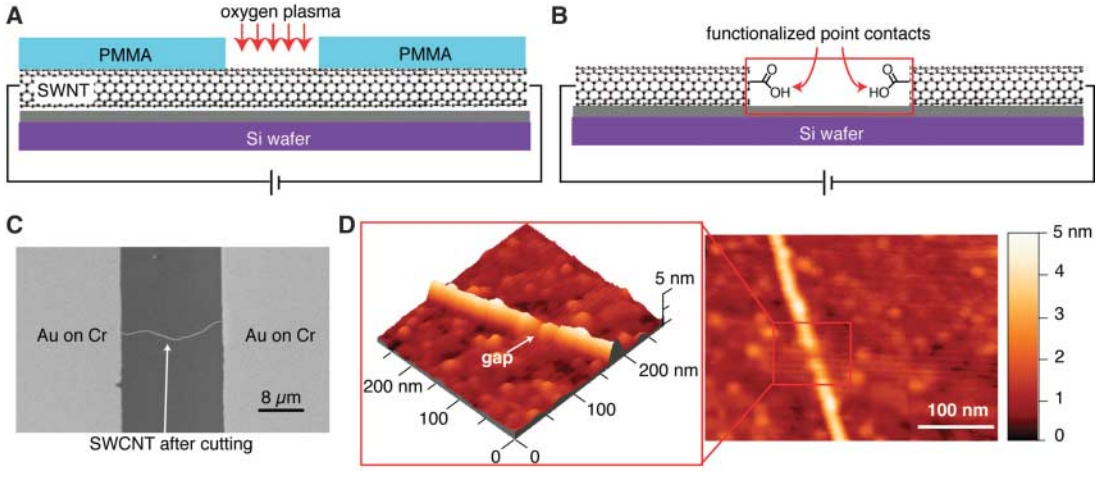

Fig. 1. (**A**) Precise cutting of SWNTs with an oxygen plasma introduced through an opening in a window of PMMA defined with e-beam lithography. (**B**) Oxidative opening of a tube produces two point-contacts functionalized on their ends with carboxylic acids and separated by as little as 2 nm. (**C**) Scanning electron micrograph of a SWNT with Au on Cr leads that had been cut using e-beam lithography and an oxygen plasma. (**D**) AFM image of the gap cut into the SWNT. (Inset) Height profile of the isolated tubes. The diameter of the SWNT is 1.6 nm, estimated from the height profile.

convolution of the AFM tip size into account and set an upper bound on the size of a typical gap opened in the SWNTs of ~10 nm for the processing conditions described above.

The statistical variability of the plasma etch process creates ensembles of SWNT devices with gaps of less than 10 nm. We speculate, on the basis of previous oxidation studies of SWNTs (*18*, *25*, *26*), that the oxidation creates or nucleates at a defect on the side wall (either present before etching or induced by the plasma) and continues to oxidatively erode the tube. We measure the electrical transport properties of the SWNT before and after oxidative etching to determine the yield of completely cut tubes. Longer etch times give higher yields of the cutting but lower the yields of the chemical connection reactions discussed below. We intentionally shorten the etch time so that the average gap can be narrower than the window in the PMMA. Under optimized conditions, ~20 to 25% of the tubes are completely cut among ~2500 devices tested.

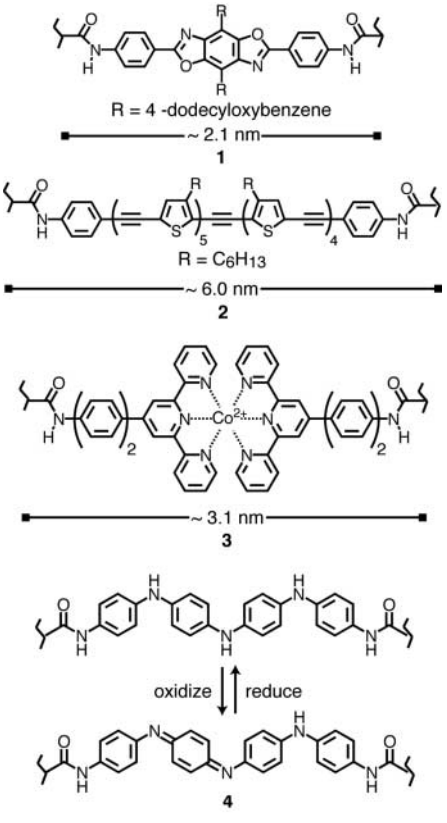

Fig. 2. Molecular bridges (**1** to **4**) spanning carbon nanotube leads. Oligoaniline **4** provides a redox- and pH-sensitive molecular bridge.

We synthesized the corresponding molecular wires (**1** to **4**) that were terminated with the requisite amine functionality according to the procedures outlined in (*24*). We attached the wires to the cut nanotube ends by immersing the diamines and the SWNT devices into a pyridine solution containing the well-known carbodiimide dehydrating/activating agent EDCI (*24*, *27*). After reaction, the devices were removed from the solution, rinsed with fresh solvent, dried, and then tested electrically. Some of the devices that were previously open showed a finite and measurable conductance after reaction.

The various molecular bridges that we have incorporated into the nanotube electrodes with this technique are shown in Fig. 2. The cruciform π-systems (**1**) (*28*) and the longer oligothiophenylethynylene (**2**) (*29*) have a path of through conjugation for electrical conduction and lateral side chains that make them highly soluble. These side chains also provide considerable width to these molecules. For example, the width of **1** with its aryldodecyloxy side chains fully extended would be ~4.3 nm. This value is substantially greater than the diameter of typical SWNTs used in this experiment (~1 to 2 nm). Similarly, the terpyridyl-containing molecules (**3**) have a substantial width compared to the diameter of a SWNT. Given the volume occupied by **1**, **2**, and **3**, it is difficult to bridge this gap with more than one molecule and certainly not more than two. The oligoaniline (**4**) is thinner, and we estimate, on the basis of its molecular volume, that a maximum of seven oligoanilines could bridge an orthogonally cut SWNT gap. The number of reactive sites is reduced further if we assume that the gaps are unevenly cut.

These amidation reactions allowed us to calibrate the etch process itself because the different species can be used as molecular rulers. For example, under optimized conditions, the yield for connection of **1** for more than 200 reactions is ~10%. Using longer etch times, which give the larger gaps, reduces the yield of the coupling reaction with **1**. Moreover, molecules of length similar to that of **1** give similar yields in these reactions, implying that the yield is dominated by the statistics of having two functional groups appropriately spaced for bridging. Under identical conditions, the longer molecules (**2** and **3**) gave lower yields in their connection reactions (~5%). To determine whether the greater length of the molecule was limiting the yield of successful contacts, we prepared a mixture of three oligomers based on **2** that ranged in length from 2 to 6 nm. The yield increased to ~20% for the connection reaction with this mixture.

Electrical measurements on devices before cutting, when cut, and after connection with **1** are shown in Fig. 3. The black curves show the source-drain current (I) plotted against the gate voltage (V_g) at constant S-D bias voltage (V_{SD} = 50 mV) for two devices before cutting. The device in Fig. 3, A and B, before cutting shows metallic behavior, and the one in Fig. 3C shows typical p-type semiconducting behavior. The red traces, taken after cutting, show no conductance down to the noise limit of the measurement (≲2.0 pA). The green traces show the devices after molecular connection of the SWNT leads. Similar I-V_{DS} curves (figs. S2 and S3) are shown for connection with the other molecular bridges (**2** to **4**) (*24*). In all cases, the reconnected devices recovered their original metallic or semiconducting behavior at reduced values of I, indicating that the gate modulates the nanotube conductance more strongly than that of the molecules.

The resistance, and thus the molecular conductance, can be estimated from the drop in current after molecular connection. For example, the resistance of the metallic tube connected in Fig. 3, A and B, with the cruciform molecule (**1**) increases from ~1 megohm before cutting to ~5 megohm after connection with the V_{SD} = 50 mV in the linear response regime. The molecular conductance for **1** in this device is calculated to be $6.4 \times 10^{-3}\ e^2/h$. Table 1 displays similar data for **2** to **4** in SWNT gaps. In some cases, the conductance is greater than $10^{-2}\ e^2/h$. Moreover, the I-V curves at low temperature (down to 1.6 K; figs. S4 and S5) have a wealth of structure

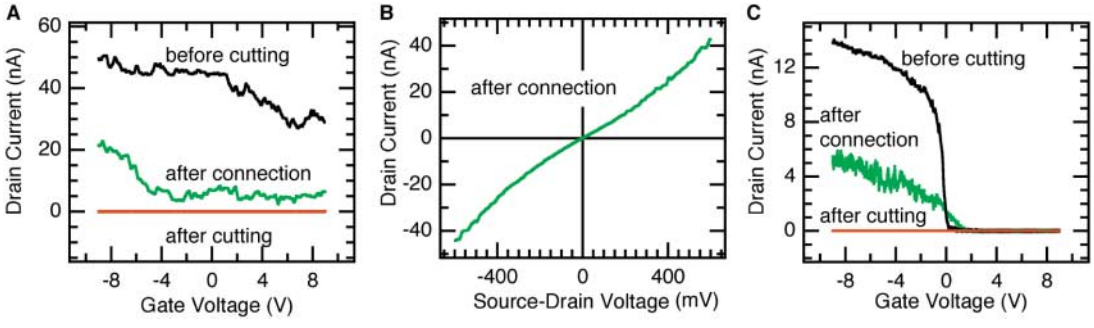

Fig. 3. (**A**) Metallic SWNT electrodes connected with **1** drain current (I) in the device as a function of the gate voltage (V_g) at V_{SD} = 50 mV for a metallic tube reconnected with **1**. Electrical measurements were made before cutting (black curve), after cutting with an oxygen plasma (red curve), and after connection (green curve). (**B**) Drain current (I_D) as a function of source-drain voltage (V_{SD}) with no gate bias. (**C**) Drain current in the device as a function of the gate voltage (V_g) at V_{SD} = 50 mV for a semiconducting SWNT connected with **1**. Colors are as described in (A).

Table 1. SWNT device properties before cutting and after molecular connection.

Before cutting		After molecular connection		
Tube type	R^* (megohm)	Molecule	R^* (megohm)	Molecular conductance (e^2/h)
Metallic	1.0	**1**	5.0	6.4×10^{-3}
Semiconducting	3.6	**1**	10.0	4.0×10^{-3}
Semiconducting	1.1	**2**	5.0	6.6×10^{-3}
Metallic	0.2	**3**	0.6	6.4×10^{-2}
Semiconducting	0.6	**3**	125	2.0×10^{-4}
Semiconducting	1.3	**4**	50.0	5.2×10^{-4}

*R is the total resistance for the device. For the semiconducting tubes this refers to ON-state resistance with V_{SD} = 50 mV.

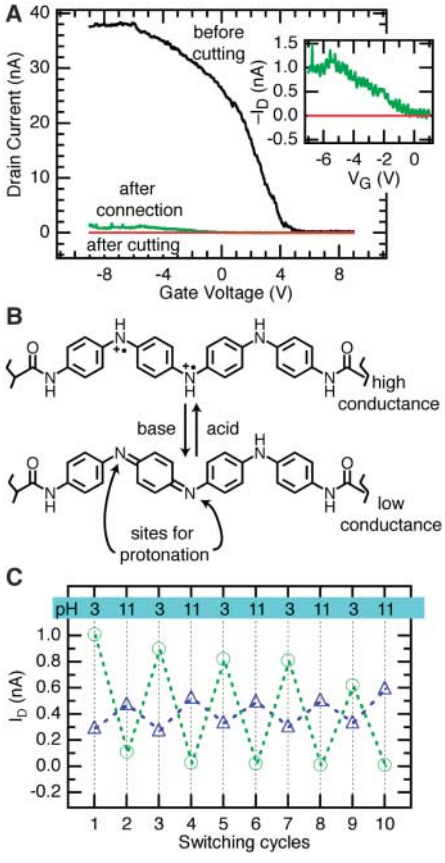

Fig. 4. Oligoaniline **4** connected to SWNT electrodes. (**A**) Drain current (I_D) in the device as a function of the gate voltage (V_g) at V_{SD} = 50 mV for a semiconducting tube connected with **4**. Electrical measurements were made before cutting (black curve), after cutting with oxygen plasma (red curve), and after connection (green curve). Inset is a magnified *y* scale showing the *I-V* curves after cutting and connection. (**B**) Protonation and deprotonation to give high- and low-conductance forms of oligoaniline **4**. (**C**) Green circles show the ON-state resistance for **4** when alternately immersed in solutions of low and high pH. The blue triangles show small changes in ON-state resistance for **2** when alternately immersed in solutions of low and high pH.

and features that gradually broaden and eventually disappear with increasing temperature (*30*). Being able to match the electronic levels of the molecule to a nanotube of a specific diameter and chirality, in principle, offers the opportunity to optimize the conductance. One factor that hampers our ability to extract more quantitative information is that these values vary for any given molecule. Variations in the conformation of the molecules on the substrate within the SWNT gap, the possibility of a second molecular bridge, and the lack of atomic-level precision in the cutting procedure are challenges for future studies to overcome.

Control experiments were performed to rule out artifacts from the connection reaction. Gaps placed in a pyridine solution of the coupling agent without the conjugated diamines did not show any connected devices. Furthermore, when we immersed these same gaps in a solution that contains the cruciform diamine (**1**) along with an aliquot of fresh coupling reagent, some of the devices then became connected. In another experiment, we used 1,12-diaminododecane because it is about the same length as the cruciform molecule but lacks the conjugated backbone. Again, all of the devices showed no detectable current and remained so when a conjugated diamine was added, presumably because the carboxylic acid sites were blocked by the alkyl amine. To determine if molecular aggregates were responsible for the conduction, we tested a monoamine of the cruciform or a cruciform that completely lacked the amine groups, and only open circuits resulted. All of these control experiments were performed on ~50 devices in order to yield a statistically significant null result.

The covalent linkages are quite robust and tolerate broad changes in environment, and we explored how these devices responded to external stimuli such as changes in temperature and pH. The response to changes in pH for the oligoaniline diamine **4** is shown in Fig. 4. The electrical characteristics for this device before cutting, after cutting, and after joining with the oligoaniline diamine are similar to those detailed for **1** to **3**. We expected that the oligoaniline would be oxidized to the emeraldine form (shown in Fig. 2) during the reaction and become pH sensitive, because the protonated form is more conductive (Fig. 4B) (*31*). We performed a series of protonations (pH = 3) and deprotonations (pH = 11) while monitoring the current changes at saturation for devices that were rinsed, dried, and tested. The molecular conductance changed by nearly an order of magnitude, from ~5.2×10^{-4} e^2/h at low pH to ~5.0×10^{-5} e^2/h at high pH over many switching cycles (Fig. 4C). These devices provide a local probe for monitoring pH on the basis of one or only a few molecules.

We also performed the same experiment on devices connected with **2**, which lacks basic nitrogens and thus should not switch with pH. The blue trace in Fig. 4C shows that the conductance of **2** changed only slightly with pH, and the change was in the opposite direction to that for the device connected with the pH- and redox-active oligoaniline **4**. Another possible cause of the pH switching in the oligoaniline devices could be charge transfer from a polyaniline that was attached but not necessarily spanning the SWNT gap (*32*). Amines (*16*), particularly polyanilines (*32*), can associate with the SWNT surface and might cause pH sensitivity that is unrelated to molecular conduction. We therefore immersed an uncut device in a solution of the polyaniline diamine (**4**) (*24*). The relative change upon protonation/deprotonation was small for these devices and in the opposite direction to that for the device connected with oligoaniline (fig. S6).

In conclusion, we present experiments that overcome the difficulty of creating covalent contact to individual molecules and reveal a way to harness the diversity and functionality inherent to molecules in electrical devices. In addition to their potential use as molecules in circuits, sensors, and switches, these devices promise a deeper understanding of electron transfer at the molecular scale.

References and Notes

1. M. A. Reed, C. Zhou, C. J. Muller, T. P. Burgin, J. M. Tour, *Science* **278**, 252 (1997).
2. A. Salomon *et al.*, *Adv. Mater.* **15**, 1881 (2003).
3. J. Chen, M. A. Reed, A. M. Rawlett, J. M. Tour, *Science* **286**, 1550 (1999).
4. X. D. Cui *et al.*, *Science* **294**, 571 (2001).
5. M. Mayor *et al.*, *Angew. Chem. Int. Ed.* **42**, 5834 (2003).
6. M. Mayor, H. B. Weber, *Angew. Chem. Int. Ed.* **43**, 2882 (2004).
7. J. Park *et al.*, *Nature* **417**, 722 (2002).
8. N. B. Zhitenev, A. Erbe, Z. Bao, *Phys. Rev. Lett.* **92**, 186805 (2004).
9. G. K. Ramachandran *et al.*, *Science* **300**, 1413 (2003).
10. H. Basch, R. Cohen, M. A. Ratner, *Nano Lett.* **5**, 1668 (2005).
11. G. S. Tulevski, M. B. Myers, M. S. Hybertsen, M. L. Steigerwald, C. Nuckolls, *Science* **309**, 591 (2005).
12. M. Siaj, P. H. McBreen, *Science* **309**, 588 (2005).
13. P. Qi *et al.*, *J. Am. Chem. Soc.* **126**, 11774 (2004).
14. K. Tsukagoshi, I. Yagi, Y. Aoyagi, *Appl. Phys. Lett.* **85**, 1021 (2004).
15. J. Appenzeller, J. Knoch, M. Radosavljevic, P. Avouris, *Phys. Rev. Lett.* **92**, 226802 (2004).
16. H. Dai, *Acc. Chem. Res.* **35**, 1035 (2002).
17. S. J. Tans, A. R. M. Verschueren, C. Dekker, *Nature* **393**, 49 (1998).
18. S. Niyogi *et al.*, *Acc. Chem. Res.* **35**, 1105 (2002).
19. P. W. Chiu, M. Kaempgen, S. Roth, *Phys. Rev. Lett.* **92**, 246802 (2004).
20. U. Dettlaff-Weglikowska *et al.*, *Curr. Appl. Phys.* **2**, 497 (2002).
21. E. Artukovic, M. Kaempgen, D. S. Hecht, S. Roth, G. Gruner, *Nano Lett.* **5**, 757 (2005).
22. A. A. Houck, J. Labaziewicz, E. K. Chan, J. A. Folk, I. L. Chuang, *Nano Lett.* **5**, 1685 (2005).
23. L. Huang, X. Cui, B. White, S. P. O'Brien, *J. Phys. Chem. B* **108**, 16451 (2004).
24. Experimental details on SWNT device fabrication, electron beam lithography, and oxidative cutting can be found in

the Supporting Online Material, along with low-temperature current-voltage curves and experimental details for the synthesis and reactions of **2** to **4.**
25. K. J. Ziegler *et al.*, *Nanotechnology* **16**, S539 (2005).
26. Z. Gu, H. Peng, R. H. Hauge, R. E. Smalley, J. L. Margrave, *Nano Lett.* **2**, 1009 (2002).
27. A. Williams, I. T. Ibrahim, *Chem. Rev.* **81**, 589 (1981).
28. J. E. Klare, G. S. Tulevski, C. Nuckolls, *Langmuir* **20**, 10068 (2004).
29. Details for the preparation of **2** to **4** can be found in the Supporting Online Material.
30. It is also noted that at low temperature the differential conductance, dI/dV_{DS}, develops a series of peaks as V_{DS} changes. The position of these peaks shifts as a function of the applied gate voltage. As an example, the low-temperature I-V_{DS} and dI/dV_{DS} curves for **1** are shown in the Supporting Online Material.
31. A. G. MacDiarmid, *Angew. Chem. Int. Ed.* **40**, 2581 (2001).
32. C. Klinke, J. Chen, A. Afzali, P. Avouris, *Nano Lett.* **5**, 555 (2005).
33. We are grateful to H. Stormer for enlightening discussions. We acknowledge primary financial support from the Academic Quality Fund (Columbia University), the Nanoscale Science and Engineering Initiative under NSF Award Number CHE-0117752, and the New York State Office of Science, Technology, and Academic Research (NYSTAR). C.N. thanks the American Chemical Society Petroleum Research Fund Type G (grant 39263-G7), the Camille Dreyfus Teacher Scholar Program (2004), and the Alfred P. Sloan Fellowship Program (2004). P.K. thanks the NSF CAREER (DMR-0349232) and Defense Advanced Research Projects Agency (N00014-04-1-0591). J.E.K. thanks the American Chemical Society Division of Organic Chemistry sponsored by Organic Syntheses for a fellowship. I.W.T. thanks the NSF for a predoctoral fellowship.

Supporting Online Material
www.sciencemag.org/cgi/content/full/311/5759/356/DC1
Materials and Methods
Figs. S1 to S6
References and Notes

5 October 2005; accepted 15 December 2005
10.1126/science.1120986

Real-Space Observation of Helical Spin Order

Masaya Uchida,[1]* Yoshinori Onose,[1]† Yoshio Matsui,[2] Yoshinori Tokura[1,3,4]

Helical spin order in magnetic materials has been investigated only in reciprocal space. We visualized the helical spin order and dynamics in a metal silicide in real space by means of Lorentz electron microscopy. The real space of the helical spin order proves to be much richer than that expected from the averaged structure; it exhibits a variety of magnetic defects similar to atomic dislocations in the crystal lattice. The application of magnetic fields allows us to directly observe the deformation processes of the helical spin order accompanied by nucleation, movement, and annihilation of the magnetic defects.

Magnetic materials are generally characterized by spin moments on respective atomic sites aligned all parallel or site-alternately antiparallel. However, many exceptions to this rule exist in which the direction of spin moments varies in space. A prototypical example is the gradual moment variation (Bloch type or Néel type) within the magnetic domain wall region in a ferromagnet (*1*) or the somewhat long-period (over several atomic sites) spin density wave as observed in Cr metal (*2*). The helical spin order (Fig. 1A) is another such example: Spins on some crystallographic planes are all parallel, but their direction rotates by a constant angle in going from one plane to a neighboring plane along the helical axis. The helical spin order was first proposed as a way to interpret neutron diffraction results for MnO_2 crystal (*3*). Similar helical spin orders have been observed in materials such as rare-earth metals and alloys (*4*) as well as members of the metal silicide family, including MnSi (*5*, *6*) and $Fe_{1-x}Co_xSi$ ($0.05 \leq x \leq 0.8$) (*7*, *8*).

The relative orientation of spin moments between magnetic planes affects the flow of electric current. The control of the spin-dependent charge transport in terms of the manipulation of the local magnetic structure forms the basis of spin-electronics or spintronics (*9*–*12*), as exemplified by the magnetoresistive field sensor in computer hard disks and the magnetic tunneling junction in magnetic random access memory (MRAM). In this context, the helical spin order can be viewed as a regular array of the magnetic domain walls every helical period. Therefore, the real-space observation of the local modification or deformation of the helical order (as induced by temperature change, magnetic field, and current injection) would provide a challenging arena to study the nanometric magnetic domain structure as well as to explore the possible spintronic application of such a self-organized magnetic nanostructure.

The family of $Fe_{1-x}Co_xSi$ with cubic but noncentrosymmetric ($B20$) structure is known to exhibit a helical spin order, with a relatively long period (>30 nm) in a concentration range $0.05 \leq x \leq 0.8$ (*7*, *8*, *11*). The helical spin order is due to the Dzyalosinsky-Moriya (DM) interaction because of the lack of centrosymmetry of the lattice (*13*–*16*). The helix period is governed by the ratio of the DM interaction to the ferromagnetic spin exchange interaction (*15*, *16*). The Néel temperature T_N and the helix period for the $x = 0.5$ crystal we investigated here are 38 K and 90 nm along the [100] direction, respectively.

Figure 2 shows a typical image of the helical spin order of $Fe_{0.5}Co_{0.5}Si$ as obtained by Lorentz transmission electron microscopy (*17*). Shown in Fig. 2, A and B, are overfocused Lorentz images taken near the [001] zone axis orientation at 40 and 20 K, respectively. The image at 20 K ($< T_N$) clearly shows periodic stripe patterns running normal to the [100] axis. In the focused image the patterns disappeared, confirming that the image is magnetic in origin. The magnetization distribution obtained by the transport of intensity equation (TIE) analysis (*18*, *19*) of the over- and underfocused images is shown in Fig. 2C. The direction and amplitude of the magnetization are represented by changes in color and brightness, respectively. The green and violet stripe pairs in the figure reflect the regions with opposite magnetic orientation; the darker area indicates the smaller amplitude of the local magnetization. The sinusoidal modulation in Fig. 2D (a profile of the amplitude of the magnetization along the line indicated in Fig. 2C) indicates that the spin order is helical, with a period of 90 nm along [100], in good agreement with the results determined by neutron diffraction (*7*, *8*).

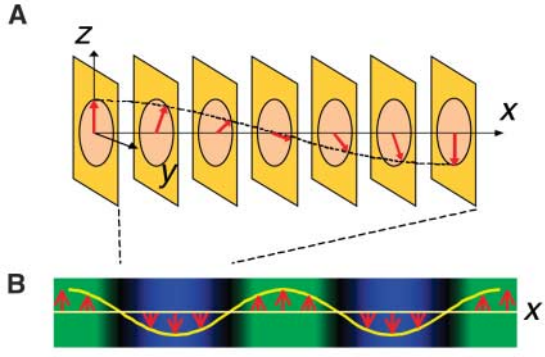

Fig. 1. Illustration of helical spin order. (**A**) Helical spin order with the helical axis along the *x* axis in an orthogonal *xyz* system. Spins are all parallel at a *yz* plane, and their direction rotates by a constant angle from one plane to a neighboring plane along the helical axis. (**B**) Magnetization distribution projected on the *xy* plane for this helical spin order, which changes as a sinusoidal wave.

[1]Spin SuperStructure Project, Exploratory Research for Advanced Technology (ERATO), Japan Science and Technology Agency (JST), Tsukuba 305-8562, Japan. [2]Advanced Materials Laboratory, National Institute for Materials Science (NIMS), Tsukuba 305-0044, Japan. [3]Correlated Electron Research Center (CERC), National Institute of Advanced Industrial Science and Technology (AIST), Tsukuba 305-8562, Japan. [4]Department of Applied Physics, University of Tokyo, Tokyo 113-8656, Japan.

*To whom correspondence should be addressed. E-mail: uchida.masaya@aist.go.jp
†Present address: Department of Physics, Princeton University, Princeton, NJ 08543, USA.

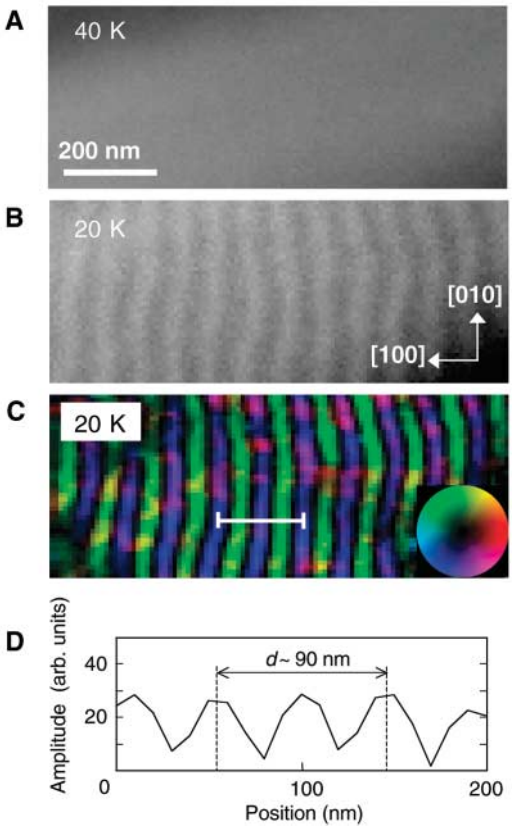

Fig. 2. Real-space observation of the helical spin order in $Fe_{0.5}Co_{0.5}Si$. (**A** and **B**) Overfocused Lorentz images (defocus length +1.4 mm) obtained at 40 and 20 K, respectively. Electron incidence is nearly parallel to the [001] direction. Stripe contrasts seen in (B) are of magnetic origin. (**C**) A color representation of magnetization distribution [projected onto the (001) plane] obtained by the TIE method, corresponding to the state shown in (B); the direction and amplitude of the magnetization are represented by changes in color and brightness with respect to the color wheel. (**D**) Amplitude profile of the magnetization along the line shown in (C). The sinusoidal modulation indicates that the spin order is helical with a period of 90 nm along [100].

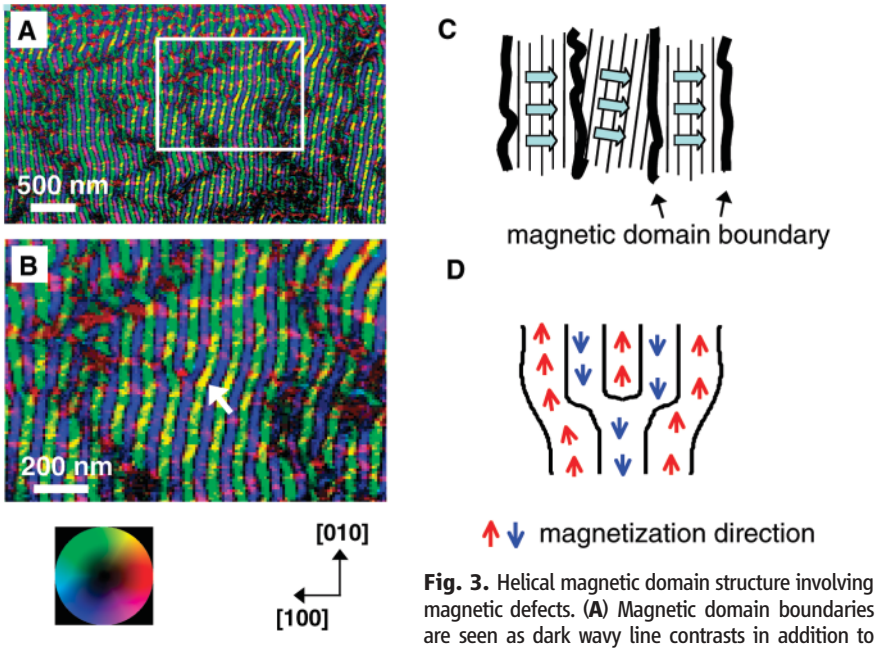

Fig. 3. Helical magnetic domain structure involving magnetic defects. (**A**) Magnetic domain boundaries are seen as dark wavy line contrasts in addition to the regular helical spin order. The image colors have the same meaning as in Fig. 2C. (**B**) Magnified image of the boxed part in (A), exhibiting a helical magnetic edge dislocation (arrow). (**C**) A schematic showing the helical magnetic domain and boundary. The fine and thick lines represent the regular helical spin order and the magnetic domain boundary, respectively. Note that the orientation of the helical axis (denoted by arrows) varies slightly from domain to domain through a boundary. (**D**) A schematic showing the magnetic edge dislocation.

The real-space observation has, however, revealed the existence of defects of this periodic magnetic state, analogous to atomic boundary and dislocation in a crystalline lattice (*1*, *20*). Figure 3 shows a low-magnification image of the magnetization distribution (*17*). An electron diffraction study confirmed that the observed area is a single crystallographic domain. The spin stripes are almost straight but are locally and slightly bent. In addition to the spin stripes, wavy dark line contrasts can be seen, nearly perpendicular to the helical axis. Careful observation shows that the spin stripes can be seen even inside the dark-contrast regions (Fig. 3B). The dark contrasts indicate the region where the helical spin order is less regular. Here, we define the helical magnetic "domain" as the region in which the periodic order of spins with the well-defined helical axis direction shows up apart from the presence of topological defects. Therefore, we may call the dark-contrast region a helical magnetic domain boundary.

The helical magnetic domain boundary is not straight but wavy and diffuse. The width between two neighboring boundaries (domain size) is hundreds of nanometers along the [100] direction. The domain structures are found to vary in shape and size after the sample is heated above T_N and then cooled to the original temperature (20 K); they are also sensitive to magnetic fields, as shown below. Most of the neighboring domains are substantially characterized by the slight misorientation of the helical axis, not by a change of the helix period (Fig. 3C).

Another interesting feature is the existence of topological magnetic defects. A branching of the spin stripe (Fig. 3, B and D) looks just like an edge dislocation in crystal, whose geometry is described by an extra atomic half-plane inserted into the lattice (*1*). What we have observed in this magnetic system is the elementary edge dislocation whose Burgers vector **b**, defined as the plane difference, is $(\pm\frac{1}{2})d$ parallel to [100] (where d is a helix period). Many edge dislocations appear to gather around the domain boundaries and to connect the spin stripe smoothly across a boundary.

Our results raise questions about the origin and role of helical magnetic defects. In all ferromagnets, domain structure is inherent because domains form to reduce the magnetostatic energy (*1*, *21*). This is not the case for the present helical magnet as well as for antiferromagnets (*22*, *23*). However, helical magnetic domain boundaries are wavy and diffuse, and they mainly run normal to the helical axis, invalidating the magnetostatic mechanism. Furthermore, whenever the sample was cooled through the Néel temperature, the experiment showed similar images, but the dislocations and the domain boundaries did not always appear at the same locations in the sample. Thus, magnetic defects are not strongly pinned by atomic defects or by strain.

It is known that atomic defects such as boundary and dislocation play a crucial role in mechanical deformation (*1*, *20*). For example, as materials deform under increasing stress, dislocations are generated, which in turn affect the deformation properties. By analogy, the magnetic defects may play some role in the deformation of the helical spin order. We therefore investigated the deformation dynamics of the helical spin order by applying magnetic fields. The sample

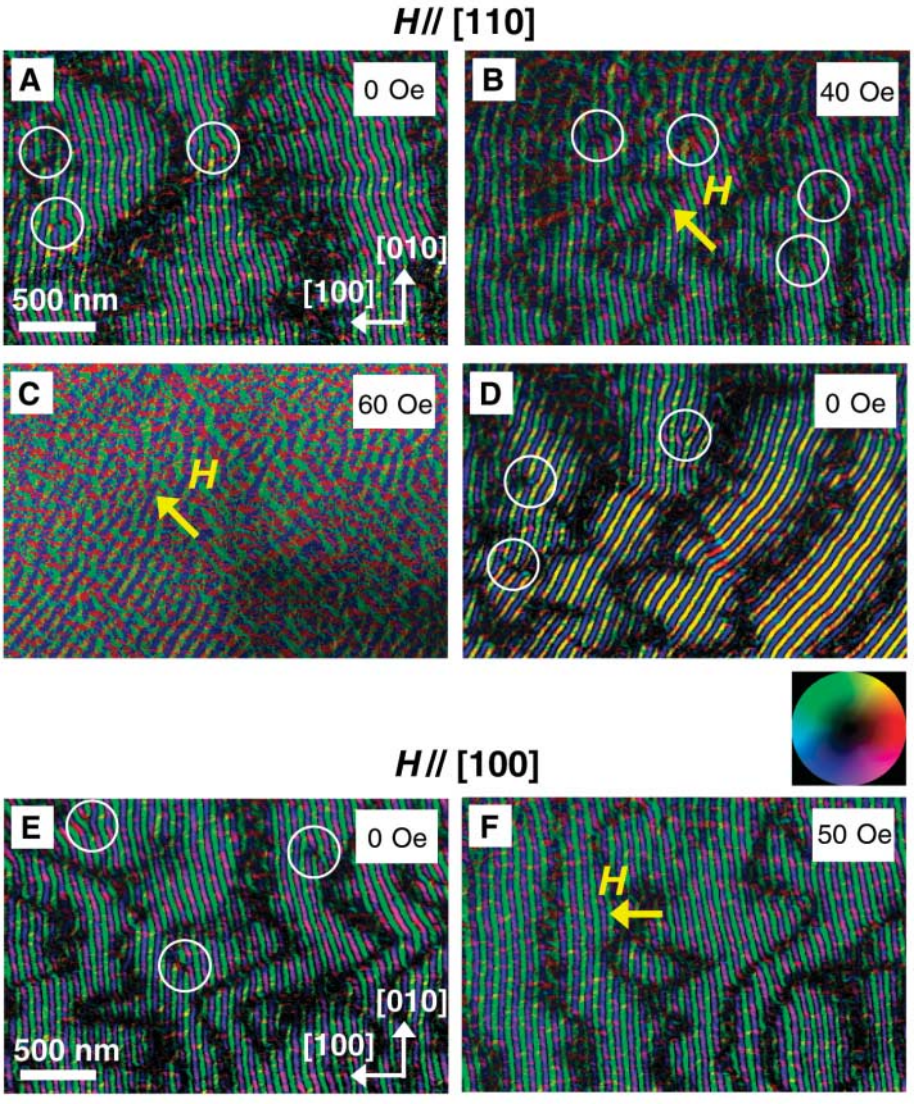

Fig. 4. Helical magnetic domain structure modified by applying magnetic field along the [110] or the [100] direction at 20 K. (**A**) Helical domain structure of the sample cooled to 20 K under the zero magnetic field. Electron incidence is nearly parallel to the [001] direction. (**B**) When the applied field *H* is 40 Oe, new magnetic domain boundaries and dislocations are nucleated. (**C**) With 60 Oe, the spin stripe rotates along the direction of the magnetic field [110]. The noisy image is due to a large image distortion by magnetic field. (**D**) Upon decreasing the field to zero, some domains remain with the helical axis along [110]. This transformation is irreversible with magnetic fields. (**E**) The same area as in (A). Note that the domain structures in (A) and (E) are different because of the different thermal history. (**F**) When magnetic field is applied along the [100] direction, the helical magnetic domains grow in size while edge dislocations diminish in number. The image colors have the same meaning as in Fig. 2C. Some magnetic edge dislocations are marked by open circles.

was first cooled to 20 K and magnetic field *H* was then gradually increased along either the [110] or the [100] axis. Figure 4 shows the changes of helical magnetic domains of the same sample. In the case of *H* // [110] (Fig. 4, A to D), the helical spin order is easily deformed to contain more magnetic defects. Even with small fields (<10 Oe), some magnetic domain boundaries and dislocations are observed to move. When the magnetic field is increased (Fig. 4B), new domain boundaries and dislocations are nucleated. The domain boundaries become more bent. The nucleation of the edge dislocations is possibly due to the tendency for the spin stripes to remain equidistant. With $H \sim 50$ Oe, the helical axes locally begin to rotate from [100] to the magnetic field direction [110]. Upon further increasing *H* to 60 Oe, the spin stripes are almost rotated so that the helical axis is along the direction of *H* (Fig. 4C), although the image becomes noisy because of the presence of *H*. Upon decreasing the magnetic field to zero (Fig. 4D), some of the domains come back to the [100] axis while others remain with the [110] axis, resulting in the irreversible formation of magnetic domains. Note that magnetic fields do not alter the helix period. Such a change of the helical magnetic domains as induced by magnetic fields has been reported in neutron diffraction studies of MnSi (*5*) and FeGe (*24*). We have also made a "real-time" observation of the deformation with temperature under magnetic fields (*25*). When magnetic field is applied along the helical axis [100] (Fig. 4F), the helical magnetic domains grow in size, accompanying the annihilation of the magnetic defects. As a result, the spin stripes as well as the domain boundaries become regular and straight, in a manner analogous to the annealing process in crystal growth. Thus, the deformation of the helical magnetic domain is characterized by nucleation, movement, and annihilation of the magnetic defects.

Our real-space observations of $Fe_{0.5}Co_{0.5}Si$ have revealed the unexpected existence of magnetic defects such as magnetic domain boundary and dislocation. In addition, by applying magnetic fields, we have observed the field direction–dependent change of the magnetic domains, in which the magnetic defects mediate the nanometer-scale modification of the magnetic structure.

References and Notes

1. C. Kittel, *Introduction to Solid State Physics* (Wiley, New York, 1995).
2. E. Fawcett, *Rev. Mod. Phys.* **60**, 209 (1988).
3. A. Yoshimori, *J. Phys. Soc. Jpn.* **14**, 807 (1959).
4. T. Nagamiya, *Solid State Physics* (Academic Press, New York, 1967).
5. Y. Ishikawa, K. Tajima, D. Bloch, M. Roth, *Solid State Commun.* **19**, 525 (1976).
6. G. Shirane *et al.*, *Phys. Rev. B* **28**, 6251 (1983).
7. J. Beille, J. Voiron, M. Roth, *Solid State Commun.* **47**, 399 (1983).
8. K. Ishimoto *et al.*, *Physica B* **213–214**, 381 (1995).
9. I. Zutic, J. Fabian, S. Das Sarma, *Rev. Mod. Phys.* **76**, 323 (2004).
10. S. A. Wolf *et al.*, *Science* **294**, 1488 (2001).
11. N. Manyala *et al.*, *Nature* **404**, 581 (2000).
12. C. Pfleiderer *et al.*, *Nature* **427**, 227 (2004).
13. I. Dzyaloshinskii, *J. Phys. Chem. Solids* **4**, 241 (1958).
14. T. Moriya, *Phys. Rev.* **120**, 91 (1960).
15. P. Bak, M. H. Jensen, *J. Phys. C* **13**, L881 (1980).
16. O. Nakanishi, A. Yanase, A. Hasegawa, M. Kataoka, *Solid State Commun.* **35**, 995 (1980).
17. See supporting material on *Science* Online.
18. S. Bajt *et al.*, *Ultramicroscopy* **83**, 67 (2000).
19. M. Uchida *et al.*, *Appl. Phys. Lett.* **86**, 131913 (2005).
20. P. Chaikin, T. Lubensky, *Principles of Condensed Matter Physics* (Cambridge Univ. Press, New York, 1995).
21. A. Hubert, R. Schäfer, *Magnetic Domains* (Springer, New York, 1998).
22. Y. Y. Li, *Phys. Rev.* **101**, 1450 (1956).
23. M. Fiebig, D. Fröhlich, S. Leute, R. V. Pisarev, *J. Appl. Phys.* **83**, 6560 (1998).
24. B. Lebech, J. Bernhard, T. Freltoft, *J. Phys. Condens. Matter* **1**, 6105 (1989).
25. M. Uchida, unpublished data.

26. Supported in part by the Nanotechnology Support Project of the Ministry of Education, Culture, Sports, Science and Technology, Japan.

Supporting Online Material

www.sciencemag.org/cgi/content/full/311/5759/359/DC1
Materials and Methods
Fig. S1

27 September 2005; accepted 1 December 2005
10.1126/science.1120639

Solvent-Free Oxidation of Primary Alcohols to Aldehydes Using Au-Pd/TiO_2 Catalysts

Dan I. Enache,[1] Jennifer K. Edwards,[1] Philip Landon,[1] Benjamin Solsona-Espriu,[1] Albert F. Carley,[1] Andrew A. Herzing,[2] Masashi Watanabe,[2] Christopher J. Kiely,[2] David W. Knight,[1] Graham J. Hutchings[1]*

The oxidation of alcohols to aldehydes with O_2 in place of stoichiometric oxygen donors is a crucial process for the synthesis of fine chemicals. However, the catalysts that have been identified so far are relatively inactive with primary alkyl alcohols. We showed that Au/Pd-TiO_2 catalysts give very high turnover frequencies (up to 270,000 turnovers per hour) for the oxidation of alcohols, including primary alkyl alcohols. The addition of Au to Pd nanocrystals improved the overall selectivity and, using scanning transmission electron microscopy combined with x-ray photoelectron spectroscopy, we showed that the Au-Pd nanocrystals were made up of a Au-rich core with a Pd-rich shell, indicating that the Au electronically influences the catalytic properties of Pd.

Selective oxidation is important in the synthesis of fine chemicals and intermediates (*1*); and, in particular, the oxidation of primary alcohols to aldehydes is a fundamentally important laboratory and commercial procedure (*1*–*8*). Aldehydes are valuable both as intermediates and as high-value components for the perfume industry (*1*, *9*, *10*). Many oxidations of this type are carried out using stoichiometric oxygen donors such as chromate or permanganate, but these reagents are expensive and have serious toxicity issues associated with them (*1*, *9*, *11*–*14*). In many cases, aldehydes are obtained only from activated alcohols in which the carbon bears a phenyl group, such as benzyl alcohol (*7*, *8*). Sheldon and co-workers (*3*) have obtained good yields from a biphasic system for the catalytic conversion of pentan-1-ol to the aldehyde, but the acid is produced in the case of hexan-1-ol. Given these limitations, there is substantial interest in the development of heterogeneous catalysts that use either O_2 or H_2O_2 as the oxidant (*15*). Au nanocrystals have been shown to be highly effective for the oxidation of alcohols with O_2 in an aqueous base, in particular diols and triols; but under these conditions, the product is the corresponding monoacid, not the aldehyde (*16*–*19*). Gold catalysts have, however, been found to be effective for the gas-phase oxidation of volatile alcohols to the corresponding aldehydes and ketones (*20*).

Most recently, two studies have shown that supported metal nanoparticles can be very effective catalysts for the oxidation of alcohols to aldehydes, using O_2 under relatively mild conditions. Kaneda and co-workers (*6*) found that hydroxyapatite-supported Pd nanoclusters (Pd/HAP) give very high turnover frequencies (TOFs) for the oxidation of phenylethanol and benzyl alcohol but show limited activity for the oxidation of primary alkyl alcohols (such as octan-1-ol oxidation). Corma and co-workers (*21*) have shown that the addition of Au nanocrystals to CeO_2 converts the oxide from a stoichiometric oxidant to a catalytic system, with TOFs similar to those obtained by Kaneda and co-workers (*6*).

Recently, we have shown that supported Au-Pd alloys are efficient catalysts for the direct synthesis of H_2O_2 from H_2 oxidation by O_2 at low temperatures (*22*–*25*). In particular, Au-Pd/TiO_2 catalysts were very selective for H_2O_2 synthesis. Hydroperoxy species are considered to be involved in this H_2O_2 formation process, and because hydroperoxy species are key reagents/intermediates in the oxidation of alcohols (*1*), we reasoned that these catalysts should also be effective for the oxidation of alcohols. We showed that TiO_2-supported Au-Pd alloy nanocrystals give significantly enhanced activity for alcohol oxidation using a green chemistry approach with O_2 under mild solvent-free conditions. When compared with monometallic supported Au (*21*) and Pd (*6*), the Au-Pd catalysts nanocrystals give TOFs that are enhanced by a factor of ~25.

The TiO_2-supported Au-Pd catalysts were initially investigated for the oxidation of benzyl alcohol at 373 K with O_2 as oxidant in the absence of solvent (Fig. 1A). The Au-Pd/TiO_2 catalysts were very active for this reaction, and the selectivity to benzaldehyde was ≥96%, with the only byproduct being benzyl benzoate. In contrast, Pd/TiO_2 also produced toluene and benzene as byproducts, and a Au/TiO_2 catalyst produced a significant amount of an acetal product. The selectivity of the Au/TiO_2 catalyst for benzaldehyde decreased with the time on line, but further oxidation of the acetal byproduct led to an increase of the final selectivity in benzaldehyde. Carbon mass balances were 100%, and no carbon oxides were formed for Au-Pd/TiO_2 or Au/TiO_2 catalysts.

The effect of adding Au to a Pd/TiO_2 catalyst is apparent in these initial studies. Al-

[1]School of Chemistry, Cardiff University, Main Building, Park Place, Cardiff, UK CF10 3AT. [2]Center for Advanced Materials and Nanotechnology, Lehigh University, 5 East Packer Avenue, Bethlehem, PA 18015–3195, USA.

*To whom correspondence should be addressed. E-mail: hutch@cf.ac.uk

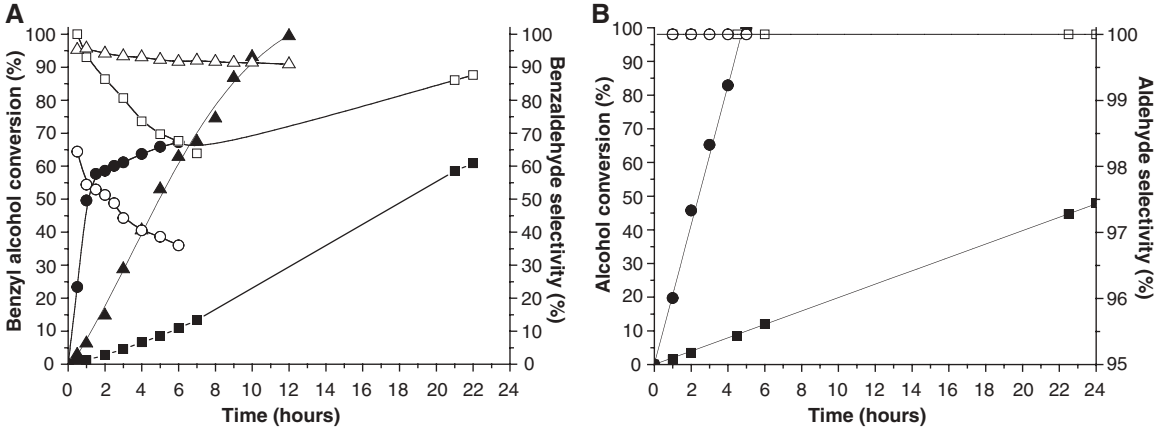

Fig. 1. (**A**) Benzyl alcohol conversion and selectivity in benzaldehyde with the reaction time at 373 K and 0.1 MPa pO_2. Squares, Au/TiO_2; circles, Pd/TiO_2; and triangles, Au-Pd/TiO_2. Solid symbols indicate conversion, and open symbols indicate selectivity. (**B**) Au-Pd/TiO_2 catalyzed reactions at 363 K, 0.1 MPa pO_2, for cinnamyl alcohol (squares) and vanillyl alcohol (circles). Solid symbols indicate conversion, and open symbols indicate selectivity to the corresponding aldehydes.

though the Pd/TiO_2 catalyst has a high initial activity, and the addition of Au decreases the activity, the $Au-Pd/TiO_2$ catalyst retained high selectivity to benzaldehyde at high conversion rates, a feature not observed with the supported pure-Au and pure-Pd catalysts. One of the key factors that must be considered for heterogeneous catalysts operating in three-phase systems is the possibility that active components can leach into the reaction mixture, thereby leading to catalyst deactivation or, in the worst case, to the formation of an active homogeneous catalyst. We have found that the catalysts calcined at 673 K are stable and do not leach Au or Pd into solution, a feature we have previously also observed in our studies on hydrogen peroxide synthesis (*24*, *25*) (see supporting online material).

Because Al_2O_3 and Fe_2O_3 were also effective supports for the formation of H_2O_2 with Au-Pd nanocrystals, these catalysts were also investigated, but the TiO_2-supported Au-Pd catalysts are preferred for the oxidation of benzyl alcohol (Table 1); it is likely that the more acidic nature of the Al_2O_3 and Fe_2O_3 supports led to enhanced byproduct formation.

The $Au-Pd/TiO_2$ catalysts were investigated with a range of substrates and conditions (Table 2). In the initial experiments conducted at 373 K (Table 2, entries 1 to 3), relatively high catalyst loadings were used, but selectivities >90% could still be achieved for the oxidation of benzyl alcohol to benzaldehyde. Subsequent experiments used much lower metal concentrations, and the effect of the pressure of O_2 (pO_2) (Table 2, entries 4 to 7) showed that the reaction was of zero order in O_2. The selectivity to the aldehydes increased with pO_2 [for conversions of benzyl alcohol, >70%, the selectivity to the aldehyde increased from 71% at low pO_2 (Table 2, entry 4) to 86% at the higher pO_2 (Table 2, entry 6)] and metal concentration, but selectivities of >80% were achieved readily under most conditions. These initial experiments were conducted in a closed autoclave with O_2 at a constant reaction pressure, so that as the reaction proceeded and O_2 was consumed, this oxygen was replenished. We have used air in place of O_2 and have obtained the same initial TOFs, which demonstrates that in principle, air can be used for industrial applications. Increasing the temperature (Table 2, entries 4 and 8 to 10) increased the rate as expected (with activation energy E_A = 45.8 kJ/mol), but the selectivity decreased to ~60% at 433 K, and the byproducts included benzylbenzoate and toluene under these more forcing conditions. The $Au-Pd/TiO_2$ catalysts were very active, and the best performance (Fig. 1A) was achieved at lower temperatures (≤373 K), higher pO_2 (0.2 to 1.0 MPa), and higher catalyst loadings, but we stress that we have

Table 1. Comparative data for benzyl alcohol oxidation and hydrogen peroxide synthesis. Results were obtained for the oxidation of benzyl alcohol after 0.5 hour and 8 hours of reaction and for H_2O_2 synthesis for 0.5 hour. The oxidation of benzyl alcohol was carried out at 373 K temperature, 0.2 MPa pO_2, and 1500 rpm stirrer speed. The H_2O_2 synthesis was carried out under the conditions described in (*26*, *27*). Productivities are quoted in units of moles of product per hour per kilogram of catalyst.

Catalyst	Benzyl alcohol oxidation					H_2O_2 productivity [mol/(hour/kg_{cat})]
	Conversion (%)		Benzaldehyde selectivity (%)		Benzaldehyde productivity* [mol/(hour/kg_{cat})]	
	0.5 hour	8 hours	0.5 hour	8 hours		
2.5% Au–2.5% Pd/Al_2O_3	2.6	83.3	90.5	86.6	174	23
2.5% Au–2.5% Pd/TiO_2	3.7	74.5	95.2	91.6	165	64
2.5% Au–2.5% Pd/SiO_2	3.6	35.7	97.3	88.0	76	80
2.5% Au–2.5% Pd/Fe_2O_3	3.6	63.4	74.9	66.4	102	16
2.5% Au–2.5% Pd/C	2.9	69.2	53.9	46.4	78	30
2.5% Au/TiO_2	0.6	15.3	96.7	63.9	24	<2
2.5% Pd/TiO_2	13.4	60.1	51.3	54.4	79	24

*Calculated for 8 hours of reaction.

Table 2. Comparison of the catalytic activity for alcohol oxidation to the corresponding aldehyde. Catalyst is 2.5% Au–2.5% Pd/TiO_2 unless noted otherwise; substrates oxidized without solvent unless specified; catalyst mass varied to give the metal concentrations indicated; and TOF was measured after first 0.5 hour of reaction. *T*, temperature.

Entry	Alcohol	Reaction conditions		[Metal] (10^{-5} mol/liter)		TOF (/hour)
		T (K)	*P* (10^5 Pa)	Au	Pd	
1	Benzyl alcohol	373	2	63.5	118	607
2	Benzyl alcohol*	373	2	63.5	0	213
3	Benzyl alcohol†	373	2	0	118	2,200
4	Benzyl alcohol	373	1	2.1	3.9	6,190
5	Benzyl alcohol	373	2	2.1	3.9	6,440
6	Benzyl alcohol	373	5	2.1	3.9	6,190
7	Benzyl alcohol	373	10	2.1	3.9	5,950
8	Benzyl alcohol	383	1	2.1	3.9	14,270
9	Benzyl alcohol	393	1	2.1	3.9	26,400
10	Benzyl alcohol	433	1	2.1	3.9	86,500
11	1-Phenylethanol	433	1	1.8	3.2	269,000
12	3-Phenyl-1-propanol	433	1	2.1	3.9	2,356
13	Vanillyl alcohol‡	363	1	21.6	40.6	10
14	Cinnamyl alcohol§	363	1	21.6	40.6	97
15	Octan-1-ol	433	1	2.5	4.7	2,000
16	Octan-2-ol	433	1	2.5	4.7	0
17	Octan-2-ol/octan-1-ol	433	1	2.1	3.9	0
18	Octan-3-ol	433	1	2.1	3.9	10,630
19	1-Octen-3-ol	433	1	2.1	3.9	12,600
20	Crotyl alcohol	433	5	2.1	3.9	12,600
21	Butan-1-ol	433	5	2.1	3.9	5,930
22	1,2-Butanediol	433	1	2.1	3.9	1,520
23	1,4-Butanediol	433	1	2.1	3.9	104,200
24	Benzyl alcohol‖	433	1	2.1	3.9	12,500
25	Benzyl alcohol¶	433	1	2.1	0	12,400
26	Benzyl alcohol#	433	1	0	3.9	24,800
27	Benzyl alcohol**	433	1	2.4	4.5	36,500
28	Benzyl alcohol††	433	1	0	3.6	37,600
29	1-Phenylethanol††	433	1	0	3.1	11,600

*2.5% Au/TiO_2. †2.5% Pd/TiO_2. ‡0.2 mol/liter in toluene as solvent. §0.2 mol/liter in water as solvent. ‖2.5% Au–2.5% Pd/HAP prepared by impregnation of HAP with $HAuCl_4{\cdot}3H_2O$ and $PdCl_2$. ¶2.5% Au/HAP prepared by impregnation of HAP with $HAuCl_4{\cdot}3H_2O$. #2.5% Pd/HAP prepared by impregnation of HAP with $PdCl_2$. **2.5% Au–2.5% Pd/TiO_2 prepared with the method of Kaneda (*6*) using TiO_2 as support. ††0.2% Pd/HAP prepared using the method of Kaneda (*6*) using HAP as support.

not attempted to optimize the performance at this time. Vanillyl alcohol and cinnamyl alcohol, two important aromatic unsaturated alcohols, were oxidized in the presence of solvents, and 100% specificity to the aldehydes was achieved in both cases at 363 K, further confirming the efficacy of these supported mixed-metal catalysts (Table 2, entries 13 and 14, and Fig. 1B).

As noted above, both Kaneda and co-workers (*6*) and Corma and co-workers (*21*) have shown that supported Pd and Au monometallic catalysts are highly effective for the oxidation of 1-phenylethanol under solvent-free conditions at 433 K with a pO_2 of 0.1 MPa. Under these conditions, the Pd/HAP and Au/CeO_2 catalysts gave TOFs of 9800 and 12,500/hour for 1-phenylethanol, and we have replicated the results for the Pd/HAP catalyst (Table 2, entries 28 and 29). With our $Au\text{-}Pd/TiO_2$ catalyst, we obtained a TOF of 269,000/hour. The $Au\text{-}Pd/TiO_2$ catalyst is also effective for a range of straight-chain, benzylic, and unsaturated alcohols (Table 2, entries 12 to 23) and, in particular, for the oxidation of primary alcohols, such as butan-1-ol and octan-1-ol (Table 2, entries 15 and 21), and high TOFs are observed. This trend was also observed with 1,4-butanediol, for which the observed reactivity is significantly enhanced over that observed for butan-1-ol. This difference may be due to the interaction of this substrate with the active site (Table 2, entry 23), but 1,2-butanediol is much less active (Table 2, entry 22). Even at high reaction temperatures, octan-2-ol is inactive (Table 2, entries 16 and 17), which is in direct contrast with the Pd/HAP and Au/CeO_2 catalysts, for which secondary alcohols are more reactive than primary alcohols. However, the effect of decreased reactivity appears to be limited to 2-alcohols, because octan-3-ol is very reactive (Table 2, entry 18). The addition of octan-2-ol to a reaction mixture leads to a total loss of activity with our catalyst (Table 2, entry 17), and the addition of octan-2-one in small amounts has a similar effect. These findings may indicate a specific interaction of these ketones with the Au-Pd catalyst. To show that TiO_2 is a particularly effective support, we contrasted catalysts prepared using HAP and TiO_2 as supports with the standard impregnation method we have used (Table 2, entries 10 and 25 to 27); it is clear that the TiO_2 support gives improved activity. There is, however, considerable scope to improve and optimize the performance of these mixed metal Au-Pd catalysts in future studies.

The TiO_2-supported Au-Pd catalyst was characterized using x-ray photoelectron spectroscopy (XPS) and scanning transmission electron microscopy (STEM). The XPS results (Fig. 2A) show that the surfaces of the metal nanoparticles in the calcined catalyst material are significantly enriched with Pd. The uncalcined sample shows XPS signals characteristic of both Au and Pd, but as we have stated earlier, these materials are not stable under the reaction conditions. Once calcined at 673 K, the catalysts are stable, and the signal for Au is significantly decreased. STEM analyses of individual metal nanoparticles in the calcined $Au\text{-}Pd/TiO_2$ catalysts were carried out, such as those presented in the montage of annular dark-field (ADF) images and energy-dispersive x-ray (XEDS) maps in Fig. 2B. The Pd x-ray signal originates from a slightly larger spatial area than that of the corresponding Au x-ray signal. This effect is best illustrated in the color map that overlays the filtered Ti, Pd, and Au x-ray signals after the application of multivariate statistical analysis (*26*). In agreement with the XPS study, we deduce that Pd surface seg-

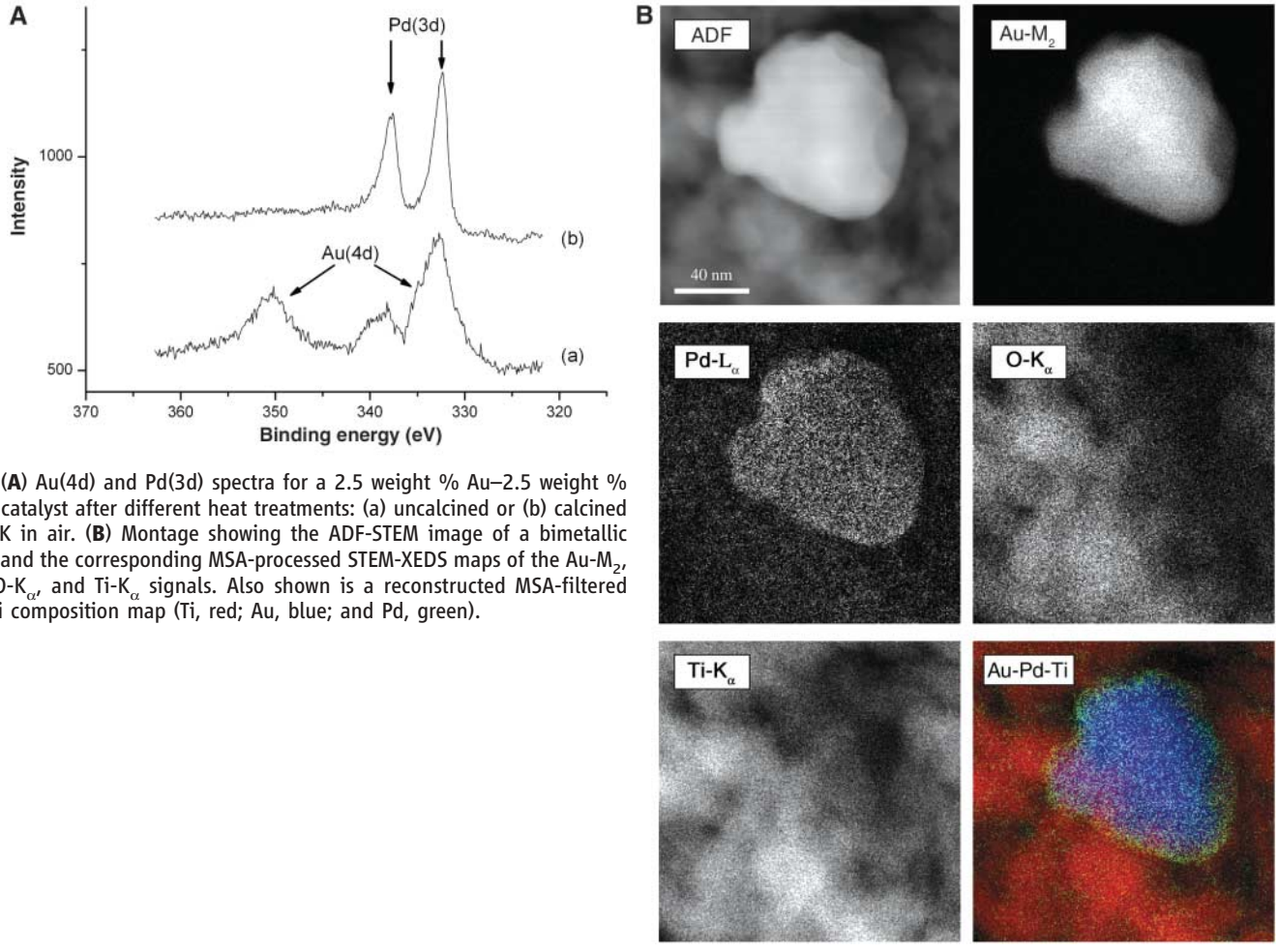

Fig. 2. (**A**) Au(4d) and Pd(3d) spectra for a 2.5 weight % Au–2.5 weight % Pd/TiO_2 catalyst after different heat treatments: (a) uncalcined or (b) calcined at 673 K in air. (**B**) Montage showing the ADF-STEM image of a bimetallic particle and the corresponding MSA-processed STEM-XEDS maps of the $Au\text{-}M_2$, $Pd\text{-}L_\alpha$, $O\text{-}K_\alpha$, and $Ti\text{-}K_\alpha$ signals. Also shown is a reconstructed MSA-filtered Au-Pd-Ti composition map (Ti, red; Au, blue; and Pd, green).

regation occurs during calcination to produce alloy nanoparticles having a Pd-rich shell surrounding a Au-rich core.

The catalytic data show that the introduction of Au to Pd improves selectivity, and we believe that the surface of the bimetallic nanoparticles will still contain some Au. Hence, we argue that the Au acts as an electronic promoter for Pd and that the active catalyst has a surface that is significantly enriched in Pd. Recent studies have started to provide insights into the nature of such effects. For example, Okazaki *et al*. (*27*) have shown, using a combination of experiment and theory, that the electronic structure of Au in Au/TiO_2 catalysts is dependent on the particle size, and Goodman and co-workers (*28*), using model studies, have shown that Au can isolate Pd sites within bimetallic systems.

References and Notes

1. R. A. Sheldon, J. K. Kochi, *Metal-Catalyzed Oxidations of Organic Compounds* (Academic Press, New York, 1981).
2. M. Beller, C. Bolm, *Transition Metals for Organic Synthesis* (Verlag GmbH & Co. KGaA, Weinheim, Germany, ed. 2, 2004).
3. G. ten Brink, I. W. C. E. Arends, R. A. Sheldon, *Science* **287**, 1636 (2000).
4. M. Vazylyev, D. Sloboda-Rozner, A. Haimov, G. Maayan, R. Neumann, *Top. Catal.* **34**, 93 (2005).
5. M. Pagliaro, S. Campestrini, R. Ciriminna, *Chem. Soc. Rev.* **34**, 837 (2005).
6. K. Mori, T. Hara, T. Mizugaki, K. Ebitani, K. Kaneda, *J. Am. Chem. Soc.* **26**, 10657 (2004).
7. I. E. Markó, P. R. Giles, M. Tsukazaki, S. M. Brown, C. J. Urch, *Science* **274**, 2044 (1996).
8. M. J. Schultz, R. S. Adler, W. Zierkiewicz, T. Privalov, M. S. Sigman, *J. Am. Chem. Soc.* **127**, 8499 (2005).
9. U. R. Pillai, E. Sahle-Demessie, *Appl. Catal. Gen.* **245**, 103 (2003).
10. M. Hudlicky, *Oxidations in Organic Chemistry* (American Chemical Society, Washington, DC, 1990).
11. W. P. Griffith, J. M. Joliffe, *Stud. Surf. Sci. Catal.* **66**, 395 (1991).
12. G. Cainelli, G. Cardillo, *Chromium Oxidants in Organic Chemistry* (Springer, Berlin, 1984).
13. D. G. Lee, U. A. Spitzer, *J. Org. Chem.* **35**, 3589 (1970).
14. F. M. Menger, C. Lee, *Tetrahedron Lett.* **22**, 1655 (1981).
15. R. Neumann, M. Levin-Elad, *Appl. Catal. A* **122**, 85 (1995).
16. L. Prati, M. Rossi, *J. Catal.* **176**, 552 (1998).
17. F. Porta, L. Prati, M. Rossi, G. Scari, *J. Catal.* **211**, 464 (2002).
18. S. Carretin, P. McMorn, P. Johnston, K. Griffin, G. J. Hutchings, *Chem. Commun.* **2002**, 696 (2002).
19. F. Porta, L. Prati, *J. Catal.* **224**, 397 (2004).
20. S. Biella, M. Rossi, *Chem. Commun.* **2003**, 378 (2003).
21. A. Abad, P. Conception, A. Corma, H. Garcia, *Angew. Chem.* **44**, 4066 (2005).
22. P. Landon, P. J. Collier, A. J. Papworth, C. J. Kiely, G. J. Hutchings, *Chem. Commun.* **2002**, 2058 (2002).
23. P. Landon *et al.*, *Phys. Chem. Chem. Phys.* **5**, 1917 (2003).
24. J. K. Edwards *et al.*, *J. Mater. Chem.* **15**, 4595 (2005).
25. J. K. Edwards *et al.*, *J. Catal.* **236**, 69 (2005).
26. To confirm that surface segregation of Pd was truly occurring in these nanoparticles, multivariate statistical analysis (MSA) was performed on the data set shown in Fig. 2B. MSA is a group of processing techniques that can be used to identify specific features within large data sets such as x-ray spectrum images and to reduce random noise components in the data sets in a statistical manner. MSA has recently been shown to be particularly useful for analysis of x-ray maps taken from nanoparticles (*29*). This statistical technique performs a data-smoothing calculation by portioning the XEDS data using a probability density function.
27. K. Okazaki, S. Ichikawa, Y. Maeda, M. Haruta, M. Kohyama, *Appl. Catal. A* **291**, 45 (2005).
28. M. Chen, D. Kumar, C.-W. Yi, D. W. Goodman, *Science* **310**, 291 (2005).
29. N. Bonnet, *J. Microsc.* **190**, 2 (1998).

30. Sponsored by the European Union AURICAT project (contract HPRN-CT-2002-00174) and the Engineering and Physical Sciences Research Council (EPSRC) as part of the ATHENA project co-sponsored by Johnson Matthey, as well as by an EPSRC-sponsored program on Speculative Green Chemistry, and we thank them for funding this research. We also thank the World Gold Council (through the GROW scheme) and Cardiff University (AA Reed studentship) for providing support for J.K.E. D.I.E. thanks the Crystal Faraday Partnership for funding. Finally, C.J.K., M.A.W., and A.A.H. gratefully acknowledge NSF funding through the Materials Research Science and Engineering Center (NSF grants DMR-0079996, DMR-0304738, and DMR-0320906).

Supporting Online Material

www.sciencemag.org/cgi/content/full/311/5759/362/DC1
Materials and Methods
Fig. S1

26 September 2005; accepted 7 December 2005
10.1126/science.1120560

Internal Rotation and Spin Conversion of CH_3OH in Solid para-Hydrogen

Yuan-Pern Lee,[1,2]* Yu-Jong Wu,[3] R. M. Lees,[4] Li-Hong Xu,[4] Jon T. Hougen[5]

The quantum solid para-hydrogen (p-H_2) has recently proven useful in matrix isolation spectroscopy. Spectral lines of compounds embedded in this host are unusually narrow, and several species have been reported to rotate in p-H_2. We found that a p-H_2 matrix inhibits rotation of isolated methanol (CH_3OH) but still allows internal rotation about the C–O bond, with splittings of the *E*/*A* torsional doublet in internal rotation–coupled vibrational modes that are qualitatively consistent with those for CH_3OH in the gaseous phase. This simplified high-resolution spectrum further revealed the slow conversion of nuclear spin symmetry from species *E* to species *A* in the host matrix, offering potential insight into nuclear spin conversion in astrophysical sources.

In a quantum solid, the de Broglie wavelength of the species with small mass becomes a substantial fraction of its size at low temperature, resulting in delocalization of the nuclei. Because of the "softness" associated with the quantum solid properties of a p-H_2 matrix (*1*–*3*), guest molecules such as methane can rotate in solid p-H_2 more readily than in other matrices; the rotational parameters of species isolated in p-H_2 are typically ~90% of those for the gaseous phase, even less affected than the parameters of species in helium droplets (*4*, *5*). For larger species, molecular rotation is less likely to occur but internal rotation (torsion) of methyl groups could well persist.

The torsional motion itself is one representative of the class of large-amplitude molecular vibrational motions. In common with overall rotation, these vibrational motions involve displacements of atoms over distances comparable to chemical bond lengths, but in contrast to rotational motions, they are hindered by potential barriers reflective of some mixture of chemical bond properties and van der Waals repulsions.

Internal rotation typically couples with other vibrational modes to give a substantial variety of energy patterns. This coupling with torsional bath states is also believed to be the mechanism responsible for the large enhancement of intramolecular vibrational energy redistribution rates in methyl rotor–containing molecules. Spectral analysis of vibration-rotation bands involving internal rotation is often challenging, but the low-temperature solid p-H_2 environment ensures that nearly all absorption lines originate from the lowest levels. Moreover, fine structure is observable because the infrared (IR) absorption lines of guest molecules in the p-H_2 matrix can be extremely sharp, with full widths at half maximum (FWHM) less than 0.01 cm^{-1} (*4*, *6*).

Here we apply the advantages of p-H_2 to vibrational spectroscopy of methanol. We have observed torsional tunneling splittings between the *A* and *E* symmetry species associated with internal rotation about the C–O bond, permitting a clear differentiation between the corresponding $I = 3/2$ and $I = ½$ nuclear spin modifications of the methyl hy-

[1]Department of Applied Chemistry and Institute of Molecular Science, National Chiao Tung University, 1001 Ta-Hsueh Road, Hsinchu 30010, Taiwan. [2]Institute of Atomic and Molecular Sciences, Academia Sinica, Taipei 10617, Taiwan. [3]Department of Chemistry, National Tsing Hua University, 101, Sec. 2, Kuang Fu Road, Hsinchu 30013, Taiwan. [4]Centre for Laser, Atomic and Molecular Sciences, Department of Physical Sciences, University of New Brunswick, 100 Tucker Park Road, Saint John, New Brunswick E2L 4L5, Canada. [5]Optical Technology Division, National Institute of Standards and Technology, Gaithersburg, MD 20899, USA.

*To whom correspondence should be addressed. E-mail: yplee@mail.nctu.edu.tw

drogens in CH_3OH. Monitoring the relative intensities in *A*/*E* transition pairs as a function of time thus permitted a determination of nuclear spin conversion rates in this molecule. Previously, the time dependence of structure associated with overall molecular rotation had been used to study spin conversion in water, methane, and ammonia in rare gas matrices (*7*–*9*). Spin conversion processes are of particular relevance in molecular astrophysics, wherein it remains unclear whether different symmetry species in astronomical sources should be viewed as independent molecular reservoirs with independent excitation temperatures, or instead should be treated as a whole and characterized by a common temperature. The question of how spin conversion is promoted by molecule-solid interactions on molecular ices also remains open.

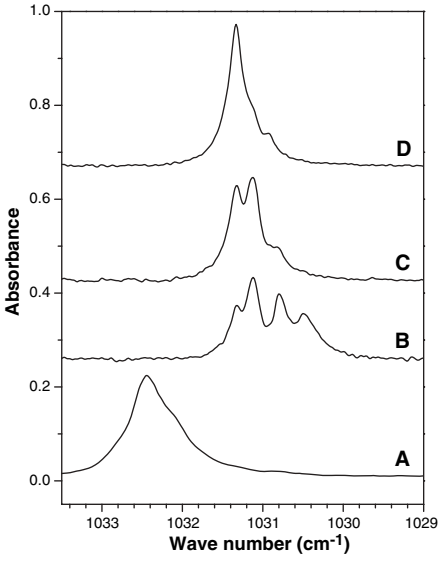

Fig. 1. Partial IR absorption spectra of the C–O stretching mode of matrix-isolated CH_3OH. (**A**) CH_3OH/Ne (1/5000). (**B**) CH_3OH/*p*-H_2 (1/5000) after deposition. (**C**) Annealing of CH_3OH/*p*-H_2 for 2 hours at 5 K. (**D**) Sample in (B) after 70 hours in darkness at 3.5 K. For each acquisition of spectral data, 200 scans corresponding to a resolution of 0.05 cm^{-1} were accumulated. The acquisition process took ~1 hour, during which time the sample was held at 3.5 K.

In our experiments, a nickel-plated copper plate served both as a cold substrate for the matrix sample and as a mirror to reflect the incident IR beam to the detector. Typically, a gaseous mixture of CH_3OH/*p*-H_2 (1/5000 to 1/3000, 0.12 mol) was deposited over a period of 4 hours (*10*, *11*). IR absorption spectra were recorded with a Fourier-transform infrared (FTIR) spectrometer (Bomem, DA8) (*12*) equipped with a KBr beamsplitter and a Hg/Cd/Te detector (cooled to 77 K) to cover the spectral range 500 to 5000 cm^{-1}. Typically, 200 scans at a resolution of 0.05 cm^{-1} were recorded at each stage of the experiment. The intense feature near 1030 cm^{-1} associated with C–O stretching in the IR spectrum (*13*, *14*) was recorded with a CH_3OH/*p*-H_2 concentration of 1/5000; absorption lines attributed to other vibrational modes are much weaker and required higher concentration (~1/3000) to achieve a practical signal-to-noise ratio.

The IR spectrum of a sample of CH_3OH/Ne (1/5000) at 3.5 K exhibits a single broad line at 1032.45 cm^{-1} with FWHM ~0.6 cm^{-1} in the C–O stretching region (Fig. 1A). In contrast, the spectrum of CH_3OH/*p*-H_2 (1/5000) at 3.5 K exhibits multiple lines at ~1031 cm^{-1} with FWHM ~0.15 cm^{-1} (Fig. 1B). A *p*-H_2 matrix prepared with direct vapor deposition has a mixed crystal structure; annealing of the matrix near 5 K converts the matrix to a hexagonal close-packed structure (*4*). After sample annealing at 5 K for 2 hours, the original multiplet has evolved to a doublet at 1031.12 and 1031.31 cm^{-1} (Fig. 1C). In separate experiments, we verified that this doublet can be obtained free from interference in the lower energy region only when the concentrations of CH_3OH and *o*-H_2 impurity are low. The matrix also undergoes self-annealing at 3.5 K; nearby lines other than this doublet disappeared 40 hours after deposition even without annealing at a high temperature.

The observed doublet wavenumbers match closely with the known subband origins at 1033.707 and 1033.896 cm^{-1} in gaseous CH_3OH (Table 1) (*13*, *14*). Because of their relaxation behavior and wavenumber separation, these two transitions can be identified with transitions from the *E* and *A* components of the ground state ($\nu_i'' = 0$ for $i = 1$ to 12 and $K'' = 0$) to the *E* and *A* components of the upper state ($\nu_8' = 1$, $\nu_{12}' = 0$, and $K' = 0$) of the C–O stretching mode, where ν_8 and ν_{12} are the C–O stretching and torsional quantum numbers, respectively. For simplicity, we denote observed transitions from the ground state by $n\nu_i$, where *n* is the vibrational quantum number of the upper state (omitted when $n = 1$) and ν_i is the vibrational mode. Although there is a matrix shift of –2.59 cm^{-1}, the *E*-*A* line separation of –0.19 cm^{-1} observed for ν_8 is identical to the value for gaseous CH_3OH. The spectrum of the matrix sample after 70 hours in the dark at 3.5 K (Fig. 1D) shows markedly increased intensity of the line at 1031.31 cm^{-1} at the expense of line intensity at 1031.12 cm^{-1}. This variation of intensity shows that, in the *p*-H_2 matrix, the molecules of *E* symmetry slowly convert to the *A* species (with an energy decrease of ~9 cm^{-1}) (*14*), a process that can only occur via conversion of the CH_3 total nuclear spin from $I = ½$ to $I = 3/2$. Fitting of a single-exponential decay (or rise) of six data points between 40 and 70 hours for component *E* (or *A*) yields a rate coefficient for the spin conversion from *E* to *A* components at 3.5 K of ~0.018 ± 0.003 $hour^{-1}$.

Because there are no obvious lines remaining in the C–O stretching region to assign to

Table 1. Comparison of line positions between CH_3OH isolated in solid *p*-H_2 and in the gaseous phase. Matrix shift is defined as $\Delta = \nu_{matrix} - \nu_{gas}$.

Mode	Description	Symmetry	Gas phase		This work§		Matrix shift
			cm^{-1}	Δ(*E*-*A*)	cm^{-1}	Δ(*E*-*A*)	
ν_2	C–H asymmetrical stretch	*E*	2994.60*	–12.39	2995.61	–7.62	1.01
		A_1	3006.99		3003.23		–3.76
ν_3	C–H symmetrical stretch	*E*	2844.66*	–0.06	2840.66	<0.1	–4.00
		A_1	2844.72		2840.66		–4.06
ν_7	CH_3 rock	*E*	1070.31†	–4.57	1073.69	–1.33	3.38
		A_1	1074.884		1075.02		0.14
ν_8	C–O stretch	*E*	1033.707†	–0.189	1031.12	–0.19	–2.59
		A_1	1033.896		1031.31		–2.59
ν_9	C–H asymmetrical stretch	*E*	2952.04*	–14.61	2951.72	–14.14	–0.32
		A_2	2966.65		2965.86		–0.79
$2\nu_4$	Overtone	*E*	2957.57‡	–0.79	2956.50	–0.54	–1.07
		A_1	2958.36		2957.04		–1.32

*$K = 0$ subband origins determined from the term values given in (*16*). †From (*13*, *14*). ‡From (*22*). §All measurements are estimated to have type B uncertainties ($k = 2$) (*23*) of ± 0.05 cm^{-1} or better.

transitions arising from the $J = K = 1$ level of methanol (~5 cm^{-1} above the $J = K = 0$ level), we conclude that methanol does not rotate about its principal a axis in the p-H_2 matrix. This finding is in contrast to earlier observations of rotational structure for water, methane, and ammonia in rare-gas matrices (*7*–*9*) and seems somewhat surprising given that nearly free rotation in p-H_2 is exhibited by methane, which has a moment of inertia for rotation about its C_3 axis only slightly smaller than that of methanol about the C–O bond axis. Nonetheless, if we assume that methanol cannot carry out overall rotations but can carry out internal rotations, this raises the question of how the internal rotation splittings are affected by the p-H_2 matrix. Given that internal rotation splitting in the C–O stretching fundamental in p-H_2 is nearly identical to the gas-phase value (Table 1), it appears that the matrix alters neither the potential barrier V_3 nor the effective internal-rotation constant F for this mode. If true, this might imply that studies of the simple rotation-free transitions in a p-H_2 matrix could greatly aid in sorting out the complex gas-phase spectra of methanol. Currently, there is a lack of experimental information about the important low-J and low-K assignments for many of the methanol vibrational fundamentals; hence, insights from the p-H_2 experiments would be extremely valuable.

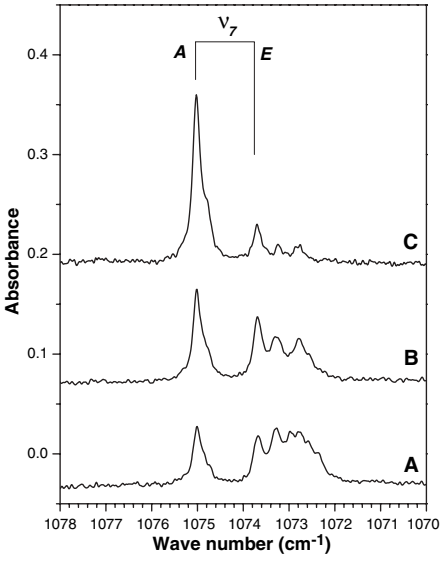

Fig. 2. Partial IR absorption spectra of in-plane CH_3-rocking mode of a CH_3OH/p-H_2 (1/3000) matrix sample, acquired (**A**) after deposition at 3.5 K, (**B**) after annealing the sample for 2 hours at 5 K, and (**C**) after 70 hours in darkness at 3.5 K. Conditions of data acquisition are the same as for Fig. 1.

Our spectra for the in-plane CH_3-rocking (ν_7) mode of CH_3OH in the region 1070 to 1078 cm^{-1} are shown in Fig. 2; traces A to C correspond respectively to CH_3OH/p-H_2 after deposition, after annealing, and 70 hours after deposition. The growing line at 1075.02 cm^{-1} is assigned in Table 1 as the A component of the ν_7 band, very close to the gas-phase value of 1074.884 cm^{-1} (*13*). However, the best candidate for the E component lies at 1073.69 cm^{-1}, distinctly higher than the reported gas-phase value of 1070.31 cm^{-1} (*13*). Thus, our E-A line separation of –1.33 cm^{-1} in Table 1 is smaller than the value of –4.57 cm^{-1} for the gas phase. The rate coefficient for conversion from our assigned E component to the A component at 3.5 K is ~0.019 ± 0.002 $hour^{-1}$, consistent with the rate derived from the ν_8 mode.

The ν_2, ν_9, $2\nu_4$, and ν_3 bands have been characterized in the C–H stretching region of the vibration-rotational spectrum of gaseous CH_3OH (*15*, *16*). The $K = 0$, A subband and $K = 0$, E subband origins deduced from the upper-state term values are listed in Table 1. The A/E splittings are less than 0.8 cm^{-1} for $2\nu_4$ and ν_3 but increase to 12.4 cm^{-1} and 14.6 cm^{-1} for ν_2 and ν_9, respectively. In the spectrum of CH_3OH/Ne in the region 2800 to 3030 cm^{-1} (Fig. 3A), no splitting was observed. The spectrum of CH_3OH/p-H_2 70 hours after deposition (Fig. 3C) exhibits a pattern similar to that for CH_3OH in the gaseous phase: no splitting for the strong ν_3 line at 2840.66 cm^{-1} nor for the $2\nu_4$ feature at 2956.77 cm^{-1}, but large splittings for lines assigned to ν_2 at 3003.23 cm^{-1} (*A*) and 2995.61 cm^{-1} (*E*) and to ν_9 at 2965.86 cm^{-1} (*A*) and 2951.72 cm^{-1} (*E*).

A further sharp doublet can be seen at 2916.92 and 2914.97 cm^{-1} (Fig. 3C). The temporal behavior of the relative intensities clearly indicates that the former is the A component and the latter the E component. A weaker line at 2933.02 cm^{-1} can also be identified as a transition of A symmetry. The corresponding bands for CH_3OH in the gaseous phase have not been unambiguously identified, but from considerations of symmetry, wavenumber, and analogy with model predictions for the ν_4 and ν_5 CH_3-bending fundamentals, we can tentatively associate the lines at 2916.92 cm^{-1} and 2933.02 cm^{-1} in the p-H_2 matrix with the $2\nu_5$ overtone and the $\nu_4 + \nu_5$ combination band, respectively.

The remaining vibrational fundamentals are the ν_1 OH-stretching mode around 3680 cm^{-1} (*17*); the ν_4, ν_5, and ν_{10} CH_3-bending modes around 1470 cm^{-1} (*18*); the ν_6 OH-bending mode around 1340 cm^{-1} (*19*); and the ν_{11} out-of-plane CH_3-rocking mode around 1280 cm^{-1} (*20*). The experimental situation at $K = 0$ for the gas-phase spectra of several of these bands is still very uncertain. No low-K subbands have been assigned for the three CH_3-bending fundamentals (*18*), nor for the ν_{11} rocking band (*20*). The OH-bending mode lies in a complex region of strong mixing with other torsional combination states, and the correct vibrational labeling of the rotationally assigned $K = 0$ subbands is not clear, leaving a number of U subbands unidentified (*19*).

Our observed spectra for methanol in p-H_2 clearly show additional splitting structure in all of the above regions. Comparison with the experimental or predicted gas-phase subband origins indicates matrix shifts of less than 10 cm^{-1} for all of the fundamentals (excluding the torsion) and internal rotation splittings in general qualitative agreement. In particular, a strong single peak at 1449.16 cm^{-1} that grows with annealing is in good agreement with the predicted 1453.4/1453.1 cm^{-1} for the ν_5 A/E doublet (*18*), and a strong peak clearly of A symmetry at 1364.43 cm^{-1} is consistent with the U_0 subband reported at 1369.69 cm^{-1}. This band, rather than the published 1320.63 cm^{-1} assignment (*19*), could actually correspond to the ν_6 OH-bending $K = 0$, A subband. However, we consider

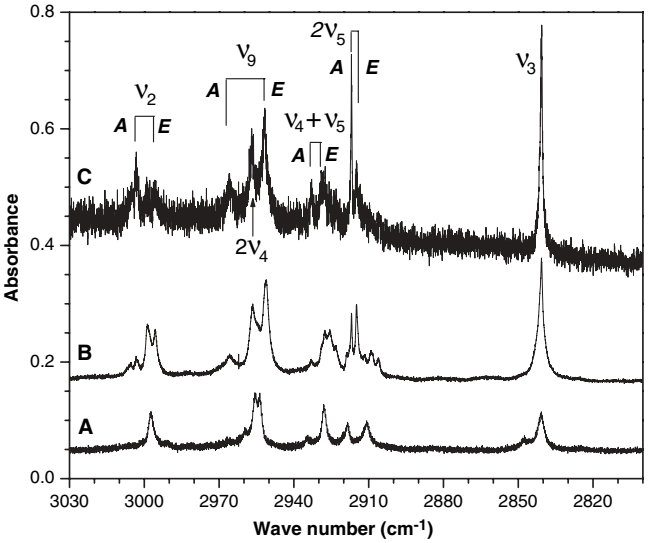

Fig. 3. Partial IR absorption spectra of the C–H stretching region of matrix-isolated CH_3OH. (**A**) CH_3OH/Ne (1/3000). (**B**) CH_3OH/p-H_2 (1/3000) after deposition at 3.5 K. (**C**) Sample in (B) after 70 hours in darkness at 3.5 K. For each data acquisition, 200 scans corresponding to a resolution of 0.05 cm^{-1} were accumulated. The acquisition process took ~1 hour, during which time the sample was held at 3.5 K. The effective spectral resolution is 0.09 cm^{-1} because of the size of the aperture used.

that firm conclusions about the effects of the p-H_2 matrix on the methanol torsion-vibration spectral structure would be premature at this stage without more definitive gas-phase data.

Taken together, these results suggest that the p-H_2 matrix will serve as an important medium for the study of large-amplitude vibrational motions and molecular spin conversion processes, providing valuable information to aid our understanding of complicated spectral patterns both in the gas phase and in molecular ices.

References and Notes

1. T. Oka, *Annu. Rev. Phys. Chem.* **44**, 299 (1993).
2. T. Momose, T. Shida, *Bull. Chem. Soc. Jpn.* **71**, 1 (1998).
3. K. Yoshioka, D. T. Anderson, *J. Chem. Phys.* **119**, 4731 (2003).
4. S. Tam *et al.*, *J. Chem. Phys.* **111**, 4191 (1999).
5. T. Momose *et al.*, *J. Chem. Phys.* **103**, 1400 (1995).
6. T. Momose *et al.*, *J. Chem. Phys.* **107**, 7707 (1997).
7. R. L. Redington, D. E. Milligan, *J. Chem. Phys.* **39**, 1276 (1963).
8. F. H. Frayer, G. E. Ewing, *J. Chem. Phys.* **48**, 781 (1968).
9. H. P. Hopkins, R. F. Curl, K. S. Pitzer, *J. Chem. Phys.* **48**, 2959 (1968).
10. We have developed a pulsed-deposition technique that can operate at a deposition temperature up to 5.5 K (*21*). Thus, it is suitable for use with our previous cryogenic refrigerator that cools to only ~5 K. As well, with a new closed-cycle refrigerator system (Janis RDK-415) capable of cooling the sample target to 3.5 K, we could use conventional continuous deposition with a flow rate of ~0.03 mol hour^{-1}.
11. CH_3OH (99.9%, Mallinckrodt, analytical reagent grade) was purified by passing the vapor though P_2O_5 to remove trace water impurity. H_2 (99.9999%, Scott Specialty Gases) was used after passage through a trap at 77 K before conversion to p-H_2. The p-H_2 converter comprised a copper cell filled with $Fe(OH)_3$ catalyst and cooled with a closed-cycle refrigerator. The efficiency of conversion is controlled by the temperature of the catalyst; at 15 K, the concentration of o-H_2 is ~100 ppm.
12. Any mention of commercial products in this paper is for information only; it does not imply recommendation or endorsement by NIST.
13. L.-H. Xu *et al.*, *J. Mol. Spectrosc.* **228**, 453 (2004).
14. G. Moruzzi, B. P. Winnewisser, M. Winnewisser, I. Mukhopadhyay, F. Strumia, *Microwave, Infrared and Laser Transitions of Methanol: Atlas of Assigned Lines from 0 to 1258 cm^{-1}* (CRC Press, Boca Raton, FL, 1995).
15. L.-H. Xu *et al.*, *J. Mol. Spectrosc.* **185**, 158 (1997).
16. X. Wang, D. S. Perry, *J. Chem. Phys.* **109**, 10795 (1998).
17. I. Kleiner, G. T. Fraser, J. T. Hougen, A. S. Pine, *J. Mol. Spectrosc.* **147**, 155 (1991).
18. M. A. Temsamani, L.-H. Xu, R. M. Lees, *J. Mol. Spectrosc.* **218**, 220 (2003).
19. R. M. Lees *et al.*, *J. Mol. Spectrosc.* **228**, 528 (2004).
20. R. M. Lees, L.-H. Xu, *Phys. Rev. Lett.* **84**, 3815 (2000).
21. Y.-J. Wu, X. Yang, Y.-P. Lee, *J. Chem. Phys.* **120**, 1168 (2004).
22. X. Wang, D. S. Perry, L.-H. Xu, unpublished data.
23. B. N. Taylor, C. E. Kugatt, *NIST Tech. Note 1297* (1994).

24. Supported by the Natural Sciences and Engineering Research Council of Canada (R.M.L. and L.H.X.) and by National Science Council of Taiwan grant NSC94-2113-M-009-017.

12 October 2005; accepted 12 December 2005
10.1126/science.1121300

Formation of Glaciers on Mars by Atmospheric Precipitation at High Obliquity

F. Forget,[1]* R. M. Haberle,[2] F. Montmessin,[3] B. Levrard,[4] J. W. Head[5]

Surface conditions on Mars are currently cold and dry, with water ice unstable on the surface except near the poles. However, geologically recent glacierlike landforms have been identified in the tropics and the midlatitudes of Mars. The ice has been proposed to originate from either a subsurface reservoir or the atmosphere. We present high-resolution climate simulations performed with a model designed to simulate the present-day Mars water cycle but assuming a 45° obliquity as experienced by Mars a few million years ago. The model predicts ice accumulation in regions where glacier landforms are observed, on the western flanks of the great volcanoes and in the eastern Hellas region. This agreement points to an atmospheric origin for the ice and reveals how precipitation could have formed glaciers on Mars.

Among the most striking recent observations by the cameras aboard the Mars Express, Mars Global Surveyor (MGS), and Mars Odyssey orbiters are low-latitude, geologically recent, morphological features that clearly formed by the action of a water ice glacier (*1*–*8*). The most characteristic landforms appear to be clustered in several specific regions that had already been identified in Viking images (*9*, *10*). First, each of the Tharsis Montes volcanoes has a fan-shaped deposit near its northwestern flank (Fig. 1A), interpreted to be the remains of geologically recent glaciers (*3*, *4*). In the same region, debris-covered piedmont glaciers along the northwest edge of the Olympus Mons scarp (Fig. 1A) were seen in Viking and Mars Odyssey Thermal Emission Imaging System (THEMIS) data (*8*, *10*). Recent images of these glacier remnants obtained by the Mars Express High Resolution Stereo Camera (HRSC) show that they are covered by very recent rock glaciers (*1*, *2*). A second notable region is a relatively small area (1000 km across) on the eastern side of the Hellas Basin (90° to 120°E and 32° to 50°S), where some of the most spectacular examples of ice-related landforms are seen. More than 90 large lobate debris aprons up to 50 km across have been identified there (*5*, *9*). Some of these debris aprons are interpreted to represent very ice-rich debris-covered glaciers (*1*). Eastern Hellas also contains a variety of smaller ice-rich flow features, including tongue-shaped lobes observed at 247°W 38.6°S (*6*), hourglass-shaped craters apparently filled by a flowing debris-covered glacier (*1*), and many of the ice-cemented mantling deposits associated with gullies (*11*). A third major area of icy Mars is the Deuteronilus–Protonilus Mensae region (0° to 80°E and 30° to 50°N) (*9*), where large concentrations of lobate debris aprons and lineated valley fills (that resemble flow lines in glacial ice on Earth) are found. Outside these three regions, glacier-like features have been observed at mid-latitudes (*7*, *9*) but in more localized or limited forms.

Where did the ice come from? It has been suggested that the features could have been emplaced by creep or a landslide of material rich in ground ice (*12*, *13*) or released from a subsurface ground ice or groundwater reservoir (*2*). A recent analysis of the HRSC images of the western edge of Olympus Mons (*2*) concluded that the observations yielded evidence for hydrothermal mobilization of water with subsequent development of glaciers. However, the geomorphologic characteristic of most glacier features is also consistent with an atmospheric precipitation origin (*1*, *3*, *4*, *7*, *8*). This hypothesis has been supported by climate model simulations that suggested that, during a period of obliquity greater than about 35° to 45° (obliquity is the tilt of the planet's spin axis), the north polar water ice may be mobilized southward and deposited at lower latitudes (*14*–*16*). However, the simple cloud ice microphysics and the coarse spatial resolutions used by these previous models did not allow a true comparison between the modeled ice accumulations and the available geological observations.

[1]Laboratoire de Météorologie Dynamique, Institut Pierre Simon Laplace, Université Paris 6 Boite Postale 99, 75252 Paris cedex 05, France. [2]Space Science Division, Mail Stop 245-3, NASA Ames Research Center, Moffett Field, CA 94035, USA. [3]Service D'Aéronomie, Institut Pierre Simon Laplace, Université Paris 6 Box Postale 102, 75252 Paris cedex 05, France. [4]Astronomie et Systèmes Dynamiques, Institut de Mécanique Céleste, 77 Avenue Denfert Rochereau, 75014 Paris, France. [5]Department of Geological Sciences, Brown University, Providence, RI 02912, USA.

*To whom correspondence should be addressed. E-mail: forget@lmd.jussieu.fr

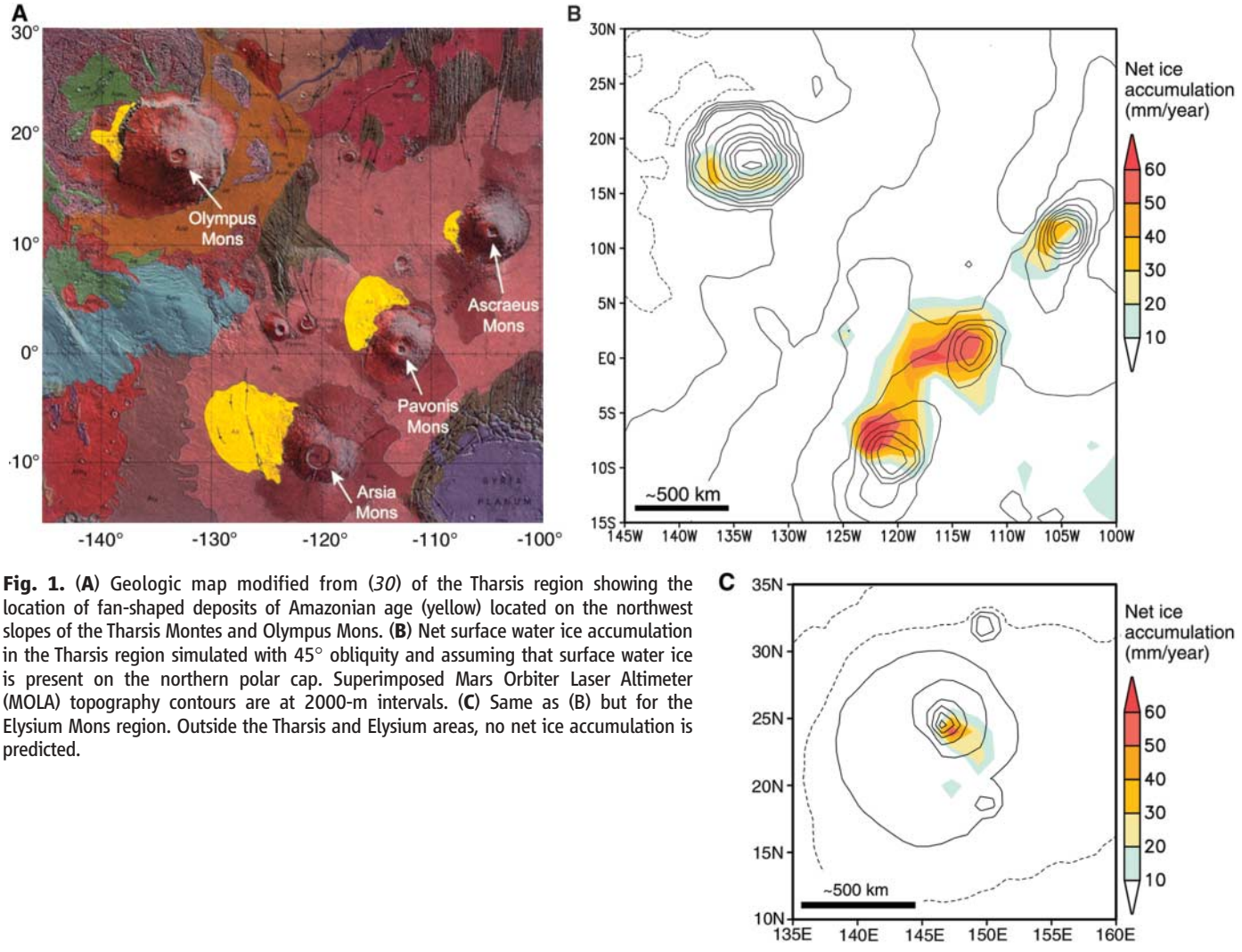

Fig. 1. (**A**) Geologic map modified from (*30*) of the Tharsis region showing the location of fan-shaped deposits of Amazonian age (yellow) located on the northwest slopes of the Tharsis Montes and Olympus Mons. (**B**) Net surface water ice accumulation in the Tharsis region simulated with 45° obliquity and assuming that surface water ice is present on the northern polar cap. Superimposed Mars Orbiter Laser Altimeter (MOLA) topography contours are at 2000-m intervals. (**C**) Same as (B) but for the Elysium Mons region. Outside the Tharsis and Elysium areas, no net ice accumulation is predicted.

Here, we use the martian global climate model of the Laboratoire de Météorologie Dynamique (LMD), which is designed to simulate the present-day climate on Mars (*17*). In particular, it provides distributions of atmospheric vapor and clouds in very good agreement with MGS Thermal Emission Spectrometer (TES) observations (*18*). It includes a full description of exchange between surface ice, atmospheric water, and transport and turbulent mixing of water in the atmosphere and a parameterization of the microphysics of cloud formation. The radiative effects of water vapor and clouds as well as the exchange of water vapor with the subsurface are not included.

To simulate a typical high-obliquity climate, we performed a simulation similar to the one presented in (*18*) for present-day Mars, except for the following modifications. First, in order not to favor any hemisphere, we set the orbit eccentricity to zero and fixed the reference visible dust optical depth (*19*) to a constant value (0.2). Second, we increased the obliquity of the planet to 45°. Such an obliquity has probably been common throughout Mars history (*20*). It last occurred on Mars 5.51×10^6 years ago and is close to the most probable value throughout Mars' history (41.8°) (*20*). Last, to better represent the atmosphere-topography interaction, we used a higher spatial resolution of 2° in latitude and 2.045° longitude (*21*).

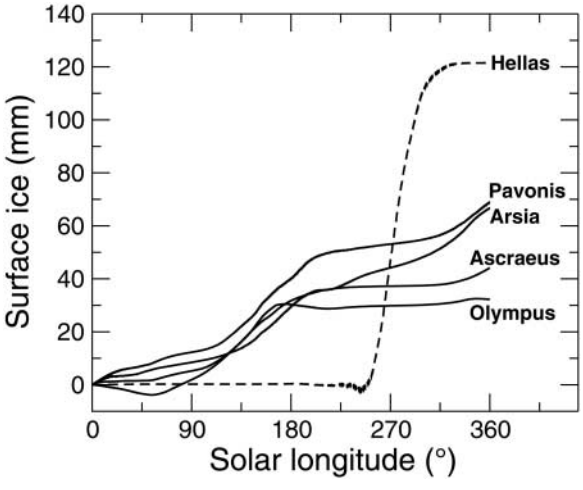

Fig. 2. Seasonal evolution of the ice accumulation over one martian year at several locations for our 45° obliquity simulations with a water ice northern polar cap (solid lines) and one simulation with a water ice southern polar cap (dashed line) near Pavonis Mons (117°W 0°N), near Arsia Mons (122°W 6°S), near Ascraeus Mons (107° W 12°N), near Olympus Mons (137°W, 16°N), and in Eastern Hellas (110°E, 40°S). Solar longitude (Ls) is the areocentric longitude of the sun, with Ls equal to 0° at northern spring equinox, 90° at summer solstice, 180° at autumn equinox, and 270° at winter solstice.

As predicted by previous climate simulations (*22*), the increased polar summer insolation enhances the polar ice sublimation and leads to a water cycle that is much more

intense than today's, with a column water abundance up to 3000 precipitable micrometers (pr-μm) above the northern polar cap around summer solstice and about 50 pr-μm in the summer tropics. Water ice accumulation reaching 30 to 70 mm per year occurs in five localized areas on the flanks of the Tharsis, Olympus, and Elysium Montes (Fig. 1, B and C), and nowhere else. After a few thousand years, such accumulations would form glaciers several hundred meters thick, and their locations can be compared to the locations of the glacier-related deposits observed in the Tharsis region (Fig. 1A). The agreement is excellent, with maximum deposition predicted on the western flanks of Arsia and Pavonis where the largest deposits are observed (Fig. 1A) (*3*, *4*) and lower deposition on the flanks of Ascraeus and Olympus. Precipitation is predicted in the upper part of the large area actually covered by the extensive Arsia Mons fan-shaped deposits, which appears to coincide with the accumulation zone of the more extensive glacial deposit (*3*).

Why does ice accumulate on the flanks of these mountains? In our simulation, most of the ice condenses in the lower atmosphere below 2 km. Precipitation occurs on Arsia and Pavonis all year long, whereas Olympus and Ascraeus only get ice during the northern summer (Fig. 2). During that season, large amounts of ice tend to condense out on the western side of the volcanoes because of strong westerly winds blowing upslope. In such a flow, the water-rich air is adiabatically cooled by 10 to 20 K (Fig. 3). Water condenses and forms ice particles of 20 to 50 μm in diameter that sediment onto the surface [compared to 6 to 8 μm in the present-day Tharsis clouds (*23*)]. The weather pattern that creates the strong westerly wind on Olympus in summer is comparable to the summer monsoon in Asia (fig. S1). At other seasons, Olympus and Ascraeus Montes do not receive precipitation because they are exposed to weaker winds and a drier atmosphere, whereas Arsia and Pavonis Montes continue to accumulate ice because of a symmetrical southern hemisphere monsoon circulation during southern spring and summer. Although our simulation predicts the accumulation of ice only on the flanks of the largest mountains, it is likely that this process occurred at smaller scales not resolved by our model, like on the subgrid-size Hecates Tholus near Elysium, where recent glacial deposits have been observed (*7*).

The location of the ice deposits predicted by our model and the accumulation rates are not too sensitive to the orbital parameters as long as the obliquity is above 40°. If the water input is enhanced by further raising the obliquity, by increasing the eccentricity with a perihelion in northern summer, or by assuming a larger northern ice cap, the model predicts an extension of the area where water ice can accumulate in the Tharsis Montes region toward Alba Patera.

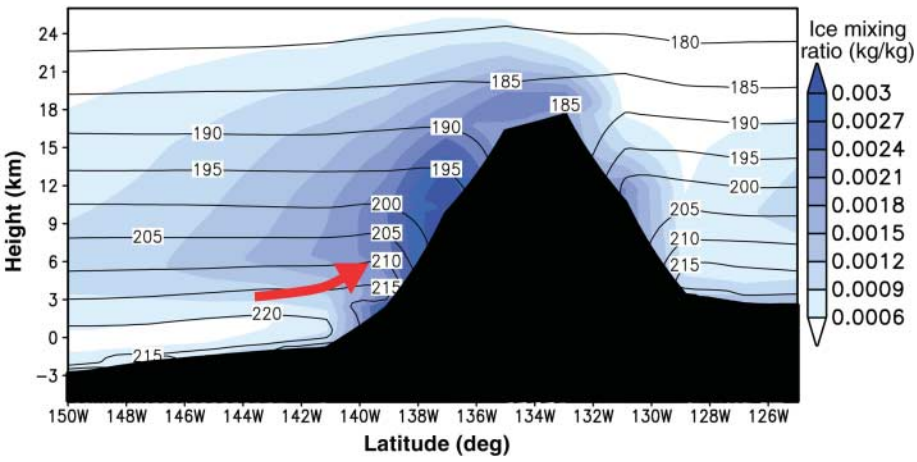

Fig. 3. Cross section of Olympus Mons along the 16°N latitude showing the mean atmospheric ice mass mixing ratio (shaded blue) and the atmospheric temperature (contour, K) averaged over the period of ice accumulation Ls = 125° to 155° (northern summer). The strong northwesterly winds induce adiabatic cooling on the flank of the volcanoes and atmospheric condensation and precipitation.

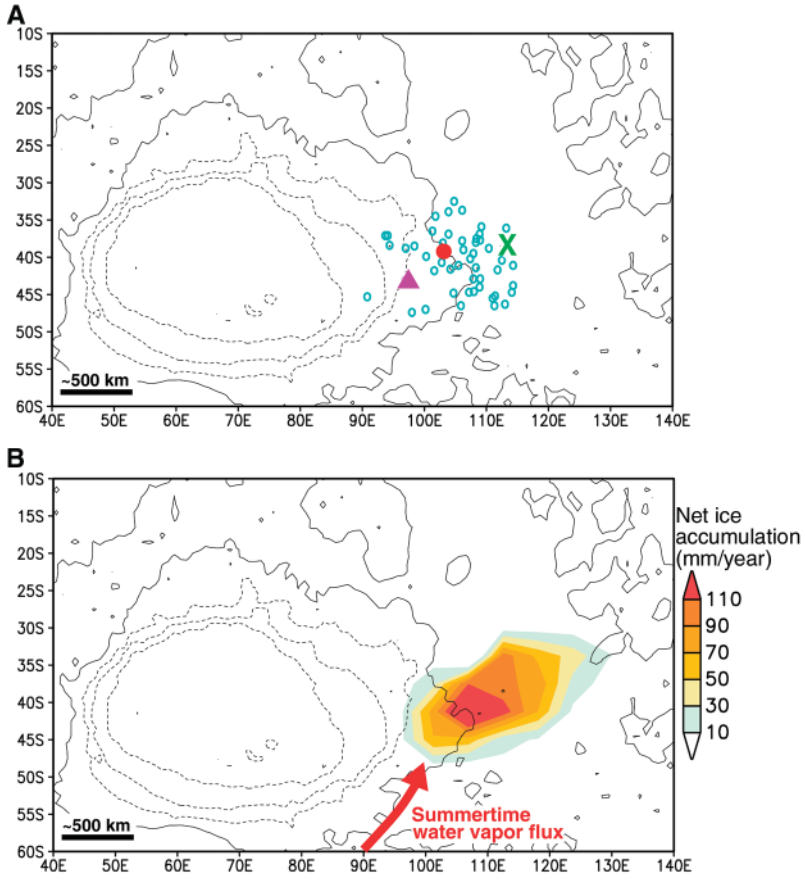

Fig. 4. (**A**) Topographic map of the Hellas Basin with contours every 2 km showing the locations of 54 debris apron complexes (*5*) (blue circles), which are interpreted as ice-rich flow features, the glacier-like landforms recently observed by Mars Express (*1*) (purple triangle, debris apron; red dot, hourglass-shaped deposits), and one of the most spectacular tongue-shaped rock glacier (green cross) observed on Mars (*6*). (**B**) Net surface water ice accumulation (in mm per martian year) predicted in the same area by our simulation performed with 45° obliquity and assuming that surface water ice is initially present only in the southern polar cap.

The north polar cap may not have always been the only source of water during high-obliquity periods. The presence of southern

polar deposits (*24*) and climate model simulations with orbital parameters different than today (*25*) suggest that the south polar region could also have played this role. On this basis, we performed a high-obliquity simulation assuming that ice was available in the south polar region (between 90°S and 80°S) rather than in the north. Under such conditions, ice accumulation still occurs in the southern part of Tharsis (Arsia-Pavonis Montes region and in Syria Planum), but the highest rates are then predicted to be in the eastern Hellas region (Fig. 4), almost exactly where the concentration of ice-related landforms is observed. Interestingly, the process leading to ice precipitation differs from the one occurring on the volcanoes. In eastern Hellas, almost all the ice is accumulated during a 90-day period around southern summer solstice (Fig. 2). At that time, the southern ice cap sublimes and releases large amounts of water vapor to the polar atmosphere. This water vapor is not easily transported toward the equator because the south polar region is isolated by a midlatitude westward summer vortex (*26*, *27*), except near eastern Hellas. There, the deep Hellas Basin forces a stationary planetary wave that results in a strong northward flow that transports large amounts of water out of the polar region (fig. S2). The moist and warm polar air meets colder air coming from northern Hellas, and the subsequent cooling results in strong condensation and precipitation (Fig. 4 and fig. S3). This is a robust mechanism that should not be model-dependent (*28*).

For all the simulations presented here, some quantitative uncertainties remain, because our model is designed to simulate present-day Mars and does not include some processes that may be substantial at high obliquity, like the radiative feedback of water vapor and ice clouds or the scavenging of dust out of the atmosphere. The amount of dust lifted into the atmosphere may also have been different (*28*, *29*). Additional simulations suggest that more atmospheric dust means less ice condensation because dust tends to warm the atmosphere.

The formation of glaciers on Mars appears to be the product of the same martian climate system as that of today, except that high obliquity increases the atmospheric water content and amplifies the circulation. In reality, the complex variations of orbital parameters probably led to several different types of regimes in the past, with water ice alternatively mobilized from the poles to tropical and midlatitude glaciers and then back to high latitudes to possibly form the meters-thick deposits whose remnants have been detected by the Mars Odyssey Gamma Ray Spectrometer (*16*). We do not predict glacier formation in the Deuteronilus–Protonilus Mensae area and other similar areas in the northern midlatitudes. These accumulations might have involved climate changes due to other origins (impacts, volcanism, or catastrophic outflows). However, some combination of orbital parameters or a higher model resolution may be sufficient to simulate ice precipitation in this region without invoking other processes. The mobilization of ice to the low and midlatitudes in preferred locations such as Eastern Hellas also supports a simple, purely atmospheric scenario for the origin of many of the martian gullies (*29*).

References and Notes

1. J. W. Head *et al.*, *Nature* **434**, 346 (2005).
2. G. Neukum *et al.*, *Nature* **432**, 971 (2004).
3. J. W. Head, D. R. Marchant, *Geology* **31**, 641 (2003).
4. D. E. Shean, J. W. Head, D. R. Marchant, *J. Geophys. Res.* **110**, E05001 (2005).
5. T. L. Pierce, D. A. Crown, *Icarus* **163**, 46 (2003).
6. W. K. Hartmann, T. Thorsteinsson, F. Sigurdsson, *Icarus* **162**, 259 (2003).
7. E. Hauber *et al.*, *Nature* **434**, 356 (2005).
8. S. M. Milkovich, J. W. Head, D. R. Marchant, *Icarus*, in press.
9. S. W. Squyres, *J. Geophys. Res.* **84**, 8087 (1979).
10. B. K. Lucchitta, *Icarus* **45**, 264 (1981).
11. P. R. Christensen, *Nature* **422**, 45 (2003).
12. B. K. Lucchitta, *J. Geophys. Res.* **89** (suppl.), 409 (1984).
13. N. Mangold, *J. Geophys. Res.* **108,** 10.1029/2002JE001885 (2003).
14. B. M. Jakosky, M. H. Carr, *Nature* **315**, 559 (1985).
15. M. A. Mischna, M. I. Richardson, R. J. Wilson, D. J. McCleese, *J. Geophys. Res.* **108**, 16-1 (2003).
16. B. Levrard, F. Forget, F. Montmessin, J. Laskar, *Nature* **431**, 1072 (2004).
17. F. Forget *et al.*, *J. Geophys. Res.* **104**, 24155 (1999).
18. F. Montmessin, F. Forget, P. Rannou, M. Cabane, R. M. Haberle, *J. Geophys. Res.* **109**, E10004 (2004).
19. The visible dust optical depth is a measure of the amount of dust in the atmosphere. It is defined as the logarithm of the vertical extinction of radiation.
20. J. Laskar *et al.*, *Icarus* **170**, 343 (2004).
21. In practice, because such a model is too computationally expensive to be run for more than 2 years, we initialized the high-resolution simulation with the atmospheric water vapor predicted at the end of a 10-year identical run but performed the simulation with a lower resolution (3.75° by 5.625°). We then ran the model for 2 additional years at high resolution, at which point the atmosphere had come to an interannually repeatable state.
22. M. I. Richardson, R. J. Wilson, *J. Geophys. Res.* **107**, 7-1 (2002).
23. R. T. Clancy, M. J. Wolff, P. R. Christensen, *J. Geophys. Res.* **108**, 2-1 (2003).
24. P. Thomas, S. Squyres, K. Herkenhoff, A. Howard, B. Murray, in *Mars*, H. H. Kieffer *et al.*, Eds. (Univ. of Arizona Press, Tucson, 1992), pp. 767–795.
25. F. Montmessin, R. M. Haberle, F. Forget, *Proc. Lunar Planet. Sci. Conf.* **35**, 1312 (2004).
26. R. M. Haberle, J. R. Murphy, J. Schaeffer, *Icarus* **161**, 66 (2003).
27. C. E. Newman, S. R. Lewis, P. L. Read, *Icarus* **174**, 135 (2005).
28. Additional simulations performed with more atmospheric water provided to the system by assuming a south water ice cap enlarged by 5° latitude or by using present-day orbit (and thus a warmer southern summer) result in stronger deposition and ice deposits further east.
29. F. Costard, F. Forget, N. Mangold, J. P. Peulvast, *Science* **295**, 110 (2002); published online 29 November 2001 (10.1126/science.1066698).
30. D. H. Scott, K. L. Tanaka, *U. S. Geol. Surv. Misc. Invest. Map I-1802-A* (1986).

31. The LMD Martian global climate model has been developed with the support of CNRS, European Space Agency (ESA), and CNES in collaboration with the Atmospheric, Oceanic, and Planetary Physics group in Oxford University (UK). Much of this work was performed while F.F. was visiting the Space Science Division of NASA Ames Research Center as a Senior National Research Council fellow. We wish to thank J. Hollingsworth, J. Schaeffer, T. Colaprete, and C. P. McKay for their support and advice. The research was also strongly motivated by the recent results from the ESA Mars Express mission within the scope of the Interdisciplinary Scientist Program. J.W.H. thanks the NASA Mars Data Analysis Program for partial support.

Supporting Online Material

www.sciencemag.org/cgi/content/full/311/5759/368/DC1
Figs. S1 to S3

19 September 2005; accepted 15 December 2005
10.1126/science.1120335

South-Seeking Magnetotactic Bacteria in the Northern Hemisphere

Sheri L. Simmons,[1,2] Dennis A. Bazylinski,[3] Katrina J. Edwards[2]*

Magnetotactic bacteria contain membrane-bound intracellular iron crystals (magnetosomes) and respond to magnetic fields. Polar magnetotactic bacteria in vertical chemical gradients are thought to respond to high oxygen levels by swimming downward into areas with low or no oxygen (toward geomagnetic north in the Northern Hemisphere and geomagnetic south in the Southern Hemisphere). We identified populations of polar magnetotactic bacteria in the Northern Hemisphere that respond to high oxygen levels by swimming toward geomagnetic south, the opposite of all previously reported magnetotactic behavior. The percentage of magnetotactic bacteria with south polarity in the environment is positively correlated with higher redox potential. The coexistence of magnetotactic bacteria with opposing polarities in the same redox environment conflicts with current models of the adaptive value of magnetotaxis.

Magnetotactic bacteria form intracellular single-domain ferrimagnetic iron oxide (magnetite, Fe_3O_4) or iron sulfide (greigite, Fe_3S_4) crystals. The torque produced by these chains causes the cells to align and to swim with respect to local or induced magnetic fields (*1–3*). Magnetotactic bacteria are globally distributed at and below the oxic-anoxic interface in chemically stratified freshwater (*4–6*) and marine environments (*7–10*), where they can

reach significant population densities (10^5 cells ml^{-1}) (*4*, *11*). Magnetotaxis is currently thought to enable these bacteria to more rapidly locate habitats with low or no oxygen in a vertical chemical and/or redox gradient (*12*). Here we describe observations that call into question this explanation for the adaptive value of magnetotaxis.

There are two predominant types of magnetotaxis in magnetotactic bacteria: polar and axial (*12*). When observed microscopically in an applied magnetic field, a polar magnetotactic bacterium swims in a preferred direction relative to the local field, whereas an axial bacterium swims back and forth in both directions (*12*). When the direction of an applied field is reversed, a polar bacterium reverses swimming direction, whereas an axial bacterium rotates 180° but continues to swim back and forth (*12*). Axial behavior has only been observed in cultivated strains of the genus *Magnetospirillum* (*12*–*14*), whereas polar behavior is exhibited far more commonly by magnetotactic bacteria in marine samples (*15*). The polarity of polar magnetotactic bacteria is defined as their swimming direction under atmospheric oxygen levels. Here we explore the environmental cues that influence polarity among magnetotactic bacteria.

Previous work asserted that virtually all polar magnetotactic bacteria (>99%) in the Northern Hemisphere have north polarity (*1*, *16*, *17*), which means that they swim toward geomagnetic north when exposed to higher than optimal oxygen levels. In the Northern Hemisphere, owing to the vertical component of the Earth's geomagnetic field, swimming toward geomagnetic north would direct bacteria downward into anoxic sediments or waters in a vertical chemical gradient. In the Southern Hemisphere, polar magnetotactic bacteria swim toward geomagnetic south, presumably for the same reason (*2*, *3*). Here we report observing significant numbers of magnetotactic bacteria in the Northern Hemisphere that swim toward geomagnetic south when exposed to high oxygen (south polarity), the opposite of all previously described magnetotactic behavior. We also show that south polarity in magnetotactic bacteria is statistically correlated with environmental redox chemistry.

A morphologically unusual bacterium with south polarity was found at high density in Salt Pond (Falmouth, MA), a small, seasonally stratified marine basin, in July 2004 (*18*). This bacterium ("barbell") formed chains of two to five cocci, which appeared refractive with differential interference contrast (DIC) microscopy (Fig. 1C). The barbell occurred in narrow layers immediately below the oxygen-sulfide interface in Salt Pond and cooccurred with previously described magnetite- and greigite-producing bacteria (*9*) (Fig. 1C). Magnetotactic bacteria were not present at depths above and below those shown in Fig. 1.

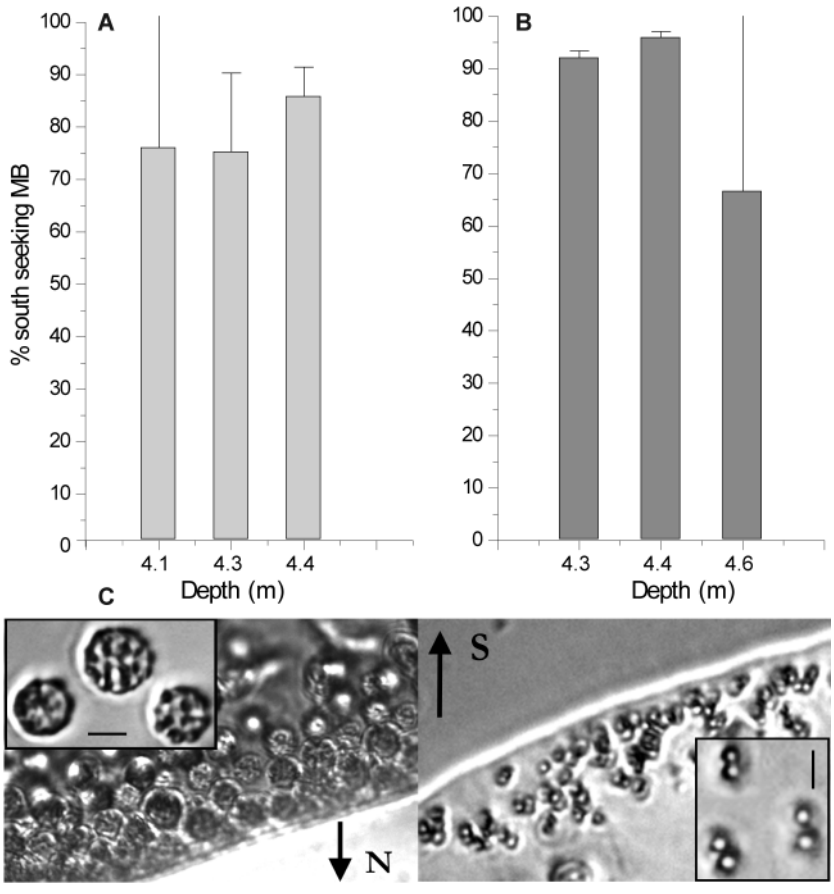

Fig. 1. The barbell and small rod-shaped cells (not shown) have primarily south polarity at discrete depths in Salt Pond. % S seekers is 100 × the ratio of magnetotactic bacteria with south polarity to total magnetotactic bacteria. The mean and standard deviation were calculated from microscopic counts of two drops from the same sample. In both samples, higher standard deviation was associated with low total cell counts. (**A**) A small rod-shaped magnetotactic bacterium had south polarity in Salt Pond on 1 July 2004. (**B**) Barbells had south polarity in Salt Pond on 2 July 2004. (**C**) MMP with north polarity (left) and barbells with south polarity (right) co-occurring in water from Salt Pond on 2 July 2004. Insets show cell morphology. All scale bars, 5 μm.

Because of the high cell density ($4.6 \pm 1.1 \times 10^4$ cells ml^{-1}, on the basis of direct counts), we were able to observe the polarity of the barbell without potential interference from prior magnetic enrichment (*18*). Over 90% of the barbells from bulk water samples showed south polarity in the standard drop assay (*18*) (Fig. 1B). Morphologically distinct populations with north polarity cooccurred with the barbell, which suggests that south polarity was not universal among all magnetotactic bacterial taxa in a given environment (Fig. 1C).

We identified the barbell as a member of the *Desulfobulbaceae* family of the delta *Proteobacteria* (Fig. 2), using sequencing of 16*S* ribosomal DNA (rDNA) and catalyzed reporter deposition–in situ hybridization (CARDFISH) with custom-designed probes (*18*). It is closely related to *Desulforhopalus singaporensis*, which also has an unusual chain morphology (*19*). The barbell is the third magnetotactic bacterium identified in the delta *Proteobacteria*; of the other two, one produces magnetite (*20*) and the other greigite (*21*).

We also observed a population of small magnetotactic rods with south polarity in Salt Pond on 1 July 2004 (Fig. 1A). These appeared at high density ($1.5 \pm 0.47 \times 10^4$ cells ml^{-1}) at and below the narrow chemocline and had nearly 100% south polarity at every depth at which they occurred. South polarity is not an artifact of our assay; we did not directly observe polarity reversal caused by the small magnets we used, and past experiments have required far higher field strengths (*2*, *22*).

We only observed these dense populations of magnetotactic bacteria with overwhelmingly south polarity on one occasion. Further observations indicated that magnetotactic bacteria more frequently occurred at lower abundance

[1]Massachusetts Institute of Technology–Woods Hole Oceanographic Institution (MIT-WHOI) Joint Program in Oceanography, [2]Geomicrobiology Group, Department of Marine Chemistry and Geochemistry, MS 52, WHOI, Woods Hole, MA 02543, USA. [3]Department of Biochemistry, Biophysics, and Molecular Biology, Iowa State University, Ames, IA 50011, USA.

*To whom correspondence should be addressed. E-mail: katrina@whoi.edu

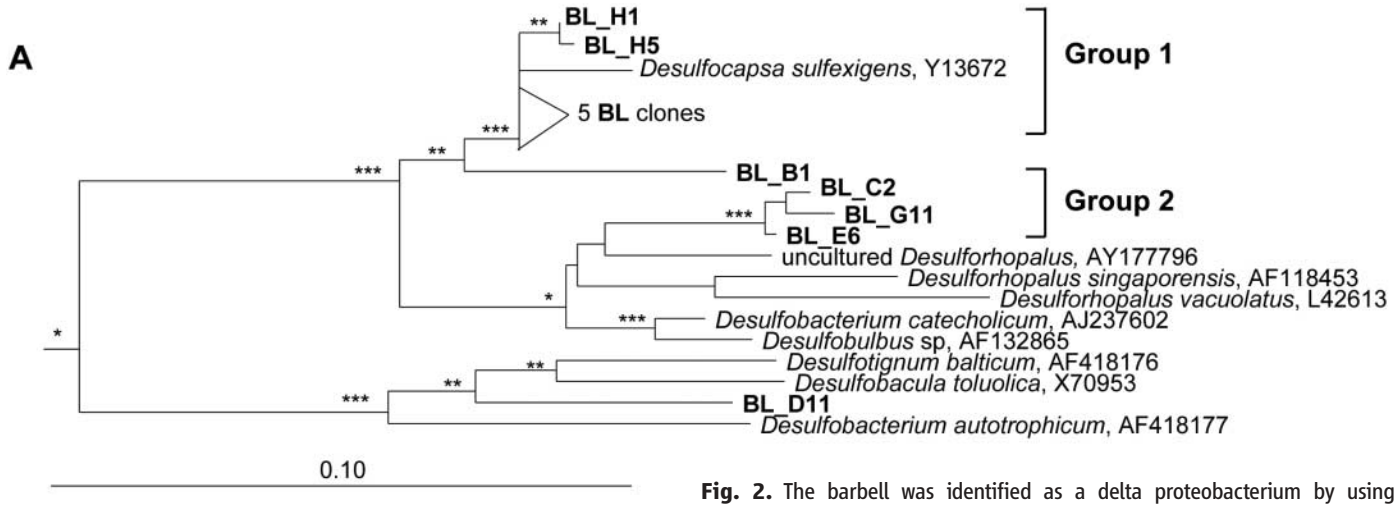

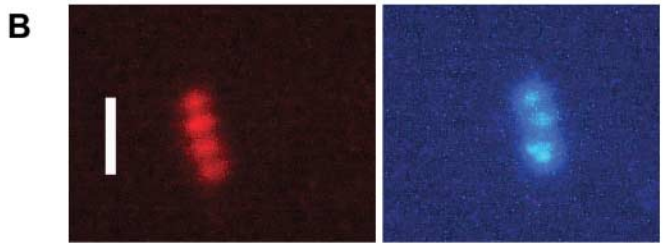

Fig. 2. The barbell was identified as a delta proteobacterium by using CARDFISH. (**A**) Two clusters of 16*S* rDNA sequences (marked with BL_*) were obtained from samples highly enriched in the barbell bacterium. GenBank sequence accession numbers are listed in (*23*). The tree was constructed using maximum likelihood analysis and 1000 bootstrap replicates in Phylip. Nodes with greater than 90% bootstrap support are marked with ***, 60 to 90% with **, and 50 to 60% with *. A mask was used to allow for inclusion of partial sequences (700 to 800 bp), and sequences were exported from ARB with a 25% homology filter based on a complete alignment of delta *Proteobacteria*. *Desulfovibrio desulfuricans* was used as an outgroup to root the tree (not shown). Short sequences were added using the ARB Parsimony tool without changing tree topology. Parsimony analysis also supported the tree topology. (**B**) Left, the barbell with south polarity hybridizes with a horseradish peroxidase (HRP)–labeled probe (visualized with Cy3-tyramides) targeting group 2 sequences (related to *Desulforhopalus* spp.). Right, a DAPI stain of the same cell. Scale bar, 5 μm.

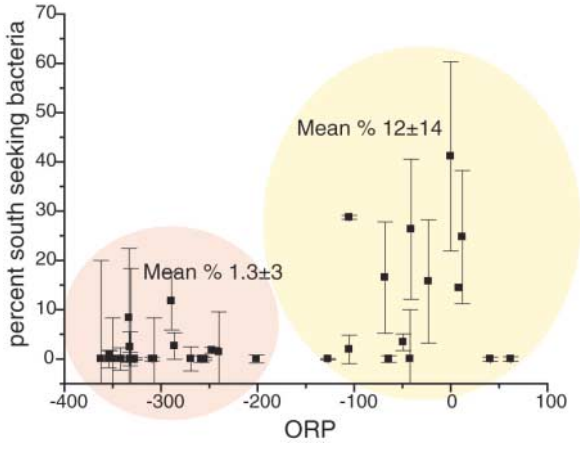

Fig. 3. South polarity is related to environmental ORP. The percentage of bacteria with south polarity is shown versus the oxidation-reduction potential of Salt Pond in situ water for all magnetotactic bacteria present in the water column for each of five dates in August and September 2005. Percentages were calculated as the total number of bacteria with south polarity divided by the total number of bacteria in three separate drops. The mean is shown ± one standard deviation. Experimental error (the variation from three separate drops) and statistical error (1/total number of cells counted) were calculated for all points, and the larger value is shown. The yellow oval denotes data points with ORP > –200, and the pink oval denotes data points with ORP < –200. As a general trend, most of the counts at ORP > –200 are for magnetotactic cocci and barbells. In 2005, the barbell did not occur at high levels comparable to our observation in 2004.

and showed a mixture of north and south polarities, with occasional blooms dominated by specific taxa. Quantitative polymerase chain reaction (PCR) on samples taken from Salt Pond in summer 2003 (*11*) showed that abundances of the barbell fluctuate greatly during the seasonal stratification of Salt Pond. The barbell is most abundant when the pond is less stratified, in the early and late season (10^4 to 10^5 cells ml^{-1}). This is consistent with our observations of dense populations of the barbell and an unidentified small rod early in summer 2004, when the chemocline was very narrow. The sharp chemocline may have contributed to the high abundance of bacteria with south polarity.

To determine whether water chemistry is correlated with the presence of magnetotactic bacteria with south polarity, we determined the total numbers of magnetotactic bacteria with north and south polarity across the Salt Pond chemocline in summer 2005 in conjunction with fine-scale physical and chemical profiling (*18*). The oxidation-reduction potential (ORP), collected in situ, provided a bulk descriptor of water chemistry; more negative values indicate a more reducing environment. Total numbers of magnetotactic bacteria peaked between ORP values of –50 and –200.

We found a significant relationship between ORP and the percentage of magnetotactic bacteria with south polarity (Fig. 3). In more reducing conditions (ORP <–200), the average percentage of bacteria with south polarity was 1.3 ± 3. Greigite-producing organisms predominated in this group. In more oxidizing conditions (ORP >–200), the average percentage of bacteria with south polarity was 12 ± 14. The barbell and small magnetite-producing cocci predominated in this group, and most organisms with south polarity were barbells. The high variance is due to the dominance of cocci with north polarity in some samples. The means of the two groups were significantly different at the $P = 0.01$ level (independent t test). There was no correlation between polarity and the total numbers of magnetotactic bacteria observed. Our results suggest that either the polarity of a single bacterium is affected by ORP (or a redox active chemical species correlated

with ORP), or that south polarity is characteristic of a particular species that occurs at a specific ORP.

The coexistence of magnetotactic bacteria with north and south polarity in the same chemical environment contradicts the current accepted model of magnetotaxis, which states that all magnetotactic bacteria in the Northern Hemisphere swim north (downward in situ) when exposed to oxidized conditions to reach their preferred microaerobic or anaerobic habitat. We observed that barbells with south polarity and cocci with north polarity coexist in microaerobic conditions in the water column. On the basis of this distributional pattern, south polarity is clearly not used to direct the barbell upward in the water column toward higher oxygen levels. The current model does not, therefore, provide any explanation that can account for the existence of south polarity.

This model implicitly assumes that polarity observed in the laboratory under atmospheric oxygen levels is equivalent to polarity in situ. Our results suggest that this assumption might be incorrect. Although the benefit of north polarity in situ is clear for microaerophilic magnetotactic bacteria, south polarity would have a clearly deleterious effect by directing the bacteria away from their preferred chemical environment. There are reasons to believe the behavior of magneotactic bacteria in situ could differ from behavior in the laboratory. Magnetotactic bacteria at the chemocline of a stratified water column rarely, if ever, experience atmospheric oxygen levels like those in the standard laboratory assay for polarity. They also experience chemical gradients (particularly of iron and sulfur species) not present in a drop of water exposed to air in the laboratory assay. It is also possible that bacteria with north and south polarity possess different chemo- or redox-sensors that have opposite responses to chemical concentrations out of the range they typically experience. On the basis of these results, new models are clearly needed to explain the adaptive significance of magnetotaxis by magnetotactic bacteria in the environment.

References and Notes

1. R. P. Blakemore, *Annu. Rev. Microbiol.* **36**, 217 (1982).
2. R. P. Blakemore, R. B. Frankel, A. J. Kalmijn, *Nature* **286**, 384 (1980).
3. J. L. Kirschvink, *J. Exp. Biol.* **86**, 345 (1980).
4. S. Spring *et al.*, *Appl. Environ. Microbiol.* **59**, 2397 (1993).
5. S. Spring, R. Amann, W. Ludwig, K.-H. Schleifer, N. Petersen, *Syst. Appl. Microbiol.* **15**, 116 (1992).
6. T. Sakaguchi, A. Arakaki, T. Matsunaga, *Int. J. Syst. Evol. Microbiol.* **52**, 215 (2002).
7. H. Petermann, U. Bleil, *Earth Planet. Sci. Lett.* **117**, 223 (1993).
8. J. F. Stolz, S.-B. R. Chang, J. L. Kirschvink, *Nature* **321**, 849 (1986).
9. S. L. Simmons, S. M. Sievert, R. B. Frankel, D. A. Bazylinski, K. J. Edwards, *Appl. Environ. Microbiol.* **70**, 6230 (2004).
10. D. A. Bazylinski *et al.*, *Appl. Environ. Microbiol.* **61**, 3232 (1995).
11. S. L. Simmons, K. J. Edwards, manuscript in preparation.
12. R. B. Frankel, D. A. Bazylinski, M. S. Johnson, B. L. Taylor, *Biophys. J.* **73**, 994 (1997).
13. R. P. Blakemore, D. Maratea, R. S. Wolfe, *J. Bacteriol.* **140**, 720 (1979).
14. A. M. Spormann, R. S. Wolfe, *FEMS Microbiol. Lett.* **22**, 171 (1984).
15. S. L. Simmons, K. J. Edwards, unpublished observations.
16. R. P. Blakemore, *Science* **190**, 377 (1975).
17. T. T. Moench, W. A. Konetzka, *Arch. Microbiol.* **119**, 203 (1978).
18. Materials and methods are available as supporting material on *Science* Online.
19. T. J. Lie, M. L. Clawson, W. Godchaux, E. R. Leadbetter, *Appl. Environ. Microbiol.* **65**, 3328 (1999).
20. R. Kawaguchi *et al.*, *FEMS Microbiol. Lett.* **126**, 277 (1995).
21. E. F. DeLong, R. B. Frankel, D. A. Bazylinski, *Science* **259**, 803 (1993).
22. A. J. Kalmijn, R. P. Blakemore, in *Animal Migration, Navigation, and Homing*, K. Schmidt-Koenig, W. Keeton, Eds. (Springer-Verlag, Berlin, 1978), pp. 354-355.

23. We thank P. Canovas and O. Rafie for field and lab assistance; R. Frankel, E. Webb, and S. Sievert for input on the manuscript; and K. Canter for use of a magnetometer. S.L.S. was partially supported by a National Defense Science and Engineering Graduate Fellowship. This work was partially funded by grants to S.L.S. and K.J.E. from the WHOI Reinhart Coastal Research Center, the WHOI Ocean Venture Fund, and the WHOI Ocean Life Institute. D.A.B. is supported by National Science Foundation grant EAR-0311950. GenBank sequence accession numbers for the sequences reported in this study are as follows. Group 1: BL_G6, DQ322653; BL_H12, DQ322654; BL_H1, DQ322655; BL_H4, DQ322662, BL_H5, DQ322656; BL_C10, DQ322657; BL_C5, DQ322658. Group 2, south-seeking bacterium: BL_C2c, DQ322659; BL_E6c, DQ322660; BL_G11c, DQ322661.

Supporting Online Material

www.sciencemag.org/cgi/content/full/311/5759/371/DC1
Materials and Methods
References

21 November 2005; accepted 20 December 2005
10.1126/science.1122843

Sampling the Antibiotic Resistome

Vanessa M. D'Costa,[1] Katherine M. McGrann,[1] Donald W. Hughes,[2] Gerard D. Wright[1]*

Microbial resistance to antibiotics currently spans all known classes of natural and synthetic compounds. It has not only hindered our treatment of infections but also dramatically reshaped drug discovery, yet its origins have not been systematically studied. Soil-dwelling bacteria produce and encounter a myriad of antibiotics, evolving corresponding sensing and evading strategies. They are a reservoir of resistance determinants that can be mobilized into the microbial community. Study of this reservoir could provide an early warning system for future clinically relevant antibiotic resistance mechanisms.

Most clinically relevant antibiotics originate from soil-dwelling actinomycetes (*1*). Antibiotic producers harbor resistance elements for self-protection that are often clustered in antibiotic biosynthetic operons (*2*, *3*). Genes orthologous to these have been identified on mobile genetic elements in resistant pathogens in clinical settings. It has been suggested that aminoglycoside-modifying kinases (*4*) and the alternate peptidoglycan biosynthetic machinery that confers resistance to vancomycin (*5*) probably originated in soil-dwelling antibiotic producers.

The presence of antibiotics in the environment has promoted the acquisition or independent evolution of highly specific resistance elements in the absence of innate antibiotic production [such as vancomycin resistance in *Streptomyces coelicolor*, *Paenibacillus*, and *Rhodococcus* (*6*, *7*)]. The soil could thus serve as an underrecognized reservoir for resistance that has already emerged or has the potential to emerge in clinically important bacteria. Consequently, an understanding of resistance determinants present in the soil—the soil resistome—will provide information not only about antibiotic resistance frequencies but also about new mechanisms that may emerge as clinical problems.

We isolated a morphologically diverse collection of spore-forming bacteria from soil samples originating from diverse locations (urban, agricultural, and forest). Strains that resembled actinomycetes both morphologically and microscopically were serially subcultured to apparent homogeneity. Amplification and sequencing of 16*S* ribosomal DNA from a subset of strains indicated that they belonged to the actinomycete genus *Streptomyces*, whose species synthesize over half of all known antibiotics (*1*). We constructed a library of 480 strains that was subsequently screened against 21 antibiotics, including natural products (such as vancomycin and erythromycin), their semisynthetic derivatives (such as minocycline and cephalexin), and completely synthetic molecules (such as ciprofloxacin and linezolid). The antibiotics encompassed all major bacterial targets (*8*) and included drugs

[1]Antimicrobial Research Centre, Department of Biochemistry and Biomedical Sciences, [2]Department of Chemistry, McMaster University, Ontario, Canada, L8N 3Z5.

*To whom correspondence should be addressed. E-mail: wrightge@mcmaster.ca

that have been on the market for decades as well as several that have only recently been clinically approved (such as telithromycin and tigecycline).

The screen was conducted at high antibiotic concentrations (Fig. 1), and strains of interest were analyzed by determination of the minimal inhibitory concentration (MIC). A subset of isolates was characterized on the basis of mode of resistance in order to distinguish resistance arising from antibiotic alteration or modification from that arising from nondestructive mechanisms (such as efflux, altered target, or transport) (Table 1).

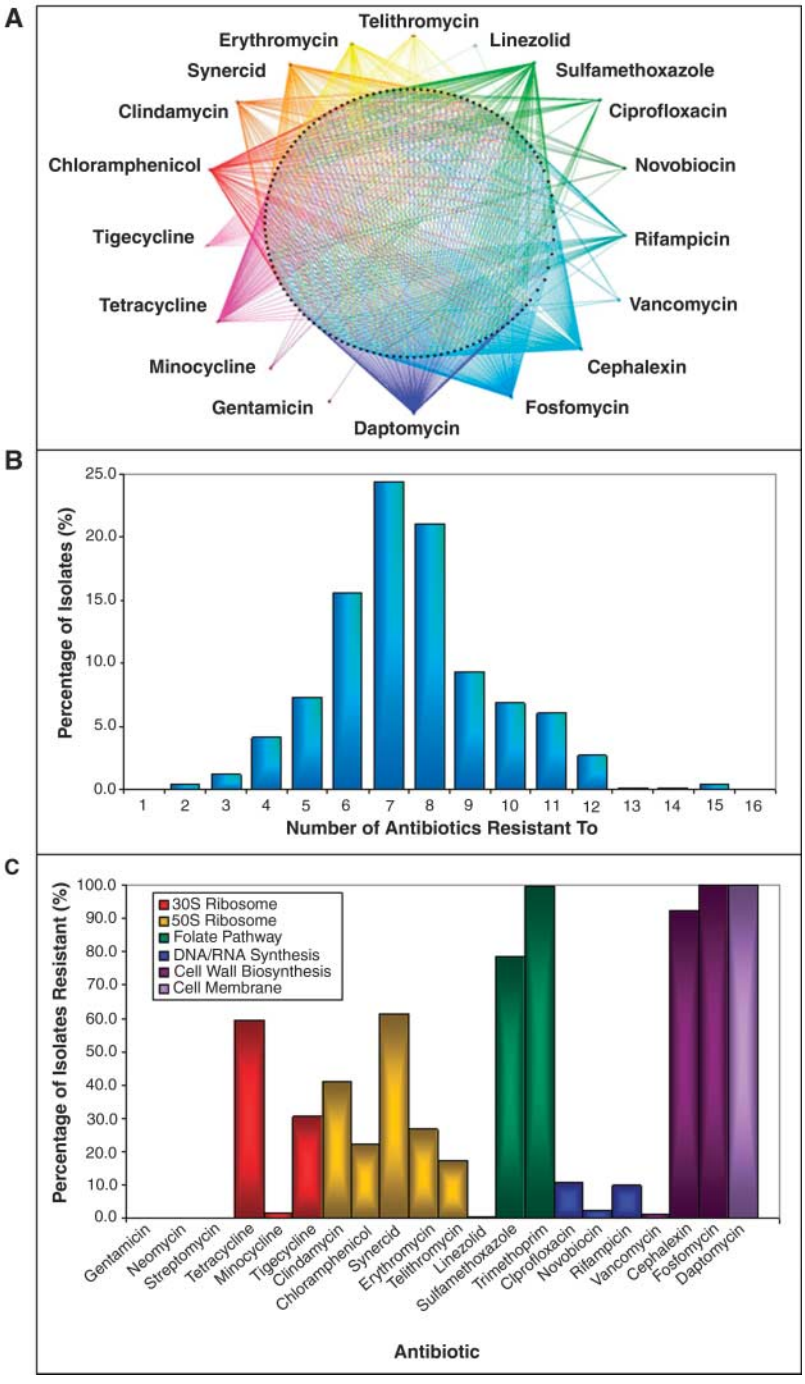

Fig. 1. Antibiotic resistance profiling of 480 soil-derived bacterial isolates. (**A**) Schematic diagram illustrating the phenotypic density and diversity of resistance profiles. The central circle of 191 black dots represents different resistance profiles, where a line connecting the profile to the antibiotic indicates resistance. (**B**) Resistance spectrum of soil isolates. Strains were individually screened from spores on solid *Streptomyces* isolation media (SIM) against 21 antibiotics at 20 μg of antibiotic per ml of medium (μg/ml). Resistance was defined as reproducible growth in the presence of antibiotic. (**C**) Resistance levels against each antibiotic of interest.

Without exception, every strain in the library was found to be multi-drug resistant to seven or eight antibiotics on average, with two strains being resistant to 15 of 21 drugs (Fig. 1B). Reproducible resistance to most of the antibiotics, regardless of origin, was observed, and almost 200 different resistance profiles were seen (Fig. 1, A and C), exemplifying the immense genetic and phenotypic diversity of the collection of bacteria.

Several antibiotics, including the synthetic dihydrofolate reductase (DHFR) inhibitor trimethoprim and the new lipopeptide daptomycin, were almost universally ineffective against the library. The genomes of *S. coelicolor* and *S. avermitilis* do not contain annotated DHFR genes, which is consistent with insensitivity to trimethoprim (*9*). However, extensive daptomycin resistance was not anticipated. Recently approved by the Food and Drug Administration (FDA), daptomycin is highly active against Gram-positive bacteria, including multi-drug–resistant pathogens (*10*, *11*). A member of a large antibiotic class commonly produced by actinomycetes, daptomycin is thought to act by insertion into the bacterial cell membrane in a Ca^{2+}-dependent manner (*12*, *13*).

Eighty percent of the resistant strains assayed inactivated daptomycin after 48 hours of cell growth, while the remaining strains retained active antibiotic in the culture media (Table 1). This finding is notable not only because it is only the second documented occurrence of daptomycin inactivation (*14*) but because of its unprecedented high frequency. Furthermore, it suggests that there are multiple mechanisms of daptomycin resistance in soil organisms.

We uncovered a wealth of inactivating enzymes produced by soil bacteria. Of the 11 antibiotics screened, bacterial isolates were detected that putatively metabolized 6 drugs (Table 1), including rifampicin and Synercid.

Rifampicin, a semisynthetic derivative of a natural *Amycolatopsis mediterranei* product, is central to the treatment of mycobacterial infections. Forty percent of resistant isolates were capable of inactivating the drug, which is intriguing because clinically, the most prevalent mechanism of rifampin resistance is through point mutations in the target: RNA polymerase's β subunit.

Synercid, which was FDA-approved in 1999 for the treatment of drug-resistant bacteremia, is a combination of two semisynthetic derivatives of *Streptomyces* metabolites, each with a distinct mode of action. Eighteen percent of resistant isolates tested were able to detoxify both antibiotics. These findings collectively reinforce the importance of enzymatic antibiotic inactivation as a means of resistance (*4*).

The screen yielded five strains that were highly resistant to the glycopeptide vancomycin (MICs of 128 to 256 μg/ml). Resistance in both clinically significant and glycopeptide-producing

bacteria is the result of the biosynthesis of an altered peptidoglycan terminating in D-alanine-D-lactate rather than D-alanine-D-alanine, resulting in a poor binding affinity to vancomycin. This mechanism is encoded by a cluster of three genes, *vanH-vanA-vanX*, which can be readily identified by polymerase chain reaction analysis in resistant *Streptomyces* (*5*). Using this strategy, the cluster was amplified in 80% of resistant strains (fig. S1). The outlying strain AA#4 appeared to be resistant by a nondestructive mechanism and displayed a distinct glycopeptide resistance profile. Although the *vanHAX* strains demonstrated vancomycin resistance (MICs of 128 to 256 μg/ml) but sensitivity to the lipoglycopeptide teicoplanin (MICs of 1 to 4 μg/ml), AA#4 was resistant to both (MICs of vancomycin and teicoplanin of 256 μg/ml).

Table 1. Antibiotic inactivation screen of the soil library. Cultures of liquid SIM supplemented with antibiotic (20 μg/ml) were grown from spore suspensions. Supernatants were used as samples in disk diffusion assays, and putative inactivating strains were identified by the absence of a zone of inhibition.

Antibiotic	Number of strains		Complete inactivation: %	
	Resistant	Screened for inactivation	Of isolates screened	Of library
Cephalexin	442	16	18.8	N/A*
Ciprofloxacin	52	52	0.0	0.0
Clindamycin	107	46	0.0	N/A
Daptomycin	480	80	80.0	N/A
Erythromycin	128	128	7.0	1.9
Novobiocin	12	12	0.0	0.0
Rifampicin	49	49	40.8	4.2
Synercid	294	71	18.3	N/A
Telithromycin	83	83	4.8	0.8
Trimethoprim	478	80	0.0	N/A
Vancomycin	5	5	0.0	0.0

*Not applicable. Statistic cannot be determined, because all resistant isolates were not assayed.

Synthetic fluoroquinolones target DNA gyrase A (GyrA)–dependent supercoiling and topoisomerase IV–dependent decatenation of bacterial DNA, inhibiting DNA replication and segregation (*15*, *16*). Clinical resistance occurs primarily through point mutations in the N-terminal region of *gyrA*, termed the quinolone resistance–determining region (QRDR) (*17*); however, resistance has also been documented through antibiotic efflux (*17*) and plasmid-mediated protection of DNA gyrase (*18*).

Despite a lack of known prior exposure to fluoroquinolones or bacterially synthesized analogs, 11% of strains demonstrated intrinsic resistance to ciprofloxacin (Fig. 1C, MICs of 6 to 128 μg/ml). Of the 52 resistant strains, none eliminated fluoroquinolone antibacterial activity, indicating that enzymatic inactivation was unlikely (Table 1). To investigate the possibility of QRDR mutation, this region was cloned and sequenced from 38 resistant isolates (Fig. 2). Eleven different amino acid substitutions were identified at nine QRDR locations in 24% of strains sequenced. These included locations commonly associated with clinical ciprofloxacin resistance (such as Ser^{83} and Asp^{87}, using the *Escherichia coli* numbering system), as well as novel sites within the QRDR (such as Met^{100} and Ser^{110}). Among these strains, the isolate with the highest MIC displayed a mutation at a novel location (Ser^{110}). The high incidence of mutations in the absence of obvious environmental selective pressures is consistent with

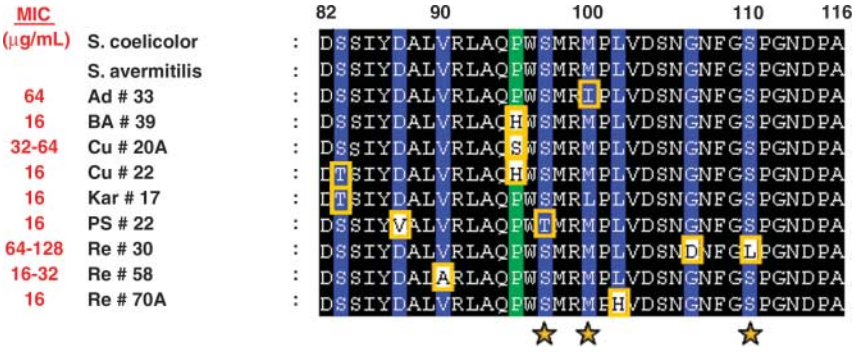

Fig. 2. Protein sequence alignment of the QRDR of ciprofloxacin-resistant strains exhibiting mutations. A 266–base pair region of *gyrA* was amplified in resistant strains and sequenced. Mutations are labeled in orange, and residues are numbered according to the *E. coli* system. Black sites are completely conserved among the 38 strains sequenced, blue sites display 80 to 99% identity, and green sites demonstrate 60 to 80% sequence identity. A white background represents amino acids not displaying similarity with their wild-type counterpart. Sites labeled with a star are novel with respect to mutations. The corresponding MICs of ciprofloxacin are indicated at the left.

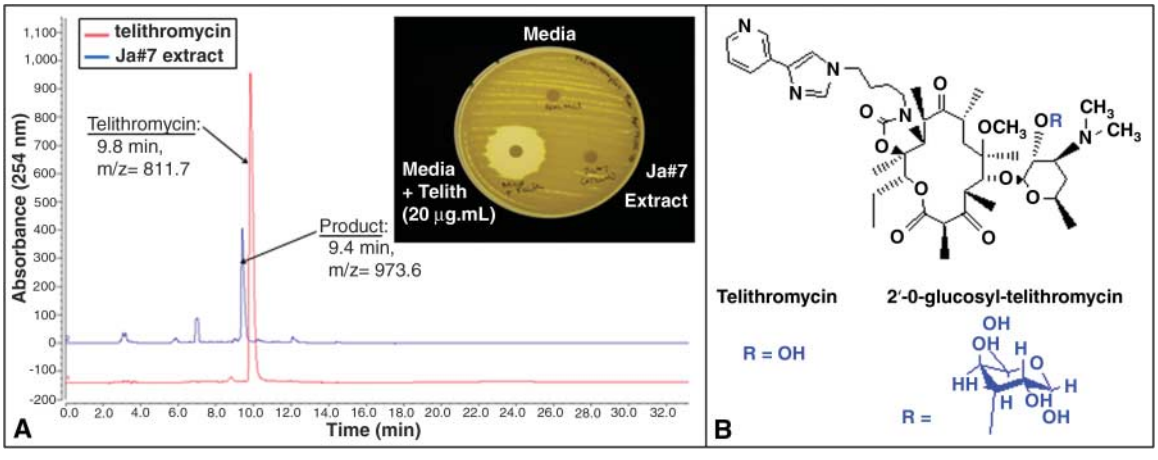

Fig. 3. Modification of telithromycin by strain Ja#7. (**A**) Culture media of Ja#7 grown in the presence of 20 μg/ml telithromycin were analyzed by high-performance liquid chromatography with in-line electrospray mass spectrometry analysis. The modification of telithromycin was accompanied by a shift in retention time, an increase in mass-to-charge (*m/z*) ratio, and the loss of antimicrobial activity against the indicator organism *Micrococcus luteus*. (**B**) Structures of telithromycin and the Ja#7 inactivation product.

previous studies that found natural sequence variation within this domain in soil bacteria (*19*). Knowledge of such natural variations could complement studies on clinical isolates to guide the rational development of next-generation fluoroquinolones that will be active against resistant strains.

Resistance to macrolide antibiotics in pathogens of clinical significance has increased considerably over recent decades and is commonly a result of antibiotic efflux and ribosomal protection mechanisms (*20*, *21*). Substantial levels of macrolide resistance were also detected in our soil isolate library, both to the natural product erythromycin (introduced in 1952, 27%), and the semisynthetic telithromycin (FDA-approved in 2004, 17%). The high frequency of telithromycin resistance was particularly intriguing, because telithromycin is known for its activity against macrolide-resistant bacteria.

Five percent of library isolates detoxified telithromycin in culture media (Table 1). One of these, *Streptomyces* strain Ja#7 (MIC of 32 μg/ml), completely modified telithromycin to an inactive hydrophilic product with a mass of 973.6 daltons (Fig. 3). This addition of 162 daltons to telithromycin (811.7 daltons) is a signature indicator of monoglycosylation. Large-scale purification of the product, followed by multidimensional and multinuclear magnetic resonance analysis, confirmed that the inactive product was 2′-*O*-glucosyl-telithromycin (table S1).

Modification of the cladinose 2′-OH of erythromycin is known to result in antibiotic resistance (*22*, *23*). However, Ja#7, despite its ability to inactivate telithromycin, was unable to completely inactivate erythromycin or its derivative clarithromycin under identical conditions. Thus, a distinct mechanism seems to be operating. Given the abundance of resistance determinants in streptomycetes that are homologous to those in clinically significant pathogens (*5*, *24*, *25*), it is evident that once this mechanism is fully characterized, it should be monitored as telithromycin use increases clinically and resistant organisms inevitably emerge.

This study provides an analysis of the antibiotic resistance potential of soil microorganisms. The frequency of high-level resistance seen in the study to antibiotics that have for decades served as gold-standard treatments, as well as those only recently approved for human use, is remarkable. No class of antibiotic was spared with respect to bacterial target or natural or synthetic origin. Although this study does not provide evidence for the direct transfer of resistance elements from the soil resistome to pathogenic bacteria, it identifies a previously underappreciated density and concentration of environmental antibiotic resistance. The level and diversity of resistance uncovered in this work is only partially reflective of the true extent of the environmental resistome, because this study was restricted exclusively to culturable spore-forming bacteria, which represent only a fraction of soil-dwelling bacteria. For example, a recent soil metagenome analysis uncovered several aminoglycoside resistance genes in uncultured organisms (*26*). Furthermore, the primary screen was conducted at high antibiotic concentrations, thereby excluding phenotypes exhibiting low to intermediate resistance. The level of resistance genes in the environment is therefore very likely to be substantially higher and the antibiotic resistome much more extensive than this study reveals.

The survey of antibiotic resistance mechanisms can assist the elucidation of novel mechanisms that may emerge clinically, as well as serve as a foundation for new antibiotic development. In addition, the study of enzymatic inactivation could lead to the development of inhibitors for combination therapies to restore antimicrobial activity.

References and Notes

1. T. Kieser, M. J. Bibb, M. J. Buttner, K. F. Chater, D. A. Hopwood, *Practical Streptomyces Genetics* (John Innes Foundation, Norwich, UK, ed. 1, 2000).
2. B. K. Hubbard, C. T. Walsh, *Angew. Chem. Int. Ed. Engl.* **42**, 730 (2003).
3. E. Cundliffe *et al.*, *Antonie Leeuwenhoek* **79**, 229 (2001).
4. J. Davies, *Science* **264**, 375 (1994).
5. C. G. Marshall, I. A. Lessard, I. Park, G. D. Wright, *Antimicrob. Agents Chemother.* **42**, 2215 (1998).
6. H. J. Hong, M. S. Paget, M. J. Buttner, *Mol. Microbiol.* **44**, 1199 (2002).
7. L. Guardabassi, A. Dalsgaard, *Appl. Environ. Microbiol.* **70**, 984 (2004).
8. C. T. Walsh, *Antibiotics: Actions, Origins, Resistance* (American Society for Microbiology Press, Washington, DC, ed. 1, 2003).
9. H. Myllykallio, D. Leduc, J. Filee, U. Liebl, *Trends Microbiol.* **11**, 220 (2003).
10. D. R. Snydman, N. V. Jacobus, L. A. McDermott, J. R. Lonks, J. M. Boyce, *Antimicrob. Agents Chemother.* **44**, 3447 (2000).
11. I. A. Critchley *et al.*, *Antimicrob. Agents Chemother.* **47**, 1689 (2003).
12. W. E. Alborn Jr., N. E. Allen, D. A. Preston, *Antimicrob. Agents Chemother.* **35**, 2282 (1991).
13. D. Jung, A. Rozek, M. Okon, R. E. Hancock, *Chem. Biol.* **11**, 949 (2004).
14. M. Debono *et al.*, *J. Antibiot. (Tokyo)* **41**, 1093 (1988).
15. M. Gellert, K. Mizuuchi, M. H. O'Dea, T. Itoh, J. I. Tomizawa, *Proc. Natl. Acad. Sci. U.S.A.* **74**, 4772 (1977).
16. H. Peng, K. J. Marians, *J. Biol. Chem.* **268**, 24481 (1993).
17. L. J. Piddock, *Drugs* **58** (suppl. 2), 11 (1999).
18. J. H. Tran, G. A. Jacoby, *Proc. Natl. Acad. Sci. U.S.A.* **99**, 5638 (2002).
19. B. Waters, J. Davies, *Antimicrob. Agents Chemother.* **41**, 2766 (1997).
20. G. V. Doern *et al.*, *Antimicrob. Agents Chemother.* **45**, 1721 (2001).
21. P. Descheemaeker *et al.*, *J. Antimicrob. Chemother.* **45**, 167 (2000).
22. N. Noguchi *et al.*, *Antimicrob. Agents Chemother.* **39**, 2359 (1995).
23. E. Cundliffe, *Antimicrob. Agents Chemother.* **36**, 348 (1992).
24. C. J. Thompson, G. S. Gray, *Proc. Natl. Acad. Sci. U.S.A.* **80**, 5190 (1983).
25. I. Chopra, M. Roberts, *Microbiol. Mol. Biol. Rev.* **65**, 232 (2001).
26. C. S. Riesenfeld, R. M. Goodman, J. Handelsman, *Environ. Microbiol.* **6**, 981 (2004).

27. We thank K. P. Koteva for helpful discussions and analytical expertise; B. Ghadaki, C. Capone, and T. Patel for help with construction of the soil library; and S. Projan, P. Bradford, and J. Silverman for careful reading of the manuscript. This work was funded by the Canadian Institutes of Health Research and by a Canada Research Chair to G.D.W. Accession numbers for nucleotide sequences deposited in GenBank run consecutively from DQ311010 to DQ311051.

Supporting Online Material

www.sciencemag.org/cgi/content/full/311/5759/374/DC1
Materials and Methods
Figs. S1 to S4
Tables S1 to S5
References

30 September 2005; accepted 12 December 2005
10.1126/science.1120800

Vaccinia Virus–Induced Cell Motility Requires F11L-Mediated Inhibition of RhoA Signaling

Ferran Valderrama, João V. Cordeiro, Sibylle Schleich, Friedrich Frischknecht,* Michael Way†

RhoA signaling plays a critical role in many cellular processes, including cell migration. Here we show that the vaccinia F11L protein interacts directly with RhoA, inhibiting its signaling by blocking the interaction with its downstream effectors Rho-associated kinase (ROCK) and mDia. RNA interference–mediated depletion of F11L during infection resulted in an absence of vaccinia-induced cell motility and inhibition of viral morphogenesis. Disruption of the RhoA binding site in F11L, which resembles that of ROCK, led to an identical phenotype. Thus, inhibition of RhoA signaling is required for both vaccinia morphogenesis and virus-induced cell motility.

The spatial and temporal regulation of cell adhesion and motility is essential during development and throughout the lifetime of multicellular organisms (*1*, *2*). Deregulation of these two fundamental cellular processes frequently occurs during pathological situations such as tumor cell metastasis (*3*, *4*). Dramatic changes in cell migration and adhesion, as well as loss of contact inhibition, are also observed during many viral infections, including that of vaccinia virus (*5*, *6*). In contrast to the wild-type Western-Reserve (WR) virus,

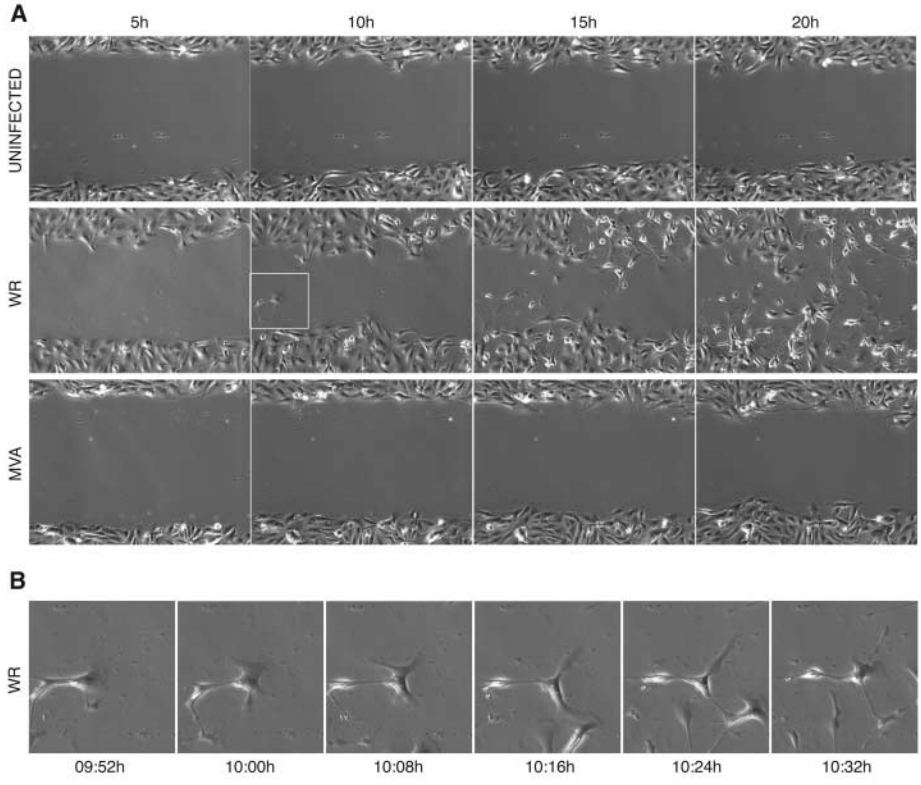

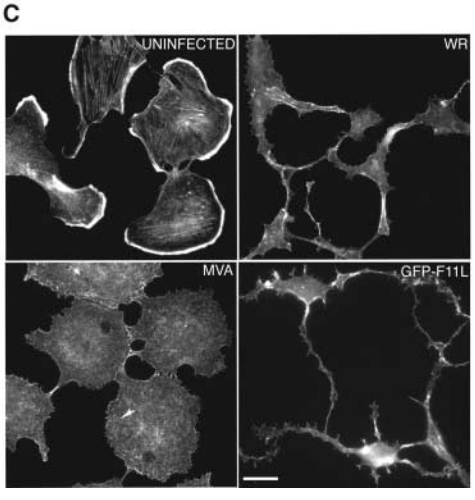

Fig. 1. F11L is required for vaccinia-induced cell motility. (**A**) Phase contrast movie stills from wound-healing assays reveal that BS-C-1 cells do not migrate into the wound site in the absence of serum (top). In contrast, infection with the wild-type Western Reserve virus (WR, middle), but not modified vaccinia Ankara virus (MVA, bottom), induces BS-C-1 cell migration. The time after the initial wound (hours) is indicated. (**B**) Enlargement of the WR-infected cell highlighted in (A) (box, 10h) reveals that migrating cells fail to retract their trailing edge and extend multiple lamellipodia. (**C**) Immunofluorescence analysis reveals that WR and MVA infection results in a loss of actin stress fibers but that only WR induces the projection phenotype. Expression of GFP-F11L induced the projection phenotype in MVA-infected cells. Bar, 10 μm.

we found that modified vaccinia Ankara (MVA), a highly attenuated virus strain containing multiple mutations and deletions in its genome (*7*–*9*), did not induce cell migration or cellular projections in the absence of serum (Fig. 1, Movies S1 to S3) (*10*).

To determine the gene (or genes) absent in MVA that are responsible for vaccinia-induced cell motility, we examined the ability of a series of recombinant MVA virus strains, which contained portions of DNA from its parental strain (*9*), to induce the projection phenotype. Only MVA recombinants rescued with cosmid 44 induced a projection phenotype (fig. S1), suggesting that the genomic region covered by cosmid 44 contained a gene (or genes) required for vaccinia-induced cell motility. Of the five genes disrupted or deleted in this genomic region, only one, F11L, or its green fluorescent protein (GFP)–tagged variant promoted the projection phenotype when expressed in MVA-infected cells (Fig. 1C, fig. S2) (*10*).

When expressed in uninfected cells, GFP-F11L induced a loss of actin stress fibers reminiscent of the dominant-negative RhoA-N19 (Fig. 2A). Furthermore, F11L inhibited stress fiber induction by coexpressed constitutively active Rho-V14 (Fig. 2A), suggesting that F11L might inhibit signaling by RhoA. To examine whether F11L interacted with RhoA or acted downstream of the guanosine triphosphatase (GTPase), we performed pull-down assays from cells coexpressing GFP-tagged RhoGTPases and F11L tagged with glutathione-*S*-transferase (GST) (*10*). RhoA but not Cdc42 or Rac copurified with F11L from cell extracts (Fig. 2B). Moreover, F11L interacted with both constitutively active RhoA-V14 and dominant-negative RhoA-N19 (Fig. 2B). Endogenous F11L and RhoA were also complexed with each other in vivo in infected cells (Fig. 2C). Moreover, a direct interaction between F11L and RhoA could be demonstrated with GST and His-tagged proteins produced in *Escherichia coli*.

Secondary-structure predictions suggest that F11L adopts a globular structure with an N-terminal domain (residues 1 to 222) rich in β sheet and a C-terminal helical domain (residues 223 to 345) containing at least one contiguous predicted helix longer than 50 residues. We found that the C-terminal helical domain of F11L but not the N-terminal region was able to interact directly with RhoA (fig. S3). Closer examination of the C-terminal region of F11L revealed that residues 299 to 312 share a limited homology to residues 998 to 1010 of Rho-associated kinase (ROCK) (fig. S3). This region of ROCK is known to mediate its interaction with RhoA (*11*). Substitution of four of the five identical residues with alanine substantially weakened the interaction between F11L and RhoA (Fig. 2D) (*10*). Combinations of double mutations resulted in a complete lack of binding (Fig. 2D). Thus, F11L appears to interact with RhoA in a manner similar to that of ROCK. Consistent with this hypothesis, the RhoA-V14E40L mutant that is deficient in ROCK binding (*12*) could not interact with F11L (Fig. 2E). In contrast to the wild-type protein, GFP-tagged F11L mutants deficient in Rho binding were also unable to stimulate the projection phenotype when expressed in MVA-infected cells (fig. S4). Thus, F11L inhibits the ability of the GTPase to signal during infection by binding directly to RhoA.

The failure of the rear of infected cells to detach and the formation of multiple lamellipodia at the front are very reminiscent of the effects of inhibition of ROCK in a variety of migrating cells (*13*–*16*). We examined whether the interaction of F11L with RhoA-V14 affected the ability of the GTPase to bind ROCK. F11L inhibited the ability of RhoA-V14 to

Cell Motility Laboratory, Cancer Research UK, London Research Institute, Lincoln's Inn Fields Laboratories, 44 Lincoln's Inn Fields, WC2A 3PX London, UK.

*Present address: Department of Parasitology, Heidelberg University School of Medicine, Im Neuenheimer Feld 324, 69120 Heidelberg, Germany.

†To whom correspondence should be addressed. E-mail: michael.way@cancer.org.uk

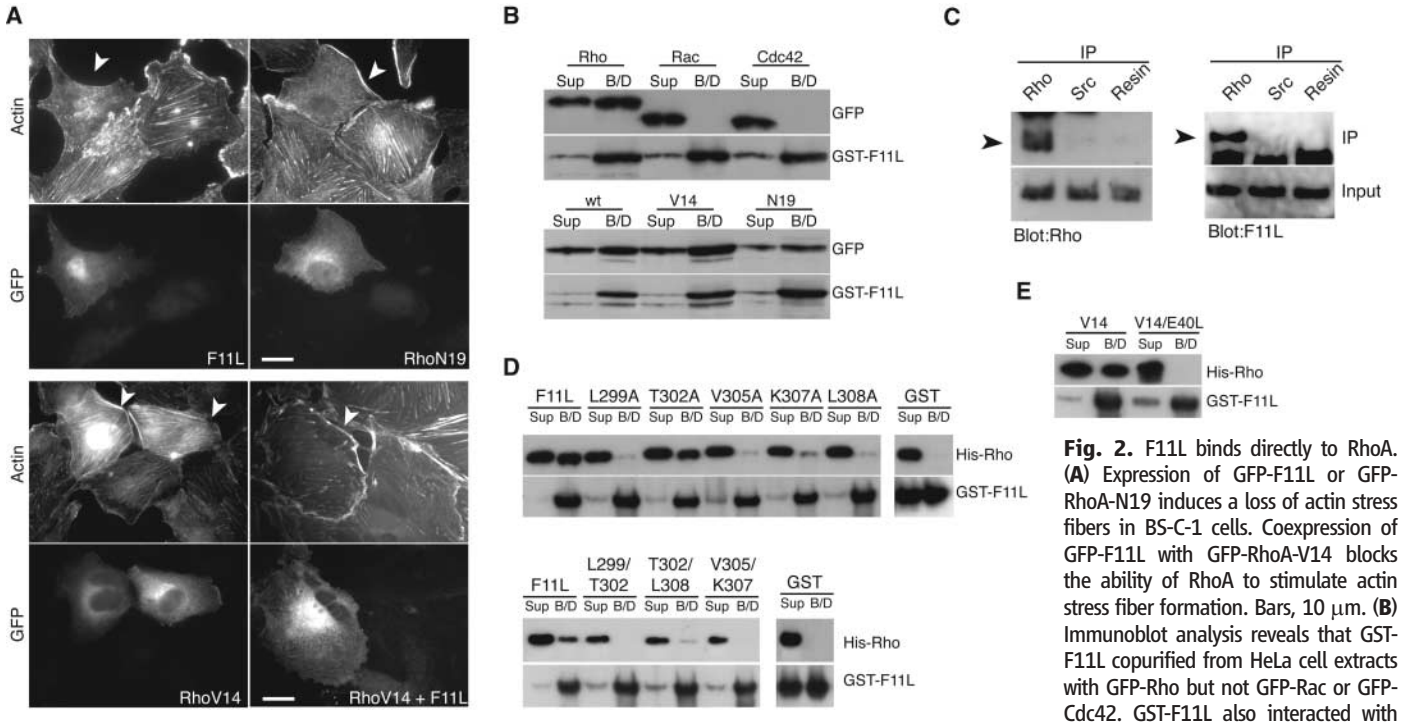

Fig. 2. F11L binds directly to RhoA. (**A**) Expression of GFP-F11L or GFP-RhoA-N19 induces a loss of actin stress fibers in BS-C-1 cells. Coexpression of GFP-F11L with GFP-RhoA-V14 blocks the ability of RhoA to stimulate actin stress fiber formation. Bars, 10 μm. (**B**) Immunoblot analysis reveals that GST-F11L copurified from HeLa cell extracts with GFP-Rho but not GFP-Rac or GFP-Cdc42. GST-F11L also interacted with GFP-RhoA-V14 and GFP-RhoA-N19. The supernatant (Sup) and bound (B/D) samples, together with the respective RhoGTPase or RhoA mutant, are indicated. (**C**) Immunoblot analysis of coimmunoprecipitation experiments revealed that F11L is complexed with RhoA in infected cells. (**D**) (Top) Immunoblot analysis of in vitro pull-down assays reveals that alanine substitution of conserved residues shared between F11L and ROCK substantially reduced the binding of F11L to RhoA. (Bottom) Double alanine substitutions in F11L resulted in a complete loss of binding. (**E**) Immunoblot analysis of in vitro pull-down assays reveals that F11L does not interact with Rho-V14/E40L.

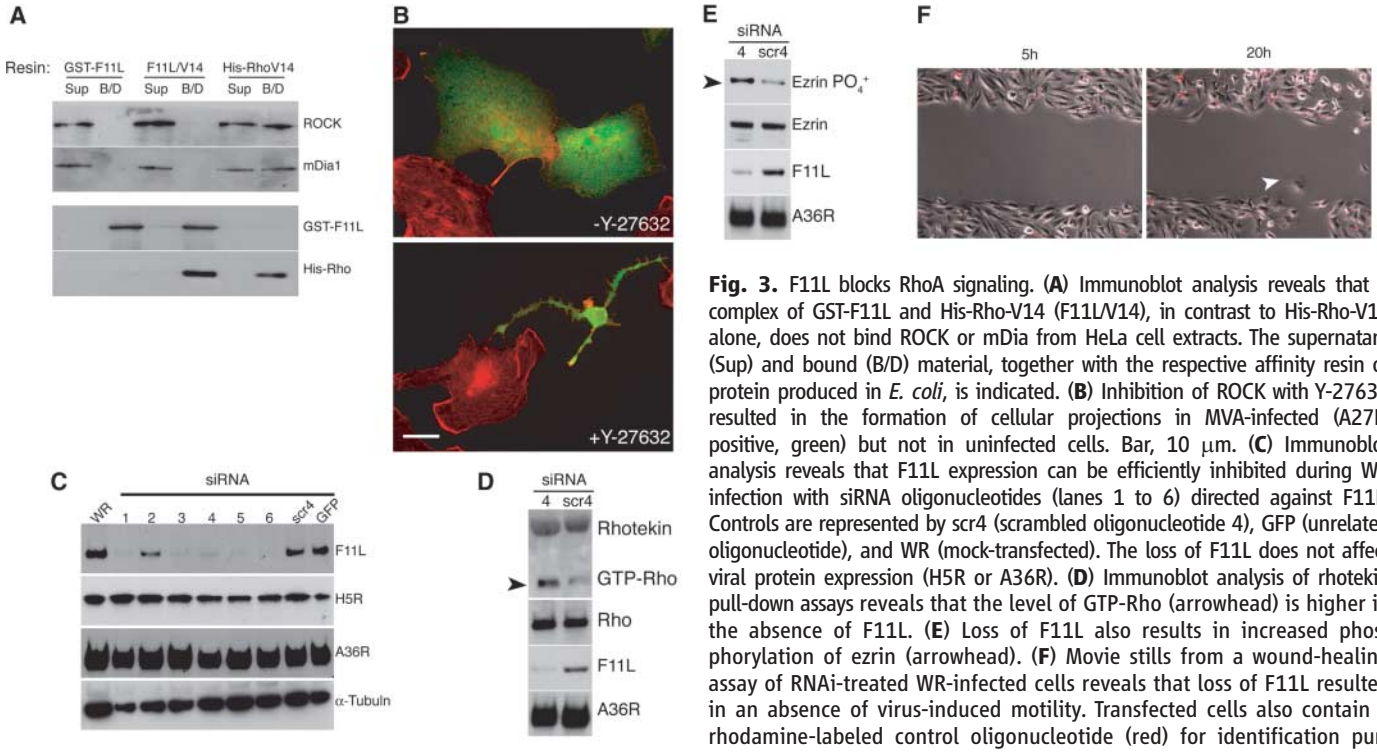

Fig. 3. F11L blocks RhoA signaling. (**A**) Immunoblot analysis reveals that a complex of GST-F11L and His-Rho-V14 (F11L/V14), in contrast to His-Rho-V14 alone, does not bind ROCK or mDia from HeLa cell extracts. The supernatant (Sup) and bound (B/D) material, together with the respective affinity resin of protein produced in *E. coli*, is indicated. (**B**) Inhibition of ROCK with Y-27632 resulted in the formation of cellular projections in MVA-infected (A27L-positive, green) but not in uninfected cells. Bar, 10 μm. (**C**) Immunoblot analysis reveals that F11L expression can be efficiently inhibited during WR infection with siRNA oligonucleotides (lanes 1 to 6) directed against F11L. Controls are represented by scr4 (scrambled oligonucleotide 4), GFP (unrelated oligonucleotide), and WR (mock-transfected). The loss of F11L does not affect viral protein expression (H5R or A36R). (**D**) Immunoblot analysis of rhotekin pull-down assays reveals that the level of GTP-Rho (arrowhead) is higher in the absence of F11L. (**E**) Loss of F11L also results in increased phosphorylation of ezrin (arrowhead). (**F**) Movie stills from a wound-healing assay of RNAi-treated WR-infected cells reveals that loss of F11L resulted in an absence of virus-induced motility. Transfected cells also contain a rhodamine-labeled control oligonucleotide (red) for identification purposes. The arrowhead indicates a single nontransfected cell, migrating into the wound. The time after the initial wound (hours) is indicated.

retain ROCK from HeLa cell extracts (Fig. 3A) (*10*). Treatment of MVA-infected cells with the ROCK inhibitor Y-27632 (*16*), although inducing the projection phenotype, was unable to stimulate cell migration (Fig. 3B), suggesting that modulation of additional signaling pathways are also required for vaccinia-induced cell motility. Consistent with this notion, F11L also inhibited the ability of RhoA to interact with

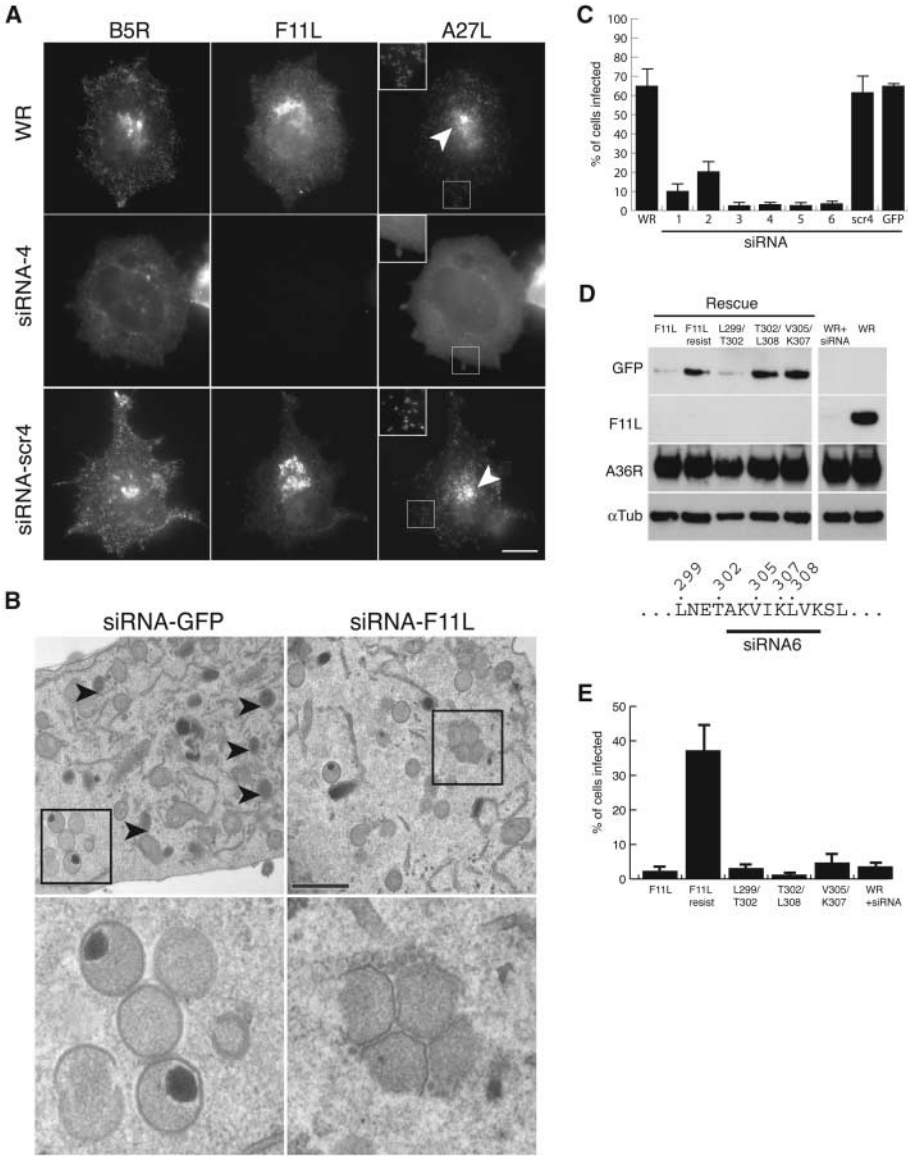

Fig. 4. Virus morphogenesis requires inhibition of RhoA signaling. (**A**) The absence of F11L resulted in disruption of perinuclear sites of virus assembly (arrowheads in WR and siRNA-scr4) and loss of assembled virus particles as judged by diffuse cytoplasmic localization of A27L and B5R (highlighted in the insets). Bar, 10 μm. (**B**) (Top) Epon sections of siRNA-treated HeLa cells infected with WR 8 hours after infection revealed that an absence of F11L resulted in loss of assembled intracellular mature virus particles (arrowheads). Immature virions were present in both samples, although their characteristic smooth curved profiles were often distorted (boxed areas are enlarged, bottom) in the absence of F11L. Bar, 1 μm. (**C**) Reinfection assays demonstrated that a loss of F11L expression resulted in a large reduction in the number of infectious particles released into the medium from WR-infected cells. Error bars represent the standard deviation of the mean from three independent experiments. (**D**) Immunoblot analysis of siRNA6-treated WR-infected cells expressing the indicated F11L rescue clone. Expression of the wild-type or L299/T302 mutant is inhibited by the siRNA6 oligonucleotide. In contrast, F11L resist, T302/L308, and V305/K307 are expressed because they contain point mutants that make them resistant to silencing by siRNA6 oligonucleotide. (**E**) Reinfection assays demonstrated that infectious virus particles are produced in siRNA6-treated WR-infected HeLa cells expressing F11L resist. In contrast, T302/L308 and V305/K307 mutants, which cannot bind RhoA, do not rescue virus morphogenesis in the absence of endogenous F11L expression. Error bars represent the standard deviation of the mean from three independent experiments.

mDia (Fig. 3A). To analyze whether F11L does indeed modulate RhoA signaling, we examined the level of GTP-bound RhoA in WR-infected cells in the absence of F11L. Transfection of small interfering RNA (siRNA) oligonucleotides against F11L before vaccinia infection markedly suppressed expression of the protein without affecting the levels of other viral proteins (Fig. 3C) (*10*). A reduction in the level of F11L expression resulted in an increase of GTP-bound RhoA in infected cell extracts (Fig. 3D). Concomitantly, the phosphorylation level of the Rho effector ezrin was increased and virus-induced cell motility was lost (Fig. 3, E and F; Movie S4). Thus, F11L inhibits the ability of RhoA to signal to its downstream effectors during vaccinia virus infection.

The sequence of F11L is strongly conserved within the genome of orthopoxviruses, suggesting that the protein may play an important role in the vaccinia virus life cycle. Indeed F11L, which is expressed from as early as 2 hours after infection, is associated with perinuclear viral factories (fig. S5). To elucidate the function of F11L in the vaccinia life cycle, we set out to delete the F11L gene in the WR genome by homologous recombination. However, in agreement with Kato *et al*. (*17*), we were unable to isolate recombinants lacking the F11L gene when using this strategy, suggesting that it is essential for the production of infectious virus in culture. To explore this possibility, we analyzed the effects of siRNA-mediated ablation of F11L expression on the vaccinia life cycle. Loss of F11L expression resulted in an absence of assembled virus particles as judged by the diffuse cytoplasmic localization of mature virus particle markers such as A27L and B5R (Fig. 4A). Analysis of siRNA-treated cells by electron microscopy (*10*) confirmed that the absence of F11L resulted in a defect in morphogenesis, with a substantial loss of assembled mature virus particles and an accumulation of aberrant immature virions (IVs) (Fig. 4B). An accumulation of IVs is also observed during the abortive life cycle of MVA in HeLa cells (*18*, *19*).

To examine whether the loss of F11L expression reduced production of infectious virus particles, we performed reinfection experiments using the tissue culture medium from siRNA-transfected cells (*10*). We observed up to a ~14-fold reduction in the number of infectious virus particles released into the tissue culture medium when compared with untreated cells (Fig. 4C). To analyze if the interaction of F11L with RhoA is required for viral morphogenesis, we examined whether expression of RNAi-resistant F11L mutants deficient in RhoA binding would rescue production of infectious virus in siRNA-transfected cells. In contrast to the wild-type protein, expression of F11L mutants deficient in RhoA binding were unable to rescue production of in-

fectious virus in siRNA-transfected cells (Fig. 4, D and E). Thus, F11L-mediated inhibition of RhoA signaling is required for both vaccinia morphogenesis and infection-induced cell motility. Our observations may also explain, at least in part, why MVA, which lacks functional F11L, is unable to replicate in most cell types in culture (*7*–*9*). They also offer molecular insights into the mechanism by which vaccinia induces cell migration (*5*, *6*). One can envisage that migration of an infected cell will increase the efficiency of virus spread because extracellular virus particles associated with the plasma membrane, which are responsible for direct cell to cell spread, will come into contact with more neighboring noninfected cells than they would if the infected cell were static.

References and Notes

1. A. J. Ridley *et al.*, *Science* **302**, 1704 (2003).
2. P. Martin, S. M. Parkhurst, *Development* **131**, 3021 (2004).
3. P. Friedl, K. Wolf, *Nat. Rev. Cancer* **3**, 362 (2003).
4. N. O. Carragher, M. C. Frame, *Trends Cell Biol.* **14**, 241 (2004).
5. C. M. Sanderson, G. L. Smith, *J. Virol.* **72**, 9924 (1998).
6. C. M. Sanderson, M. Way, G. L. Smith, *J. Virol.* **72**, 1235 (1998).
7. M. W. Carroll, B. Moss, *Virology* **238**, 198 (1997).
8. I. Drexler, K. Heller, B. Wahren, V. Erfle, G. Sutter, *J. Gen. Virol.* **79**, 347 (1998).
9. L. S. Wyatt *et al.*, *Virology* **251**, 334 (1998).
10. See supporting data on *Science* Online.
11. R. Dvorsky, L. Blumenstein, I. R. Vetter, M. R. Ahmadian, *J. Biol. Chem.* **279**, 7098 (2004).
12. E. Sahai, A. S. Alberts, R. Treisman, *EMBO J.* **17**, 1350 (1998).
13. R. A. Worthylake, S. Lemoine, J. M. Watson, K. Burridge, *J. Cell Biol.* **154**, 147 (2001).
14. R. A. Worthylake, K. Burridge, *J. Biol. Chem.* **278**, 13578 (2003).
15. A. Smith, M. Bracke, B. Leitinger, J. C. Porter, N. Hogg, *J. Cell Sci.* **116**, 3123 (2003).
16. K. Riento, A. J. Ridley, *Nat. Rev. Mol. Cell Biol.* **4**, 446 (2003).
17. S. E. Kato, F. A. Greco, C. R. Damaso, R. C. Condit, N. Moussatche, *J. Virol. Methods* **115**, 31 (2004).
18. M. C. Sancho, S. Schleich, G. Griffiths, J. Krijnse-Locker, *J. Virol.* **76**, 8318 (2002).
19. J. C. Gallego-Gomez *et al.*, *J. Virol.* **77**, 10606 (2003).

20. We thank J. Krijnse-Locker (European Molecular Biology Laboratory, Heidelberg, Germany) and A. Alberts (Van Andel Research Institute, Grand Rapids, MI) for providing antibodies. We also thank B. Moss (National Institute of Allergy and Infectious Diseases, Bethesda, MD) for providing MVA recombinants, E. Sahai (Cancer Research UK, London) for the RhoV14E40L clone, and P. Traktman (Department of Microbiology and Molecular Genetics, WI) for discussions about siRNA in infected cells. We thank the Way lab, E. Sahai, N. Hogg, and R. Treisman (Cancer Research UK, London) for helpful comments on the manuscript. F.V. was supported by a European Community Marie Curie Fellowship (Number HPMF-CT-2000-01021).

Supporting Online Material

www.sciencemag.org/cgi/content/full/311/5759/377/DC1
Materials and Methods
Figs. S1 to S6
Movies S1 to S4
References

9 November 2005; accepted 20 December 2005
10.1126/science.1122411

Core Knowledge of Geometry in an Amazonian Indigene Group

Stanislas Dehaene,[1,2]* Véronique Izard,[1] Pierre Pica,[3] Elizabeth Spelke[4]

Does geometry constitute a core set of intuitions present in all humans, regardless of their language or schooling? We used two nonverbal tests to probe the conceptual primitives of geometry in the Mundurukú, an isolated Amazonian indigene group. Mundurukú children and adults spontaneously made use of basic geometric concepts such as points, lines, parallelism, or right angles to detect intruders in simple pictures, and they used distance, angle, and sense relationships in geometrical maps to locate hidden objects. Our results provide evidence for geometrical intuitions in the absence of schooling, experience with graphic symbols or maps, or a rich language of geometrical terms.

> *Through natural selection, our mind has adapted to the conditions of the external world,* […] *it has adopted the geometry most advantageous to our species; or, in other words, the most convenient.*
> –Henri Poincaré, *La Science et l'Hypothèse*

Euclidean geometry is one of the deepest and oldest products of human reason, but its foundations remain elusive. Many of its propositions—that two points determine a line, or that three orthogonal axes localize a point—are judged to be self-evident (*1*, *2*) and yet have been questioned on the basis of logical argument, physical theory, or experiment [(*3*–*5*); for a historical review, see (*6*)]. Here we ask whether the conceptual principles of geometry are inherent in the human mind, by studying the spontaneous geometrical knowledge of the Mundurukú, an Amazonian indigene group (*7*). The present data were collected by one of us (P.P.) during a field trip in 2004–2005 to remote sites along the Cururu river. Most of the children and adults who took part in our experiments inhabit scattered, isolated villages and have little or no schooling, rulers, compasses, or maps. Furthermore, the Mundurukú language has few words dedicated to arithmetical, geometrical, or spatial concepts, although a variety of metaphors are spontaneously used (see Supporting Online Material for a list).

Our first test [inspired from (*8*)] was designed to probe the Mundurukú's intuitive comprehension of the basic concepts of geometry, including points, lines, parallelism, figures, congruence, and symmetry (*9*). For each such concept, we designed an array of six images, five of which instantiated the desired concept while the remaining one violated it (Fig. 1). The participants were asked, in their language, to point to the "weird" or "ugly" one. Care was taken to minimize cues other than the desired conceptual relation that could be used to identify the target. For instance, if the desired concept was "trapezoid," the target was a nontrapezoidal quadrilateral whose size and orientation fell within the range of variation of the other five trapezoids. There are many ways in which the participants could have selected an odd picture out of the six, including size, orientation, or personal preference. If the Mundurukú share with us the conceptual primitives of geometry, however, they should infer the intended geometrical concept behind each array and therefore select the discrepant image.

All participants, even those aged 6, performed well above the chance level of 16.6% (average 66.8% correct, minimum 44.2% correct, $P < 0.001$). Performance was higher than chance in all but 6 of the 45 slides ($P \ll 0.001$) and was indistinguishable for Mundurukú adults and children. There was no significant influence of the bilingualism or schooling exhibited by some of the participants (*9*). As shown in Fig. 1, the Mundurukú succeeded remarkably well with the core concepts of topology (e.g., connectedness), Euclidan geometry (e.g., line, point, parallelism, and right angle), and basic geometrical figures (e.g., square, triangle, and circle). They experienced more difficulty, but still achieved higher-than-chance performance, in detecting symmetries and metric properties (e.g., equidistance of points). They performed poorly only in two domains: a series of slides assessing geometrical transformations, for instance, by depicting two triangles in a mirror-symmetry relation; and another two slides in which the intruder shape was a randomly oriented mirror image of the other shapes. Interestingly, both types of slides require a mental transformation of one shape into another, followed by a second-order judgment about the nature of this transformation. It is possible that geometrical transformations are inherently more difficult mathematical

[1]INSERM-CEA Cognitive Neuroimaging Unit, Service Hospitalier Frédéric Joliot, Commissariat à l'Energie Atomique, 91401 Orsay Cedex, France. [2]Collège de France, 11, place Marcelin Berthelot, 75231 Paris Cedex 05, France. [3]Unité Mixte de Recherche 7023 "Formal Structure of Language," CNRS and Paris VIII University, Paris, France. [4]Psychology Department, Harvard University, Cambridge, MA 02139, USA.

*To whom correspondence should be addressed. E-mail: dehaene@shfj.cea.fr

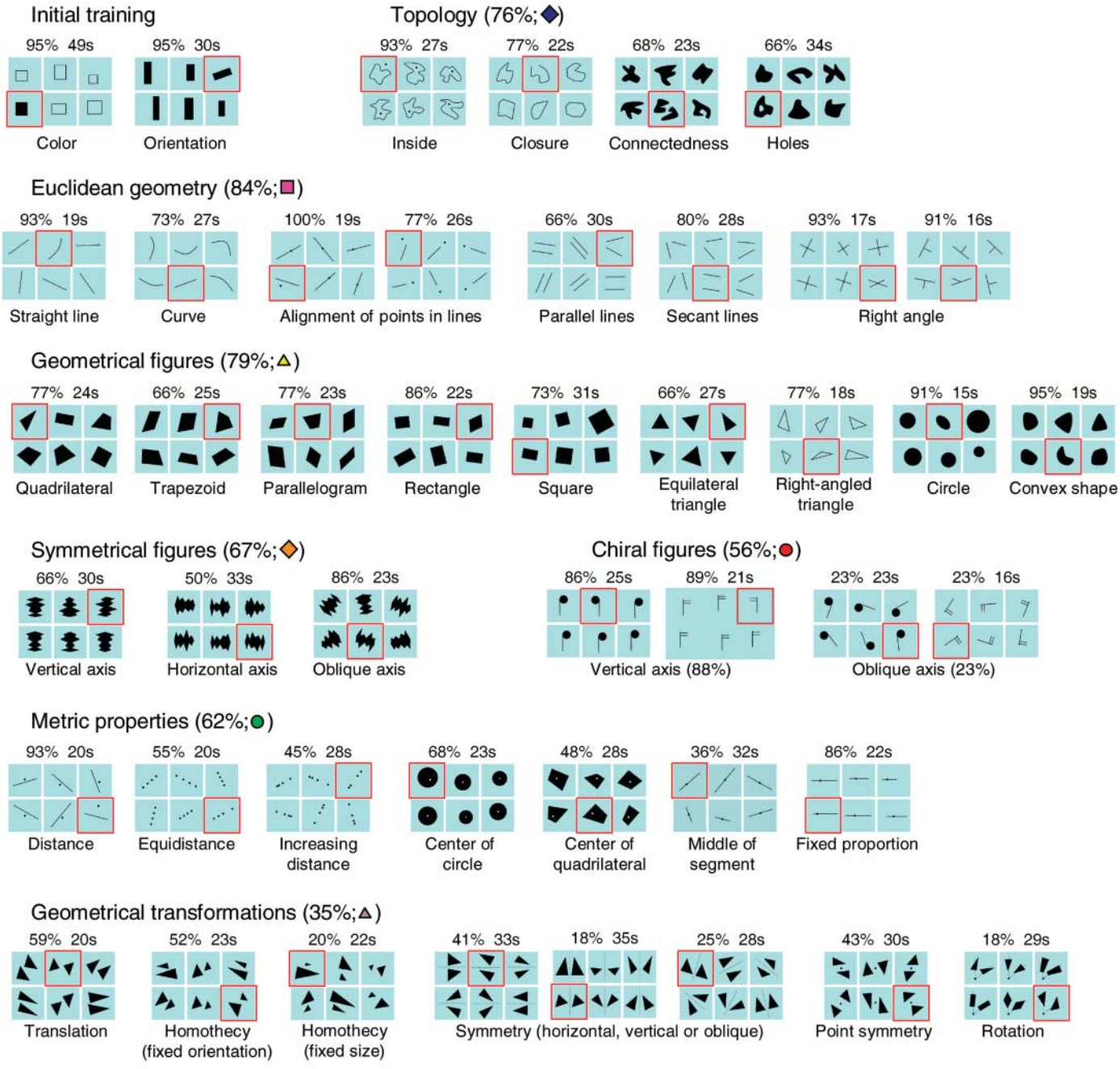

Fig. 1. Performance of Mundurukú participants in a multiple-choice test of the core concepts of geometry, rearranged in hierarchical order. In each slide, five images instantiate a specific concept indicated below, whereas the sixth (surrounded in red) violates it. The percentage of participants choosing the correct intruder is shown on top of each slide. Chance level is 16.6% correct; 28% correct corresponds to $P < 0.05$, and 35% correct to $P < 0.001$. Mean response times (in seconds) are also indicated. For each category of concept, the averaged percentage of correct answers is shown along with a color symbol used to refer to individual test items in Fig. 3.

concepts. Alternatively, such transformations may be more difficult to detect in static images.

To assess the generality of the patterns of difficulty of our images, we also tested American children and adults. An analysis of variance with factors of age (children or adults) and culture (Mundurukú or American) revealed effects of age ($P < 10^{-6}$), culture ($P < 10^{-5}$), and their interaction ($P = 0.0002$). As shown in Fig. 3A, the performance of Mundurukú children and adults was identical to that of American children, whereas the performance of American adults was significantly higher. Indeed, we observed a well-defined profile of difficulty common to both cultures. Across the 45 slides, the mean performance of the Mundurukú children correlated closely with that of the American children ($r^2 = 61.8\%$, $P < 10^{-9}$). In this regression, the intercept and the slope were nonsignificantly different from 0 and 1, respectively, confirming that performance was highly similar in both cultures (Fig. 3B). Furthermore, despite their vastly different cultures and levels of schooling, Mundurukú and American adults also showed a shared profile of difficulty ($r^2 = 49.4\%$, $P < 10^{-7}$), although American adults performed at a higher overall level (Fig. 3C). This reproducible ordering of error rates does not support Piaget's hypothesis of a developmental and cultural progression from topology to projective and Euclidian geometry (*10*), but rather suggests that geometrical intuition cuts across all of

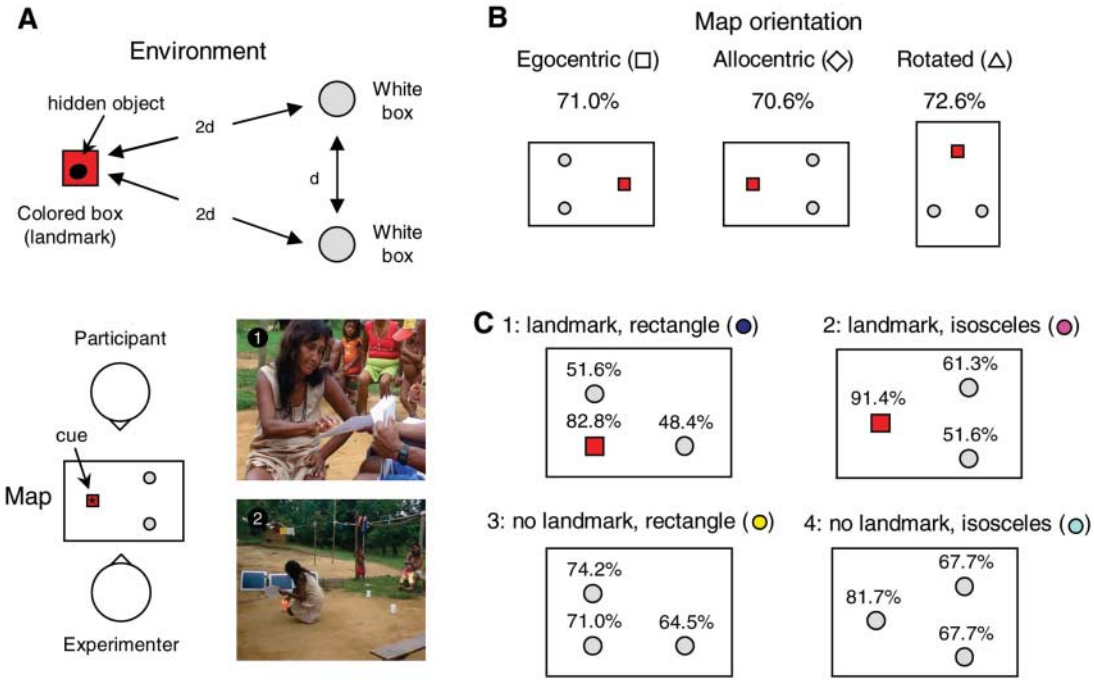

Fig. 2. Performance of Mundurukú participants in the map test. (**A**) Schematic representation of the spatial layout of the experiment. On each trial, the participant was shown a "map" representing the location of three boxes, one of which contained a cue symbolizing a hidden object. Then he or she turned around and searched for the hidden object (distance $d \approx 1.5$ m). (**B**) Performance in the three map orientations. The map and the environment could be aligned as seen from the top (allocentric condition), aligned relative to the participant before and after turning (egocentric condition), or nonaligned (90° rotation condition). (**C**) Performance at each location in the four successive blocks of the experiment. The symbols in (B) and the colors in (C) are used to refer to individual test items in Fig. 3.

these domains. In summary, uneducated adults from an isolated culture, as well as young children from the same culture or from a Western culture, exhibit a shared competence for basic geometrical concepts.

Although the multiple-choice test was designed so that the target picture could only be identified once the relevant geometrical property had been grasped, it could be argued that the test requires solely a visual judgment of dissimilarity among closely similar images. We argue, however, that judgments of visual similarity do not merely result from superficial sensory computations, but reflect deep properties of cognitive architecture (*11*). Geometrical intuitions, in the final analysis, may rest on a spontaneous imposition of stable conceptual relations onto variable and imperfect sensory data, a process well captured by the multiple-choice test. Nevertheless, we sought to replicate and extend our findings in a second task that would demonstrate more directly the use of abstract geometrical knowledge and its transfer across widely different contexts.

Etymologically, "geo-metry" is the science of measuring the Earth. Geometrical concepts first were used to measure and chart the length, area, and shape of land surfaces. To investigate whether the Mundurukú spontaneously understand and use geometry in this sense, we designed an abstract map test. Three boxes or cans were arranged in a right-angled or isosceles triangle, and an object was hidden in one of them (*9*) (Fig. 2). With his or her back to this array, each participant was presented with a sheet of paper in which square and circular symbols represented the three containers, and a star on one of the forms marked the location of the hidden object. This "map" preserved the two-dimensional geometrical relationships between the objects, as viewed from above, except for scale. The orientation of the map relative to the array varied across trials, so that only the geometrical relationships among the forms specified the hidden object's location. By recording where each participant first searched for the object, we evaluated whether participants could relate the geometrical information on the map to the geometrical relations in the environment, over changes in orientation, an ~10-fold change in size, and a change from two dimensions to three.

The map test is likely to be entirely novel to the Mundurukú. Although they live in widely dispersed villages between which they navigate by boat or foot, and although they also manipulate tools, build baskets, craft necklaces and bracelets, sculpt symbolic miniatures, and are renowned for their elaborate traditional face- and body-painting schemes, the Mundurukú do not typically possess maps or spontaneously draw pictures of their houses, villages, or environment. Across several trips to the Mundurukú territory, we occasionally observed spontaneous activities such as the drawing of circles on the ground to represent villages. These drawings were coarse, however, and failed to preserve metric information about the angles and distances between the referents. Our map test, by contrast, could not be accomplished without attending to metric information.

Overall, the participants' success rate averaged 71%, which was well above the chance level of 33.3% (across subjects, $P < 0.0001$). Performance did not differ between children (73.3% correct) and adults (70.4% correct; both $P <$ 0.0001 relative to chance). There was also no effect of map orientation (Fig. 2B): Performance with allocentric, egocentric, and rotated maps did not differ ($F < 1$) and was always significantly above chance, suggesting that participants either extracted the geometrical relationships directly or performed a mental rotation so as to align the map with the environment.

An interesting insight into the cues used by the participants came from an analysis of the evolution of their performance. During training, and in the first half of testing, one of the hiding locations was a red box quite distinct from the other hiding locations (white cans) and depicted as a red square on the map. Although performance did not differ overall as a function of presence or absence of this landmark ($F < 1$), there was a significant landmark by object location interaction ($P < 0.0001$), as well as a triple interaction with age ($P = 0.003$), indicating that the effect of the landmark on search patterns was more pronounced in adults. During the first two experimental blocks in which the red box was present, participants performed well when the object was placed at this landmark location (87.1% correct) but less well when the object was placed in one of the other two unmarked locations (54.3% correct). An analysis of errors indicated that, in the latter case, they avoided the landmark location (only 9.1% of responses) but tended frequently to select the wrong nonmarked location (36.6% of responses). Still, participants chose the incorrect, unmarked location less frequently than the correct one ($P < 0.003$ on a t test comparing the two nonmarked locations), thus providing evidence for sensitivity to purely geometrical information.

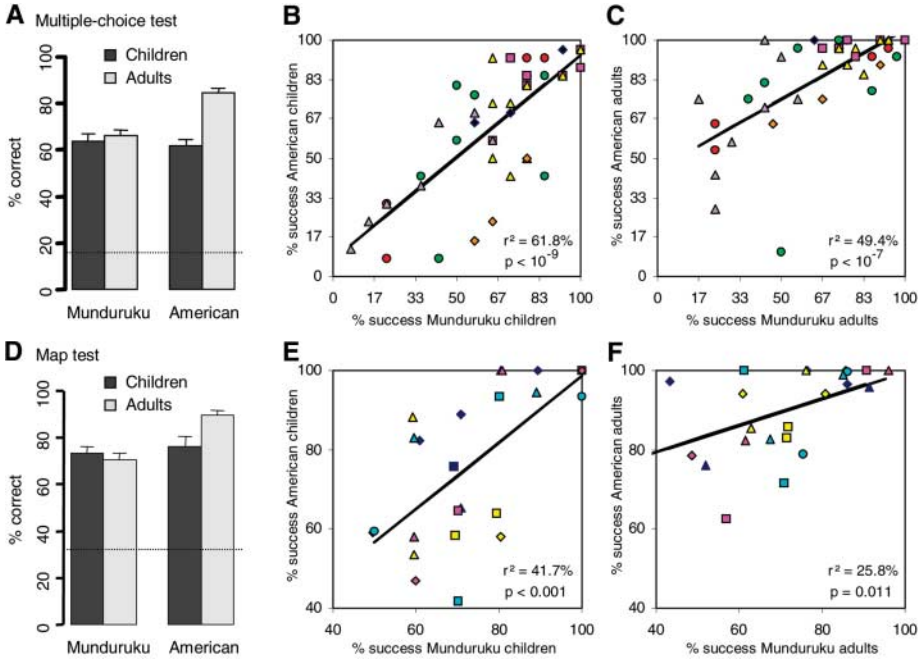

Fig. 3. Comparison of the geometrical performance of Mundurukú and American participants. (**A** to **C**) Multiple-choice test; (**D** to **F**) map test. (A) and (D) show the percent success averaged across participants and test items, as a function of age and culture (horizontal line = chance level; vertical bar = standard error). (B), (C), (E), and (F) show the correlation of performance level across test items, separately for children and adults. Each symbol represents average performance in response to a given test item. In (B) and (C), the symbol shapes and colors refer to the categories of slides defined in Fig. 1. In (E) and (F), symbol shapes refer to map orientation and color to map layout, as defined in Fig. 2. In both cases, r^2 and P values indicate the significance of the observed linear correlation in performance across the two cultures.

Geometrically driven behavior became much more evident in the trials in which the landmark was absent, such that only the geometrical relationships between the circles and cans specified the position of the hidden object. In this situation, performance was high on average (72.0% correct) and far exceeded chance level at all locations and with both triangular configurations (all P values < 0.0003). In the final block with an isosceles configuration, performance was good even at the two symmetrical locations of the isosceles triangle (67.7% correct). The Mundurukú therefore were able to use sense relationships, as well as distance or angle, to relate the map to the environment.

For direct comparison, we also tested educated American children and adults in this map task (Fig. 3D). All of the above effects were replicated. An analysis of variance revealed effects of age ($P = 0.043$), culture ($P < 10^{-4}$), and their interaction ($P = 0.013$). As in the multiple-choice test, the Mundurukú children and adults performed at a level indistinguishable from that of American children, whereas the American adults performed significantly better. Nevertheless, even the latter group made some errors, and we observed high correlations between the performance profiles of American and Mundurukú participants across the test items, both within children and within adults (Fig. 3, E and F). Those results again point to a shared pattern of core geometrical knowledge despite increases in absolute performance levels in the educated American adults.

Studies of the universality of human geometrical knowledge have a long history. As chronicled by Plato in the *Meno* (~380 B.C.), Socrates probed the geometrical intuitions of an uneducated slave in a Greek household, leading him, through a series of questions, to discover relations between the areas of squares drawn in the sand. He concluded of the slave that "his soul must have always possessed this knowledge" (*12*). Nevertheless, the slave shared a language with educated Greeks, likely was familiar with pictures and other products of Greek culture, and revealed his intuitions by engaging in a conversation about lines, areas, and number. Our experiments, in contrast, provide evidence that geometrical knowledge arises in humans independently of instruction, experience with maps or measurement devices, or mastery of a sophisticated geometrical language. This conclusion is consistent with paleoanthropological evidence (*13*) and with previous demonstrations of a right-hemisphere competence for nonverbal tests of geometry in split-brain patients (*8*). Further research is needed to establish to what extent this core knowledge is shared with other animal species (*14*, *15*) and whether it is available even in infancy or is acquired progressively during the first years of life (*4*, *10*, *16*–*18*). There is little doubt that geometrical knowledge can be substantially enriched by cultural inventions such as maps (*19*), mathematical tools (*3*, *4*, *6*), or the geometrical terms of language (*18*, *20*–*25*). Beneath this fringe of cultural variability, however, the spontaneous understanding of geometrical concepts and maps by this remote human community provides evidence that core geometrical knowledge, like basic arithmetic (*7*, *26*), is a universal constituent of the human mind (*11*).

References and Notes

1. Euclid, *Elements* (Green Lion, Santa Fe, NM, 2002).
2. I. Kant, *A Critique of Pure Reason* (Palgrave Macmillan, London, 1781, 1920).
3. B. Riemann, *Nature* **8**, 183 (1873).
4. H. Poincaré, *La Science et l'Hypothèse* (Flammarion, Paris, 1902).
5. A. Einstein, *Relativity: The Special and the General Theory* (Henry Holt, New York, 1920).
6. L. Boi, *Le problème mathématique de l'espace. Une quête de l'intelligible* (Springer, Berlin, 1995).
7. P. Pica, C. Lemer, V. Izard, S. Dehaene, *Science* **306**, 499 (2004).
8. L. Franco, R. W. Sperry, *Neuropsychologia* **15**, 107 (1977).
9. Materials and methods are available as supporting material on *Science* Online.
10. J. Piaget, *Child's Conception of Geometry* (Routledge and Kegan Paul, London, 1948, 1960).
11. R. N. Shepard, *Behav. Brain Sci.* **24**, 581 (2001).
12. Plato, *Meno* (~380 B.C.), available online at classics.mit.edu.
13. O. Keller, *Aux origines de la géométrie. Le paléolithique, le monde des chasseurs-cueilleurs* (Vuibert, Paris, 2004).
14. C. R. Gallistel, *The Organization of Learning* (MIT Press, Cambridge, MA, 1990).
15. K. Cheng, N. S. Newcombe, *Psychon. Bull. Rev.* **12**, 1 (2005).
16. N. S. Newcombe, J. Huttenlocher, *Making Space* (MIT Press, Cambridge, MA, 2000).
17. A. Berthoz, *The Brain's Sense of Movement* (Harvard Univ. Press, Cambridge, MA, 2000).
18. J. S. DeLoache, *Science* **238**, 1556 (1987).
19. D. P. Marzolf, J. S. DeLoache, *Child Dev.* **65**, 1 (1994).
20. S. J. Hespos, E. S. Spelke, *Nature* **430**, 453 (2004).
21. L. Hermer, E. Spelke, *Cognition* **61**, 195 (1996).
22. A. Majid, M. Bowerman, S. Kita, D. B. Haun, S. C. Levinson, *Trends Cogn. Sci.* **8**, 108 (2004).
23. S. C. Levinson, *Space in Language and Cognition: Explorations in Cognitive Diversity* (Cambridge Univ. Press, Cambridge, MA, 2003).
24. S. C. Levinson, S. Meira, *Language* **79**, 485 (2003).
25. P. Li, L. Gleitman, *Cognition* **83**, 265 (2002).
26. S. Dehaene, *The Number Sense* (Oxford Univ. Press, New York, 1997).

27. Authors are listed in alphabetical order. This work would not have been possible without the help of A. Arnor, V. Poxõ, A. Ramos, C. Tawé, F. Tawé, and A. Tawé, and of the Department of Studies and Research of Funai. It is based on data collected by P.P. within a larger project on the nature of quantification and functional categories developed jointly by the linguistic section of the Department of Anthropology of the National Museum of Rio and the Unité Mixte de Recherche 7023 of the CNRS, with the agreement of Funai and the Conselho Nacional de Desenvolvimento Científico e Technológico (CNPq). We thank M. Crofts for helpful comments, P. Mesureur for video transfer, and A. Grace, L. Hegg, and K. La Mont for help with data collection in Boston. Supported by INSERM, the Département de Sciences Humaines et Sociales of CNRS (P.P.), NIH (E.S.), and a McDonnell Foundation Centennial Fellowship (S.D.).

Supporting Online Material

www.sciencemag.org/cgi/content/full/311/5759/381/DC1
Materials and Methods
SOM Text
References

24 October 2005; accepted 29 November 2005
10.1126/science.1121739

A Molecular Framework for Plant Regeneration

Jian Xu,[1] Hugo Hofhuis,[1] Renze Heidstra,[1] Michael Sauer,[2] Jiří Friml,[2] Ben Scheres[1]*

Plants and some animals have a profound capacity to regenerate organs from adult tissues. Molecular mechanisms for regeneration have, however, been largely unexplored. Here we investigate a local regeneration response in *Arabidopsis* roots. Laser-induced wounding disrupts the flow of auxin—a cell-fate–instructive plant hormone—in root tips, and we demonstrate that resulting cell-fate changes require the PLETHORA, SHORTROOT, and SCARECROW transcription factors. These transcription factors regulate the expression and polar position of PIN auxin efflux–facilitating membrane proteins to reconstitute auxin transport in renewed root tips. Thus, a regeneration mechanism using embryonic root stem-cell patterning factors first responds to and subsequently stabilizes a new hormone distribution.

Among vertebrates, salamanders represent a rarity in their ability to regenerate lost structures, such as limbs. In contrast, the ability to regenerate organs is wide-spread in the plant kingdom. Here we investigate regeneration in *Arabidopsis* roots. In normal root development, the root meristem produces root cap cells on its distal face and produces various cell types on its proximal face (fig. S1). The quiescent center (QC), a mitotically inactive organizing center required for stem-cell maintenance (*1*), lies between the stem cells for these cell populations. The GRAS family transcription factors—SHORTROOT (SHR) and SCARECROW (SCR) (*2*–*5*)—and the auxin-responsive AP2/EREBP (APETALA2/ethylene responsive element binding protein) family transcription factors PLETHORA1 (PLT1) and PLT2, contribute to QC and stem cell patterning (*6*). *PLT* mRNA distribution is regulated by an auxin maximum that is distal to the vascular precursors (*6*, *7*). PIN transmembrane proteins localize asymmetrically at plasma membranes of auxin-transporting cells, correlated with the direction of auxin flow (*8*–*11*). PIN proteins restrict *PLT* transcription and maintain the auxin response maximum by mediating polar auxin transport (PAT) (*8*). Therefore, auxin redistribution after wounding may induce organ regeneration. Here we analyze regeneration after auxin modulation by using patterning and polarity markers in wild type (WT) and key patterning mutants to reveal the interaction network that reestablishes a new root tip.

QC laser ablation results in complete respecification of the root cap and QC from distal provascular tissue (*12*). Root cap and QC markers appeared in the respecified region 24 hours or more after proximal displacement of an auxin response maximum (*7*). To explore the role of auxin in this process, we monitored auxin response and the expression of patterning genes after QC ablation in real time.

A shift in auxin response occurred proximal to ablated QC cells as early as 3 hours after ablation, when the auxin distribution marker DR5rev::GFP (green fluorescent protein) (*10*) (Fig. 1A) appeared in vascular stem cells, cortex/endodermis stem cells, and their daughters (Fig. 1B, inset). DR5rev::GFP formed a new maximum within 16 hours after ablation (Fig. 1B, bracket) and expanded into more cell layers above the ablated QC (Fig. 1, C and D), where starch granules marked distal root cap respecification (Fig. 1D, inset).

pPLT1::ERCFP (endoplasmic reticulum–targeted cyan flourescent protein) predominantly marks the QC and surrounding stem cells (Fig. 1E). pPLT1::ERCFP expression relocalized rapidly around 6 hours after ablation, in line with the auxin response factor dependency of *PLT* genes (Fig. 1F, bracket) (*6*). A more pronounced proximal shift of the pPLT1::ERCFP expression domain was observed from day 2 after ablation onwards (Fig. 1, G and H), tightly following the auxin maximum.

The QC-specific marker pWOX5::ERGFP (Fig. 1I) (*8*) appeared in former cortex/endodermis stem cells and their daughters and in 1 to 2 cell layers proximal to the ablated QC around 16 hours after ablation (Fig. 1J, bracket). pWOX5::ERGFP was gradually confined to central former provascular cells, which acquired other QC markers later (Fig. 1, K and L).

pSHR::SHRGFP is nuclear and cytoplasmic in provascular cells but exclusively nuclear in endodermis and QC (Fig. 1M) (*13*). pSHR::SHRGFP became restricted to the nucleus of provascular cells about 16 hours after ablation (Fig. 1, N to P, arrows).

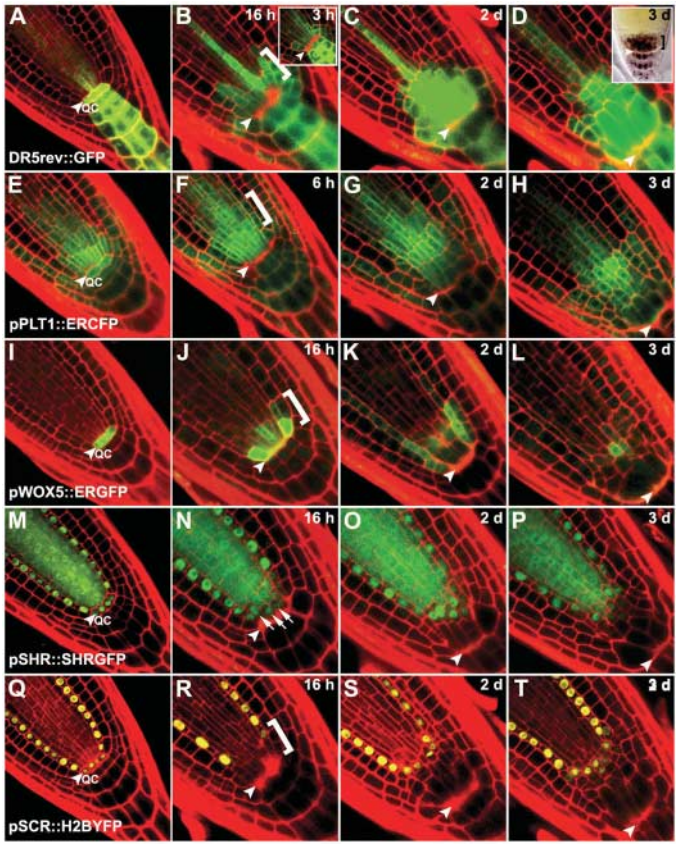

Fig. 1. Dynamic changes of auxin distribution and cell-fate identity markers after QC ablation. (**A** to **D**) DR5rev::GFP. (**E** to **H**) pPLT1::ERCFP. (**I** to **L**) pWOX5::ERGFP. (**M** to **P**) pSHR::SHRGFP. (**Q** to **T**) pSCR::H2BYFP. The left-most column shows controls before ablation. The inset in (B) is 3 hours after ablation. (F) is 6 hours after ablation. (B), (J), (N), and (R) are 16 hours after ablation. The column third from the left shows images 2 days after ablation. The images in the right-most column are 3 days after ablation. Arrowheads indicate QC cells in the left-most column and the position of ablated QC elsewhere. Arrows in (N) point to restricted pSHR::SHRGFP expression in the nucleus of former vascular stem cells. The inset in (B) shows up-regulation of DR5rev::GFP 3 hours after ablation. The inset and bracket in (D) show provascular-columella identity switches by starch granule staining. The brackets in (B), (F), (J), and (R) indicate expression changes of markers. The red signal is propidium iodide (PI) staining. The green signal is GFP except for [(E) to (H)], where it is cyan fluorescent protein (CFP). The yellow signal is yellow fluorscent protein (YFP).

[1]Department of Molecular Genetics, Utrecht University, Padualaan 8, 3584CH Utrecht, Netherlands. [2]Zentrum für Molekularbiologie der Pflanzen, Universität Tübingen, Auf der Morgenstelle 3, 72076 Tübingen, Germany.

*To whom correspondence should be addressed. E-mail: b.scheres@bio.uu.nl

Endodermis and QC marker pSCR::H2BYFP (Fig. 1Q) (*5*) were downregulated in cortex/endodermis stem cells and their daughters within 16 hours after ablation (Fig. 1R, bracket). pSCR::H2BYFP expression appeared in the respecified region in the following 2 days to mark the new QC, as reported earlier (Fig. 1, S and T) (*7*).

Together, our results reveal that disruption of auxin flow by QC ablation rapidly upregulates the auxin response in 1 to 2 cell layers proximal to the ablated QC, which is followed by cell fate changes. Ablation of columella stem cells provoked similar effects, indicating that regeneration occurs when auxin flow is disrupted (fig. S2).

To reveal whether auxin distribution influences PIN localization, we monitored functional PIN-GFP fusions after QC ablation. pPIN1::PIN1EGFP mainly resides at basal and lateral sides of vascular cells, but a weak GFP signal can be detected in epidermis, cortex, QC, and in columella stem cells (Fig. 2A). No obvious changes of pPIN1::PIN1EGFP polarity appeared within 16 hours after ablation (Fig. 2B); however, pPIN1::PIN1EGFP expression decreased in 1 to 2 cell layers proximal to the ablated QC, associated with the proximally shifted auxin maximum (Fig. 2B, bracket). Over the following 2 days, pPIN1::PIN1EGFP expression was lost in these cells (Fig. 2, C and D).

pPIN2::PIN2EGFP localizes apically in epidermal and lateral root cap cells and predominantly basally in cortex cells (Fig. 2E) (*14*). pPIN2::PIN2EGFP expression in cortex and epidermis approached the ablated QC after 16 hours and resumed its original expression site relative to the new QC at later stages (Fig. 2, F and G, bracket). No obvious changes in pPIN2::PIN2EGFP polarity were observed after a proximal shift of the auxin maximum (Fig. 2, F to H).

pSCR::PIN2EGFP clearly visualizes polar PIN localization in QC and endodermal cells (Fig. 2I). pSCR::PIN2EGFP localizes to the basal-lateral membrane of endodermal cells and is preferentially distributed on the basal-lateral plasma membrane of QC cells, consistent with the normal PIN localization of PIN1 and PIN4 in these cells (*15*). pSCR::PIN2EGFP expression was downregulated in the cortex/endodermis stem cells and their daughter cells after ablation (Fig. 2J, bracket), similar to pSCR::H2BYFP (Fig. 1R, bracket). pSCR::PIN2EGFP expression reappeared in cells at the position where the new QC cells were expected to be specified at day 2 after ablation, and expression was weakly and uniformly distributed on the plasma membrane (Fig. 2K, arrows). Around day 3, however, pSCR::PIN2EGFP expression became preferentially localized to the lateral and basal membranes (Fig. 2L, arrows), suggesting that QC-specific PIN polarity is reestablished at later stages.

Immunolocalization of PIN1 and PIN2 in WT roots after ablation confirmed that the observed changes of PIN-GFP expression and localization genuinely reflect the in vivo dynamics of PIN expression and localization after ablation (fig. S3) (*16*). PIN4 immunolocalization reveals predominant expression in the QC, stem cells, and their abutting daughters, with a polar localization oriented toward the QC and columella stem cells (Fig. 2M) (*15*). PIN4 could no longer be detected in columella stem cells and at the basal ends of the former vascular stem cells 16 hours after ablation (Fig. 2N, bracket), and the PIN4 expression domain shifted proximally in the following 2 days (Fig. 2, O and P), in correlation with the proximally shifted *PLT1* expression domain and auxin maximum.

Our data demonstrate that disruption of auxin flow by QC ablation alters expression but not polar localization of PIN proteins. The timing of PIN protein distribution changes and the intermediate polarization patterns in respecifying cells suggest that PIN proteins become correctly polarized in response to auxin distribution changes only after renewed cell specification.

To test directly whether redistribution of auxin affected PIN polarity only after changes in cell identity, we exogenously applied indoleacetic acid (IAA) to the root and locally induced auxin biosynthesis in the QC, which enhances endogenous auxin levels and flux (*8*). Four-hour treatments neither changed expression level nor polarity for pPIN1::PIN1EYFP and pPIN2:PIN2EGFP fusions in the central root meristem (fig. S4, A to F). However, prolonged auxin biosynthesis in the root meristem completely eliminated PIN protein expression, consistent with previous reports on auxin- and AUXIN RESISTANT1-dependent PIN degradation (fig. S4, G to I) (*17*, *18*).

Our data indicated that cell specification was necessary for new PIN protein expression and localization after ablation. We therefore sought to investigate the role of key patterning genes in the induced regeneration process. The *PLT1* and *PLT2* genes are auxin-inducible and convey root identity when ectopically expressed (*6*). Double *plt1 plt2* mutants have a misspecified QC (*6*), although pSCR::H2BYFP and nuclear pSHR::SHRGFP are detected at its position (Fig. 3; A, B, E, and G inset).

DR5rev::GFP expression in *plt1-4 plt2-2* double mutants spread throughout root vascular tissues 16 hours after ablation (Fig. 3C). However, only faint expression of DR5rev::GFP was detected in 1 to 2 cell layers proximal to the ablated QC cells (Fig. 3C, bracket), which disappeared at day 2 (Fig. 3D, bracket). Moreover, these cell layers lacked starch granules (Fig. 3D, inset and bracket), indicating that no respecification of columella cells occurs in *plt1-4 plt2-2* double mutants. Furthermore, pSHR::SHRGFP expression was lost in former vascular stem cells and their daughters, and nucleus-restricted pSHR::SHRGFP expression was undetectable in their abutting GFP-expressing provascular cells (Fig. 3F, bracket). These findings indicated defects in nuclear SHR targeting as well as QC respecification, both associated with root regeneration.

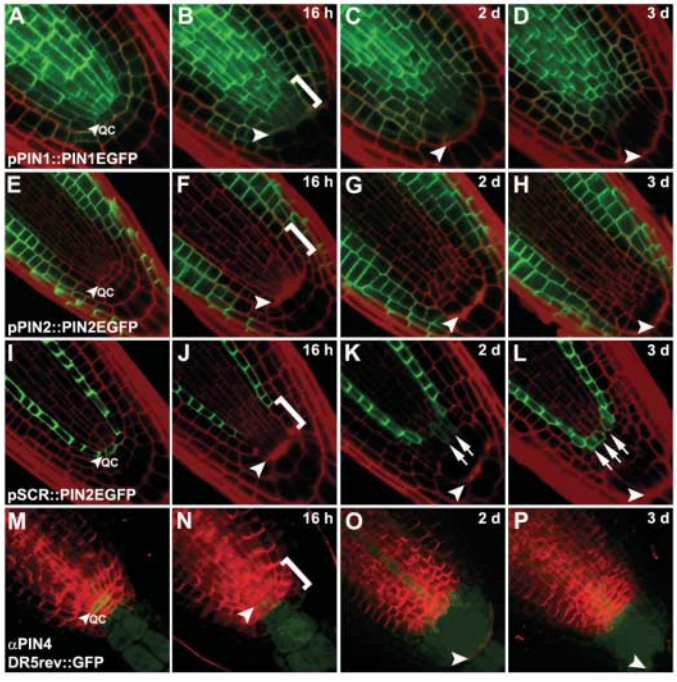

Fig. 2. PIN expression and polarity after QC ablation. (**A** to **D**) pPIN1::PIN1EGFP and (**E** to **H**) pPIN2::PIN2EGFP. (**I** to **L**) *SCR* promoter drove PIN2EGFP protein fusion. (**M** to **P**) PIN4 immunolocalization in WT roots containing DR5rev::GFP. The leftmost columns shows control before ablation. The images in the column second from the left are 16 hours after ablation. The column third from the left is 2 days after ablation. The right-most column is 3 days after ablation. Arrowheads indicate QC cells in the left-most column and the position of ablated QC elsewhere. Arrows in (K) and (L) show localization changes of pSCR::PIN2EGFP in cells at the position where the new QC cells were expected to be specified. The brackets in (B), (J), and (N) indicate down-regulation of markers and PIN expression. The bracket in (F) shows pPIN2::PIN2EGFP expression in cortex and epidermis approached the ablated QC. The red signal in [(A) to (L)] is PI staining; in [(M) to (P)] is Cy3 signal. The green signal is GFP.

No obvious defects in PIN1 expression and distribution were observed in *plt1-4 plt2-2* double mutants (Fig. 3G), suggesting no role for *PLT* genes in PIN1 localization. Down-regulation of PIN1 expression followed ablation as in WT (Fig. 3H, bracket), indicating that *PLT* genes are not required for this response.

SCR is cell-autonomously required for specification of QC cells and thereby required for maintenance of the surrounding stem cells (*4*). DR5rev::GFP and pWOX5::ERGFP are properly expressed in the *scr-4* null allele (*19*) before the root ceases growth (Fig. 3, I and M), although several QC-specific markers are absent in *scr* mutants (*4*). DR5rev::GFP expression accumulated above the ablated QC cells within 16 hours after ablation in *scr-4* roots (Fig. 3J, bracket) but remained restricted to about 2 layers proximal to the ablated QC cells (Fig. 3, K and L), where specification of columella cells occurred as indicated by starch granule staining (Fig. 3L, inset and bracket). However, no fate changes occurred in the proximally abutting layer, which should become the new QC, and pWOX5::ERGFP expression was lost 3 days after ablation (Fig. 3P), despite an initial response (Fig. 3, N and O, bracket). These data suggest that the role of SCR in QC specification is critical during regeneration.

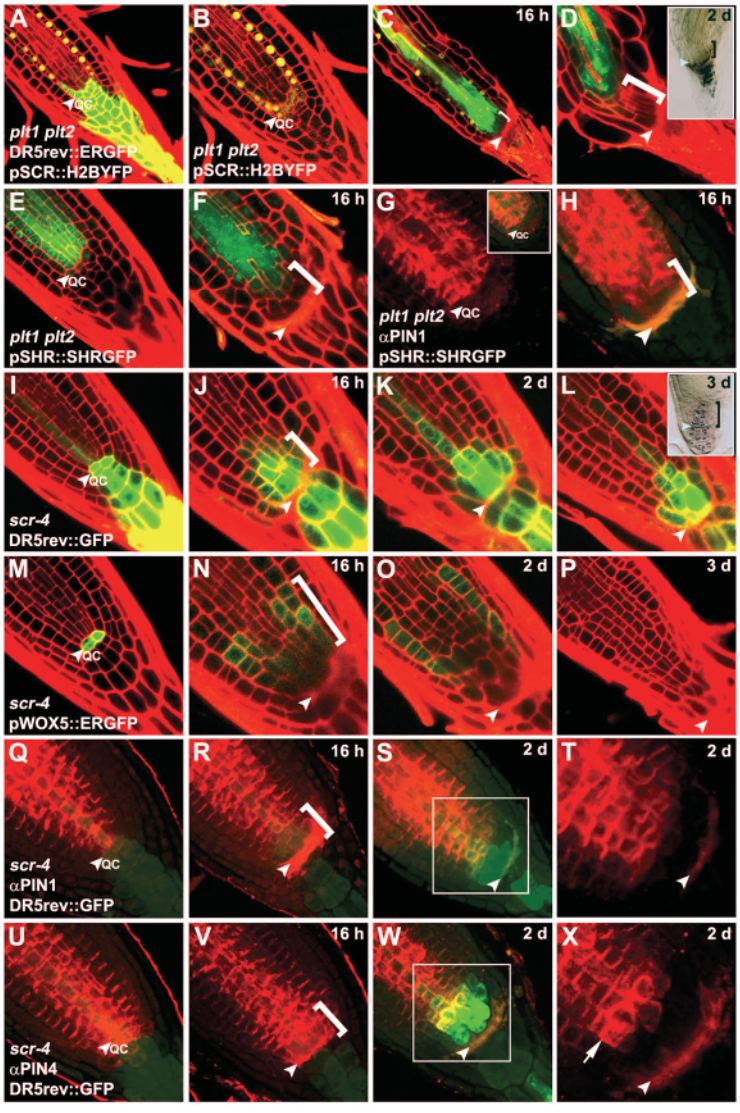

Fig. 3. The roles of *PLT*s and *SCR* are critical during regeneration. (**A** to **D**) DR5rev::GFP and pSCR::H2BYFP expression in *plt1-4 plt2-2* roots. (**E** and **F**) pSHR::SHRGFP expression in *plt1-4 plt2-2* roots. (**G** and **H**) PIN1 immunolocalization in *plt1-4 plt2-2* roots containing pSHR::SHRGFP. (**I** to **L**) DR5rev::GFP and (**M** to **P**) pWOX5::ERGFP expression in *scr-4* roots. (**Q** to **T**) PIN1 and (**U** to **X**) PIN4 immunolocalization in *scr-4* roots containing DR5rev::GFP. (T) and (X) show the enlarged box regions in (S) and (W), respectively. (A), (B), (E), (G), (I), (M), (Q), and (U) show control before ablation. (C), (F), (H), (J), (N), (R), and (V) are 16 hours after ablation. (D), (K), (O), (S), (T), (W), and (X) are 2 days after ablation. (L) and (P) are 3 days after ablation. Arrowheads indicate QC cells in (A), (B), (E), (G), (I), (M), (Q), and (U) and the position of ablated QC elsewhere. The inset and bracket in (D) show no provascular-columella identity switches in *plt1-4 plt2-2*. Brackets in (C) and (D) show faint or no expression in 1 to 2 cell layers proximal to the ablated QC. The bracket in (F) shows down-regulation of pSHR::SHRGFP and no nuclear-restricted pSHR::SHRGFP expression. The inset and bracket in (L) shows provascular-columella identity switches in *scr-4*. The brackets in (H), (J), (N), (R), and (V) indicate changes of markers and PIN expression. The arrow in (X) points to a basal-to-apical shift of PIN4 localization. The red signal in [(A) to (F)] and [(I) to (P)] is PI staining; in [(G), (H), and (Q) to (X)] is a Cy3 signal. The green signal is GFP and the yellow signal is YFP.

We asked whether the restricted expression of DR5rev::GFP proximal to the ablated QC of *scr-4* was caused by alterations in auxin re-routing. Therefore, we investigated PIN1 and PIN4 expression and localization in *scr-4* before and after QC ablation. PIN1 and PIN4 expression and distribution in *scr-4* mutants (Fig. 3, Q and U) was largely as in WT (Fig. 2M and fig. S3, A and B). Down-regulation of PIN1 and PIN4 expression in the cells abutting the ablated QC (Fig. 3, R and V, brackets) also occurred as in WT (Fig. 2N and fig. S3D, brackets), suggesting that SCR function is not required for this response. Cells at the proximal end of the proximally shifted auxin maximum, where the new QC should form, displayed a basal-to-apical shift of PIN4 localization (Fig. 3, W and X, arrow); whereas PIN1 expression and localization remained WT-like (Fig. 3, S and T). The PIN4 repolarization in the absence of *SCR* may cause auxin to be transported away from the proximally-shifted maximum and thereby explain the restricted expression of the auxin response marker DR5rev::GFP proximal to the ablated QC.

SHR, like *SCR*, is required for QC cell specification (*4*). *SHR* transcription occurs in the stele while the protein moves one cell layer outward, as shown by pSHR::SHRGFP expression (Fig. 1M) (*13*). Indeed, we found that *SHR* is also required for QC but not columella respecification and for proper PIN4 expression and localization by using the same set of fluorescent markers and antibodies in the null allele of *SHR*, *shr-2* (fig. S5) (*19*). As observed in *scr-4*, PIN4 was repolarized in provascular cells of *shr-2* roots (fig. S5P, arrow).

Our studies reveal essential roles for *PLT*, *SCR*, and *SHR* genes in respecifying pattern and polarity in the *Arabidopsis* root. They also provide further evidence that PIN proteins can become correctly polarized in response to auxin distribution changes only after renewed cell specification, rather than directly in response to auxin distribution changes. PIN4 localization is reversed in cells nearby the new auxin response maximum in the absence of *SCR* or *SHR*.

Our data suggest a model in which auxin-induced cell-fate changes depend on new expression domains and activity of PLT, SCR, and

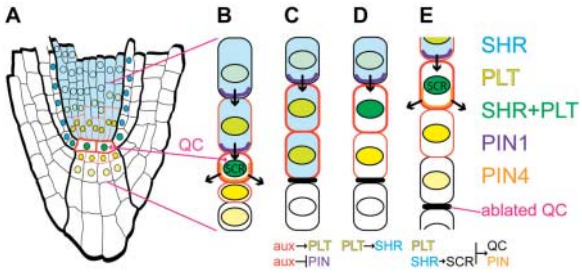

Fig. 4. A model for root regeneration. (**A**) *Arabidopsis* root meristem. (**B**) Enlarged cell file as marked in (A). (**C**) After ablation, auxin accumulation shifts, which induces *PLT* genes and downregulates PIN expression. (**D**) *PLT* genes promote SHR nuclear localization. (**E**) Nuclear SHR promotes *SCR* expression and, together with *PLT* genes, new QC specification. New, correctly polarized PIN expression depends on *PLT*, *SHR*, and *SCR* genes and reconstitutes auxin transport (black arrows). The red outline of cells marks auxin accumulation.

SHR transcription factors (Fig. 4). *PLT* genes are first upregulated where the auxin response builds up. The rapid response of *PLT1* transcription to local alteration of auxin distribution suggests that *PLT* genes are key effectors transducing the auxin signal into a repatterning process. Buildup of a new maximum is facilitated by transcription factor–independent downregulation of PIN expression. Dependent on *PLT* genes, SHR attains nuclear localization in a single provascular cell layer, which allows *SCR* expression and new QC specification. New PIN expression depends on *PLT*, *SHR*, and *SCR* genes, and PIN polarity is set only after these patterning genes have adopted their new expression domains. New correctly polarized PIN expression in turn reconstitutes the auxin transport route in the root tip and facilitates the completion of the regeneration process.

Our finding that auxin distribution changes the polar localization of PIN proteins only in the absence of fate regulators suggests that, in the root meristem, defined cell types have intrinsic polar marks to which PIN proteins are delivered. The PINOID (PID) kinase acts as a binary switch to position PIN proteins at opposing membranes, which supports the idea that an underlying, PIN-independent mechanism sets polarity (*20*). By influencing factors such as PID, but also protein trafficking regulators such as the GNOM ARF-GEF [guanine nucleotide exchange factor for adenosine diphosphate (ADP)–ribosylation factor] (*21*, *22*), cell-fate regulators may alter PIN protein trafficking. Classical canalization hypotheses proposed feedback between auxin flow and auxin transport in auxin-dependent developmental processes (*23*–*25*). Our results show that in the root, auxin redistribution first induces complex cell-fate changes and, only consequently, induces changes in the polarity of auxin flow, indicating that the classical canalization dogma does not apply here. However, in the absence of cell-fate determinants, such as in *scr* and *shr* mutants, or in other developmental contexts, such as during shoot-derived primordium positioning (*26*) or leaf vascularization, the PIN protein localization machinery may respond to other cues such as to auxin itself.

References and Notes

1. C. van den Berg, V. Willemsen, G. Hendriks, P. Weisbeek, B. Scheres, *Nature* **390**, 287 (1997).
2. L. Di Laurenzio *et al.*, *Cell* **86**, 423 (1996).
3. Y. Helariutta *et al.*, *Cell* **101**, 555 (2000).
4. S. Sabatini, R. Heidstra, M. Wildwater, B. Scheres, *Genes Dev.* **17**, 354 (2003).
5. R. Heidstra, D. Welch, B. Scheres, *Genes Dev.* **18**, 1964 (2004).
6. M. Aida *et al.*, *Cell* **119**, 109 (2004).
7. S. Sabatini *et al.*, *Cell* **99**, 463 (1999).
8. I. Blilou *et al.*, *Nature* **433**, 39 (2005).
9. E. Benková *et al.*, *Cell* **115**, 591 (2003).
10. J. Friml *et al.*, *Nature* **426**, 147 (2003).
11. D. Reinhardt *et al.*, *Nature* **426**, 255 (2003).
12. C. van den Berg, V. Willemsen, W. Hage, P. Weisbeek, B. Scheres, *Nature* **378**, 62 (1995).
13. K. Nakajima, G. Sena, T. Nawy, P. N. Benfey, *Nature* **413**, 307 (2001).
14. J. Xu, B. Scheres, *Plant Cell* **17**, 525 (2005).
15. J. Friml *et al.*, *Cell* **108**, 661 (2002).
16. J. Xu *et al.*, data not shown.
17. T. Sieberer *et al.*, *Curr. Biol.* **10**, 1595 (2000).
18. A. Vieten *et al.*, *Development* **132**, 4521 (2005).
19. H. Fukaki *et al.*, *Plant J.* **14**, 425 (1998).
20. J. Friml *et al.*, *Science* **306**, 862 (2004).
21. T. Steinmann *et al.*, *Science* **286**, 316 (1999).
22. N. Geldner *et al.*, *Cell* **112**, 219 (2003).
23. G. J. Mitchison, *Philos. Trans. R. Soc. London Ser. B* **295**, 461 (1981).
24. T. Sachs, *Adv. Bot. Res.* **9**, 152 (1981).
25. T. Sachs, *Dev. Suppl.* **1**, 83 (1991).
26. M. G. Heisler *et al.*, *Curr. Biol.* **15**, 1899 (2005).

27. We thank I. Blilou, J. M. Pérez-Pérez, and V. Willemsen for comments. This work was supported by a PIONIER award from the Dutch Organization for Science, a Utrecht excellence fellowship, and by the VolkswagenStiftung.

Supporting Online Material

www.sciencemag.org/cgi/content/full/311/5759/385/DC1
Materials and Methods
Figs. S1 to S5
References

25 October 2005; accepted 14 December 2005
10.1126/science.1121790

Chromosomes Can Congress to the Metaphase Plate Before Biorientation

Tarun M. Kapoor,[1,2] Michael A. Lampson,[1] Polla Hergert,[3] Lisa Cameron,[2,4] Daniela Cimini,[4] E. D. Salmon,[2,4] Bruce F. McEwen,[3] Alexey Khodjakov[1,2,3]*

The stable propagation of genetic material during cell division depends on the congression of chromosomes to the spindle equator before the cell initiates anaphase. It is generally assumed that congression requires that chromosomes are connected to the opposite poles of the bipolar spindle ("bioriented"). In mammalian cells, we found that chromosomes can congress before becoming bioriented. By combining the use of reversible chemical inhibitors, live-cell light microscopy, and correlative electron microscopy, we found that monooriented chromosomes could glide toward the spindle equator alongside kinetochore fibers attached to other already bioriented chromosomes. This congression mechanism depended on the kinetochore-associated, plus end–directed microtubule motor CENP-E (kinesin-7).

Successful cell division requires proper "biorientation" of chromosomes, whereby microtubule bundles (K fibers) connect sister kinetochores of each chromosome to opposite spindle poles (*1*). Biorientation errors are linked to chromosome loss and cancers (*2*). Formation of sister K fibers occurs asynchronously (*3*), and once a kinetochore captures microtubules growing from a spindle pole, the chromosome is transported toward this pole and becomes "monooriented" (*4*). Monooriented chromosomes remain near the spindle pole for variable times (*3*, *4*) until they suddenly "congress" to the spindle equator. Current models of mitotic spindle formation (*5*, *6*) postulate that chromosome congression occurs as the result of biorientation (*7*).

We followed movements of individual chromosomes in mammalian cells by differential interference contrast (DIC) time-lapse microscopy (*8*). In addition to the chromosome oscillations that occur toward and away from spindle poles, we frequently observed monooriented chromosomes making direct movements to the metaphase plate as if they were attempting to congress (fig. S1). Centromeres

[1]Laboratory of Chemistry and Cell Biology, the Rockefeller University, New York, NY 10021, USA. [2]Marine Biological Laboratory, Woods Hole, MA 02543, USA. [3]Division of Molecular Medicine, Wadsworth Center, Albany, NY 12201–0509, USA. [4]Department of Biology, University of North Carolina at Chapel Hill, Chapel Hill, NC 27599, USA.

*To whom correspondence should be addressed. E-mail: khodj@wadsworth.org

on these congressing chromosomes were frequently stretched, which indicated force generation by the leading kinetochore (Movie S1). However, these movements did not always result in a stable alignment on the metaphase plate, because chromosomes often returned to the spindle pole after a 3- to 4-μm excursion. This chromosome behavior was observed in essentially every cell we imaged and has also been previously reported (*9*–*12*). To determine whether these chromosomes were bioriented, we followed mitotic cells by DIC microscopy until one of the chromosomes exhibited an extended linear movement toward the metaphase plate, and we fixed the cell when the chromosome had almost reached the metaphase plate (~5 to 7 μm from the proximal spindle pole) (Fig. 1; Movie S2). Three of five chromosomes analyzed by electron microscopy (EM) (*8*) were already bioriented, as expected for congressing chromosomes (*7*). However, in the other two cases, no microtubules emanated from the leading kinetochore plate on the congressing chromosome. Instead, this kinetochore laterally interacted with microtubules of a mature K fiber attached to a kinetochore of another bioriented chromosome positioned on the metaphase plate (Fig. 1D). The trailing kinetochore was attached to the proximal spindle pole via a mature K fiber. This unexpected type of kinetochore-microtubule interaction suggested that chromosomes may not need to be bioriented during congression.

Because individual K fibers are not resolved by DIC microscopy, we could not correlate the trajectory of an individual chromosome moving toward the spindle equator with the positions of surrounding K fibers. To overcome this limitation, we simultaneously imaged both microtubules and kinetochores by live-cell dual-channel fluorescence microscopy. PtK_1 epithelial cells derived from the marsupial rat kangaroo, *Potorous tridactylis*, were coinjected with a fluorescein-conjugated antibody against the kinetochore protein CENP-F that does not perturb its function (to label kinetochores) and X-rhodamine–conjugated αβ-tubulin (to label microtubules) (*13*). In 12 of the 49 cells analyzed, we found at least one monooriented chromosome whose trajectory, during the movement toward the spindle equator, precisely followed K fibers of other, already bioriented chromosomes (Fig. 2; Movie S3). This pattern indicated that such congressing chromosomes were not simply ejected away from the pole by the spindle ejection force acting on the entire chromosome (*11*, *14*), but glided on the microtubules of mature K fibers.

The time a monooriented chromosome spends at a spindle pole is variable, and the number of attempts it makes before finally achieving stable positioning on the metaphase plate is unpredictable (*15*). To examine the state of kinetochore-microtubule interaction during the first congression attempt, we established an experimental system in which several chromosomes congressed in a single cell within a narrow time window (Fig. 3A). We combined high-resolution imaging and chemical inhibitors to manipulate chromosome positions in dividing cells. Cells were treated with monastrol, a small-molecule inhibitor of the kinesin Eg5 (kinesin 5). This treatment blocked cells in monopolar mitosis with high incidence of syntelic (both sister kinetochores attached to the same spindle pole) chromosomes (*16*). Then, cells were released from monastrol into an Aurora kinase inhibitor. Under these conditions, spindles bipolarized while many chromosomes remained syntelic (*17*). Relief from Aurora kinase inhibition resulted in the transport of syntelic chromosomes to spindle poles from where they congressed to the metaphase plate (*17*). This assay allowed us to accumulate monooriented chromosomes whose congression was temporally controlled through washout of cell-permeable chemical inhibitors.

Using this assay, we imaged individual cells by time-lapse DIC and spinning-disk confocal microscopy. Once several monooriented chromosomes initiated their movement toward the metaphase plate, the cell was fixed for correlative serial-section EM analysis. On six out of seven congressing chromosomes analyzed by this approach, the leading kinetochore was laterally associated with a mature K fiber that extended from a different bioriented chromosome toward the proximal spindle pole (Fig. 3B; fig. S2). By contrast, the trailing kinetochore was attached in typical tip-on fashion to a K fiber connected to the proximal spindle pole (Fig. 3B; fig. S2). Thus, ~85% of chromosomes lacked microtubule attachments to the

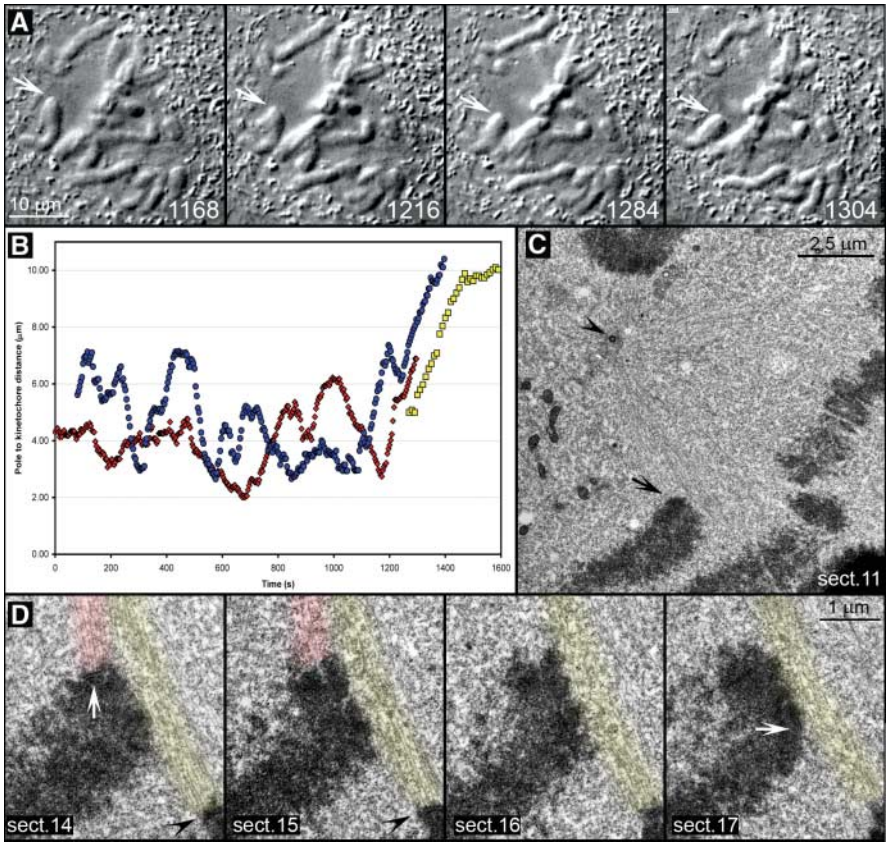

Fig. 1. Leading kinetochores are not properly attached to microtubules during a chromosome's attempt to congress. (**A**) Selected frames from a DIC time-lapse recording (also see Movie S2). The cell was fixed as one chromosome (arrows) moved toward the spindle equator (1304 s). (**B**) Distance versus time plot confirmed that the chromosome's movement (red curve) was typical for chromosome congression [compare with blue and yellow curves, which represent movements of chromosomes shown in fig. S1 and Fig. 2, respectively]. (**C**) Lower-magnification EM image of the cell showing the position of the chromosome of interest (arrow) with respect to the spindle pole (arrowhead). (**D**) Selected 100-nm EM section from a full series through the centromere region of the chromosome. Note the prominent bundle of microtubules (highlighted red) connecting the trailing kinetochore (white arrow in section 14) to the proximal spindle pole. These microtubules approached the kinetochore at ~90° angle and terminated within the trilaminar kinetochore plate. By contrast, the leading kinetochore (white arrow, section 17) lacked attached microtubules but was laterally associated with a mature kinetochore fiber (highlighted yellow) that was attached to the kinetochore of a bioriented chromosome (black arrowheads in sections 14 and 15) positioned on the metaphase plate.

distal spindle pole (that is, remained monooriented) during congression in our experimental system. Importantly, centromeres on the congressing chromosomes were stretched (>2 μm) (Fig. 3B; fig. S2), which indicated a force acting at the leading kinetochore.

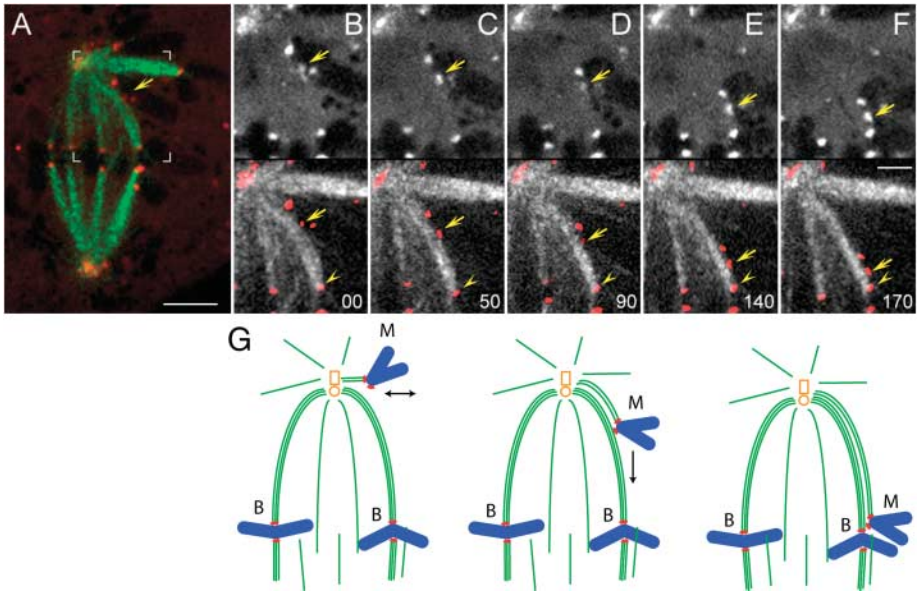

Fig. 2. Monooriented chromosomes are transported toward the spindle equator along kinetochore fibers of other chromosomes. (**A**) Two-color fluorescence image of a live PtK_1 cell in which kinetochores were labeled with CENP-F/Alexa488 (red) and microtubules with tubulin/rhodamine (green). Area marked with white brackets is enlarged in (B to F). (**B** to **F**) selected frames from the two-color time-lapse recording. In each frame, CENP-F/Alexa488 fluorescence (kinetochores) is shown alone (top) and overlaid in red on microtubules (bottom). Arrows mark the kinetochore that moved toward the spindle equator. Note that trajectory of this kinetochore coincided with a prominent kinetochore fiber that extended from the spindle pole to a kinetochore on a bioriented chromosomes already positioned on the metaphase plate (arrowhead). Time in seconds. Scale bars: (A) 5 μm, (F) 2.5 μm. (**G**) Schematic illustrating the sequence of events presented in (B to F).

Chromosomes fixed before initiating congression were either syntelic [five out of six (fig. S3)] or monooriented [one of six (fig. S4)]. In the latter case, one of the kinetochores was connected to the pole by a K fiber, while its sister was laterally associated with a bundle of microtubules bypassing the kinetochore and extending toward the spindle equator (fig. S4). This configuration, once again, suggests that chromosome congression can be initiated by sliding of the unattached kinetochores alongside mature K fibers.

We next considered the molecular mechanisms responsible for congression of monooriented chromosomes. Because microtubule polarity within a K fiber is uniform (*18*), this movement is likely to depend on a motor protein that transports cargo toward the microtubule plus ends. Further, this motor must be concentrated at kinetochores during prometaphase. CENP-E (a member of the kinesin-7 family) is the only plus end–directed motor that meets both criteria (*19*, *20*). Depleting CENP-E in human cells results in a mitotic arrest, with significant numbers of monooriented chromosomes positioned very close to the spindle pole (*21*, *22*). In addition, recombinant CENP-E binds the sides of microtubule bundles in vitro (*23*). We used our chemical inhibitor–based assay and small interfering RNA (siRNA) to determine whether CENP-E was responsible for the congression mechanism observed for monooriented chromosomes. Because the rat kangaroo CENP-E has not yet been cloned, we used human cells for these experiments.

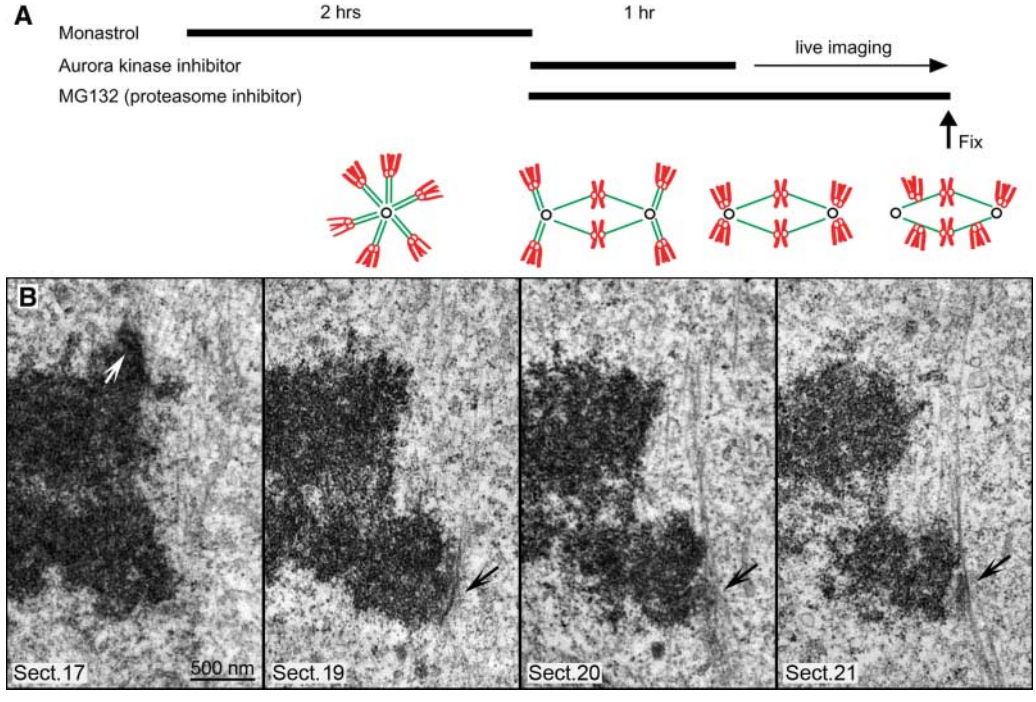

Fig. 3. Leading kinetochores are laterally associated with kinetochore fibers of other chromosomes during chromosome congression. (**A**) Protocol for inducing synchronous chromosome congression. Cells were arrested in mitosis with monastrol to accumulate monopolar mitosis with high incidence of syntelic chromosomes (green, microtubules; red, chromosomes). Then, monastrol was removed and Hesperadin was added with MG132 for 1 hour. This resulted in spindle bipolarization, although many chromosomes remained syntelic. After 1 hour, Hesperadin was removed, and cells were imaged live until fixation. Removal of Hesperadin resulted in simultaneous correction of syntelic attachments. Syntelic chromosomes moved to the pole, became monooriented, and then attempted to congress. (**B**) Selected 100-nm EM sections from a full series through the centromere of a congressing chromosome. Note that, similarly to untreated cells (Fig. 1), chromosomes congressed with their leading kinetochores unattached (black arrows) but slide alongside mature kinetochore fibers of other chromosomes. By contrast, trailing kinetochores (white arrow) were always attached to prominent kinetochore fibers that terminated within the trilaminar plate.

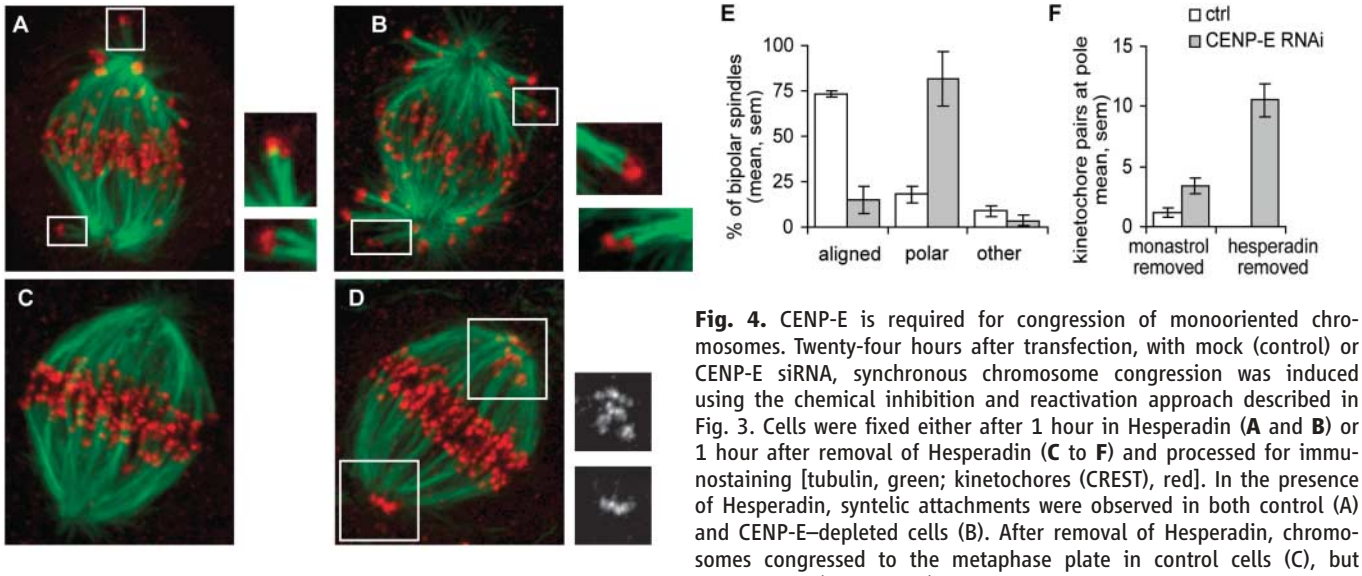

Fig. 4. CENP-E is required for congression of monooriented chromosomes. Twenty-four hours after transfection, with mock (control) or CENP-E siRNA, synchronous chromosome congression was induced using the chemical inhibition and reactivation approach described in Fig. 3. Cells were fixed either after 1 hour in Hesperadin (**A** and **B**) or 1 hour after removal of Hesperadin (**C** to **F**) and processed for immunostaining [tubulin, green; kinetochores (CREST), red]. In the presence of Hesperadin, syntelic attachments were observed in both control (A) and CENP-E–depleted cells (B). After removal of Hesperadin, chromosomes congressed to the metaphase plate in control cells (C), but monooriented chromosomes were observed near spindle poles in CENP-E–depleted cells (Insets in D) CREST staining. For cells fixed 1 hour after removal of Hesperadin, bipolar spindles were counted and classified as fully aligned or containing polar chromosome(s) (E) (average of four experiments). To quantify the number of chromosomes at the pole, the number of kinetochore pairs with no detectable K fiber was counted in three-dimensional confocal images [(F), averages from 19 CENP-E–depleted or 7 control cells for each condition, two experiments]. All images presented as maximal-intensity projections. (Insets in A and B) Optical sections at 2× magnification.

Multiple syntelic chromosomes were observed after spindle bipolarization in the presence of an Aurora kinase inhibitor in control and CENP-E–depleted HeLa cells (Fig. 4, A and B). Thus, kinetochores remained capable of capturing microtubules in the absence of CENP-E. Within 1 hour after Aurora kinase activation by inhibitor removal, all chromosomes were positioned at the metaphase plate in 73 ± 2% of the controls but only in 15 ± 7% of CENP-E–depleted cells (four experiments, >80 cells per experiment; Fig. 4, C to E). At the same time, the number of polar chromosomes in CENP-E–depleted cells increased dramatically (from 3.4 ± 0.7 to 10.5 ± 1.3) after Aurora activation (Fig. 4F). Thus, syntelic chromosomes that reside at a substantial distance from their poles move to the pole and become monooriented after activation of Aurora kinase in CENP-E–depleted cells. However, these monooriented chromosomes are not subsequently transported to the metaphase plate in the absence of CENP-E. Hence, depletion of CENP-E does not affect chromosome attachment to the proximal spindle pole. Instead, it diminishes the probability for monooriented chromosomes to be transported from the spindle pole toward the spindle equator, where they can acquire connections to the distal pole and become bioriented. Our EM data revealed that sliding of kinetochores toward the plus ends of mature K fibers is a major mechanism for aligning monooriented chromosomes positioned near a pole, and this mechanism is missing in the absence of CENP-E. This defect explains why persistent monooriented chromosomes positioned very close to the spindle pole have been found consistently in CENP-E–deficient cells (*19*, *21*, *22*, *24*).

Our findings address a long-standing question in cell division. It was unclear how chromosome accumulation at spindle poles in prometaphase and during correction of syntelic attachments leads to biorientation (*25*). Our data reveal that at spindle poles, monooriented chromosomes are likely to find mature K fibers that are attached to other, already bioriented chromosomes and to congress alongside these K fibers via a CENP-E–dependent mechanism. In this congression mechanism, the probability that a monooriented chromosome will be transported toward the spindle equator progressively increases as more and more chromosomes become bioriented, which increases the density of K fibers in the spindle. Thus, chromosome congression is a cooperative process that depends on chromosome positions relative to the mitotic spindle and is promoted for those chromosomes that remain monooriented as the spindle fully assembles and establishes a metaphase plate. Abrogating this cooperativity would mostly affect chromosomes that congress late during spindle formation, thereby inducing loss of one or two chromosomes, as has been observed after CENP-E depletion in murine cells (*26*).

References and Notes

1. C. L. Rieder, E. D. Salmon, *Trends Cell Biol.* **8**, 310 (1998).
2. H. Rajagopalan, C. Lengauer, *Nature* **432**, 338 (2004).
3. U. P. Roos, *Chromosoma* **54**, 363 (1976).
4. C. L. Rieder, S. P. Alexander, *J. Cell Biol.* **110**, 81 (1990).
5. M. Kirschner, T. Mitchison, *Cell* **45**, 329 (1986).
6. A. W. Murray, T. J. Mitchison, *Curr. Biol.* **4**, 38 (1994).
7. B. F. McEwen, A. B. Heagle, G. O. Cassels, K. F. Buttle, C. L. Rieder, *J. Cell Biol.* **137**, 1567 (1997).
8. Materials and methods are available as supporting material on *Science* Online.
9. R. V. Skibbens, C. L. Rieder, E. D. Salmon, *J. Cell Biol.* **122**, 859 (1993).
10. J. C. Waters, R. V. Skibbens, E. D. Salmon, *J. Cell Sci.* **109**, 2823 (1996).
11. A. Khodjakov, C. L. Rieder, *J. Cell Biol.* **135**, 315 (1996).
12. A. Khodjakov, R. W. Cole, B. F. McEwen, K. F. Buttle, C. L. Rieder, *J. Cell Biol.* **136**, 229 (1997).
13. D. Cimini, L. A. Cameron, E. D. Salmon, *Curr. Biol.* **14**, 2149 (2004).
14. C. L. Rieder, E. D. Salmon, *J. Cell Biol.* **124**, 223 (1994).
15. C. L. Rieder, A. Schultz, R. Cole, G. Sluder, *J. Cell Biol.* **127**, 1301 (1994).
16. T. M. Kapoor, T. U. Mayer, M. L. Coughlin, T. J. Mitchison, *J. Cell Biol.* **150**, 975 (2000).
17. M. A. Lampson, K. Renduchitala, A. Khodjakov, T. M. Kapoor, *Nat. Cell Biol.* **6**, 232 (2004).
18. U. Euteneuer, J. R. McIntosh, *J. Cell Biol.* **89**, 338 (1981).
19. K. W. Wood, R. Sakowicz, L. S. B. Goldstein, D. W. Cleveland, *Cell* **91**, 357 (1997).
20. X. Yao, K. L. Anderson, D. W. Cleveland, *J. Cell Biol.* **139**, 435 (1997).
21. B. T. Schaar, G. K. T. Chan, P. Maddox, E. D. Salmon, T. J. Yen, *J. Cell Biol.* **139**, 1373 (1997).
22. B. F. McEwen *et al.*, *Mol. Biol. Cell* **12**, 2776 (2001).
23. Y. Mao, A. Desai, D. W. Cleveland, *J. Cell Biol.* **170**, 873 (2005).
24. F. R. Putkey *et al.*, *Dev. Cell* **3**, 351 (2002).
25. S. Hauf, D. Watanabe, *Cell* **119**, 317 (2004).
26. B. A. Weaver *et al.*, *J. Cell Biol.* **162**, 551 (2003).

27. We acknowledge use of Wadsworth Center's EM core facility. Supported by grants from the NIH (GM59363 to A.K., GM65933 to T.M.K., GM24364 to E.D.S, and GM06627 to B.F.M.) and NSF (MCB 0110821 to B.F.M.).

Supporting Online Material

www.sciencemag.org/cgi/content/full/311/5759/388/DC1
Materials and Methods
Figs. S1 to S5
References
Movies S1 to S3

2 November 2005; accepted 9 December 2005
10.1126/science.1122142

Metagenomics to Paleogenomics: Large-Scale Sequencing of Mammoth DNA

Hendrik N. Poinar,[1,2,3]* Carsten Schwarz,[1,2] Ji Qi,[4] Beth Shapiro,[5] Ross D. E. MacPhee,[6] Bernard Buigues,[7] Alexei Tikhonov,[8] Daniel H. Huson,[9] Lynn P. Tomsho,[4] Alexander Auch,[9] Markus Rampp,[10] Webb Miller,[4] Stephan C. Schuster[4]*

We sequenced 28 million base pairs of DNA in a metagenomics approach, using a woolly mammoth (*Mammuthus primigenius*) sample from Siberia. As a result of exceptional sample preservation and the use of a recently developed emulsion polymerase chain reaction and pyrosequencing technique, 13 million base pairs (45.4%) of the sequencing reads were identified as mammoth DNA. Sequence identity between our data and African elephant (*Loxodonta africana*) was 98.55%, consistent with a paleontologically based divergence date of 5 to 6 million years. The sample includes a surprisingly small diversity of environmental DNAs. The high percentage of endogenous DNA recoverable from this single mammoth would allow for completion of its genome, unleashing the field of paleogenomics.

Complete genome sequences of extinct species will answer long-standing questions in molecular evolution and allow us to tackle the molecular basis of speciation, temporal stages of gene evolution, and intermediates of selection during domestication. To date, fossil remains have yielded little genetic insight into evolutionary processes because of poor preservation of their DNA and our limited ability to retrieve nuclear DNA (nDNA). Most DNA extracted from fossil remains is truncated into fragments of very short length [<300 base pairs (bp)] from hydrolysis of the DNA backbone, cross-linking due to condensation (*1*, *2*), and oxidation of pyrimidines (*3*), which prevents extension by *Taq* DNA polymerase during polymerase chain reaction (PCR). In addition, DNA extracts are a mixture of bacterial, fungal, and often human contaminants, complicating the isolation of endogenous DNA. In the past, these problems could only be indirectly overcome by concentrating on the small number of genes present on the maternally inherited mitochondrial genome, which is present in high copy number in animal cells. This approach severely limits access to the storehouses of genetic information potentially available in fossils of now-extinct species. In a few rare cases, investigators have managed to isolate and characterize nuclear DNA from fossil remains preserved in arid cave deposits (*4*–*6*) or, more commonly, permafrost-dominated environments (*7*, *8*) and ice (*9*), where the average burial temperature can be as low as –10°C (*10*). Under these conditions, preservation is enhanced by reduced reaction rates: In permafrost settings, theoretical calculations predict DNA fragment survival up to 1 million years (*11*, *12*).

Although more nuclear DNA is present in cells than mitochondrial DNA, access to the nuclear genome even in well-preserved fossil material remains difficult with PCR-based approaches, which must target known sequences from specific genes. To find the ideal sample and analytical approach for paleogenomics, we screened eight of the morphologically best preserved mammoth remains in the collections of the Mammoth Museum, a dedicated permafrost "ice cave" facility in the town of Khatanga in the southeastern part of the Taimyr Peninsula, Russian Federation, and maintained by Cerpolex/Mammuthus Expeditions (CME). We extracted DNA from these samples, using ancient DNA methodology, to avoid to the greatest extent possible exogenous DNA (*13*), because we are well aware of the problems and pitfalls associated with potential contamination. These samples were screened with a quantitative PCR (qPCR) assay designed for the mammoth mitochondrial cytochrome *b* gene (*14*), with primers designed to amplify mitochondrial DNA molecules from both African and Asian elephants (*Loxodonta africana* and *Elephas maximus*). We quantitated the number of amplifiable mitochondrial DNA (mtDNA) molecules of 84 bp in length. The eight samples ranged from 1×10^6 copies per gram to 96×10^6 copies per gram, all excellent samples as judged by ancient DNA standards (*15*). However, one sample in particular, CME 2005/915, was exceptional. The specimen, an edentulous mandible dated to 27,740 ± 220 ^{14}C years before the present (uncorrected; Beta 210777), was recovered on the shore of Baikura-turku, a large bay on the southeastern side of Lake Taimyr, the largest freshwater body in Eurasia north of the Arctic Circle. The large numbers and high quality of late Quaternary fossils recovered from the Taimyr Peninsula have prompted several major investigations in recent years (*16*), including studies of ancient DNA (*14*, *17*, *18*). Taimyr's extremely cold winters, combined with short, cool summers and little annual precipitation, have ensured that conditions optimal for the preservation of bones and teeth prevailed there for most or all of the late Pleistocene.

To obtain a better perspective on the preservational integrity of this sample, we quantitated the number of amplifiable mtDNA cytochrome *b* gene fragments of increasing length up to 1 Kb (fig. S1) (*13*). The DNA extract (from 58 mg bone) contained $\sim 7 \times 10^6$ copies of the 84-bp mtDNA fragment in 100 μl or 121×10^6 copies per gram of bone (*13*). On the basis of this, we estimated that the concentration of total amplifiable DNA in our sample (assuming a copy-number ratio of 1000:1, mtDNA:nDNA) was on the order of 0.73 μg of mammoth DNA per gram of bone. We extracted 1 g of bone and concentrated the DNA to 100 μl, which was subsequently used for library construction and sequencing technology that recently became available (*13*, *19*). This in vitro technique circumvents amplification or cloning biases by compartmentalizing single DNA molecules before the amplification step in a lipid vesicle, thereby maintaining the original DNA template distribution. The lipid-enclosed single DNA molecule, attached to a sepharose bead 28 μm in diameter, undergoes a PCR reaction, yielding sufficient DNA copies for sequencing. Sequencing is performed with a pyrosequencing methodology (*19*).

We obtained 302,692 sequence reads averaging 95 bp, with read length being limited by the sequencing approach rather than by the 630-bp average DNA fragment size obtained from the extract after shearing. The total sequence data produced for the bone metagenome was 28×10^6 bp. We aligned the sequencing reads with current (November 2005) assemblies of the genome sequences of African elephant (*L. africana*), human, and dog (*Canis familiaris*), downloaded from www.genome.ucsc.edu (Table 1 and Fig. 1). Alignments were computed by the program BLASTZ (*20*), with parameters chosen to identify only regions of about 90% identity or higher (*13*). As we have not detected any convincing mappings of a read to the human Y chromosome, despite random distribution across the genome, we conclude that our mammoth was a female.

A total of 137,527, or 45.4% of all reads, aligned to the African elephant genome (Fig. 1, Table 1) (*13*), currently available at 2.2-fold coverage, with an estimated number of base pairs in the genome of 2.3×10^9 bp (www.broad.mit.edu/mammals/#chart). A twofold cov-

[1]McMaster Ancient DNA Center, [2]Department of Anthropology, [3]Department of Pathology and Molecular Medicine, McMaster University, 1280 Main Street West, Hamilton ON, L8S 4L9 Canada. [4]Pennsylvania State University, Center for Comparative Genomics and Bioinformatics, 310 Wartik Building, University Park, PA 16802, USA. [5]Henry Wellcome Ancient Biomolecules Centre, Department of Zoology, Oxford University, South Parks Road, Oxford, OX1 3PS, UK. [6]Division of Vertebrate Zoology/Mammalogy, American Museum of Natural History, 79th Street and Central Park West, New York, NY 10024, USA. [7]#2 Avenue de la Pelouse, F-94160 St. Mandé, France. [8]Zoological Institute, Russian Academy of Sciences, Universitetskaya nab.1, Saint Petersburg 199034, Russia. [9]Center for Bioinformatics (ZBIT), Institute for Computer Science, Tübingen University, 72076 Tübingen, Germany. [10]Garching Computing Center (RZG), Boltzmannstrasse 2, D-85748 Garching, Germany.

*To whom correspondence should be addressed. E-mail: poinarh@mcmaster.ca (H.N.P.); scs@bx.psu.edu (S.C.S.)

Table 1. Total percent of aligned reads and their relative identities to African elephant, human, and dog.

	Elephant	Human	Dog
Total no. reads	302,692 (100%)	302,692 (100%)	302,692 (100%)
Aligned reads	137,527 (45.4%)	4,237 (1.4%)	3,775 (1.2%)
Uniquely aligning reads	44,442 (14.7%)	3,901 (1.3%)	3,548 (1.2%)
Multiply aligned reads	93,085 (30.8%)	336 (0.1%)	227 (0.1%)
Reads with at least 95% identity	90,507 (30.0%)	1,184 (0.4%)	1,140 (0.4%)
Reads with 100% identity	21,952 (7.3%)	116 (0.04%)	142 (0.05%)
Uniquely aligning base pairs	4,332,350	318,966	291,714
Identity in unique alignments	98.55%	92.68%	92.91%
Mitochondrial reads	209	–	–
Identity in mitochondrial reads	95.93%	–	–
Mitochondrial base pairs	16,419	–	–

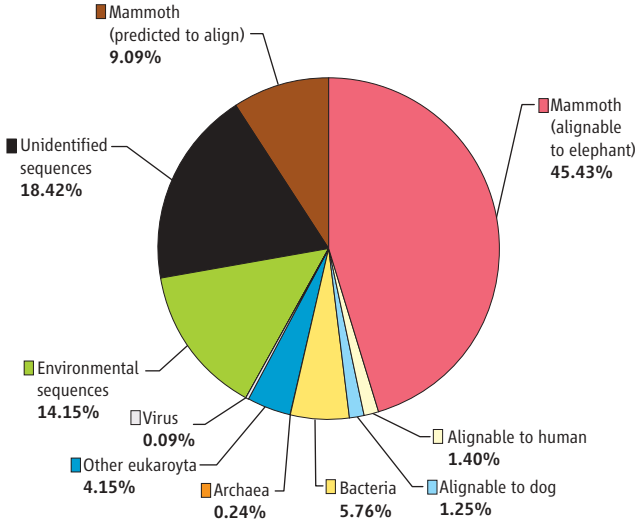

Fig. 1. Characterization of the mammoth metagenomic library, including percentage of read distributions to various taxa. Host organism prediction based on BLASTZ comparison against GenBank and environmental sequences database.

erage approximates only 80% of the total genome, so a conservative estimate is that half of our reads would align to a completed elephant sequence. Among all reads, 44,442 (14.7%) aligned to only one position in the elephant genome, and 21,952 (7.3%) exhibited a perfect (100%) match, up to a read length of 132 bp. To test whether the observed hits were more likely to be derived from endogenous mammoth DNA, as opposed to potential contaminants such as human DNA, we repeated the BLASTZ analyses as above, this time comparing our sequence reads to the currently available versions of the human and dog genomes. Only 4237 reads (1.4%) aligned to human and 3775 (1.2%) to dog (at our threshold of approximately 90% identity). Between 1% and 5% of any two distantly related mammalian genomes should align at 90% identity or greater, because roughly 0.5% of these genomes consist of protein-coding segments conserved at that level (*21*), and noncoding DNA contributes a somewhat larger fraction (*22*). Thus, the fraction of our reads that show at least 90% identity with human and dog is what is expected if only mammoth DNA were sequenced.

To further assess the possibility of contamination in our DNA sample, we explicitly considered what would be expected if contaminating human DNA sequences were present. If some of our reads were human DNA, then these reads should align with nearly 100% identity to human, and at most, 5% of these could be expected to align at 90% identity or higher to any nonprimate mammalian genome (only about 5 to 6% of the genome appears to be under negative selection (*23*), and our 90% threshold is far above the neutral level). If our data contained human reads, we could be essentially certain that a large fraction of them would align to human at or above 97% identity over at least 80% of their length and not align to either elephant or dog. Only 14 reads satisfy these criteria. Thus, there are, at most, trace levels of human contamination in the sample or the process, and the 14 potential examples may simply be regions that are well conserved between mammoth and all other mammals but that happen to be missing from the current assemblies of the dog and elephant genomes. We applied the same approach to look for potential contamination of dog DNA in our sample and found none.

To determine substitution patterns between mammoth and other species (table S2), we used the subset of reads that aligned to only one position. We observed 98.55% identity between mammoth and elephant. As this number does not correct for alterations of the sequence due to damage caused by base decomposition, we are likely underestimating the amount of sequence similarity. Base damage in fossil matrices can result in a myriad of base changes; however, the most commonly observed change has been deamination of cytosine to uracil (*24*, *25*) resulting in C-to-T and G-to-A substitutions. We therefore looked for asymmetries in base composition between modern and ancient genomes (table S2). We reasoned that C-to-T transitions due to DNA damage would manifest as an excess of elephant C aligned to mammoth T over elephant T aligned to mammoth C. Indeed, the ratio of the rates to and from mammoth relative to elephant is 1.91 (15297/7990) for C-to-T and 1.15 (9530/8252) for G-to-A [C-to-T human 0.96 (3849/4027); dog 1.11 (3622/3276); G-to-A human 0.87 (3541/4060); and dog 0.97 (3321/3440)]. Thus, we find noticeable deamination of cytosines in our extract. In addition, we analyzed the frequencies with which substitutions likely to be attributable to postmortem damage occurred in the amplified fragments of mtDNA by comparison with the publicly available mammoth mitochondrion genome (GenBank accession #NC_007596, DQ188829) (*13*). We found 222 reads that aligned to the public GenBank mammoth mitochondrial genome (Fig. 2). Two hundred nine reads gave a total of 18,581 bp, 7617 bp of which were overlapping, resulting in a total coverage of 10,964 bp of a possible 16,770 bp (65%). One hundred fourteen of the 209 reads (55%) matched the previously published sequence exactly. One hundred nine base differences were observed between the reads and the published sequence, 49 of which were not supported by overlapping reads. The majority of these substitutions (84%) were either C-to-T or G-to-A transitions, as is expected if the substitutions were due to postmortem DNA deamination. The remaining 13 reads differed significantly from the published data and may be evidence of potential nuclear inserts of DNA from the mitochondrion (*13*), which have been reported previously to be common in elephants and mammoths (*26*).

These findings are well within the predicted levels of damage for ancient DNA and demonstrate the feasibility and benefits of ancient whole-genome sequencing without previous amplification, as overlapping reads from a multifold coverage would easily correct for decompositional base changes accrued during the sample's depositional history and serve as a DNA damage correction filter. The ratio of mtDNA to nuclear DNA for our sample was 1:658, which agrees with what one would expect given a 1:1000 copy-number ratio for nDNA versus mtDNA.

Despite the presence in our sample of an exceptionally high percentage (54.5%, including reads predicted to align to elephant) of mammoth DNA, relative to environmental contaminants, 45.5% of the total DNA derives from

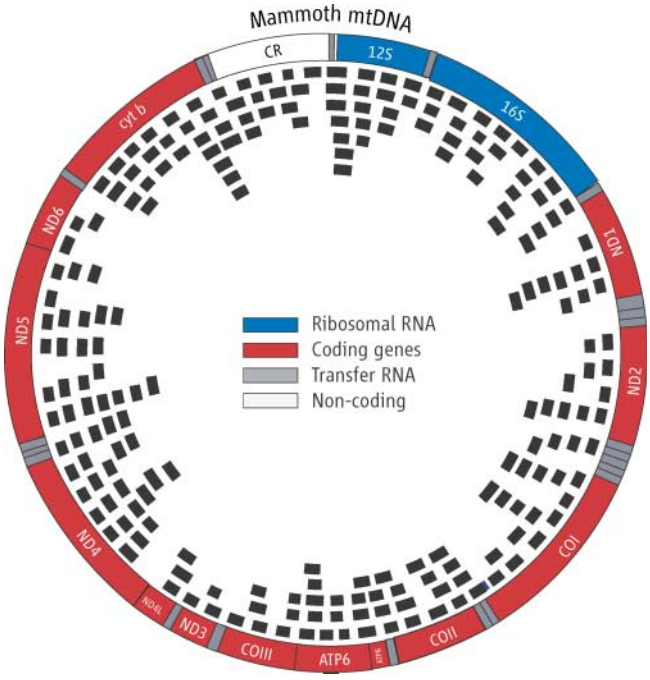

Fig. 2. Distribution of 209 reads along the mammoth mitochondrial genome (GenBank accession #NC_007596, DQ188829). Average fragment length was 89 bp; not shown to scale. To determine whether the reads were randomly distributed along the genome, we compared the distribution of fragment lengths that would result from cutting the genome at the 5′ end of each read against that resulting from 100 million randomly generated distributions of 209 reads. Despite multiple overlapping regions, the real distribution was not significantly different from the empirical distribution of fragment lengths (P = 0.069).

endogenous bacteria and nonelephantid environmental contaminants. In addition to ubiquitous contaminants resulting from handling or conditions of storage, these exogenous species are likely to represent taxa present at or immediately after the time of the mammoth's death, thereby contributing to the decomposition of the remains. To acquire a glimpse of the biodiversity of these communities, we have devised software (GenomeTaxonomyBrowser) (*27*, *28*) that allows for the taxonomic identification of various species on the basis of sequence comparison and current phylogenetic classification at the National Center for Biotechnology Information (NCBI) taxonomy browser as of November 2005 (www.ncbi.nlm.nih.gov/Taxonomy/taxonomyhome.html). We compared 302,692 reads (100%) against the nonredundant (nr) and the environmental database (env_nr). Using an adjustable factor for bitscore (*13*), we classified the reads simultaneously to the individual kingdom, phylum, class, order, family, and genus down to the species level wherever possible (fig. S2 and table S3), excluding all hits matching Gnathostomata (jawed vertebrates).

The remaining 12,563 hits within the Eukaryota (4.15%) were only surpassed by the number of bacterial hits, 17,425 (5.76%), and hits against the environmental database, 42,816 (14.15%). The kingdom Archaea was hit infrequently with only 736 hits (0.24%). Within this group, the Euryarchaeota dominated the Crenarchaeota by a ratio of 16:1. In the bacterial superkingdom, the most prevalent species were found to be proteobacteria, 5282 (1.75%); Firmicutes (gram-positives), 940 (0.31%), mostly Bacilli and Chlostridia; Actinobacteria, 2740 (0.91%); Bacteroidetes, 497 (0.16%); and the group of the Chlorobi bacteria, 248 (0.08%). Other identified microorganisms included the fungal taxa *Ashbya*, *Aspergillus*, and *Neurospora*/*Magnaporte* with 440 hits (0.14%). We also found 278 hits against viral sequences, which could be assigned to dsDNA viruses, 193 hits (0.06%); retrotranscribing viruses, 20 hits (0.01%); and ssRNA viruses, 46 hits (0.02%).

The soil-inhabiting eukaryotic species, *Dictyosteliida*, with 127 hits (0.04%), and *Entamoeba*, with 64 hits (0.02%), were found to be underrepresented, as were hits against the two nematode genomes, 277 hits (0.09%). A detailed identification of plant species is handicapped, because presently only the two plant genomes, *Arabidopsis thaliana* (mouse-ear cress) and *Oryza sativa* (rice), are publicly available. We found the hits against grass species to outnumber the ones from Brassicales by a ratio of 3:1, which could be indicative of ancient pastures on which the mammoth is believed to have grazed.

From this classification, it is evident that nonvertebrate eukaryotic and prokaryotic species occur at approximately equal ratios, with the mammalian fraction dominating the identifiable fraction of the metagenome. The paucity of fungal species is surprising, as is the low number of reads from nematodes.

Recently, a whole-genome approach was attempted from DNA of the extinct cave bear *Ursus spelaeus*, yielding ~27,000 bp of endogenous genetic material from 1.1 to 5.8% of all DNA reads (*29*). We have produced 13 million bp of endogenous genetic material from 45% of all DNA reads, some 480 times as much DNA sequence and 15 times the percentage. The ability to obtain this level of genetic information from extinct species makes it possible to consider detailed analysis of functional genes and fine-scale refinement of mutation rates. A rapid identification assay of single nucleotide polymorphisms (SNPs) would be of great value for studying population genetics of Pleistocene mammals and plants, which in turn could help elucidate their responses to climate changes during late glacial and early postglacial time and ultimately shed new light on the cause and consequences of late Quaternary extinctions.

References and Notes

1. S. Pääbo *et al.*, *Annu. Rev. Genet.* **38**, 645 (2004).
2. H. N. Poinar *et al.*, *Science* **281**, 402 (1998).
3. M. Höss, P. Jaruga, T. H. Zastawny, M. Dizdaroglu, S. Pääbo, *Nucleic Acids Res.* **24**, 1304 (1996).
4. H. N. Poinar, M. Kuch, G. McDonald, P. S. Martin, S. Pääbo, *Curr. Biol.* **13**, 1150 (2003).
5. V. Jaenicke-Despres *et al.*, *Science* **302**, 1206 (2003).
6. M. Bunce *et al.*, *Nature* **425**, 172 (2003).
7. M. Höss, S. Pääbo, N. K. Vereshchagin, *Nature* **370**, 333 (1994).
8. A. D. Greenwood, C. Capelli, G. Possnert, S. Pääbo, *Mol. Biol. Evol.* **16**, 1466 (1999).
9. E. Willerslev, A. J. Hansen, B. Christensen, J. P. Steffensen, P. Arctander, *Proc. Natl. Acad. Sci. U.S.A.* **96**, 8017 (1999).
10. E. Willerslev, A. J. Hansen, H. N. Poinar, *Trends Ecol. Evol.* **19**, 140 (2003).
11. C. I. Smith, A. T. Chamberlain, M. S. Riley, C. Stringer, M. J. Collins, *J. Hum. Evol.* **45**, 203 (2003).
12. H. N. Poinar, M. Hoss, J. L. Bada, S. Pääbo, *Science* **272**, 864 (1996).
13. Materials and methods are available as supporting material on *Science* Online.
14. R. Debruyne, V. Barriel, P. Tassy, *Mol. Phylogenet. Evol.* **26**, 421 (2003).
15. O. Handt, M. Krings, R. H. Ward, S. Pääbo, *Am. J. Hum. Genet.* **59**, 368 (1996).
16. R. D. E. MacPhee *et al.*, *J. Arch. Sci.* **29**, 1017 (2002).
17. R. MacPhee, A. Tikhonov, D. Mol, A. D. Greenwood, *BMC Evol. Biol.* **5**, 49 (2005).
18. A. D. Greenwood, C. Capelli, G. Possnert, S. Pääbo, *Mol. Biol. Evol.* **16**, 1466 (1999).
19. M. Margulies *et al.*, *Nature* **437**, 376 (2005).
20. S. Schwartz *et al.*, *Genome Res.* **13**, 103 (2003).
21. W. Makalowski, J. H. Zhang, M. S. Boguski, *Genome Res.* **6**, 846 (1996).
22. A. Siepel *et al.*, *Genome Res.* **15**, 1034 (2005).
23. R. H. Waterston *et al.*, *Nature* **420**, 520 (2002).
24. T. Lindahl, *Nature* **362**, 709 (1993).
25. M. Hofreiter, V. Jaenicke, D. Serre, A. von Haeseler, S. Pääbo, *Nucleic Acids Res.* **29**, 4793 (2001).
26. A. D. Greenwood, S. Pääbo, *Mol. Ecol.* **8**, 133 (1999).
27. D. H. Huson, A. Auch, J. Qi, S. C. Schuster, in preparation.
28. GenomeTaxonomyBrowser will be made available to readers upon request.
29. J. P. Noonan *et al.*, *Science* **309**, 597 (2005).

30. We thank D. Poinar, C. Flemming, and E. Willerslev for help in mammoth sampling; N. E. Wittekindt and A. Rambaut for help with the manuscript; and two anonymous reviewers. We also thank the Natural Sciences and Environmental Research Council of Canada (299103-2004) for a grant to H.N.P. and McMaster University for financial support. R.D.E.M. was supported by NSF OPP 0117400, B.S. was supported by the Wellcome Trust, and W.M. was supported by NIH grant HG02238. S.C.S. thanks The Pennsylvania State University for initial funding.

Supporting Online Material

www.sciencemag.org/cgi/content/full/1123360/DC1
Materials and Methods
Figs. S1 and S2
Tables S1 to S4
References

2 December 2005; accepted 15 December 2005
Published online 20 December 2005;
10.1126/science.1123360
Include this information when citing this paper.

Methylation of tRNA^{Asp} by the DNA Methyltransferase Homolog Dnmt2

Mary Grace Goll,[1] Finn Kirpekar,[2] Keith A. Maggert,[3] Jeffrey A. Yoder,[4] Chih-Lin Hsieh,[5] Xiaoyu Zhang,[6] Kent G. Golic,[7] Steven E. Jacobsen,[6] Timothy H. Bestor[1]*

The sequence and the structure of DNA methyltransferase-2 (Dnmt2) bear close affinities to authentic DNA cytosine methyltransferases. A combined genetic and biochemical approach revealed that human DNMT2 did not methylate DNA but instead methylated a small RNA; mass spectrometry showed that this RNA is aspartic acid transfer RNA (tRNA^{Asp}) and that DNMT2 specifically methylated cytosine 38 in the anticodon loop. The function of DNMT2 is highly conserved, and human DNMT2 protein restored methylation in vitro to tRNA^{Asp} from Dnmt2-deficient strains of mouse, *Arabidopsis thaliana*, and *Drosophila melanogaster* in a manner that was dependent on preexisting patterns of modified nucleosides. Indirect sequence recognition is also a feature of eukaryotic DNA methyltransferases, which may have arisen from a Dnmt2-like RNA methyltransferase.

The DNA (cytosine 5) methyltransferases of the Dnmt1 and Dnmt3 families establish and maintain patterns of methylation at cytosine residues in flowering plants, deuterostomes, and a subset of protostomes (*1*). Proteins of the Dnmt2 family show all the sequence and structural characteristics of DNA methyltransferases (*2*–*5*) except for a putative nucleic acid binding cleft that cannot easily accommodate duplex DNA (*1*). Despite the sequence and structural affinities between Dnmt2 and authentic DNA methyltransferases, genomic methylation patterns are not measurably altered in Dnmt2-deficient mouse embryonic stem (ES) cells (*6*).

Localization experiments indicate that Dnmt2 does not have the properties expected of a DNA methyltransferase. Human DNMT2 protein (hDNMT2) is primarily localized to the cytoplasm of transfected mouse 3T3 fibroblasts (Fig. 1). The cytoplasmic localization of DNMT2 contrasts with the exclusively nuclear localization of Dnmt1 and Dnmt3 (*7*, *8*).

The biological function of Dnmt2 was evaluated in strains of mouse, *Arabidopsis thaliana*, and *Drosophila melanogaster* that lack Dnmt2 (Fig. 2). The mouse deletion allele excised amino acids 181 to 359; this region includes the highly conserved Cys-Phe-Thr-XX-Tyr-XX-Tyr (where X is any amino acid) motif unique to Dnmt2 homologs (*1*, *4*) and DNA cytosine methyltransferase motifs VIII and IX (Fig. 2A and fig. S1). The *MT2*/*Dnmt2* (hereafter *dDnmt2*) gene of *D. melanogaster* was disrupted by insertion of 28 base pairs of sequence that contained three in-frame stop codons and a +1 frameshift 5′ of the region that encodes motif IV (Fig. 2B), which is required for enzymatic activity (*9*). Wild-type *Dnmt2* sequence was not present in flies homozygous for this mutation (fig. S2). A strain of *A. thaliana* that contains a large *Agrobacterium* transferred DNA (T-DNA) insertion adjacent to exon 7 (Fig. 2C) was obtained from the Salk T-DNA collection (*10*). The introduction of deletion or truncating mutations in all three organisms causes loss of catalytic motifs that

[1]Department of Genetics and Development, College of Physicians and Surgeons, Columbia University, New York, NY 10032, USA. [2]Department of Biochemistry and Molecular Biology, University of Southern Denmark, Campusvej 55, DK-5230 Odense M, Denmark. [3]Department of Biology, Texas A&M University, College Station, TX 77843, USA. [4]Department of Molecular Biomedical Sciences, College of Veterinary Medicine, North Carolina State University, Raleigh, NC 27606, USA. [5]Department of Urology and Department of Biochemistry and Molecular Biology, University of Southern California, Los Angeles, CA 90089, USA. [6]Howard Hughes Medical Institute (HHMI) and Department of Molecular, Cell, and Developmental Biology, University of California, Los Angeles, CA 90095, USA. [7]Department of Biology, University of Utah, Salt Lake City, UT 84112, USA.

*To whom correspondence should be addressed. E-mail: THB12@Columbia.edu

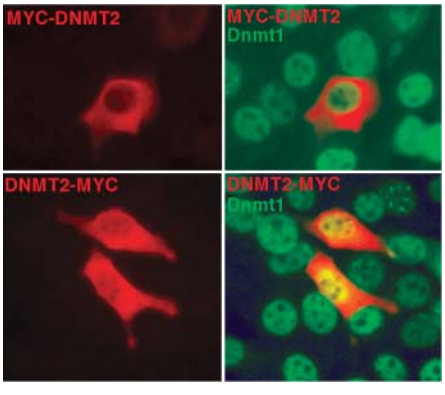

Fig. 1. Cytoplasmic localization of hDNMT2 in NIH3T3 cells. Cells were transiently transfected with hDNMT2 expression constructs that added an N- or C-terminal Myc epitope tag. Immunofluorescence shows localization of hDNMT2 (red) primarily in the cytoplasm, whereas Dnmt1 (green) is exclusively nuclear.

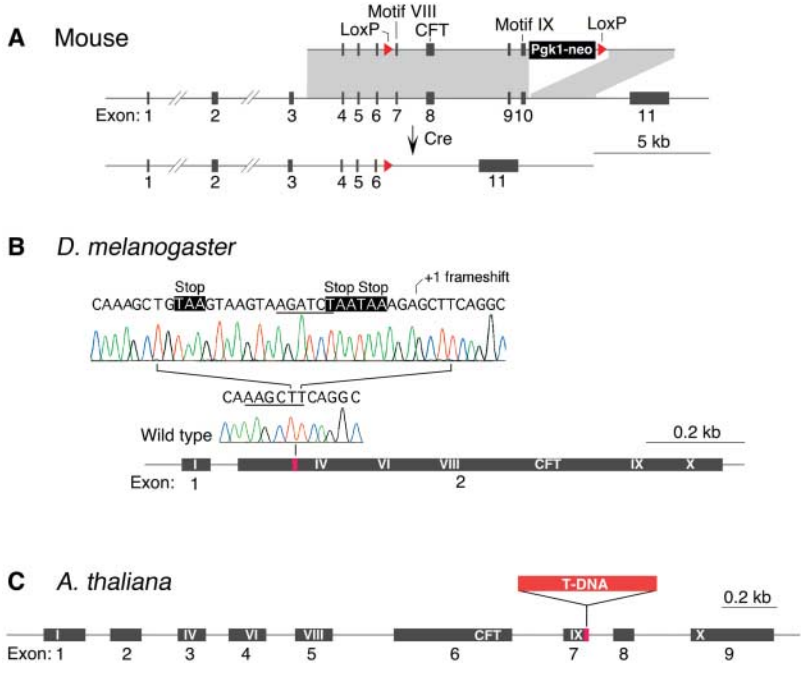

Fig. 2. Mutant alleles of *Dnmt2* homologs in mouse, *D. melanogaster*, and *A. thaliana*. (**A**) loxP sites were introduced into the mouse *Dnmt2* gene by homologous recombination in ES cells, and the indicated deletion was induced by exposure to Cre recombinase (fig. S1). Roman numerals indicate DNA cytosine methyltransferase catalytic motifs. The conserved Cys-Phe-Thr-XX-Tyr-XX-Tyr motif diagnostic of Dnmt2 proteins is indicated by CFT. (**B**) Homologous recombination was used to introduce three in-frame stop codons and a +1 frameshift at the HindIII site in exon 2 of *D. melanogaster dDnmt2*. No wild-type *Mt2/dDnmt2* sequence was present in the homozygous fly stock (fig. S2). (**C**) A large T-DNA insertion 3′ of exon 7 of the *A. thaliana Dnmt2* gene allele truncates the mRNA (fig. S3).

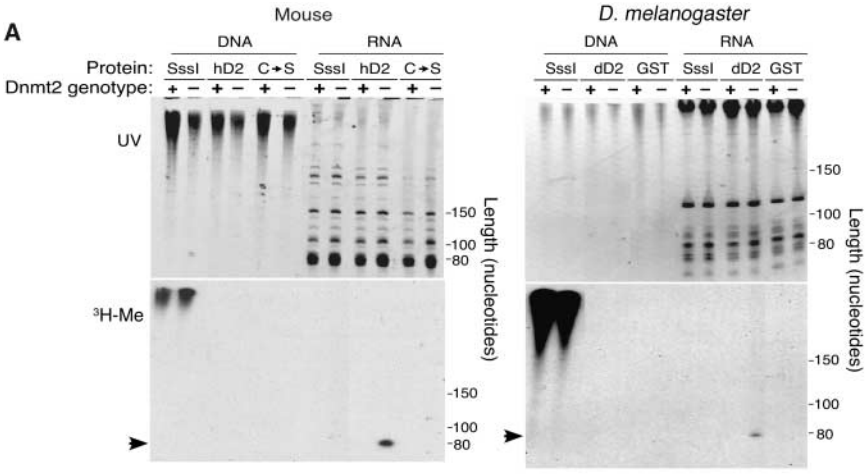

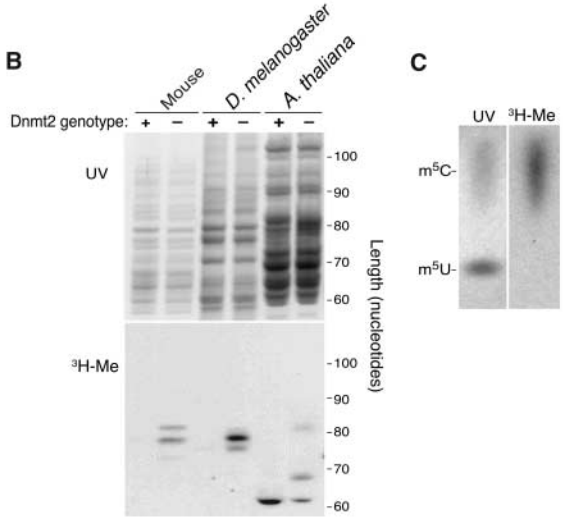

Fig. 3. DNMT2 methylates only a small RNA from DNMT2-deficent tissues. (**A**) Total DNA or RNA from wild-type or *Dnmt2*$^{-/-}$ mice was incubated with ^{3}H-AdoMet and either the bacterial DNA cytosine methyltransferase M.Sss1, His-tagged hDNMT2, or His-tagged hDNMT2 in which Cys^{79} in motif IV was substituted with serine. Nucleic acids were separated by electrophoresis, stained with ethidium bromide, and then prepared for fluorography. No evidence of methylation of DNA by hDNMT2 was seen, but a single small RNA was labeled (arrow) when that RNA originated from Dnmt2$^{-/-}$ mice. Total DNA or RNA from wild-type or *dDnmt2*$^{-/-}$ adult *D. melanogaster* was incubated with M.SssI, glutathione *S*-transferase (GST)-tagged *D. melanogaster* dDnmt2 purified from *E. coli*, or GST alone as on the left-hand gel. Only a small RNA was methylated (arrow). UV, ultraviolet. (**B**) High-resolution analysis of the Dnmt2 target RNA. hDNMT2 was incubated with ^{3}H-AdoMet and total RNA isolated from wild-type and *Dnmt2*$^{-/-}$ mice, *D. melanogaster*, and *A. thaliana*. An additional methylated band with a size of ~68 nucleotides present in RNA from *Dnmt2*$^{-/-}$ *A. thaliana* RNA is likely to represent an additional Dnmt2 substrate in flowering plants. The ~63-nucleotide band in the *A. thaliana* samples is a hDNMT2 substrate even when wild-type RNA is used, which suggests that this RNA species is not methylated in vivo. (**C**) Mouse *Dnmt2*$^{-/-}$ RNA was incubated with hDNMT2 and ^{3}H-AdoMet and hydrolyzed to nucleosides, which were resolved by thin-layer chromatography. The methylated product comigrated with 5-methyl cytosine (m^{5}C).

are required for enzymatic activity (Fig. 2 and figs. S1 to S3).

Strains of mouse, *D. melanogaster*, and *A. thaliana* homozygous for inactivating mutations in *Dnmt2* were viable, fertile, and morphologically indistinguishable from wild-type counterparts. The homozygous *Dnmt2* mutation did not modify the phenotype of mice homozygous for mutations in *Dnmt1*, nor did the homozygous *Dnmt2* mutation modify the phenotypes of *A. thaliana* homozygous for mutations in *drm1* and *drm2* (domains rearranged methyltransferases 1 and 2) or *cmt3* (chromomethylase 3) (*11*). Genomic methylation patterns were not detectably altered in Dnmt2-deficient mouse tissues (fig. S4).

We developed a combined biochemical and genetic approach to address the function of Dnmt2. Purified hDNMT2 was tested for its ability to transfer tritium-labeled methyl groups from the cofactor [^{3}H-*methyl*] S-adenosyl-L-methionine (^{3}H-AdoMet) to genomic DNA and RNA purified from wild-type or *Dnmt2*$^{-/-}$ mice. No DNA methylation was observed (Fig. 3A), but hDNMT2 specifically methylated a small RNA molecule when RNA from *Dnmt2*$^{-/-}$ mouse tissues was the substrate; wild-type RNA from mouse was not labeled (Fig. 3A). This implied that the small RNA molecule was the in vivo target of Dnmt2 and that wild-type RNA is methylated in vivo and cannot serve as substrate for methylation in vitro. Mutation of a key catalytic residue (Cys^{79} in motif IV) (*9*) abolished RNA methyltransferase activity (Fig. 3A). Purified *D. melanogaster* Dnmt2 protein (MT2, hereafter dDnmt2) did not methylate DNA but methylated a small RNA molecule only when that RNA was isolated from *Dnmt2*$^{-/-}$ flies (Fig. 3A).

Dnmt2 was found to have the same function in mammals, flowering plants, and dipteran insects. Purified hDNMT2 methylated one or two RNA molecules of ~80 nucleotides in length when RNA was isolated from *Dnmt2*-deficient mouse, *D. melanogaster*, or *A. thaliana* (Fig. 3, A and B). In all three organisms, hDNMT2 specifically methylated these RNAs only when the RNA was derived from Dnmt2-deficient tissues.

Inspection of the organization of functional groups within the putative active site of hDNMT2 (*4*) indicated that either cytosine or uracil might be the methylation target (*12*). The identity of the modified base was determined by thin-layer chromatography of nucleosides from hydrolysates of RNA labeled with hDNMT2 and ^{3}H-AdoMet. The product of hDNMT2 comigrated with authentic 5-methylcytidine and was clearly resolved from the 5-methyluridine standard (Fig. 3C).

The identity of the RNA substrate was determined by comparison of mass spectra of ribonuclease (RNase) T1 oligonucleotides from the Dnmt2 substrate purified from *Dnmt2*$^{-/-}$ and *Dnmt2*$^{+/+}$ mouse tissues. Matrix-assisted laser desorption/ionization–time-of-flight (MALDI-TOF) mass spectrometry identified a single oligonucleotide that showed a difference of 14 atomic mass units when the wild-type and *Dnmt2*$^{-/-}$ samples were compared, which indicated the loss of a single methyl group (Fig. 4A). Mass spectrometry analysis of this oligonucleotide revealed a hypermodified hexose-queuosine base in the T1 fragment that contained the Dnmt2 target cytosine. Hexose-queuosine has been found in only tRNA^{Tyr} and tRNA^{Asp}, which contain galactosylqueuosine and mannosylqueuosine, respectively; in both cases, the hexose-queuosine is located in the wobble position of the anticodon (*13*, *14*). Tandem mass spectrometry on the T1 fragment that contained the Dnmt2 target cytosine yielded the sequence of the T1 oligonucleotide of the tRNA^{Asp} anticodon loop. Methylation was observed at cytosine 38 of wild-type tRNA^{Asp}, the second nucleotide 3′ of the anticodon, but this position was unmethylated in RNA from Dnmt2-deficient tissues (tables S1 and S2 and fig. S5).

Confirmation that the Dnmt2 target is tRNA^{Asp} was provided by Northern blot analysis of RNA from *Dnmt2*$^{-/-}$ and *Dnmt2*$^{+/+}$ tissues with probes to tRNA^{Asp}. In *Dnmt2*$^{-/-}$ mice, the tRNA substrate showed increased mobility relative to that of the wild type; the mass spectrometry data indicated that this mobility shift was the result of a loss of one methyl group.

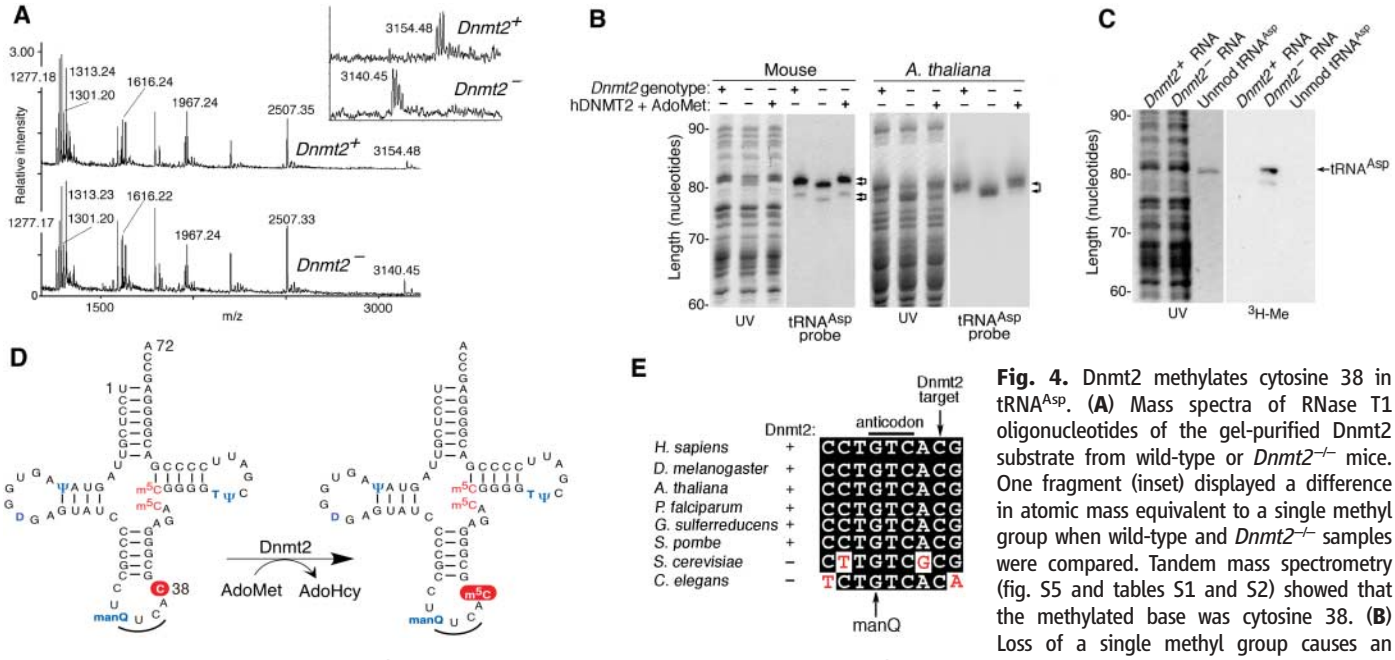

Fig. 4. Dnmt2 methylates cytosine 38 in $tRNA^{Asp}$. (**A**) Mass spectra of RNase T1 oligonucleotides of the gel-purified Dnmt2 substrate from wild-type or *Dnmt2*$^{-/-}$ mice. One fragment (inset) displayed a difference in atomic mass equivalent to a single methyl group when wild-type and *Dnmt2*$^{-/-}$ samples were compared. Tandem mass spectrometry (fig. S5 and tables S1 and S2) showed that the methylated base was cytosine 38. (**B**) Loss of a single methyl group causes an increase in electrophoretic mobility of $tRNA^{Asp}$. Electrophoresis and Northern blot analysis with $tRNA^{Asp}$ probes from mouse and *A. thaliana* confirmed that the target of Dnmt2 is $tRNA^{Asp}$. Identical results were obtained with probes complementary to the 3′ and 5′ ends of $tRNA^{Asp}$. Double arrows indicate the methylation-dependent mobility shift. Dnmt2 in *A. thaliana* has one additional target of ~68 nucleotides in addition to $tRNA^{Asp}$. (**C**) Methylation of $tRNA^{Asp}$ is dependent on preexisting modifications. Unmodified $tRNA^{Asp}$ produced by in vitro transcription was inactive as a hDNMT2 substrate. (**D**) Summary of pattern of modifications of $tRNA^{Asp}$. The mass spectrometry data show that Dnmt2 is required for methylation of position 38 in the anticodon loop of $tRNA^{Asp}$; formation of m^5C at positions 48 and 49 is independent of Dnmt2. Anticodon bases are underlined; mannosylqueuosine is indicated as manQ; other modified nucleosides are shown in blue; pseudouridine is indicated as Ψ; m^5C, in red. (**E**) Sequence alignment of the anticodon loops of $tRNA^{Asp}$. The sequence is invariant among organisms that contain Dnmt2, but base substitutions have occurred at positions adjacent to the target cytosine in $tRNA^{Asp}$ of *S. cerevisiae* and *C. elegans*, whose genomes do not contain a *Dnmt2*-related gene.

Incubation of *Dnmt2*$^{-/-}$ RNA with hDNMT2 and AdoMet restored the wild-type mobility (Fig. 4B). In mouse, the $tRNA^{Asp}$ probe hybridized to two bands of similar mobility, both of which showed a modification-dependent mobility shift (Fig. 4B). These bands are likely to represent populations of differentially modified $tRNA^{Asp}$; heterogeneity of tRNA modification patterns (*15*) and methylation-dependent shifts in electrophoretic mobility of tRNAs (*16*) have been observed. Northern blot analysis of RNA from *A. thaliana* with a $tRNA^{Asp}$ probe revealed a single band that had a Dnmt2-dependent mobility shift, which confirmed that $tRNA^{Asp}$ is the Dnmt2 target in mouse and *A. thaliana* (Fig. 4B). Cytosine 38 had been previously reported to be methylated in $tRNA^{Asp}$ from mouse and *Xenopus laevis* (*14*, *17*) (Fig. 4B). Unmodified $tRNA^{Asp}$ produced by in vitro transcription was not a substrate for DNMT2 (Fig. 4C), which suggests that methylation is guided to cytosine 38 by other modifications; mannosylqueuosine is likely to be involved, because it is unique to $tRNA^{Asp}$.

Analysis of $tRNA^{Asp}$ sequences showed complete conservation of the anticodon loop in species whose genomes encode Dnmt2 homologs, but the $tRNA^{Asp}$ anticodon loops in *Caenorhabditis elegans* and *Saccharomyces cerevisiae*, which lack Dnmt2 homologs, have diverged (Fig. 4E). The bacterium *Geobacter sulferreducens* contains a Dnmt2 homolog, and the $tRNA^{Asp}$ anticodon loop of this organism is identical to that of Dnmt2-containing eukaryotes. These findings indicate coevolution of Dnmt2 and the anticodon loop of $tRNA^{Asp}$. The strong conservation of Dnmt2 across divergent taxa indicate that it is under positive selection and suggests that Dnmt2 increases fitness under unidentified sources of stress or has an incremental effect on fitness that is not apparent under laboratory conditions.

The data shown here indicate that Dnmt2 methylates an RNA, even though the sequence and the order of catalytic motifs of Dnmt2 are characteristic of DNA rather than RNA methyltransferases (*18*, *19*). Methylation of $tRNA^{Asp}$ by Dnmt2 requires information beyond the RNA sequence, and structural information is involved in target selection by other RNA methyltransferases (*20*, *21*). Indirect sequence recognition is also a feature of eukaryotic DNA cytosine methyltransferases (*1*), whereas bacterial restriction methyltransferases have innate sequence specificity that determines the structure of genomic methylation patterns in these organisms [reviewed in (*22*)]. This raises the possibility that eukaryotic DNA cytosine methyltransferases were derived from an ancestral Dnmt2-like RNA methyltransferase rather than prokaryotic restriction DNA methyltransferases, which could explain the profound differences in mechanisms of target selection by DNA cytosine methyltransferases of prokaryotes and eukaryotes (*1*).

References and Notes

1. M. G. Goll, T. H. Bestor, *Annu. Rev. Biochem.* **74**, 481 (2005).
2. C. R. Wilkinson, R. Bartlett, P. Nurse, A. P. Bird, *Nucleic Acids Res.* **23**, 203 (1995).
3. J. A. Yoder, T. H. Bestor, *Hum. Mol. Genet.* **7**, 279 (1998).
4. A. Dong *et al.*, *Nucleic Acids Res.* **29**, 439 (2001).
5. J. Posfai, A. S. Bhagwat, G. Posfai, R. J. Roberts, *Nucleic Acids Res.* **17**, 2421 (1989).
6. M. Okano, S. Xie, E. Li, *Nucleic Acids Res.* **26**, 2536 (1998).
7. H. Leonhardt, A. W. Page, H. U. Weier, T. H. Bestor, *Cell* **71**, 865 (1992).
8. K. E. Bachman, M. R. Rountree, S. B. Baylin, *J. Biol. Chem.* **276**, 32282 (2001).
9. D. V. Santi, C. E. Garrett, P. J. Barr, *Cell* **33**, 9 (1983).
10. J. M. Alonso *et al.*, *Science* **301**, 653 (2003).
11. M. G. Goll *et al.*, unpublished data.
12. M. Sprinzl, K. S. Vassilenko, *Nucleic Acids Res.* **33**, D139 (2005).
13. G. D. Johnson, I. L. Pirtle, R. M. Pirtle, *Arch. Biochem. Biophys.* **236**, 448 (1985).
14. Y. Kuchino, N. Shindo-Okada, N. Ando, S. Watanabe, S. Nishimura, *J. Biol. Chem.* **256**, 9059 (1981).
15. H. Taniguchi, N. Hayashi, *Nucleic Acids Res.* **26**, 1481 (1998).
16. D. Mangroo, P. A. Limbach, J. A. McCloskey, U. L. RajBhandary, *J. Bacteriol.* **177**, 2858 (1995).
17. E. Haumont, K. Nicoghosian, H. Grosjean, R. J. Cedergren, *Biochimie* **66**, 579 (1984).

18. C. Gustafsson, R. Reid, P. J. Greene, D. V. Santi, *Nucleic Acids Res.* **24**, 3756 (1996).
19. M. Y. King, K. L. Redman, *Biochemistry* **41**, 11218 (2002).
20. P. G. Foster, C. R. Nunes, P. Greene, D. Moustakas, R. M. Stroud, *Structure* **11**, 1609 (2003).
21. T. T. Lee, S. Agarwalla, R. M. Stroud, *Cell* **120**, 599 (2005).
22. X. Cheng, R. J. Roberts, *Nucleic Acids Res.* **29**, 3784 (2001).
23. We thank K. Anderson and M. Damelin for comments on the manuscript; X. Cheng for helpful discussions; and B. Berkovits, S. Chen, B. Erlanger, A. Getz, A. Kljuic, C. Köhrer, N. Papavasiliou, K. Politi, and U. RajBhandary for advice and assistance. Supported by grants from the NIH and the Danish Natural Science Research Council.

Supporting Online Material
www.sciencemag.org/cgi/content/full/311/5759/395/DC1
Materials and Methods
Figs. S1 to S5
Tables S1 and S2

5 October 2005; accepted 20 December 2005
10.1126/science.1120976

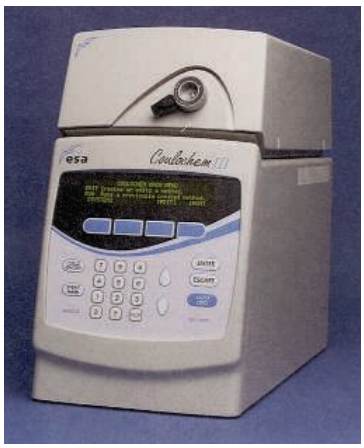

Electrochemical Detector

The Coulochem III combines coulometric and amperometric detection in a flexible high-performance electrochemical detector system. In combination with ESA's patented electrodes, the Coulochem III detector is the only electrochemical detector to offer redox capability in a single cell. Compatible with all high-performance liquid chromatography columns and offering a wide choice of operating modes, the instrument readily quantifies picogram to femtogram levels of oxidizable or reducible neurochemical, clinical, pharmaceutical, environmental, and biological compounds in a sample. The instrument's advanced electronics give it stability and low limits of detection.

ESA Biosciences For information 978-250-7000 www.esainc.com

Druggable Genome siRNA Set

The Human Druggable Genome siRNA Set V2.0 is a second-generation small-interfering RNA (siRNA) set that enables gene silencing studies of 6992 potential human druggable targets. The siRNAs are designed using the innovative HiPerformance siRNA Design Algorithm, ensuring maximum silencing and minimum risk of nonspecific effects. Applications for the siRNAs include being used in combination with an assortment of high-throughput phenotypic screening technologies to interrogate novel mammalian gene function in cell-based assays.

Qiagen
For information 800-426-8157 www.qiagen.com

Upright/Inverted Research Microscope

The Up/Down Microscope combines an upright and an inverted microscope in one instrument. It is designed primarily for researchers who are performing two different imaging techniques on a single specimen, such as doing total internal reflection fluorescent microscopy on the bottom and electrophysiology with water dripping on the top. It can be used with multiple cameras and accessories.

Olympus
For information 800-446-5967
www.olympusamerica.com/microscopes

Evaporation of Acidic Chemicals

A new version of the popular HT-12 Series II, the HT-12 HCl system, enables chemists to evaporate high concentrations of hydrogen chloride, achieving cleaner synthesis and de-protection than can be achieved with other acids, such as trifluoroacetic acid. The innovative design of the HT-12 HCl system presents advantages for all chemists faced with removing both regular solvents and strongly acidic chemicals. The HT-12 HCl makes use of inert and corrosion-proof materials to enable high concentrations of hydrochloric acid and other acid chlorides to be removed without any loss of performance or long-term deterioration in the system. The HT-12's high performance and high sample capacities make it a suitable workhorse for applications that require high-throughput evaporation, including combinatorial chemistry, parallel synthesis, liquid chromatography/mass spectrometry purification, compound purification, plate re-formatting, and plate replication.

Genevac
For information 845-267-2211 www.genevac.com

Drug-Like Screening Compounds

The MyriaScreen Diversity Collection of drug-like screening compounds is the result of careful evaluation, filtering, and refinement of selections from each of the menu's screening compound collections. The collection is comprised of 10,000 high-purity screening compounds picked to maximize chemical diversity while maintaining drug-likeness. The collection was assembled from a pool over more than 300,000 screening compounds using a combination of filters, diversity predictors, and manual selection. The resulting 10,000 compounds are drug-like, chemically diverse, and amenable to follow-up chemistry and optimization. The collection is well-suited for researchers looking for a small, cost-effective, ready-to-screen set of high-quality screening compounds.

Sigma-Aldrich
For information 314-286-7626 www.sigma-aldrich.com

Laser Scanning Microscopes

The LSM 5 DUO is a combination of two state-of-the-art confocal laser scanning microscopes, the LSM 510 META and LSM 5 Live, to form a multipurpose workstation with great experimental versatility. The qualities of the LSM 5 DUO allow fast line scanning, ultra-precise point scanning, spectral and non-linear imaging, and flexible optical sample micromanipulation. The LSM 5 DUO brings a breadth of benefits previously unmatched in a single workstation. Dynamic processes up to the kHz range can be observed using the system's fast acquisition capabilities. The combination of the groundbreaking beam splitter and high quantum-efficiency charge-coupled device line detection delivers the necessary system sensitivity. Acquisition in multiple channels makes time-saving, specimen-preserving spectral imaging possible. Two independent scanner groups provide great flexibility in optical sample micromanipulation for applications utilizing fluorescence recovery after photobleaching or photoactivatable and photoconvertible variants of fluorescent proteins. Real-time electronics and computing allow gigabytes of data to be handled effortlessly.

Zeiss +49 3641 64 2770 www.zeiss.com

Newly offered instrumentation, apparatus, and laboratory materials of interest to researchers in all disciplines in academic, industrial, and government organizations are featured in this space. Emphasis is given to purpose, chief characteristics, and availability of products and materials. Endorsement by *Science* or AAAS of any products or materials mentioned is not implied. Additional information may be obtained from the manufacturer or supplier by visiting www.science.labvelocity.com on the Web, where you can request that the information be sent to you by e-mail, fax, mail, or telephone.